Developing tools to investigate initiating events of mitochondrial translation

Yasmin Proctor-Kent

Thesis submitted to Newcastle University for the Degree of Doctor of Philosophy

Biosciences Institute

Faculty of Medical Sciences

Wellcome Centre for Mitochondrial Research

April 2021

For my Dad

Author Declaration

This thesis is submitted for the degree of Doctor of Philosophy at Newcastle University. This research was conducted in the Wellcome Centre for Mitochondrial Research, Biosciences Institute, Newcastle University under the supervision of Professor Zofia Chrzanowska-Lightowlers and Professor Robert Lightowlers. I declare that the work described here is my own, unless stated otherwise. I certify that none of the material presented here has been previously submitted by me for any degree or qualification at this or any other university.

Yasmin Proctor-Kent

Abstract

Mitochondria are the predominant source of adenosine triphosphate (ATP) in nucleated human cells. ATP is required as cellular energy source and mitochondria synthesise ATP by coupling the oxidative phosphorylation (OXPHOS) system. Mitochondria contain their own circular DNA (mtDNA) which encodes 11 messenger RNA (mt-mRNA), 2 ribosomal RNA (mt-rRNA), and 22 tRNA (mt-tRNA) molecules which are all utilized for the synthesis of 13 proteins, all key components of the multi-subunit OXPHOS complexes, by the mitochondrial ribosome (mitoribosome). Much of the life cycle of mt-RNA and the process of translation is still unclear, in particular a full understanding of mt-mRNA stability, delivery, and loading onto the mt-SSU (or mitoribosomes) is lacking. The aim of this research was to investigate these processes using super resolution imaging of mt-rRNA and proximity-dependent proteomic analysis.

I have visualised mt-rRNA molecules beyond the diffraction limit by the development and application of RNA Fluorescent In Situ Hybridisation (FISH) compatible with STimulated Emission Depletion (STED) microscopy. This technique was used to validate the loss of the 16S mt-rRNA upon induction of the mitochondrially-targeted VapC20 endonuclease and has contributed to a model wherein the formation of the monosome is an important factor in mt-mRNA transcript stability.

To further understand the process of mt-mRNA loading onto the mitoribosome, I employed proximity-dependent biotin identification (BioID) to uncover proteins which may be enriched at the mitoribosome mt-mRNA entry site. Multiple mitoribosomal proteins were fused to the BioID moiety, expressed in human cells, and screened for their ability to assemble into the mitoribosome. Mass spectrometry was used to characterise the proximal interaction network of MRPS39 and MRPS27 which uncovered the heterodimeric proteins PHB and PHB2. These proteins were then investigated to further understand their roles in mitochondrial translation.

This thesis presents a thorough investigation into mt-RNA and mitochondrial translation and provides tools and techniques that complement the current literature.

Acknowledgements

Firstly, I would like to thank my supervisors Zosia and Bob for the unending support throughout this research. Thank you for the opportunity to research in such a fantastic laboratory and for your patience in supporting me to submission.

Thank you to all of the members of the Mitochondrial Research Group for creating such a great place to work and research. There are many fantastic scientists who have provided support and guidance that I would like to mention specifically. Thank you to Francesco Bruni, Rolando Berlinguer-Palmini, Fei Gao, Rawaa Ali Zahid Bakr Al-Faresi, Dr Richard Temperley, Thomas Nicholls, Christin Albus, Anetta Svitorka Hartlova, Frederic Lamoliatte, Akshada Gajbhiye for your contributions. I would like to thank my internal PhD assessors Dr Alex Laude, Dr Laura Greaves, and Dr Oliver Russell for insight and assistance.

A special mention has to go to the wonderful Kretins: Charlotte, Shane, Adam, Nish, Matt, Hannah, Pav and Carla. You made long lab days actually enjoyable, and made the fun bits exceptional. To my office, Shane, Adam, Matt, and Ana – I couldn't have asked for a better group of mates to spend the last few years chatting, complaining, singing, and laughing with. My housemates, Ruth and Charlotte, I don't know how you put up with me, but I am so fortunate to have made so many memories with you (mostly hungover McDonalds).

Thank you to my friends in Newcastle who have kept me sane and definitely not sober over the last few years. I would not have been able to get this far without Novocastrians Rugby Club; whether playing or coaching, I always had rugby to go to as a distraction and a comfort.

My utter faves Rob, Ell, and Will - you are totally adequate company but cheers, nonetheless.

Sophie, you have put up with more than everyone else combined. I will never understand how I got lucky enough to have you in my life. Thank you for every conversation, every hug, and every kiss. Thank you for always believing in me, and for looking so good while you do it.

To my best friend Ellie, words can't describe how much I cherish our friendship. You truly mean the world to me and I am thankful every day that fate put us next to each other in halls- I have never looked back since.

Finally, I want to thank my family for the constant support you have given me and pride you have had in me. Mum, you are one of the strongest people I know, you taught me how to make it through the difficult times. Dad, you are my favourite person. You are the reason that I cherish learning, creativity, and healthy debate. You will continue to inspire me every day.

List of publications

Zorkau M*, **Proctor-Kent Y*,** Berlinguer-Palmini R, Hamilton A, Chrzanowska-Lightowlers ZM, Lightowlers RN. Visualizing Mitochondrial Ribosomal RNA and Mitochondrial Protein Synthesis in Human Cell Lines. Methods Mol Biol. 2021;2192:159-181. doi: 10.1007/978-1-0716-0834-0_13. PMID: 33230773.

runi F, **Proctor-Kent Y**, Lightowlers RN, Chrzanowska-Lightowlers ZM. Messenger RNA delivery to mitoribosomes - hints from a bacterial toxin. FEBS J. 2021 Jan;288(2):437-451. doi: 10.1111/febs.15342. Epub 2020 May 11. PMID: 32329962; PMCID: PMC7891357.

Courses and Conferences attended

Light microscopy workshop – Training course at Newcastle University (2016)

Newcastle University Practicalities of Cellular Analysis – Poster (2017)

Royal Microscopical Society Microscience Microscopy Congress – Attendee (2017)

Early Career Mitoscientist Meeting, Newcastle – Oral presentation (2017)

Conference organiser and chair

FEBS EMBO Advanced Lecture Course: Mitochondria in life, death and disease, Bari – Poster presentation (2018)

Awarded Youth Travel Grant

Abbreviations

ADP	Adenosinediphosphate
AIF	Apoptosis inducing factor
APS	Ammonium persulfate
A-site	Aminoacyl site
ATP	Adenosine triphosphate
ATPn	Subunit of complex V (n= number and/or letter)
BioID	Proximity-dependent biotin identification
Bp	Base pair
BSA	Bovine serum albumin
C610	Cal fluor610
cDNA	Complementary DNA
CM	Cristae membrane
CMV	Cytomegalovirus
CO2	Carbon dioxide
COX	Subunit of complex IV
Ct	Cycle threshold
CyB	Cytochrome B
DAP3	Death associated protein 3
DDX28	DEAD-box helicase 28
DEPC	Diethyl pyrocarbonate
dH2O	Distilled water
D-loop	Displacement loop

DMEM	Dulbecco's modified eagle medium
DMSO	Dimethyl sulphoxide
DNA	Deoxyribonucleic acid
dNTP	Deoxynucleotide
Drp1	Dynamin related protein 1
DTT	Dithiothreitol
DW	Distilled water
EDTA	Ethylene diamine tetraacetic acid
EGTA	Ethylene glycol tetraacetic acid
eIF4e	Eukaryotic translation initiation factor 4E
ELAC2	Elac homologue 2
EM	Electron microscopy
ERAL1	Era-like 12S mitochondrial rna chaperone 1)
E-site	Exit site
EtBr	Ethidium bromide
FAD	Flavin adenine dinucleotide
FASTK	Fas activated serine/threonine kinase
FCS	Foetal calf serum
Fe/S	Iron-sulphur
Fis1	Mitochondrial fission protein 1
FMN	Flavin mononucleotide
GA	Glutaraldehyde
GDH	Glutamate dehydrogenase
GDP	Guanosine diphosphate

GRSF1	G-rich RNA sequence binding factor 1
GTP	Guanosine triphosphate
H+	Hydrogen
h44	Helix 44
HEK	Human embryonic kidney
HeLa	Henrietta lacks
HSP	Heavy strand promoter
Hsp60	Heat shock protein 60
IBM	Inner boundary membrane
ICT1	Immature colon carcinoma transcript 1
IMM	Inner mitochondrial membrane
IMS	Inter membrane space
IP	Immunoprecipitation
KCl	Potassium chloride
kDa	Kilodalton
LACTB2	Lactamase beta 2
LB	Luria bertani
LRPPRC	Leucine rich pentatricopeptide repeat containing
LSFC	Leigh syndrome French Canadian
LSP	Light strand promoter
M	Manders coefficient
MERF	Myoclonic epilepsy and ragged red fibres
Mff	Mitochondrial fission factor
MFI	Mean fluorescence intensity

MgCl2	Magnesium chloride
MIB	Mitochondrial intermembrane space bridging
MICOS	Mitochondrial contact site and cristae organizing system
MiD	Mitochondrial dynamics protein
Min	Minute
Mitoprep	Mitochondrial preparation
MITRAC	Mitochondrial translation regulation assembly intermediate of cytochrome c ox
Mnf	Mitofusin
MRG	Mitochondrial RNA granules
MRM	Mitochondrial methyl transferase
mRNA	Messenger RNA
MRP	Mitoribosomal protein
mtDNA	Mitochondrial DNA
mtEF-G	Mitochondrial elongation factor G
mtEF-Ts	Mitochondrial elongation factor thermo stable
mtEF-Tu	Mitochondrial elongation factor thermo unstable
mt-Hsp70	Mitochondrial heat shock protein 70
mtIF2	Mitochondrial initiation factor 2
mtIF3	Mitochondrial initiation factor 3
mt-LSU	Large subunit of the mitoribosome
mt-NAPs	Nucleoid associated proteins
MTPAP	Mitochondrial Poly(A) Polymerase
mtRRF	Ribosomal recycling factor
MTS	Mitochondrial targeting sequences

mt-SSB	Mitochondrial single stranded DNA-binding
mt-SSU	Small subunit of the mitoribosome
NaCl	Sodium chloride
NADH	Nicotinamide adenine dinucleotide
NaOH	Sodium hydroxide
NDUFA9	NADH:Ubiquinone oxidoreductase Subunit A9
NDUFB8	NADH:Ubiquinone oxidoreductase Subunit B8
NH4Cl	Ammonium chloride
NH4OH	Ammonium hydroxide
NP-40	Nonyl phenoxypolyethoxylethanol
NT-siRNA	Non targeting silencing RNA
O/N	Over night
OH	Origin of replication of H-strand
OL	Origin of replication of L-strand
OMM	Outer mitochondrial membrane
Opa1	Optic atrophy 1
ORF	Open reading frame
OXA1L	Oxidase (cytochrome c) assembly 1-like
OXPHOS	Oxidative phosphorylation
PAGE	Polyacrylamide gel electrophoresis
PAM	Presequence translocase-associated motor
PCC	Pearson correlation coefficient
PCR	Polymerase chain reaction
PEO	Progressive external ophthalmoplegia

PES	Polypeptide exit site
PFA	Paraformaldehyde
PHB	Prohibitin
PMSF	Phenylmethylsulfonyl fluoride
PNPase	Polynucleotide phosphorylase
POLG	DNA polymerase γ
POLRMT	Mitochondrial DNA-directed RNA polymerase
PPR	Pentatricopeptide repeat
PSF	Point-spread function
P-site	Peptidyl site
PTC	Peptidyl transferase centre
Q	Uniquinone
Q570	Quasar 570
Q670	Quasar 570
QH2	Uniquinol
qPCR	Real-time PCR
RBP	Ribosome-binding protein
REXO2	RNA exonuclease 2
RF	Release factor
RFI	Relative fluorescence intensity
RITOLS	RNA incorporation through-out the lagging strand
RNA	Ribonucleic acid
ROS	Reactive oxygen species
Rpm	Rounds per minute

rRNA	Ribosomal RNA
S	Svedberg
SAM	Sorting and assembly
SDH70	Succinate dehydrogenase 70 kda
SDS	Sodium dodecyl sulphate
Sec	Seconds
siRNA	Small interfering RNA
SLIRP	Stem-loop interacting RNA binding protein
SLP-2	Stomatin-like protein 2
Smac	Second mitochondria-derived activator of caspases
SMP	Submitochondrial particle
SOB	Super optimal broth
SOC	Super optimal broth with catabolite repression
SPG7	Paraplegin
SSC	Saline-sodium citrate buffer
ssDNA	Single-stranded DNA
STED	Stimulated emission depletion
SUPV3L1	Suv3-like RNA helicase
TACO1	Transcriptional activator of complex I
TAE	Tris-acetate EDTA
TBST	Tris-buffered saline, tween 20%
TCA	Tricarboxylic acid
TEFM	Mitochondrial transcription elongation factor
TFAM	Mitochondrial transcription factor A

TFB2M	Mitochondrial transcription factor B2
TIM	Translocase of inner mitochondrial membrane
Tm	Melting temperature
TOM	Translocase of outer mitochondrial membrane
TOP3α	Topoisomerase 3α
tRNA	Transfer RNA
U	Unit
U2OS	Human osteosarcoma cell line
UTR	Untranslated region
V	Volt
VDAC	Voltage dependent anion channels
WL	White light

Contents

List of Figures

List of Tables

List of Equations

Chapter 1:

Introduction

1.1 Mitochondria: an introduction

Mitochondria are dynamic and distinctive eukaryotic organelles that play a critical role in the maintenance of cellular homeostasis. Mitochondria existed as an independent organism from ancestral eukaryotic cells until environmental pressure led to a favourable endosymbiosis event. The capacity of mitochondria to generate adenosine triphosphate (ATP) through the process of oxidative phosphorylation (OXPHOS) brought about this relationship (Margulis, 1971). Mammalian mitochondria contain their own circular, approximately 16.6 kb, DNA molecule (mtDNA) that is located in the matrix of the mitochondria (Anderson et al., 1981). This genome encodes 2 ribosomal RNAs (rRNAs), 22 transfer RNAs (tRNAs) and 13 polypeptides, the latter are all translated into subunits of OXPHOS complexes. All additional proteins required for mitochondrial function are encoded by the nuclear genome, translated in the cytosol, and imported into mitochondria (Mokranjac et al., 2005).

In addition to OXPHOS, mitochondria are involved in a multitude of other functions including the citric acid cycle (Rustin et al., 1997), iron-sulphur cluster biogenesis (Lill, 2009), apoptosis (Wang and Youle, 2009), and calcium homeostasis (Rizzuto et al., 2012). As a consequence of these diverse roles, dysfunctional mitochondria are associated with a heterogeneous group of disorders called mitochondrial diseases (Reviewed in Lightowlers et al., 2015). There is a marked variety of clinical features in patients with mitochondrial diseases that range from neurological disorders, such as epilepsy and neuropathy, to multisystem disorders such as diabetes mellitus (Reviewed in Chinnery, 2015). Mitochondrial diseases can occur as a result of mutations in either the sequence of the small circular mitochondrial genome or in the nuclear genome encoding proteins that are subsequently imported into or affect mitochondria.

1.2 Mitochondrial origins and evolution

The most recognised theory of mitochondrial origin is the endosymbiotic hypothesis, which proposes mitochondria evolved from an α-proteobacteria via symbiosis with an archaea host to form a eukaryotic cell (Gray, 2012; Lang et al., 1999). Phylogenetic studies have estimated this assimilation event to have occurred around 1.5 billion years ago and resulted in the predecessor to modern mitochondrial forms. These forms include: the mitochondrion which produces ATP aerobically, mitosomes which do not contain mtDNA or carry out OXPHOS, and hydrogenosomes which produce ATP anaerobically and generate hydrogen in the process (Embley et al., 2003; Schneider et al., 2011). There is great diversity in the structure of modern mitochondrial genomes, for example metazoan mitochondrial genomes contain very few non-

coding regions in contrast to many plant mitochondrial genomes which contain multiple non-coding and repeated regions and can reach sizes of >7 megabase pairs (Kitazaki and Kubo, 2010; Wu et al., 2015). Regarding modern mammalian mitochondrion, the once independent invading α-proteobacteria has now become highly dependent on the host cell (Andersson and Kurland, 1998; Burger et al., 1996). It is thought that over time the size of the mitochondrial genome has decreased due to endosymbiotic gene transfer to the nuclear genome (Timmis et al., 2004). Consequently, the vast majority of the ~1500 proteins present in the mitochondria are encoded by the nuclear genome and imported into the organelle (Anderson et al., 1981; Mokranjac et al., 2005).

1.3 Mitochondrial structure

1.3.1 Mitochondrial structure

Mitochondria are double-membrane organelles consisting of an outer mitochondrial membrane (OMM) and inner mitochondrial membrane (IMM) that are separated by the intermembrane space (IMS) (Figure1.1 A). While often depicted as independent units, mitochondria are most often observed as a network that is dynamic in nature (Figure 1.1 B).

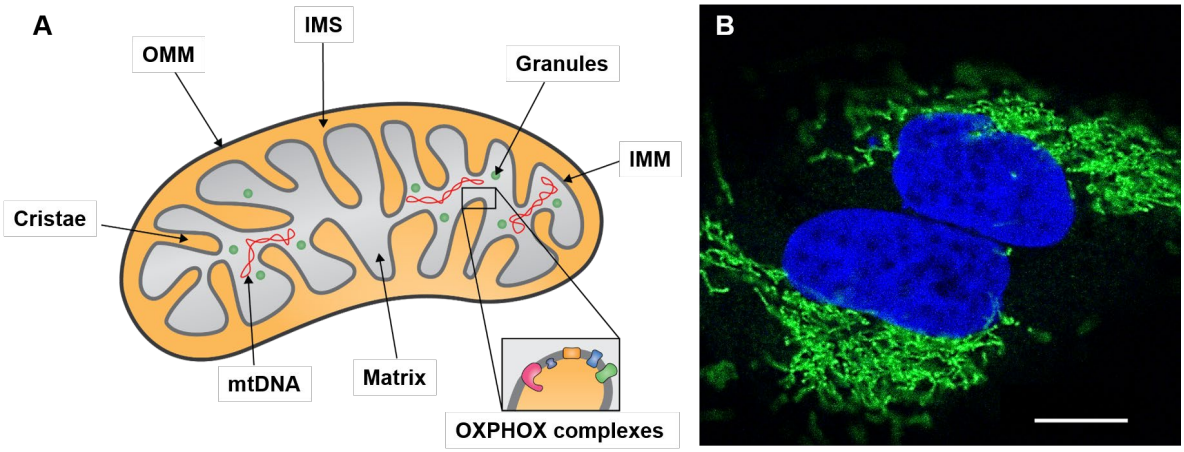

Figure 1.1: Mitochondrial Structure. A: A schematic depicting a mitochondrion displaying: the mitochondrial outer membrane (OMM, black), the mitochondrial inner membrane (IMM, dark grey) which form infolds called cristae, the inter-membrane space (IMS, orange), the matrix (light grey) which contains mitochondrial DNA (mtDNA, red)) and ribonucleoprotein structures called mitochondrial RNA granules (green). Highlighted are the oxidative phosphorylation (OXPHOS) complexes on the IMM. **B:** Confocal imaging illustrating the mitochondrial network of a U2OS cell. Mitochondria are visible by RNA fluorescent in-situ hybridisation (FISH) of the 16S mt-rRNA (green) and the nucleus stained with DAPI (blue). Scale bar 10µm.

The composition of the OMM is similar to that of eukaryotic plasma membranes and it is permeable to ions and small molecules (Benz, 1994; Mannella, 1992). This permeability is

mediated by porins, such as voltage dependent anion channels (VDAC) and Translocase of the Outer Membrane (TOM) complexes, that selectively allow mitochondrially-targeted proteins across the lipid bilayer. In contrast, the IMM is far less permeable in order for the maintenance of the mitochondrial membrane potential (ψ_m). The ψ_m is essential for the synthesis of ATP by oxidative phosphorylation. There is no membrane potential across the OMM. The IMM consists of two main regions: the inner boundary membrane (IBM) and the cristae membrane (CM), which are connected at cristae junctions. The IBM is found parallel to the OMM and interacts with the OMM to facilitate protein import (Edwards et al., 2021; Neupert and Herrmann, 2007). The involuted structure formed by CM increases the surface area of the IMM and houses the majority of proteins for OXPHOS. There are also fundamental differences in the compositions of the OMM and IMM. The IMM is far richer in proteins, comprising of a 3:1 protein:lipid ratio, compared to the OMM which has a ratio of 1:1 (Gohil and Greenberg, 2009).

As described earlier, a prominent feature of the IMM is the presence of cristae that extend into the mitochondrial matrix. This requires substantial curvature of the membrane at the cristae juncture that is modulated by the mitochondrial contact site and cristae organising system (MICOS) (Kozjak-Pavlovic, 2017). The MICOS associates with the SAM (sorting and assembly) complex on the OMM to create the mitochondrial intermembrane space bridging (MIB) complex. The physical interaction of the IMM and the OMM by these protein complexes is essential for cristae formation. Phospholipid asymmetry is also a requirement at the sites of membrane curvature (Renner and Weibel, 2011). The phospholipid membrane in the lumen of cristae, where there is the most curvature, is composed mostly of cardiolipin and phosphatidylethanolamine (PE) (Reviewed in Ikon and Ryan, 2017). Also localised to the IMM, and a known interactor of cardiolipin, are prohibitins, PHB and PHB2 (discussed further in 1.9), and stomatin-like protein 2 (SLP-2) (Christie et al., 2011). SLP-2 has a role as a scaffolding protein to form cardiolipin-rich domains in the IMM and is associated with modulation of mitochondrial translation (Christie et al., 2011).

1.3.2 Mitochondrial dynamics

Mitochondria exist as motile reticular networks (Figure 1.1 B). These networks constantly undergo fusion and fission events within single cells (Figure 1.2). Classical mitochondrial fusion events are initiated by the docking of two OMM-located Mitofusin GTPase proteins (Mfn1 and Mfn2) on adjacent mitochondria (Figure 1.2 A) (Chen et al., 2003). GTP hydrolysis then drives the fusion of the two outer membranes. Opa1 mediates mitochondrial inner membrane fusion and works in consort with Mfn1/ 2.

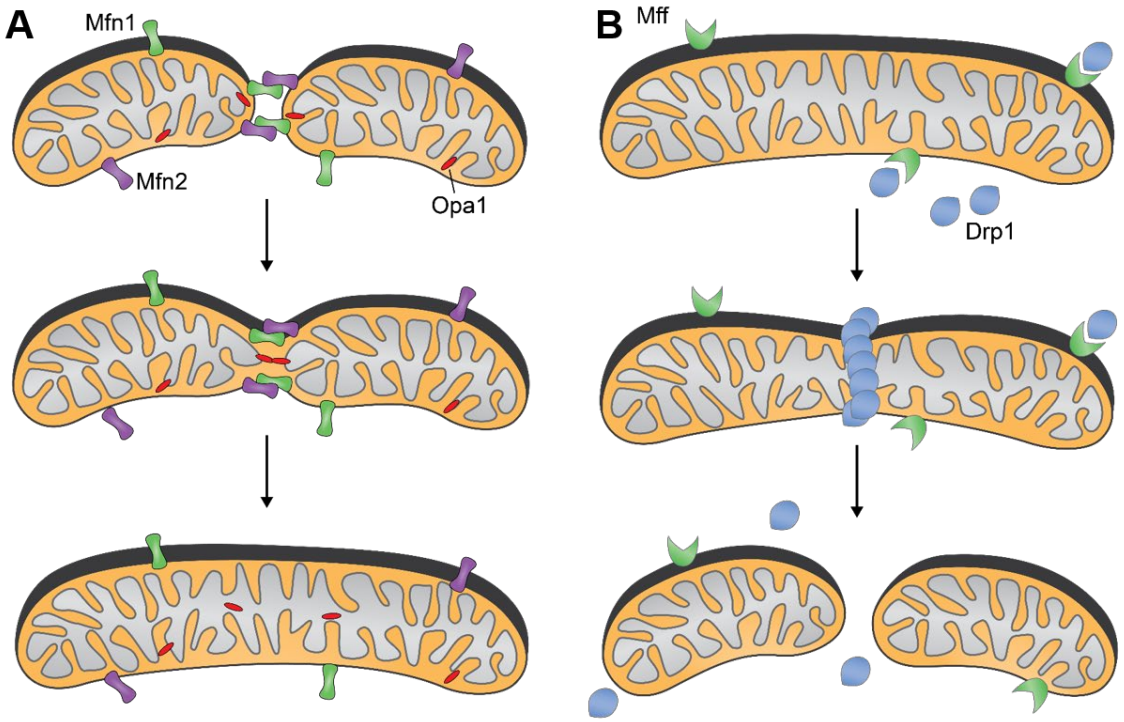

Figure 1.2: Mitochondrial Fusion and Fission. A: Mitochondrial fusion is initiated by mitofusion proteins Mfn1 and Mfn2, located on the outer mitochondrial membrane. Opa1 regulates the fusion of the inner mitochondrial membrane. **B:** Mitochondrial fission is driven by the recruitment of Drp1 to the outer mitochondrial membrane by interaction with a variety of proteins including Mff. Drp1 monomers oligomerize and form contractile rings which constrict, and scission occurs.

Mitochondrial fission occurs when Drp1 (Dynamin-related protein 1) is recruited to the OMM and oligomerizes to form contractile rings around the mitochondrion (Figure 1.2 B) (Labrousse et al., 1999). Following GTP hydrolysis, the diameter of this ring decreases constricting the mitochondrial membrane and allowing scission to occur (Mears et al., 2011). There are several factors associated with Drp1 binding to the OMM, including mitochondrial fission factor (Mff), mitochondrial fission protein 1 (Fis1), and mitochondrial dynamics proteins MiD49 and MiD51 (van der Bliek et al., 2013).

1.4 Mitochondrial functions

1.4.1 Oxidative phosphorylation

The process of oxidative phosphorylation (OXPHOS) is the most studied and characterized function of mitochondria (Figure 1.3) (Mitchell, 1967). OXPHOS is reliant on the processes of cellular respiration and electron transport to generate an electrochemical gradient that is utilised to generate ATP on the IMM.

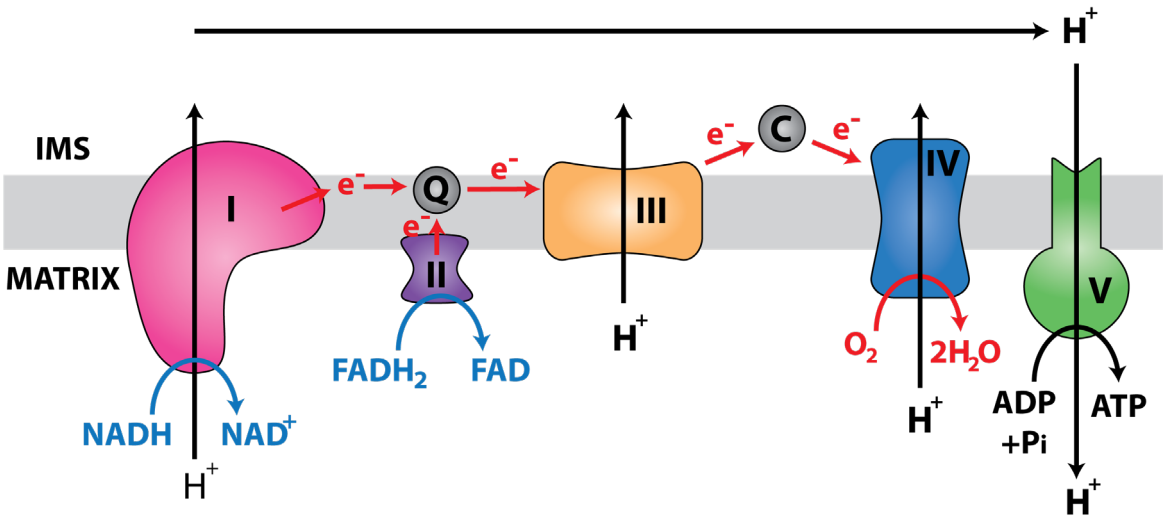

Figure 1.3: The OXPHOS system. Graphic of the major components of the OXPHOS system. Complex I (pink), Complex II, (purple), Complex III (orange), Complex IV (blue) and Complex V (green). Co-factors coenzyme Q (Q, grey) and cytochrome *c* (C, grey) are depicted as spheres. The flow of electrons is shown as red arrows and the direction of the protons movement shown by black arrows. NAD=nicotinamide-adenine dinucleotide, FAD=flavin-adenine dinucleotide, ADP=adenosine diphosphate, ATP=adenosine triphosphate, Pi (inorganic phosphate).

The citric acid cycle and beta-oxidation cascade breakdown metabolic substrates and fats, respectively, to generate reduced cofactors NADH and $FADH_2$. These cofactors are re-oxidised via the electron transport chain resulting in the generation of a proton gradient across the inner membrane. The electron transport chain and OXPHOS rely on the formation of multiprotein complexes that are formed on nuclear- and mitochondrial-encoded subunits (Table 1.1)

Table 1.1: Composition of each complex of oxidative phosphorylation

Complex	mtDNA encoded subunits	n-DNA encoded subunits
I	7 (ND1, ND2, ND3, ND4, ND5, ND6, ND4L)	38
II	0	4
III	1 (CyB)	10
IV	3 (COXI, COXII, COXIII)	10
V	2 (ATP6, ATP8)	14

***Complex I*:** The first and largest complex (~980 kDa) in the electron transport chain is NADH:ubiquinone oxidoreductase (Chomyn, 2001). This complex contains 45 proteins, of which 7 are mtDNA-encoded (Carroll et al., 2006; Zhu et al., 2016). The subunits assemble into an L-shape comprised of a hydrophobic arm embedded in the IMM and a hydrophilic arm extended into the matrix (Hunte et al., 2010). Electrons from an NADH molecule enter via Complex I, oxidising the cofactor to NAD^+. These electrons are transferred through a series of iron-sulphur (Fe-S) clusters to a Coenzyme Q/ubiquinone molecule in the IMM, reducing it to ubiquinol (Zhu et al., 2016). During this process, two protons are taken up by Complex I from the matrix and pumped to the IMS.

***Complex II*:** Complex II, succinate dehydrogenase, is the only OXPHOS complex that is solely comprised of subunits encoded by the nucleus. It is comprised of four subunits (A-D) and contains an FAD (flavin adenine dinucleotide), a haem group, and 3 Fe-S clusters (Rutter et al., 2010). Subunits A and B are hydrophilic and project into the matrix. Subunits C and D anchor complex II into the IMM. The main function of this complex is the oxidation of succinate to fumarate. These electrons are used to reduce FAD to $FADH_2$ which Complex II then re-oxidises in order to reduce ubiquinone (Q) to ubiquinol (QH_2) (Rutter et al., 2010). Complex II does not move any protons across the IMM and therefore does not contribute to the proton gradient directly.

***Complex III*:** Complex III, is a dimer consisting of 11 different subunits. Each subunit is composed of four monomers: cytochrome *b*, cytochrome *c1*, and Rieske Fe-S cluster protein (Mulkidjanian, 2010). Only one of these proteins, cytochrome *b*, is mtDNA-encoded. Complex III is another electron-transferring molecule that oxidises QH_2 by reducing two cytochrome *c* molecules in the two-step Q cycle (Saraste, 1999). Each of these steps on the Q cycle, transfers a proton from the matrix to the IMS (Mulkidjanian, 2010).

***Complex IV*:** The last complex in the electron transport chain is Complex IV, cytochrome *c* oxidase. It is composed of 13 subunits, 3 of which are encoded by mtDNA and form the functional core of the protein. The active form of Complex IV is thought to exist as a dimer in the IMM, with each monomer connected by a cardiolipin molecule (Fontanesi et al., 2006). This complex mediates the transfer of electrons to the terminal electron acceptor, oxygen. This process oxidises cytochrome *c* and reduces oxygen to water (Saraste, 1999). This reduction of oxygen can generate reactive oxygen species (ROS) that can damage DNA (Ray et al., 2012; St-Pierre et al., 2006). The direct pumping of protons from the matrix to the IMS and the

consumption of protons by oxygen to generate water both contribute to the proton gradient across the IMM.

***Complex V*:** The proton gradient produced by the electron transport chain is utilised by the final OXPHOS complex, adenosine 5'-triphosphate (ATP) synthase (F_1F_0 ATPase), Complex V. This complex is an integral membrane protein composed of 16 proteins, 2 of which are mtDNA encoded (Reviewed in Jonckheere et al., 2012). The formation of ATP, by the hydrolysis of ADP and Pi, is driven by the movement of protons back into the matrix.

1.4.2 Additional functions of mitochondria

In addition to OXPHOS, mitochondria are responsible for a plethora of functions. Fe-S clusters are involved in numerous fundamental pathways including Complexes I, II and III, ferredoxins, and DNA polymerases. Mitochondria are the site of iron-sulphur cluster biogenesis (Lill, 2009). It has been proposed that formation of Fe-S clusters is the primary role of mitochondria as the process is heavily conserved throughout evolution (Embley and Martin, 2006).

Mitochondria also function as a site of calcium accumulation and also calcium buffering within the cell via the calcium uniporter (De Stefani et al., 2011). The activity of the Na+/Ca2+exchanger, controlling efflux of calcium from the mitochondria, allows mitochondria to act as a perpetual calcium sink. Calcium molecules are involved in a multitude of signalling pathways in the cell, which can, in effect, be regulated by influx/efflux rates by the mitochondria (Kamer and Mootha, 2015).

Mitochondria are directly linked to the main apoptotic pathway through a cell signalling cascade (Martinou and Youle, 2011). Apoptotic cell death is characterised by membrane blebbing, cell shrinkage and nuclear fragmentation as a result of an intracellular signalling pathway involving mitochondria. The main signalling cascade involves the Bcl-2 family members BAX/BAK which oligomerise and accumulate on the outer mitochondrial membrane. This association promotes cytochrome *c* release from the intermembrane space which drives caspase activation and apoptosis (Martinou and Youle, 2011; Ow et al., 2008).

1.5 Mitochondrial genome

1.5.1 Genome organisation

The presence of mitochondria is ubiquitous in mammalian cells (except mature red blood cells that lack a nucleus) with many of the functions described above conserved across species.

However, the size, organisation and genetic composition of mitochondrial DNA displays incredible variation (Lang et al., 1999; Reviewed in Smith and Keeling, 2015). The human mitochondrial genome is a small, double-stranded, 16.569 bp circular genome that is maternally inherited (Figure 1.4) (Anderson et al., 1981). Each of the 13 polypeptides encoded by human mtDNA function within OXPHOS complexes. The genome is extremely concise; there are no introns, and all non-coding and regulatory information is clustered together on the non-coding region (NCR) which also contains the displacement loop (D-loop). There are two cases where genes overlap, *MT-ND4/MT-ND4L* and *MTATP6/MT-ATP8* and the RNA species are maintained as bicistrons.

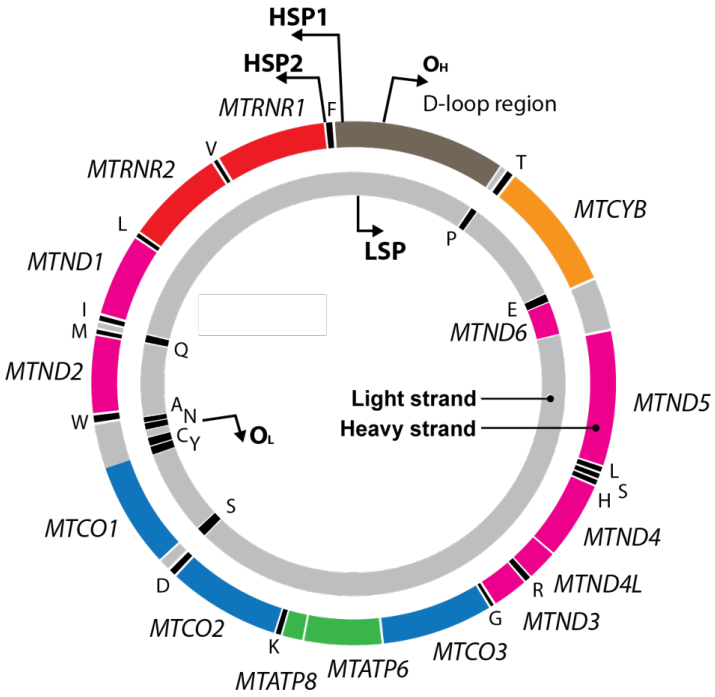

Figure 1.4: Organization of human mitochondrial genome. The double stranded mtDNA molecule (16.569kb) encodes 37 genes. The 13 ORFs are colour coded according to their OXPHOS complex (complex I = pink, complex III = orange, complex IV = blue, complex V = green). The rRNA is visible in red and the tRNA genes are visible as black lines and their respective single letter code. D-loop: Displacement loop, HSP: heavy strand promoter, LSP: light strand prompter, O_H/O_L = Origin of replication (Heavy/Light).

A single mitochondrion is estimated to contain 2-10 copies of the mtDNA molecules bound by DNA-binding proteins in packages called nucleoids (Bogenhagen et al., 2008; Wiesner et al., 1992). The multi-copy nature of the mitochondrial genome, multiple mtDNA moelcules in a mitochondrion and multiple mitochondria in a cell, can lead to complicated non-Mendelian genetics. If mtDNA molecules are all wild type or if a mutation is present in all mtDNA copies in the cell, the cell is said to be homoplasmic. If a mixture of mutated and wild type mtDNA mutation exist in a cell, the cell is said to be heteroplasmic. In a heteroplasmic cell there is only

a measurable phenotype if the proportion of mutated mtDNA is increased such that the wild type mtDNA can no longer compensate for the biochemical defect; this is called the biochemical threshold (Russell and Turnbull, 2014; Taylor and Turnbull, 2005).

1.5.2 Replication of mitochondrial DNA

Human mitochondria have maintained their own replication and translation machinery. All the associated proteins are nuclear-encoded proteins that are imported into the organelle (Holt and Reyes, 2012). Replication occurs independent of the cell cycle within the nucleoids and initiates from two origins of replication found on the heavy strand (O_H) and light strand (O_L) (Figure 1.4) (Reviewed in Chapman et al., 2020; Uhler and Falkenberg, 2021) . Proteins required for the replication process include DNA polymerase γ (POLG), the helicase Twinkle, topoisomerases that remove supercoils from the DNA, mitochondrial RNA polymerase (POLRMT), and mitochondrial single-stranded binding protein (mtSSB).

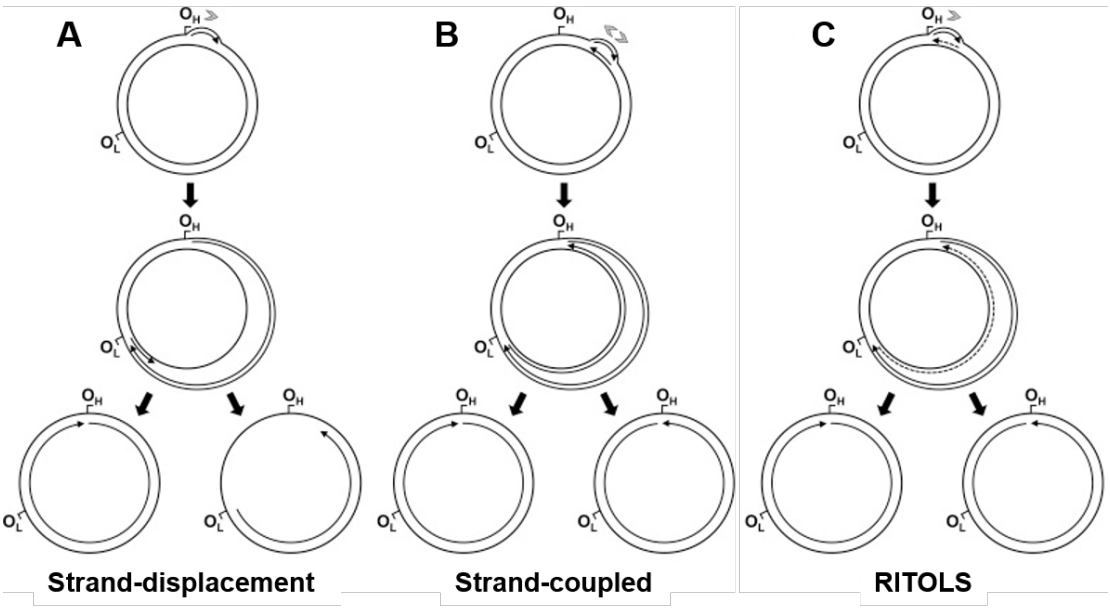

Figure 1.5: Models of mtDNA replication. A: The strand-displacement model. **B:** The strand-coupled model. **C:** RNA incorporation throughout the lagging strand (RITOLS) model. Models are explained in text. Image adapted from (McKinney and Oliveira, 2013)

There is still debate about the process of mtDNA replication and several models of replication have been proposed (Figure 1.5). The first model of mtDNA replication, the strand-displacement model (Figure 1.5 A), was first proposed in the 1970s (Berk and Clayton, 1974; Kasamatsu and Vinograd, 1973; Robberson et al., 1972). In this model an RNA primer initiates synthesis of the heavy strand from the O_H and advances approximately two-thirds of the way around the genome before exposing the O_L. Light strand synthesis displaces the leading strand and begins synthesising in a counter-clockwise direction (Holt and Reyes, 2012). The stand-

coupled model (Figure 1.5 B) proposes that the initiation of replication at a site downstream of O_H called ori-z and occurs simultaneously though short Okazaki fragments (Holt et al., 2000; Holt and Reyes, 2012; Robberson et al., 1972). Advancements in 2D agarose gel electrophoresis and purification of replication intermediates adapted our understanding of mDNA replication. This led to proposal of the RNA Incorporation Throughout the Outer Lagging Strand (RITOLS) model (Figure 1.5 C). In RITOLS, nascent RNA molecules bind to the lagging strand during leading strand replication. When lagging strand synthesis occurs, these RNA molecules are displaced or converted to DNA (Holt and Reyes, 2012).

Once mtDNA replication has completed, the circular genomes will be connected through a short single-stranded overlap at the O_H, called a hemicatenane. Topoisomerase 3α (TOP3α) resolves this structure by cleavage and allowing separation of the two mtDNA molecules (Nicholls et al., 2018).

1.5.3 Mitochondrial transcription

Mitochondrial polycistronic transcripts containing mt-mRNA and mt-tRNA are transcribed from LSP and HSP1, covering each strand of the genome (Chang and Clayton, 1984). A third, shorter, transcript is thought to originate from HSP2 that encodes for mt-tRNAs and the two ribosomal RNAs, 12S rRNA (*RNR1*) and 16S rRNA (*RNR2*) (Figure 1.6). Transcription is performed by the mitochondrial RNA polymerase (POLRMT). Initiation requires the mitochondrial transcription factor A (TFAM) to bend the promoter region of the mtDNA and stimulates the recruitment POLMRT. The mitochondrial transcription factor B2 (TFB2M) assists by melting of mtDNA and the mitochondrial transcription elongation factor (TEFM) promotes initiation (Falkenberg et al., 2002; Reviewed in Gustafsson et al., 2016). The mechanism of termination of transcription are not yet fully characterised. In vitro transcription from LSP undergoes terminations which are managed by mitochondrial termination factor (mTERF). Furthermore, when mouse mTERF was knocked out, LSP-led transcription was affected (Terzioglu et al., 2013). This factor is also thought to have a role in the recycling of the initiation complex (Scarpulla, 2008). It is worth noting that the existence of HSP2 is debated in the literature (Litonin et al., 2010). Initiation from HSP2 was unreproducible in vivo the

presence of TFAM, casting doubt on whether or not it is a functional site (Lodeiro et al., 2012). Full characterisation of mitochondrial transcription initiation is actively being investigated.

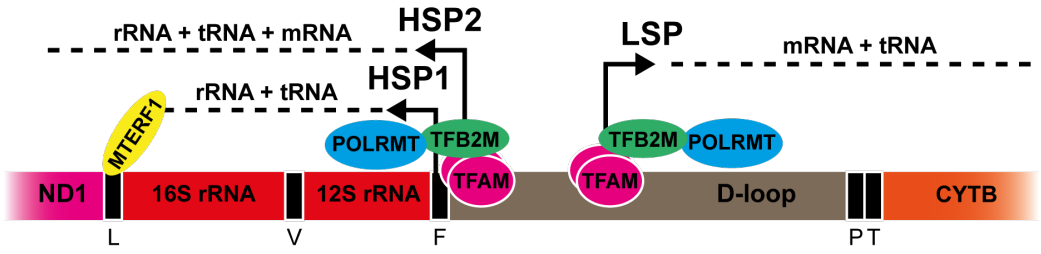

Figure 1.6: The Mitochondrial Transcription Machinery. Transcription initiation requires TFAM TFB2M and POLRMT. Initiation at HSP1 results in transcription of the two rRNAs 12S and 16S and the tRNAs which flank them. This transcription is terminated at the tRNALeu gene by MTERF1. Initiation from HSP2 transcribes the full length of the H-strand and initiation from LSP transcribes the full-length of mtDNA in the opposite direction.

The transcription of long polycistronic transcription may lead to the expectation that the steady state levels of mitochondrial transcripts should be relatively similar, with *RNR1* and *RNR2* more abundant due to additional transcription from HSP1. However, there is variation in the steady state levels of mt-mRNA transcripts, shown by RNASeq data (Mercer et al., 2011). The polycistronic transcript is not usually observed *in vivo* and is thought to quickly undergo extensive processing (described in 1.6.1) and degradation of the mirror transcripts (Borowski et al., 2013).

1.5.4 RNA granules

Regulation of mt-mRNA is crucial to the control of gene expression to enable rapid changes in protein synthesis in response to stress and changing cellular conditions. A level of this modulation is thought to occur at ribonucleoprotein structures, called RNA granules. Mitochondrial RNA granules (MRGs) were first identified when mtRNA processing enzyme RNase P, RNA binding protein GRSF1 (G-rich sequence factor 1), and nascent mitochondrial transcripts were found in discrete foci within the mitochondrial matrix (Buchan, 2014; Jourdain et al., 2013). RNA processing enzymes associated with MRGs have been shown to be enriched near nucleoids, suggesting the tight coupling of mtDNA replication and the transcription and processing of mtRNA (Bogenhagen et al., 2014).

1.6 Mitochondrial translation

Mitochondrial translation represents the unification of multiple molecular process, such as transcription, RNA processing, and protein import into the mitochondria. As such, mitochondrial translation is reliant on the successful execution of these process (Figure 1.7). These processes will be explained in detail in this section. For information on the process of mtDNA transcription (see 1.5.3).

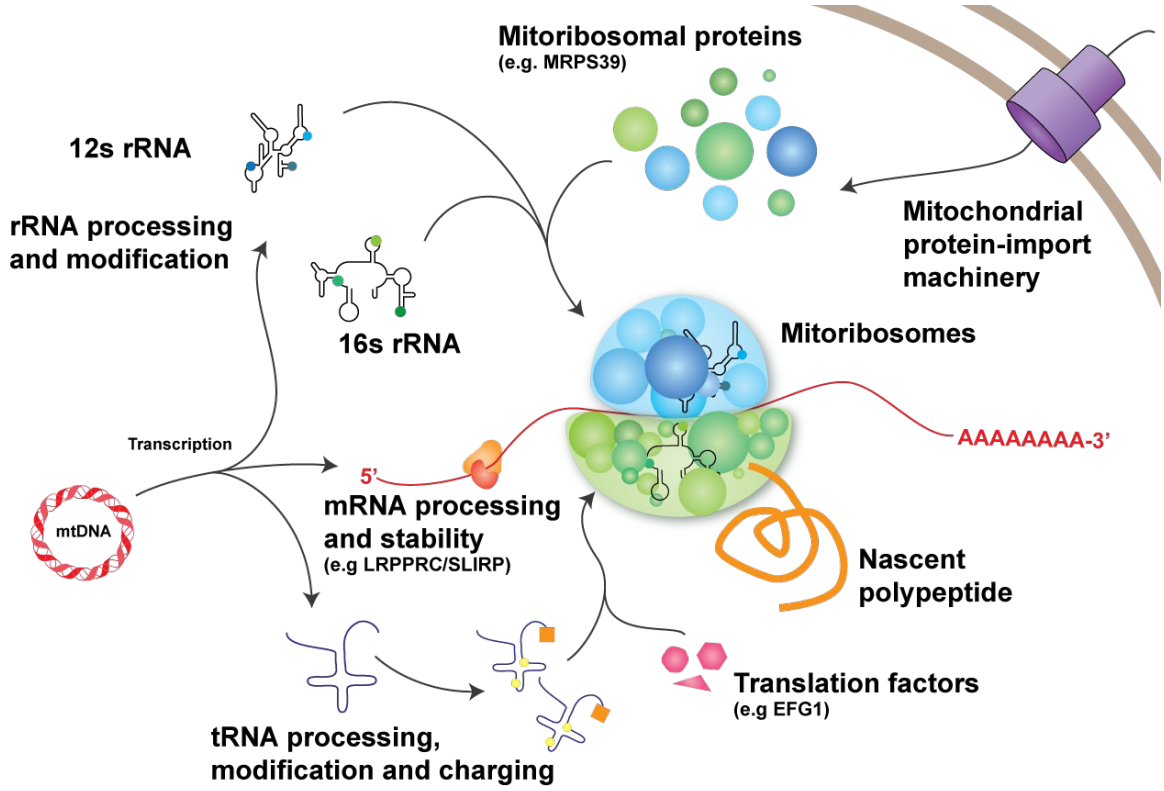

Figure 1.7: Processes underpinning mitochondrial translation. A schematic of molecular processes that generate substrates for mitochondrial translation to occur. In violet (top right) is depicted the import of protein subunits that form the mitochondrial ribosome. Also pictured is the transcription of mtDNA to generate mt-mRNA, mt-rRNA and mt-tRNA. All of these RNA molecules are processed prior to use by the mitochondrial ribosome.

1.6.1 Mitochondrial protein import

As described earlier, only 13 of the polypeptides that make up the OXPHOS complexes are encoded by the mitochondrial DNA. The other proteins required to build OXPHOS complexes, and all mitoribosomal proteins, are nuclear-encoded and must be imported into mitochondria.

Almost all proteins imported into the mitochondria are translocated through the translocase of the outer membrane (TOM) complex. This is a multiprotein complex that is responsible for recognition of mitochondrial targeting sequences (MTSs) and then stable translocation (Roises and Schatz, 1988). MTSs can include N-terminal presequences and internal targeting

sequences. After import through the OM, there is a variety of complexes and chaperones that are responsible for the movement of proteins to their specific destinations. For mitoribosomal proteins (MRPs), they require transport into the mitochondrial matrix. These proteins classically have cleavable presequences that comprise an amphipathic α-helix that contains a positively charged face and a hydrophobic face, which is recognised by TOM receptor proteins, Tom20, Tom40, and Tom70 (Endo et al., 2011). Presequence-carrying proteins are presented to the TIM23 complex that can modulate transport into the mitochondrial matrix. Upon entry to the matrix, the presequence is cleaved by the mitochondrial processing peptidase, MPP. The OXPHOS proteins require translocation into the IMM. These proteins often contain internal targeting sequences that allow for correct distribution, though these sequences have not yet been fully characterised. These proteins are translocated across the OM via the TOM complex which recruits small TIM chaperones of the intermembrane space. These chaperones facilitate the transport of IMM-designated proteins to the insertase protein TIM22. The insertion of these proteins into the inner membrane occurs in a membrane potential-driven manner. There are alternative routes for delivery of proteins to the OMM and the IMS, in addition to specific matrix and IMM proteins which have other associated cofactors (Reviewed in Mohanraj et al., 2020 and Wiedemann and Pfanner, 2017).

A number of studies have postulated there must be coordination between the synthesis and import of these cytosolic proteins and the mitochondrial gene expression machinery (Mick et al., 2012; Neupert and Herrmann, 2007; Priesnitz and Becker, 2018). The formation of Complex IV from multiple nuclear-encoded and mitochondrially-encoded proteins is coordinated by the MITRAC (mitochondrial translation regulation assembly intermediate of cytochrome *c* oxidase) (Mick et al., 2012). The early form of MITRAC, containing C12orf62 and MITRAC12, assembles onto COX1 proteins and is present in the IMM (Richter-Dennerlein et al., 2015). There is growing research that supports the idea that that mitoribosomes can demonstrate plasticity in response to the levels of OXPHOS complex required (Richter-Dennerlein et al., 2016; Wang et al., 2020).

1.6.2 Mitochondrial RNA processing, maturation and stability

Mitochondrial transcription generates polycistronic transcripts that comprise mt-rRNA, mt-mRNA and mt-tRNAs. Processing enzymes release mt-tRNAs that punctuate the messenger and ribosomal RNAs. This process involves the folding and cleavage of mt-tRNAs by GRSF1/RNase P at the 5'end and ELAC2 at the 3' end (Brzezniak et al., 2011; Holzmann et al., 2008; Jourdain et al., 2013). The result of this process are the individual mt-rRNA and mt-

mRNA transcription units and two bicistronic mt-mRNA units (*ND4L/ND4* and *ATP8/ATP6*) (Temperley et al., 2010b). This model therefore cannot be the sole system for mt-mRNA release from the polycistron, as it does not account for these bicistronic units. Mitochondrial tRNA molecules are matured by the post-transcriptional addition of a CCA motif by the ATP(CTP):tRNA nucleotidyltransferase (Nagaike et al., 2001). These transcripts are then charged via ligation to the cognate amino acid by the appropriate mitochondrial aminoacyl-tRNA synthetase (Diodato et al., 2014), equipping them for mitochondrial translation.

The mt-rRNA molecules are subjected to extensive modifications prior to assembly into the mitochondrial ribosome. Early investigations into mt-rRNA in hamsters found that the rRNAs required pseudouridylation, base methylation and 2'-O-ribose methylation modification at conserved sites (Dubin and Taylor, 1978). It is now established that the five base methylations of the 12S mt-rRNA (*RNR1*) are consistent with modifications by TFB1M, TRMT2B, METTL15 and NSUN4 (Metodiev et al., 2009, 2014; Lopez Sanchez et al., 2020). Modifications of the 16S mt-rRNA (*RNR2*) are executed by methyltransferases, MRM1, MRM2, and MRM3 (Lee and Bogenhagen, 2014; Rorbach et al., 2014). Prior to mature mitoribosome assembly, mt-rRNA associates in RNA granules which have been implicated in aiding stability of RNA or assembly of the ribosome. For example, the 3' terminus of *RNR1* is bound by the RNA-binding GTPase ERAL1 which acts to stabilise the transcript prior to mitoribosomal small subunit (mt-SSU) assembly. In addition, *RNR2* immunoprecipitation assays have identified many proteins required for mitoribosomal large subunit (mt-LSU) assembly such as mTERF3, FASTKD2, and the helicase DDX28 (Popow et al., 2015; Tu and Barrientos, 2015; Wredenberg et al., 2013).

Once released from the polycistron, mt-mRNAs also undergo post-transcriptional modifications (Reveiwed in Barchiesi and Vascotto, 2019). Mitochondrial mRNAs are different from their cytosolic counterparts. For example, mt-mRNA lack a 5' 7-methylguanosine cap modification and they do not contain introns. Mitochondrial mRNAs can harbour the 5' modification of a nicotinamide adenine dinucleotide (NAD+) cap. There is modification at the 3' end of mt-mRNA to have a poly(A) tail, however this is much shorter than those found on nuclear encoded mRNAs (Temperley et al., 2010b). *MTND6* is an exception that completely lacks a poly(A) tail and is competently translated. *MTND5* is also capable of being translated without a polyadenylation, however sometimes it is oligo-adenylated. Polyadenylation is completed by the mitochondrial poly(A) polymerase (MTPAP) which has been shown to localise to RNA granules (Nagaike et al., 2005; Tomecki et al., 2004).

Effective *in vitro* knockdown of MTPAP resulted in a reduction in polyadenylation of mt-mRNA transcripts and reduced translation (Nagaike et al., 2005). Whereas mutations in MTPAP in humans are known to cause a form of spastic ataxia (Crosby et al., 2010). The precise role of the poly(A) tail has not been determined. However, since a number of mt-mRNA open reading frames lose their canonical stop codon as the mt-tRNAs are cleaved away, one undeniable function is to provide stop codons at the ends of 7 transcripts(Anderson et al., 1981; Wilson et al., 2014). Polyadenylation is associated with transcript stability of some mt-mRNAs but causes increased instability in others (Wilson et al., 2014).

GRSF1 was one of the first identified RNA granule proteins. Silencing of GRSF1 resulted in mt-mRNA instability, aberrant processing, and abnormal loading onto the mitoribosome (Antonicka et al., 2013). GRSF1 can also mediate the early processing of the polycistronic transcript as described earlier (Jourdain et al., 2013). Further mt-mRNA processing is completed by the FASTK (FAS-activated serine/threonine kinase 1–5) family proteins.

The stability of mt-mRNA and regulation of turnover are essential in mediating mitochondrial translation. Leucine-rich pentatricopeptide repeat (PPR)-containing protein/SRA stem-loop-interacting RNA-binding protein (LRPPRC/SLIRP) is the best characterised complex involved in this process. Knockdown of either LRPPRC (Gohil et al., 2010) or SLIRP (Baughman et al., 2009) resulted in a specific reduction of the steady state levels of mt-mRNA. The LRPPRC/SLIRP complex suppressed the PNPase and SUV3-mediated degradation of mt-mRNA and modulation of polyadenylation by MTPAP (Chujo et al., 2012; Wilson et al., 2014). Mutations in *LRPPRC* cause the mitochondrial disorder, Leigh Syndrome French Canadian (LSFC) (Sasarman et al., 2015) and are accompanied by decreased levels of SLIRP (Oláhová et al., 2015). A reciprocal state was seen where a reduction of SLIRP mimicked the post-transcriptional defect observed in LSFC patient fibroblasts, highlighting their functional dependence (Sasarman et al., 2015).

1.6.3 Delivery of mt-mRNA to the mitoribosome

As previously mentioned, human mt-mRNAs are unusual in that that lack conventional features of human mRNA, and yeast mt-mRNA such as 3’- and 5’-untranslated regions, 5’ 7-methylguanosine cap, and Shine-Delgarno/Kozak sequences. Many of these features have been shown to aid transfer of mRNA from stabilising factors to ribosomes for translation (Reviewed in Rackham et al., 2012).

In bacteria, the Shine-Delgarno sequence found upstream of the start codon which promotes the association of the transcript to the ribosome via the anti-Shine-Delgarno sequence found on the 16S rRNA. These sequences are not present in human mitochondria, therefore this process for recruitment to the mitoribosome is no analogous to bacteria. The delivery mt-mRNA in yeasts *S. cerevisiae* and *S. pombe* is regulated by the interactions of RNA-binding proteins (RBPs) with the 5'-untranslated region (5'UTR) of transcripts. These proteins contain pentatricopeptide repeat (PPR) motifs which confers the ability to bind single-stranded RNA (Yin et al., 2013). In *S. pombe* alone, 10 PPR proteins have been identified and found to have roles in mt-mRNA stability and translation activation (Kühl et al., 2011). For example, Ppr10 acts as a generalised activator of translation as deleting of *ppr10* resulted in the impairment of the translation of mtDNA- encoded subunits (Luo et al., 2021).

As human mt-mRNA lack 5'-UTR, a different mechanism of recruitment to the mitoribosome must be present. In addition, while there are many translational activators in yeasts, there is only 1 known translational activator for human mitochondrial transcripts, translational activator of CO1 (TACO1). Mutation of TACO1 causes a specific mutation in CO1 which causes Leigh Syndrome. TACO1 acts by associating with the mitoribosome, followed by specific recruitment of the mRNA by specific binding of the CO1 coding sequence (Weraarpachai et al., 2009). An additional factor to consider is the LRPPRC/SLIRP complex described previously, which is involved in chaperoning of mt-mRNA. The close link between this complex and the differential promotion of polyadenylation and degradation has led to proposals that LRPPRC/SLIRP could also coordinate translation. Suggestions have been made that LRPPRC/SLIRP could preferentially stabilise pools of transcripts awaiting delivery to the ribosome, or that LRPPRC binding to specific transcripts promotes translation by inhibiting formation of the mt-mRNA secondary structure (Lagouge et al., 2015; Ruzzenente et al., 2012). More recently, and published after the research presented in this thesis, the RNA-binding PPR region of the mitochondrial small subunit protein MRPS39 has been proposed as a site where the mt-mRNA may directly associate with the mitoribosome (Aibara et al., 2020).

1.6.4 The mitochondrial ribosome

A distinct characteristic of mitochondrial translation is the mitochondrial ribosome (mitoribosome). The mammalian mitoribosome was identified and isolated from rat liver cells (Mclean et al., 1958; O'Brien, 1971). Similar to the other ribosomes, the mitoribosome is composed of a small subunit (28S, mt-SSU) and a large subunit (36S, mt-LSU) that together form a monosome (55S). Each subunit is formed of ribosomal RNA encoded by the mtDNA

and associated mitochondrial ribosomal proteins (MRPs). All MRPS are encoded by the nuclear DNA, synthesized in the cytosol and imported into the mitochondria (See 1.6.1). Recent structural cryo-EM data revealed that the mt-LSU contained a second RNA component that unconventionally was a tRNA, and more unusually, was an mtDNA encoded tRNA. This was found to be mt-tRNA^{Val} in humans, mt-tRNA^{Phe} in pigs (Brown et al., 2014; Greber et al., 2014). An investigation into other mammals and other tissues found that these are the only 2 mt-tRNAs used and that there is no evidence of tissue specificity (Rorbach et al., 2016).

The sedimentation densities for the human mitoribosome are markedly different than the eukaryotic cytosolic (80S monosome) or bacterial (70S monosome) ribosomal species. It was proposed that the mitochondrial ribosome may resemble its bacterial counterpart following the endosymbiotic theory (see 1.2). This similarity is seen clearly in some aspects of mitochondrial function such as the decoding centre and peptide bond formation (Mai et al., 2016). Furthermore, there is conservation of translation initiation and elongation factors; this was demonstrated by the ability of mammalian mitochondrial translation factors to functionally replace the bacterial ones (Gaur et al., 2008). Conversely, there are several fundamental differences in the human mitochondrial ribosome and its prokaryotic equivalent (Table 1.2) (Amunts et al., 2015; Desai et al., 2017).

Table 1.2: Characteristics of bacterial and mammalian mitochondrial ribosome. Adapted from Mai et al., 2016.

Feature		**Human mitoribosome**	**Prokaryotic ribosome**
Monosome sedimentation		55S	70S
RNA:Protein		30:70	70:30
Small Subunit	**Sedimentation**	28S;	30S
	RNA	12S mt-rRNA	16S rRNA
	Proteins	~30 proteins	21 proteins
Large Subunit	**Sedimentation**	39S	50S
	RNA	16S mt-rRNA + mt-tRNA^{Val}	23S rRNA + 5S rRNA
	Proteins	~50 proteins	34 proteins

One of the most striking differences between the bacterial and the human mitochondrial ribosomes is the differences in RNA:Protein ratio. The human mitoribosome has a much higher protein content and observes a much shorter RNA molecule (Koc et al., 2001a, 2001b). Furthermore, structural studies of the bovine, porcine and human mitochondrial monosomes have highlighted the structural and compositional differences across mammals (Brown et al., 2014; Greber et al., 2014; Sharma et al., 2003).

An overview of the human mitoribosome SSU and LSU structure in comparison to the bacterial ribosome is presented here before reviewing the phases of mitochondrial translation.

1.6.5 The human mitoribosomal small subunit

The human mt-SSU is divided into two main parts: the body and the head (Figure 1.8). The mt-SSU is composed of *RNR1* and 30 nuclear-encoded proteins, 14 of which are mt-specific (Amunts et al., 2015). These mt-specific proteins have caused an elongation in the structure at the head via MRPS29 and the body via MRPS27, compared to the bacterial ribosome. The mt-SSU lacks homologs of uS4, uS8, uS13, uS19, and bS20. All of these proteins, except uS4, are replaced by mt-specific proteins (Amunts et al., 2015).

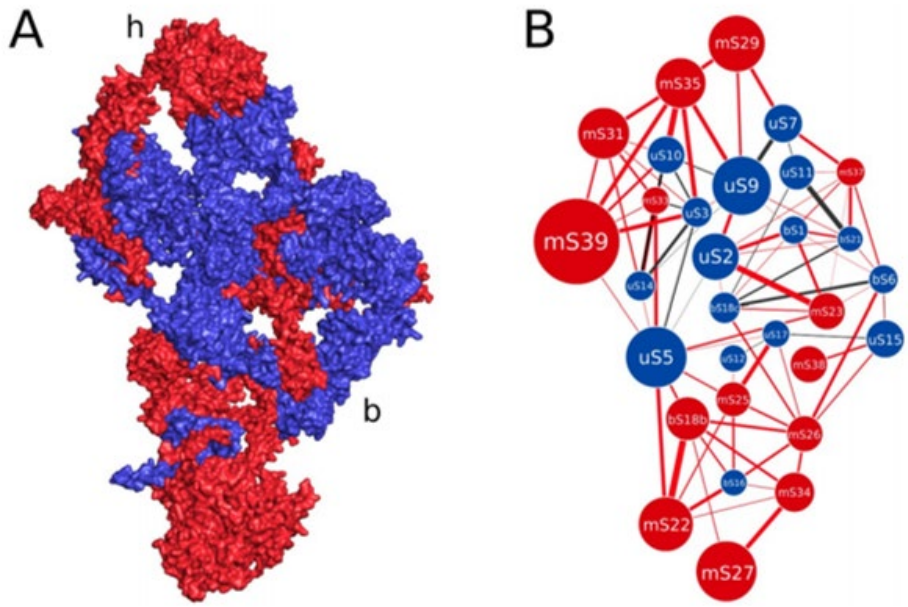

Figure 1.8: Interactions between mitoribosomal proteins of the mt-SSU. A: Surface representation showing interaction between mitoribosomal proteins with homologs in bacteria (blue) and mitochondria-specific proteins(red). h= head, b=body. **B:** Protein-protein network of A. Diagram uses new nomenclature from (Ban et al., 2014). The node size represents the relative molecular mass of the protein. Interactions conserved with bacteria are shown in black, and mitochondria-specific interactions in red. Image is taken from Amunts, A., Brown, A., Toots, J., Scheres, S.H.W., and Ramakrishnan, V. (2015).

The RNA content of the mt-SSU is approximately half that of its bacterial counterpart however the remaining content is conformationally very similar. The exception to this is helix 44 (h44) which is a highly conserved element in ribosomes and forms part of the decoding centre. In the mt-SSU, the lower part of h44 has increased flexibility due to loss of stabilising interactions with the mt-LSU rRNA, which has also diverged from the bacterial equivalent (Amunts et al., 2015). Critical intersubunit bridges to the mt-LSU rRNA are formed by the mt-specific protein MRPS38, which stabilises the upper part of h44 where the decoding centre is located. A recent

study has found that in yeast MRPS38 has an additional role in the selection of mRNAs that will be translated and they proposed a possible similar role in humans (Mays et al., 2019).

One of the most remodelled areas of the mt-SSU compared to the bacterial ribosome is the mRNA entry site (Figure 1.9) (Reviewed in Mai et al., 2016). In the bacterial ribosome, uS3, uS4, and uS5 form a ring structure in the head of ribosome. A key feature of uS3 and uS4 is their helicase activity that unwinds the mRNA upon entry to the ribosome. In the human mt-SSU, uS4 is notably absent from the structure in addition to a C-terminal deletion of the uS3 homolog MRPS24. The entry site is instead dominated by an extension to uS5 homolog MRPS5, and the addition of MRPS39. The morphological changes to the entry site include widening of the channel from 9 to 15 Å, and the introduction of a number of basic residues from the MRPS5 extension. MRPS39 is a pentatricopeptide repeat (PPR) protein which confers the ability to bind single-stranded RNA, including the 5' ends of mRNA (Yin et al., 2013). Knockdown of MRPS39 resulted in a decrease of mitochondrial protein synthesis (Davies et al., 2009).

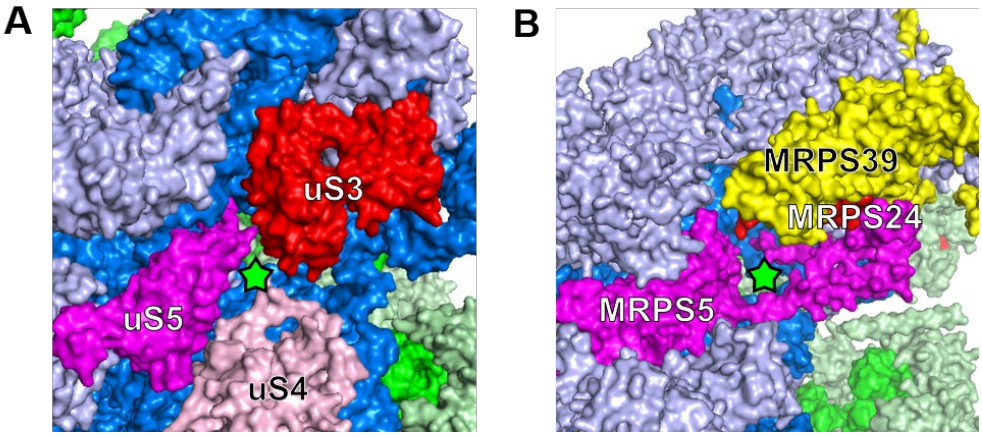

Figure 1.9: mRNA entrance site for the bacterial and human mitochondrial ribosomes. In each structure, colouring is as follows: large subunit (LSU) proteins (pale green), LSU RNA (bright green), mt-SSU proteins (light blue), mt-SSU RNA (dark blue), and the mRNA entry site (green star). **A:** The structure of the *E. coli* ribosome (PDB 4YBB) at the mRNA entry site. Surrounding this site are uS5 (magenta), uS3 (red) and uS4 (light pink). **B:** The structure of human mitoribosome (PDB 39JM) at the mt-mRNA entry site. Surrounding this site are MRPS24 (red), MRPS5 (magenta), and MRPS39 (yellow).

1.6.6 The human mitoribosomal large subunit

The human mt- LSU is composed of *RNR2*, mt-tRNA^{Val} and the recent ribosomal nomenclature lists 53 proteins, of which 22 are mt-specific proteins (Amunts et al., 2015; Greber et al., 2014). Structurally, the main features of the LSU are the central protuberance (cp), the L7/L12 stalk and the L1 stalk (Figure 1.10). The mt-LSU contains the polypeptide exit site (PES) where

nascent proteins will emerge from the mitoribosome. Regarding *RNR2*, similarly to *RNR1*, there is an approximately 50% reduction in the RNA content compared to the bacterial 23S rRNA equivalent. One area of sequence conservation is the sarcin-ricin loop, which is essential for GTP-catalyzed steps of translation (Brown et al., 2014). Many of the mt-specific proteins do not have homologs in bacteria and they are preferentially found in the cp and in solvent-exposed areas.

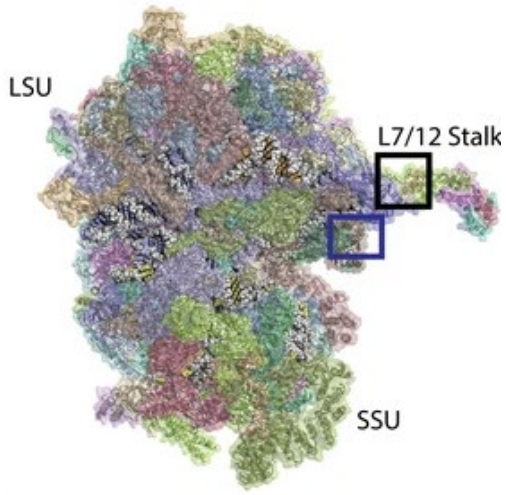

Figure 1.10: Overview of the human mt-LSU. Mitoribosomal proteins are shown in cartoon with transparent surface, rRNA is shown as spheres. Displayed is the improved model of the N-terminal L7/12 stalk mitochondrial extension. Image is taken from Aibara, S., Singh, V., Modelska, A., and Amunts, A. (2020). Structural basis of mitochondrial translation. Elife 9, 1–17.

The LSU of bacterial ribosomes contain a 5S rRNA species which is replaced by mt-tRNA^{Val} in human mt-LSU. This may be linked to the location of tRNA^{Val} in the mitochondrial genome, as it is found punctuating the genes for *RNR1* and *RNR2* and is part of the same polycistronic transcript (Brown et al., 2014). The L7/L12 stalk is a protrusion from the LSU that is responsible for the recruitment of translation factors in both bacterial and human mitoribosomes (Aibara et al., 2020). There is extensive remodelling of this region in human mt-LSU through mt-specific MRPL53 and extension to the MRPL10 and MRPL16 which have bacterial homologs. These changes have conferred increased stability of the stalk which has reduced the ability of functionally replacing human translation factors with bacterial homologs, such as EF-G (Brown et al., 2014). Another area of broad remodelling is the PES, wherein many mt-specific proteins are congregated on top of a group of proteins conserved from bacterial ribosomes. It has recently been shown that insertase OXA1L binds to the LSU at this exit sit and aids the translocation of nascent proteins into the IMM. LSU confirmational

changes and specific folding of MRPL45 inside the exit tunnel facilitate the insertion of nascent proteins by limiting helix formation (Englmeier et al., 2017; Itoh et al., 2021).

1.6.7 Phases of mitochondrial translation

Mitochondrial transcription yields 9 monocistronic transcripts and 2 bicistronic transcripts. Through the process of mitochondrial translation of these mt-mRNA transcripts, proteins will be synthesised in anticipation of incorporation into OXPHOS complexes. There are four main steps in the process of mitochondrial translation: initiation, elongation, termination, and ribosome recycling (Reviewed in Christian and Spremulli, 2012; Mai et al., 2016). The mitochondrial protein synthesis machinery more closely resembles prokaryotic translation than that occurring in the eukaryotic cytosol (Smits et al., 2010). However, there are a number of distinct characteristics present in the mitochondrial system. For example, in mammalian mitochondria, AUA codes for methionine, the canonical UGA stop codon is read as tryptophan, and AGA and AGG are unassigned codons (Chrzanowska-Lightowlers et al., 2011).

Initiation: The first step in mitochondrial translation is initiation, which involves the formation of distinct pre-complexes (Figure 11 A). At this point, the mitochondrial initiation factor mtIF3 binds to mt-SSU to prevent premature formation of the monosome (Koc and Spremulli, 2002). mtIF3 and MRPS37 stabilize the head of the mt-SSU to allow accommodation of mtIF2:GTP (Khawaja et al., 2020). The exact process of mt-mRNA loading onto the ribosome is far from fully characterised, however LPPRC/SLIRP are thought to interact with MRPS39 to facilitate the process (Amunts et al., 2015; Borna et al., 2019). mtIF2 recruits a formylated methionyl-tRNA which recognises AUG, AUA, AUU as start codons. In the event of an accepted codon: anticodon interaction, the 28S initiation complex (or the stable complex) is formed. It has been recently demonstrated that the binding of mtIF3 and fMet-tRNA^{fMet} is mutually exclusive (Khawaja et al., 2020). Therefore either, monosome formation results in the hydrolysis of GTP to GDP, the release of the initiation factors and the binding of both mRNA and tRNA, or the release of initiation factors precedes the binding of mRNA and tRNA and monosome formation. The result of these processes is the 55S monosome loaded with an initiator tRNA and an mRNA transcript.

Elongation: Formation of the monosome indicates that the elongation phase of mitochondrial translation can begin (Figure 11 B). Three factors are known to be involved in elongation: mitochondrial elongation factors -Tu (mtEF-Tu), -Ts (mtEF-Ts), and G1 (mtEF-G1).

Monosome formation brings together a complex consisting of mtEF-Tu, GTP and a charged mt-tRNA which is able to enter the aminoacyl site (A-site) of the mitoribosome. The formation of this complex promotes GTP hydrolysis, triggering the release of MtEF-Tu-GDP and allowing the tRNA to move into the peptidyl site (P-site). The formation of the peptide bond is catalysed in the mt-LSU and the tRNA is deacylated. Interaction of the elongation factor mtEF-G1 causes a conformational change in the mitoribosome, which leads to the release of the deacylated mt-tRNA and a new, charged, mt-tRNA to move into the P-site. There is recent evidence of the presence of an exit site (E-site) in the mitoribosome and that the deacylated mt-tRNA moves into this site before exiting the mitoribosome (Amunts et al., 2015; Greber et al., 2015).

Termination: Termination of translation is initiated when a stop codon enters the A-site of the mitoribosome (Figure 11 C). Mitochondrial stop codons only include the canonical UAA and UAG stop codons that are used in nuclear encoded transcripts, as the canonical stop codon UGA encodes tryptophan in mitochondrial translation (Osawa et al., 1992). Originally AGA and AGG were considered to be unusual stop codons present in the mitochondrial transcripts *MTCO1* and *MTND6* respectively. However, investigations identified that there is a -1 frameshift that occurs to place a UAG stop codon at the end of these transcripts allowing recognition by the release factor mtRF1a (Temperley et al., 2010a, 2010b). Release factors (RFs) are also associated with the termination of translation in mitochondria. These factors recognise stop codon sequences and promote hydrolysis of the ester bond between the polypeptide chain and the mt-tRNA in the P site. Within mitochondria there are four members of the RF family, mtRF1, mtRF1a, ICT1 and C12orf65. Of these mtRF1a promotes conventional peptide release. ICT1 has become a structural component of the mt-LSU but may have other roles in quality control (Kummer et al., 2021; Richter et al., 2010). C12orf65 is important in translation as many patients harbouring mutations in this gene showing mt-translation defects (Desai et al., 2020; Perrone et al., 2020).

Ribosome recycling: The mitoribosome is recycled by the action of two mitochondrial ribosome recycling factors, mtRRF1 and mtEF-G2 (Figure 11 C) (Kummer et al., 2021). These factors bind to the A site to facilitate the release of the nascent mRNA and the deacylated tRNA from the monosome via GTP hydrolysis (Tsuboi et al., 2009). The monosome is then dissociated into the mt-LSU and mt-SSU, which can then enter a new round of translation. Premature monosome formation is prevented by the binding of mtIF3.

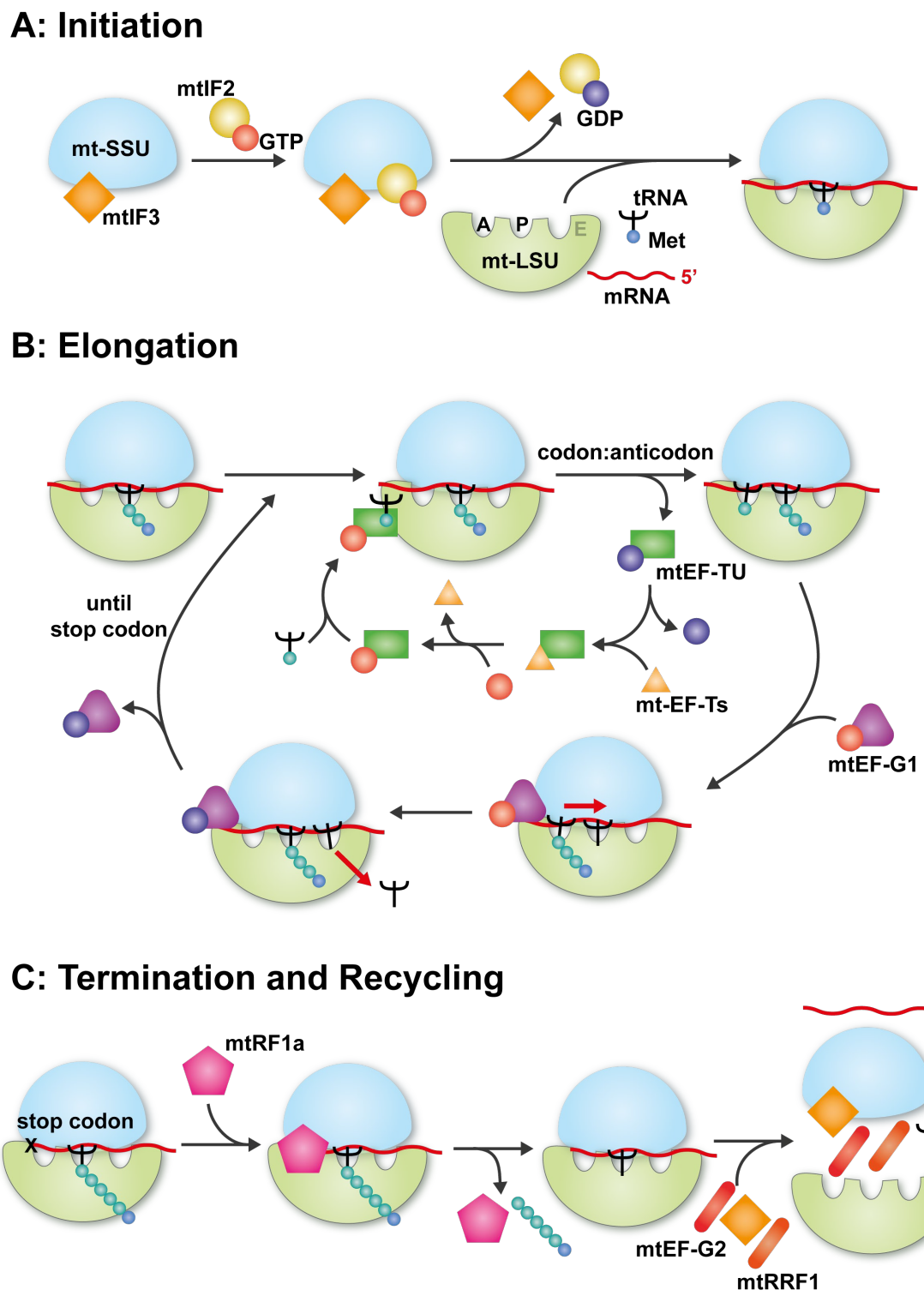

Figure 1.11: The phases on human mitochondrial translation. A full explanation of these phases is in the text. The process is divided into **A:** Initiation, **B:** Elongation, **C:** Termination and Recycling. Figure is adapted and updated Mai N, Chrzanowska-Lightowlers ZM, & Lightowlers RN. (2016).

1.7 Super resolution microscopy

The following section will give a short overview of the principles that are used in this thesis. This includes an understanding of microscopy beyond the diffraction limit, specifically STED microscopy and the benefits and limitations of this method.

1.7.1 Fluorescence microscopy

Classical microscopy is wide field microscopy, which uses bright white light and lenses to enlarge objects. Basic optical microscopes are thought to have been used since the 17th century and have increased in complexity over the centuries providing better resolution and using new illumination techniques. Wide field microscopy has been developed by scientists to include multiple types of microscopy such as phase contrast, confocal, and fluorescence microscopy. First described by Stokes in 1852 (Stokes, 1852), fluorescence is the emission of light by a substance that has absorbed light. This substance, a fluorophore, always emits light at a longer wavelength, lower energy, than the excitation light (Figure 12). When a fluorescent molecule is excited by light it moves electrons in the molecule to an excited energy state (Figure 12). These electrons lose a small amount of energy due to vibrational relaxation. The excited electrons return to the ground state by releasing light. As some energy was lost during vibrational relation, the light emitted by the molecule is at a lower energy level (longer wavelength) than the light absorbed. The movement between absorbed and emitted light is known as the Stokes shift.

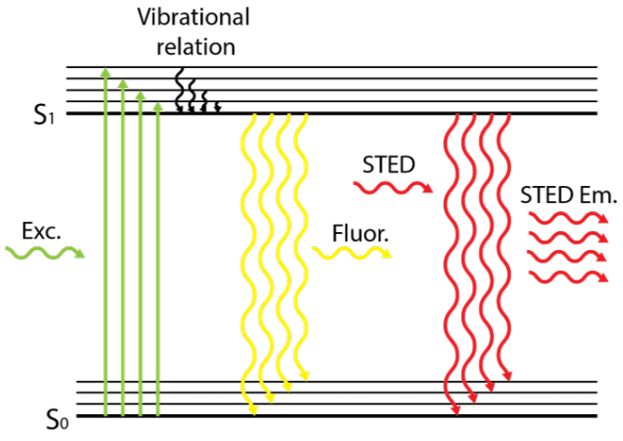

Figure 1.12: A simplified Jablonski diagram of the electronic states of electrons during fluorescence microscopy. Excitation (Exc.) light causes electrons to be excited a higher energy level (S_0). A small amount of energy is lost due to vibrational relaxation. The excited electrons return to the ground state and release photons called fluorescence (fluor.). During STED, the excited electrons interact with a STED photons, the electrons are forced to relax into a red-shifted ground state.

Many fluorophores are susceptible to photobleaching whereby the fluorophore permanently loses the ability to fluoresce. This is caused by the irreversible covalent modification of fluorophores when they are in their excited state. The occurrence of photobleaching is dependent on the fluorophore chemical structure; some fluorophores bleach quickly and others can undergo multiple excitation and emission cycles before bleaching.

1.7.2 Microscopy beyond the diffraction limit

Conventional optical microscopy has a resolution limit of ~250nm in the *x* and *y* direction and >450nm in the *z* direction called the point-spread function (PSF). Any object smaller than the PSF will appear this size, and objects closer in space than the PSF are indistinguishable. Microscopes that can resolve beyond the PSF by a factor greater than two are considered super resolution.

Confocal microscopy is a microscopy technique that can marginally resolve beyond the PSF but is not considered a super resolution technique. Confocal microscopy, however, is extremely useful in fluorescence imaging as it is able to eliminate out-of-focus fluorescent light from samples. Conventional light microscopes bathe the entire sample in light and consequently fluorophores will emit light multiple depths in the sample Z plane, creating background. In contrast, confocal microscopes illuminate the sample using one or more focussed beams of light that illuminate specific depths of the sample. The light is shone through a pinhole aperture to eliminate all but a narrow beam of light that is focussed using an objective. The loss of light intensity after the pinhole is offset by highly sensitive detectors.

STimulated Emission Depletion (STED) microscopy is built from the foundation of confocal microscopy, by shaping the excitation light. STED microscopes effectively decrease the PSF using a doughnut-shaped depletion laser that deactivates fluorophores within the doughnut, creating a sharper spot of fluorescence (Figure 13) (Galbraith and Galbraith, 2011; Hell and Wichmann, 1994). The STED beam is a red-shifted laser that returns fluorophores within the beam to their ground state by means of stimulated emission, before the fluorescence emission can occur (Figure 1.13). STED microscopy of mitochondria has been shown to reach resolution laterally (~30-40nm) and axially (~100nm) (Jakobs and Wurm, 2014).

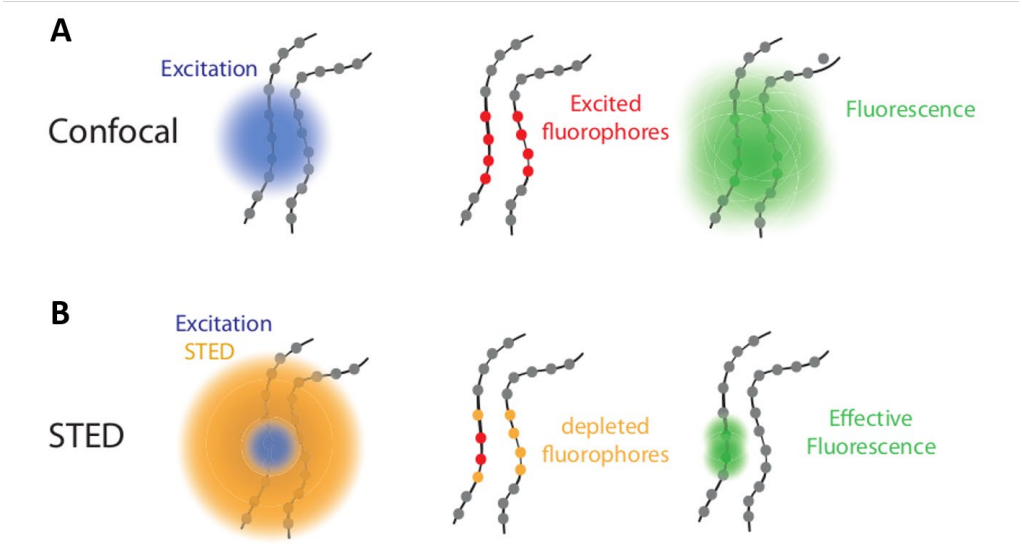

Figure 1.13: Graphic illustration illustrating resolution increase by STED. **A:** In conventional confocal microscopy most of the fluorophores in the focal region are excited (red) and fluoresce, resulting in a low resolution. **B:** When STED is applied, a doughnut-shaped beam (orange) is overlapped with the excitation spot in the focal region. This leads to depletion of the excited fluorophores in the overlapping region (yellow dots). Only the fluorophores in the centre of the doughnut fluoresce (green), increasing the resolution. Image taken from https://svi.nl/STED-Microscopy.

1.8 Proximity labelling using BioID

The understanding of protein-protein interactions is becoming increasingly necessary in order to understand the functions of proteins, in the context of their biological environment. Conventional affinity purifications are well suited to detect specific and direct interactions but are limited in their ability for the discovery of weak interactions. With the aim of reviewing transient molecular associations, a proximity-dependent biotin identification technique called BioID was developed (Roux et al., 2012). BirA is a highly selective biotin ligase from *Escherichia coli* that specifically biotinylates BirA target protein, acetyl-CoA carboxylases. The introduction of a R118G mutation in the ligase removed this specificity allowing promiscuous biotinylation of proximal primary amines in a biotin rich background. The fusion mutated BirA, also called BioID, to a protein of interest allows biotinylation of proteins in close proximity, regardless of the type of protein-protein association - direct, indirect or simply occupying the same subcellular region. The biotin remains on the prey protein allowing for stringent purification using streptavidin and identification with mass spectrometry (Figure 1.14).

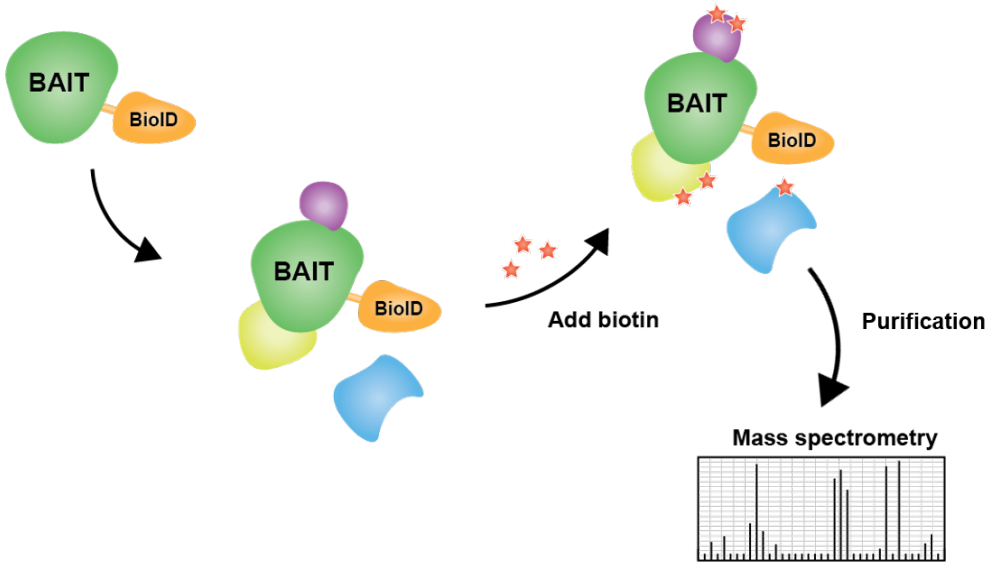

Figure 1.14: Overview of the basic principle of the BioID system. A bait protein is fused to BioID. This protein is expressed in cells and interactions with other proteins. The addition of biotin facilitates biotinylation of proximal prey proteins. These prey proteins are purified and identified by mass spectrometry.

One limitation of BioID is the size of the ligase (7.8 x 3.0 nm) which may affect the ability of tagged proteins to form complexes as part of their molecular roles. This was partially resolved by discovery of a smaller biotin ligase from *Aquifex aeolicus* (3.8 x 3.0 nm) was likewise mutated to remove specificity (Kim et al., 2016). Due to its substantially smaller size, BioID2

comes with its many advantages including its ability to improve correct localisation and function of the fusion protein, and improved biotinylation in lower concentrations of biotin.

Since the introduction of this method in 2012, it has been applied to a broad range of biological questions. This has included research into mitochondria and mitochondrial expression (Antonicka et al., 2020; Silva et al., 2018).

1.9 Prohibitins: PHB and PHB2

As previously introduced, the prohibitin proteins PHB and PHB2 are localised to the inner mitochondrial membrane. These proteins are ubiquitously expressed and assemble into heterodimeric rings in the IMM (Nijtmans et al., 2000). The stability of PHB and PHB2 is closely linked to the formation of the prohibitin complex; loss of either protein causes the loss of the other (Merkwirth and Langer, 2009). The role of PHB and PHB2 is yet to be fully characterised; they have been implicated in multiple mitochondrial processes including biogenesis, network morphology, mitophagy, OXPHOS homeostasis (Bavelloni et al., 2015; Nijtmans et al., 2000; Signorile et al., 2019; reviewed in Peng et al., 2015). The majority of prescribed roles have been linked to modulation of membranes in a variety of organisms.

PHB/PHB2 has been shown to have a conserved role in determining the lifespan of organisms via modulation of metabolic pathways (Artal-Sanz and Tavernarakis, 2009a, 2009b, 2010). This was shown by depletion of the prohibitin complex in nematodes, resulting in shortened lifespan in metabolically compromised strains, and exhibiting an extension of lifespan in long-life mutants (Artal-Sanz and Tavernarakis, 2009b). This mutant displayed increased triacylglycerol content, a membrane component which PHB is known to modulate in young adult nematodes (Lourenço et al., 2015). Within *C. elegans* mitochondria, PHB2 has a defined role in Parkin induced mitophagy (Wei et al., 2017). Upon depolarization and out membrane rupture, PHB acts as the receptor for the autophagosomal membrane-associated protein LC3.

The prohibitin heterodimer has been shown to control membrane composition by its interaction with Stomatin-like protein-2 (SLP-2) and cardiolipin in human cells (Christie et al., 2011; Da Cruz et al., 2008; Mitsopoulos et al., 2017). There is evidence that these proteins act to stabilise cristae tubules and protect against cristae collapse as loss of these proteins results in alterations in crista morphology (Osman et al., 2009). As there is an association between mitochondrial translation and the inner membrane, there have been speculations of prohibitin/SLP-2 involvement in the regulation of translation (Pfeffer et al., 2015; Mitsopoulos et al., 2017). One

possible method of this modulation is via regulation of mitochondrial nucleoids, which are also IMM localised (Kasashima et al., 2008). Depletion of PHB/PHB2 has been shown to cause disruption of nucleoid organisation, a disruption of mitochondrial biogenesis, and reductions in the expression of mitochondrially-encoded proteins (He et al., 2012; Merkwirth and Langer, 2009; Merkwirth et al., 2012).

1.10 Aims

Much of the life cycle of mt-RNA and the process of translation is still unclear, in particular a full understanding of mt-mRNA stability, delivery and loading onto the mt-SSU is lacking. At the beginning of this study, I focused my attention on utilising fluorescence microscopy to investigate the distribution of mt-rRNA within the mitochondria. I aimed to determine the proportion of the mitoribosomal subunits that were found as monosome, and therefore competent to accept mt-mRNA. This was to take advantage of the advances in super resolution microscopy that could allow discrimination of RNA molecules at a ribosome level using RNA Fluorescent In Situ Hybridisation. The plan was to harness this ability and to pair this technique with super resolution immunofluorescence to investigate the submitochondrial localisation of each subunit and other possible proximal proteins. There were many limitations with this chosen method and, although validation and publication of the technique were successful, I chose to diversify my investigation into a different aspect of mitochondrial translation. How the mt-mRNA is delivered to the mitoribosome was still unclear and so I devised tools to use the promiscuous biotin ligase, BioID2 method, to tag interacting and proximal proteins around the mt-mRNA entry site. Fusion proteins of the BioID2 moiety with a number of mt-SSU proteins were then used to identify proteins that are proximal to this discrete location on the mitoribosome.

The specific aims of this study were to:

- Develop and optimise an RNA FISH protocol compatible with super resolution microscopy
- Characterise and quantify the distribution and co-localisation of 12S mt-RNA (*RNR1*) and 16S mt-rRNA (*RNR2*) in combination with immunofluorescence of mt-markers
- Examine the distribution of mt-RNA following targeted depletion of 16S mt-rRNA
- Generate proximity labelling tools to investigate mt-mRNA loading onto the mitoribosome

- Validate the expression, localisation, and integration into the ribosome of the MRP-BioID2 fusion proteins
- Characterise protein-protein associations of mitoribosomal proteins using biotin capture and subsequent mass spectrometry
- Investigate and characterise the interactions of proteins identified to be proximal to the mRNA entry site.

The following chapters will describe the progress made on each of these aims.

Chapter 2:

Materials and Methods

2.1 Microbiological techniques

2.1.1 Bacterial culture and storage

Bacteria were cultured in Luria-Bertani (LB) media (5 g NaCl, 5 g bacto-tryptone, 2.5 g yeast extract prepared in 500 ml dH_2O, pH 7.4) broth or on LB agar (3% agar) plates. The LB was autoclaved and allowed to cool to 55 °C before antibiotics were added at the appropriate concentration (Table 2.1). For long term storage of bacterial strains, bacteria were frozen at -80 °C in LB media containing 18% glycerol. Bacterial strains were recovered from glycerol storage using a flame-sterilised inoculation loop. The loop was sterilised in the flame, allowed to cool for 10 seconds then placed in the stock to gather bacterial cells, this was streaked onto an LB agar plate containing the appropriate antibiotic and allowed to culture overnight at 37 °C.

Table 2.1: Antibiotic concentrations for plasmid amplification in LB broth or on agar

Antibiotic	Stock concentration (mg/ml)	Working concentration (µg/ml)
Ampicillin	100	100
Chloramphenicol	50	50
Kanamycin	50	50

2.1.2 Transformation of bacterial cells

For each transformation, a 40 µl aliquot of chemically competent cells (Bioline α-select bronze efficiency BIO-85025) was thawed on ice. Isolated DNA (4 µl) was added and the mixture incubated on ice for 30 minutes. The cells were heat shocked at 42 °C for 45 seconds before returning to ice for 2 minutes. Pre-warmed SOC (900 µl, Table 2.2) media was added and incubated at 37 °C for 1 hour with agitation. The cells were centrifuged at 240 g for 1 minute and the cell pellet resuspended in 100 µl of SOC media. 20 µl and 80 µl aliquots of this solution were plated on agar plates with the appropriate antibiotic and incubated, inverted, overnight at 37°C. Single colonies were re-plated for colony screening and future propagations.

Table 2.2: Composition of transformation broth

Broth	Composition
Super Optimal Broth (SOB medium)	2% bacto-tryptone, 0.5% yeast extract, 0.05% NaCl, 2.5 mM KCl; autoclaved.
Super Optimal broth with Catabolite repression (SOC)	SOB medium + filter sterilised MgCl2 and glucose to 10 mM and 20 mM concentrations, respectively

2.2 DNA manipulations

2.2.1 Plasmid DNA isolation

Single bacterial colonies containing plasmid DNA were picked using sterile pipette tips and used to inoculate ~5 ml LB broth containing the appropriate antibiotics. To amplify the plasmid, the cultures were grown overnight at 37 °C in an orbital shaker (300 rpm) to amplify the plasmid number. Plasmid DNA was extracted using the Monarch® Plasmid Miniprep Kit (NEB T1010) following the manufacturers protocol.

The concentration and purity of isolated DNA was measures using the Nano-drop spectrophotometer (ND-100) using 1 µl of the sample.

2.2.2 Restriction digestion of DNA

Restriction digests, using appropriate restriction enzymes and buffers, were carried out differently depending on the intended purpose as outlined below.

Diagnostic digest to verify plasmid molecular weight: 0.5 U of restriction enzyme, 1x restriction buffer, 0.5 µg plasmid DNA, sterile dH_2O up to 10 µl final volume. Digests were incubated at 37 °C for a minimum of 3 hours.

Plasmid DNA double digest to prepare inserts or vectors for transfection: 0.5 U of each restriction enzyme, 1x restriction buffer, 1 µg DNA, sterile dH_2O up to 20 µl final volume. Where a large volume of digested DNA was required, the digest was scaled up to a maximum 50 µl volume (5 µg DNA and 2 U of each enzyme). Digests were incubated at 37 °C overnight.

Digest of polymerase chain reaction (PCR) amplified and gel extracted DNA: 0.5 U of restriction enzyme, 1x restriction buffer, ~500 ng DNA, sterile dH_2O up to 20 µl. Digests were incubated at 37 °C overnight.

2.2.3 DNA amplification by polymerase chain reaction (PCR)

PCR reactions were carried out using the Applied Biosystems ProFlex PCR System. Each reaction contained: 1X Phusion HF buffer (with 1.5 mM $MgCl_2$), 200 µM dNTPs (final concentration) (Roche), 0.25 µl Phusion® Hot Start II DNA Polymerase (ThermoFisher, F549L), 0.5 µM of forward primer, 0.5 µM of reverse primer, ~10 ng plasmid DNA, and sterile dH_2O up to 25 µl.

Where a large volume of amplified DNA was required, the PCR amplification was scaled up to a maximum 50 µl reaction. To aid denaturation of high GC content templates, 2-5% DMSO

was added to PCR reaction mixtures when required. All primers used in this study were custom synthesized by Eurogentec. A full list of primers is included in Appendix I.

The annealing temperatures and extension times for each PCR amplification were optimised for each reaction. These were designed to amplify the open reading frame of target proteins. An annealing temperature was initially predicted using the ThermoFisher Scientific Tm Calculator. If the PCR was unsuccessful, temperature gradient PCR reactions were used to identify the optimal annealing temperature. Gradient PCR reactions were carried out on PTC-200 MJ Research PCR machine using the same reaction mixture detailed above. The final optimised conditions for the amplification of each target are detailed in Table 3.3. Cycles (35x) of denaturation, annealing and extension were repeated before a final extension step. After reactions were complete, tubes were stored at 4°C.

Table 2.3: PCR conditions for gene product amplification

Target	Size (kb)	PCR Conditions (m=minutes, s=seconds)				
		Initial Denaturation	Denaturation	Annealing	Extension	Final Extension
MRPS27	1.273	95 °C - 3 m	95 °C – 15 s	64 °C - 45 s	72°C - 90 s	72°C - 7 m
SLIRP	0.360			60 °C - 45 s	72 °C - 45 s	
			35 cycles			

2.2.4 Gel extraction of amplified or digested DNA fragments

Following digest or PCR reactions, DNA was separated by size using agarose gel electrophoresis (2.2.8). Signals were visualized using a UV transilluminator, those of the correct molecular weight were excised, removing as much of the gel as possible. DNA was extracted using the QIAquick Gel Extraction Kit according to the manufacturer's protocol.

2.2.5 Dephosphorylation of linearized DNA

Dephosphorylation of linearized vectors was carried out immediately after digestion by addition of 2 µl 1M Tris pH 9.4, 2 µl 10% SDS and 0.5 µl alkaline phosphatase to a 20 µl digestion mixture. The dephosphorylation reaction was carried out at 37 °C for 30 minutes.

2.2.6 DNA purification by phenol/chlorophorm extraction and ethanol precipitation

Reaction digests (for both plasmid DNA and PCR products) were adjusted to a volume of 50 µl. An equal volume (50 µl) of phenol pH 7.4 (Sigma P-4557) was added, tubes were briefly vortexed and centrifuged 15000 g for 2 minutes. The upper aqueous phase (~50 µl) was

carefully removed and transferred into a fresh microcentrifuge tube. Half a volume of phenol (~25 µl) and half a volume of 24:1 chloroform:isoamylalcohol (~25µl) was added. As before, the samples were briefly vortexed and centrifuged. The upper aqueous phase (~50 µl) was again transferred to a fresh microcentrifuge tube. An equal volume of 24:1 chloroform:isoamylalcohol was added and tubes were vortexed and centrifuged as above.

The upper aqueous phase phase (~50 µl) was transferred to a fresh microcentrifuge tube, and DNA was precipitated by adding a tenth of the volume (5 µl) of 3M sodium acetate pH 5.3, 1 µl of linear acrylamide and two times the total volume (110 µl) of 100% ethanol. The samples were incubated at -80°C for 1 hour before the DNA was pelleted by centrifugation at 15000 g at 4 °C for 30 minutes. The supernatant was discarded, and the DNA pellet was briefly air dried. DNA was resuspended in 12 µl of autoclaved dH_2O.

2.2.7 DNA fragment ligation

The Rapid DNA Ligation Kit (ThermoFisher Scientific) was used to ligate digested inserts (PCR products or gel-extracted digested DNA fragments) into digested and dephosphorylated vectors. Ligation reagents were mixed according to the recommended protocol and the reaction allowed to occur overnight at 22 °C.

2.2.8 DNA agarose gel electrophoresis

Agarose gels were used to analyse linearized vectors, PCR products or gel-extracted digested DNA fragments. Agarose (NBS-Biologicals, NBS-AG500) was dissolved in 1x Tris-Acetate EDTA (TAE) buffer prepared from a 50x stock (Table 2.4). The mixture was boiled in the microwave until all the agarose had dissolved. Once the agarose had reached ~45 °C, ethidium bromide (EtBr) was added to a final concentration on 0.5 µg/ml and mixed before pouring into a gel cast. The set gel was placed into an electrophoresis chamber and immersed in 1x TAE buffer with addition of EtBr to a final concentration of 0.5 µg/ml. Samples were loaded in 1x DNA loading buffer (3% glycerol, 0.025% bromophenol blue, and 0.025% xylene cyanol) except when the PCR buffer/digestion buffer contained dye. Depending on the sample to be analysed, one of four molecular weight markers were used as a reference: NEB® 1 kb Ladder, HyperLadder™ 1 kb (Bioline), MassRuler™ High Range DNA Ladder (ThermoFisher Scientific), or GeneRuler 1 kb Plus DNA Ladder (ThermoFisher Scientific). Samples were electrophoresed at a constant voltage of 70 Volts.

Table 2.4: TAE Buffer composition

TAE Buffer	Composition
50x TAE Buffer	12.1 g Trizma base, 2.86 ml glacial acetic acid, and 5 ml EDTA 0.5 M, made up to 50 ml with autoclaved dH2O.

2.2.9 DNA sequencing

Following diagnostic digest analysis (2.2.2), plasmids containing an insert of the correct size were analysed by Sanger sequencing. A 300-600bp region of interest was PCR amplified using custom synthesised primers (Eurogentec). A complete list of primers used to amplify a region for sequencing of each construct is listed in Table 2.5. Amplification was confirmed by analysis of the PCR product by gel electrophoresis. To avoid interference with downstream reactions, unincorporated dNTPs and primers were removed using the ExoSAP-IT protocol (ThermoFisher Scientific). In a 95 well plate, the PCR (5 µl) was incubated with 1.5 µl of ExoSAP-IT reagent and heated to 37 °C for 15 minutes, followed by 80 °C for 15 minutes. The sample was stored at 4 °C until needed.

In the same 95 well plate, the clean products were then cycle sequenced using the Big Dye Termination system (Applied Biosciences) by the addition of: 3 µl 5x Big Dye Buffer, 2 µl Big Dye Terminator, 1 µl primer (either forward or reverse), and 7 µl autoclaved dH_2O was added to each sample. The cycle sequencing conditions are given in Table 2.5.

Table 2.5: Big Dye Termination cycle sequencing conditions

Step	Temperature (°C)	Time	Cycles
Initial Denaturation	96	1 min	
Denaturation	96	10 sec	25 cycles
Annealing	50	5 sec	
Extension	60	4 min	
Hold	4	∞	

The DNA in each sample was precipitated by the addition of 2 µl 125 mM EDTA, 2 µl 3 M NaOAc, and 70 µl of absolute ethanol. Samples in the plate were sealed then mixed by inversion and incubated at room temperate for 15 minutes. The plate was centrifuged at 2000 g for 30 minutes and the supernatant discarded by inversion and tapping with the lid removed. 70 µl of 70% ethanol was added to each sample and centrifuged at 1650 g for 15 minutes. The supernatant was discarded as above, before a final spin of 100 g. The samples were allowed to

air dry in the dark for 10 minutes with the lid removed. Pellets were resuspended in 10 µl Hi-Di™ Formamide (ThermoFisher Scientific) and heated to 95 °C for 2 minutes. The samples were cooled on ice before analysis by the 3130 Genetic Analyzer (Applied Biosystems). In most cases, samples were kindly prepared by Dr Ruth Glasgow. A full list of sequences for bait-BioID2-Ha constructs can be found in Appendix IV.

2.3 Tissue culture

2.3.1 Cell lines used in this study

The following mammalian cell lines were used:

- **U2OS** - an immortalised human osteosarcoma cell line, wild type, selected for their stability, fast doubling time, and large cytoplasm, allowing for efficient mitochondrial imaging
- **HEK293 Flp-In™ T-Rex™** (Invitrogen) - Human embryonic kidney cell line containing the Flp-In™/TRex™ system
- **HeLa**: Human cervical epithelial cancer cells line derived from Henrietta Lacks
- **Custom generated tetracycline inducible (Flp-In™ T-Rex™) cell lines as part of this thesis unless described otherwise:**
    - HEK293-VapC20-His (Prepared by F. Bruni)
    - HEK293-MRPS5-BioID2-HA
    - HEK293-MRPS24-BioID2-HA
    - HEK293-MRPS27-BioID2-HA
    - HEK293-MRPS33-BioID2-HA
    - HEK293-MRPS35-BioID2-HA
    - HEK293-MRPS39-BioID2-HA
    - HEK293-SLIRP-BioID2-HA
    - HEK293-COX8MTS-BioID2-HA

2.3.2 General maintenance, thawing, and freezing human cells

All cells were cultured as monolayers in tissue culture vessels (Sarstedt) and incubated at 37 °C in a humidified 5% CO_2 atmosphere. All cell culture work was performed in a class II Microflow biological safety cabinet and cell confluency monitored using an Axiovert25 microscope (Zeiss).

Cells were propagated in Dulbecco's Modified Eagle's medium (DMEM, D6429) containing 1 mM pyruvate, 4500 mg/L glucose and 2 mM L-glutamine supplemented with 10% foetal calf serum (FCS), 1x non-essential amino acids, and 50 µg/ml uridine (Sigma U3003). In general, 2 ml media was used per well in 6 well plates or 35 mm dishes, 5 ml media for 25 cm^2 flasks, 12 ml media for 75 cm^2 flasks, 25 ml media for T175 cm^2 flasks, 35 ml media for T225 cm^2 flasks and 50 ml media for T300 cm^2 flasks. Media was changed approximately every 3-4 days. Transfected HEK293 Flp-In™ and U2OS Flp-In™ were supplemented with 10 µg/mL Blasticidin^S (Melford B1105) every third feed.

Cells were removed from liquid nitrogen stores and briefly thawed at 37 °C before the addition of warm complete media to a 10 ml volume. This solution was centrifuged at 217 g for 4 minutes to pellet the cells. Cells were resuspended in complete medium and transferred to a cell culture flask of the same size the cells were grown in before freezing.

When cells reached high (~80%) confluency, they were passaged by addition of an appropriate volume of 1xPBS/1 mM EDTA. After the cells had detached from the surface, the cell solution was centrifuged at 217 g for 4 minutes to pellet the cells. The pellet was resuspended in pre-warmed media and a fraction of cells seeded in a fresh flask(s) depending on the intended application of the cells.

Cells were regularly tested at 2-month intervals for mycoplasma infection using the MycoAlertTM mycoplasma testing kit (Lonza, LT07-118). A 1 ml aliquot of cell media from a flask cultured for at least 24 hours was tested. Upon detection of mycoplasma, the flask was discarded, and an earlier passage thawed that had been negative for mycoplasma on storage or treated with plasmocin until the infection had been eradicated.

For long term storage, cells were harvested as described above, and the cell pellet resuspended in 500-1500 µl of FCS supplemented with 10% dimethyl sulphoxide (DMSO). The volume of FCS/DMSO added depended on the volume of cells frozen. This volume was transferred to a cryostorage vial and stored in a Nalgene® Mr Frosty at -80 °C overnight before transferring to a liquid nitrogen storage tank.

2.3.3 Cell counting

Cells were counted using the Nexcelon Cellometer® Auto 1000 Cell Viability Counter. Following cell harvest, pelleting and resuspension in media, a 10 µl aliquot was mixed 1:1 with trypan blue (Sigma, T8154) and placed into Cellometer® cell counting chambers (SD100).

2.3.4 Cell culture for fluorescent imaging

Fluorescent imaging was carried out on sample cultures on high performance 0.17 mm glass coverslips (Carl Zeiss) that had been placed into 6 well plates or 35 mm cell culture dishes. To seed cells (HEK or U2OS) for approximately 10-15% confluency the following day, a dilution of cell was prepared from 75 cm^2 flasks. An 80% confluent 75 cm^2 flask was harvested (2.3.2) and the cell pellet resuspended in 5 ml of complete media. An aliquot (40 µl) of this cell suspension was added to a tube containing 2 ml complete media and mixed by inversion 5 times. An aliquot (100 µl) of this dilution suspension was carefully pipetted onto the centre each of the coverslips and allowed to adhere for a minimum of 2 hours. After adherence, 2 ml of complete media was added to the well and the cells were incubated overnight.

2.3.5 Transfection of cells using the Flp-In™ system

Multiple genes of interest were independently stably transfected into cells engineered with the Flp-In™ system. Cells were seeded into 6 well plates at ~15% such that the following day they were at 30% confluency. The transfections were carried out at two ratios of DNA:Superfect (Qiagen), 1:5 and 1:7.5. Plasmid DNA encoding the FRT recombinase, pOG44, 1.2 µg, was mixed with 0.8 µg of pcDNA™5/FRT/TO plasmid DNA containing the gene of interest and made up to a 100 µl volume with DMEM without supplements. The DNA mix (total 2 µg) was combined with 10 µl (1:5) or 15 µl (1:7.5) Superfect, mixed gently by pipetting and incubated at room temperature for 10 minutes. Pre-warmed complete cell culture media (600 µl) was added to each DNA-Superfect mix. Media was removed from cells, which were then washed with 1 ml 1xPBS before addition of the DNA/Superfect/media mixture. Two wells were incubated with just complete media to be used as controls. After 2.5-3 hours incubation, the DNA/Superfect/media mixture was removed and replaced with complete media. After 2 days selection for transfected clones commenced by removing the media from all the experimental and one control well and replacing with complete media containing 100 µg/mL $Hygromycin^B$ (Sigma H9773) and 10 µg/ml $Blasticidin^S$. The second control to indicate maximal growth of untransfected cells, and was fed with complete media. When all the cells in the control well

containing Hygromycin^{B} and Blasticidin^{S} had died, surviving individual clones from the experimental wells were picked and expanded in new wells.

Overexpression of the protein of interest in stably transfected cells was induced with tetracycline (1 ug/ml) (Sigma T7660) or doxycycline (Sigma D9891) at a variety of concentrations and induction durations. Expression levels were verified by western blot analysis.

2.4 Protein manipulation

2.4.1 Human cell lysate preparation

Cells were harvested from tissue culture vessels (2.3.2), pelleted immediately and resuspended in 50-200 µl in cell lysis buffer (50 mM Tris-HCl pH 7.5, 130 mM NaCl, 2 mM $MgCl_2$, 1 mM PMSF, 1% NP40, 1x protease inhibitor cocktail), dependent on cell volume. The suspension was vortexed briefly and incubated on ice for 15 minutes. The samples were vortexed again before centrifugation at 1000 g for 5 minutes to remove nuclei and any remaining whole cells. The supernatant was transferred to a new microcentrifuge tube and stored at -20 °C until use.

2.4.2 Protein concentration estimation (Bradford assay)

Protein concentration was determined by Bradford assay. A bovine serum albumin (BSA) standard curve was prepared using 0, 2, 5, 10, 15 and 20 µl BSA (1mg/ml) in a total volume of 800 µl with autoclaved dH_2O. For each sample, 2 µl was added to a total volume of 800 µl autoclaved dH_2O. 200 µl of Bradford Reagent (BioRad) was added and mixed thoroughly by vortexing. Aliquots (200 µl) of each sample was placed into a flat-bottomed 96 well plate and analysed at 595 nm, with reference to the standard curves on an aELx800 microplate reader (BioTek) by absorbance at 595 nm.

2.4.3 Mitochondrial isolation (Mitoprep)

Mitochondria were isolated from an ~80% confluent 300 cm^2 or two 175 cm^2 tissue culture flasks per sample. Cells were harvested (2.3.2) into 2 ml tubes and the pellet resuspended in 1.5 ml of homogenisation buffer (0.6 M mannitol, 1 mM EGTA, 10 mM Tris pH 7.4; supplemented with 0.1% BSA and 1 mM PMSF). The suspension was transferred to a glass:teflon Dounce homogeniser, on ice. Samples were homogenised by 15 passes before centrifugation at 400 g, 4 °C, 10 minutes. The supernatant was transferred to a fresh 2 ml, pre-cooled, microcentrifuge tube and the pellet was rehomogenised as above. The supernatant was again retained in a pre-cooled microcentrifuge tube and all supernatant tubes were centrifuged

at 400 g for 10 minutes. The supernatants were transferred into fresh microcentrifuge tubes and centrifuged at 11000 g for 10 minutes, 4 °C, to pellet the mitochondria. The pellets were combined and washed twice with homogenisation buffer, lacking BSA and PMSF, before being resuspended in a 40-100 µl of homogenisation buffer, depending on the pellet size. The protein concentration of mitochondrial prep samples was calculated by Bradford assay (2.4.2). The whole sample was then analysed via western blot (2.4.6) or fractionated to analyse sub-mitochondrial compartments (5.2.4).

2.4.4 Sucrose gradient analysis

The sucrose gradient was prepared by dissolving sucrose in sucrose buffer (50 mM Tris pH 7.2, 10 mM MgOAc, 40 mM NH_4Cl, 100 mM KCl, 1 mM PMSF and 50 µg/ml chloramphenicol) to generate 10% and 30% sucrose solutions. 0.5 ml of 10% sucrose was added to a 1 ml polycarbonate ultracentrifuge tube (Beckman, 343778). 0.5 ml of the 30% sucrose solution was carefully added below the 10% sucrose layer using a syringe and needle, such that two distinct layers were visible. The tubes were sealed using rubber plugs and placed into a Magnabase tube holder (Biocomp). A Gradient Master machine (Biocomp) was used to form the linear gradient using the programme TLS55, 10-30%, S1/1 0:55/85.0/22, which designated the rotor for later centrifugation, the sucrose compositions, the times, and the angle of rotation used to make the gradient. Following gradient formation, tubes were kept on a flat surface for 1 hour at 4 °C to stabilise.

Cells were harvested from 175 cm^2 tissue culture flasks (2.3.2) and resuspended in 100-150 µl (depending on pellet size) of sucrose gradient lysis buffer (1.8% Triton X-100, 50 mM Tris pH 7.4, 150 mM NaCl, 1 mM EDTA, 1 mM PMSF, and 10 mM $MgCl_2$). Samples were lysed on a rotator wheel at 4 °C for at least 30 minutes before centrifuging at 12000 g for 10 minutes, 4 °C. The supernatants were transferred to a fresh microcentrifuge tube and the protein concentration determined by Bradford Assay (2.4.2). 700 µg in a total volume of 100 µl was gently loaded on top of the prepared sucrose gradient. The samples were centrifuged in a Beckman Optima TLX bench ultracentrifuge (rotor TLS55, Accel 1, Decel 4) at 100000 g for 2.25 hours at 6 °C. Fractions (100 µl) were collected from the top of the gradient into 11 separate microcentrifuge tubes, on ice. Aliquots (10-25 µl) of these fractions were mixed with sample dissociation buffer (final concentration: 6.25 mM Tris/HCl pH 6.8, 2% SDS, 10% glycerol, ~0.01% bromophenol blue and 100 mM DTT) and analysed via western blotting (2.4.6).

2.4.5 SDS-polyacrylamide gel electrophoresis

SDS-PAGE was used to separate proteins by molecular weight using 10% or 12% acrylamide resolving gels. Resolving and stacking gels were prepared as described in Table 6 using the Bio-Rad Mini-Protean® Tetra Cell system. Isopropanol (200 µl) was added above the resolving gel to aid the formation of a level meniscus. After polymerisation of the resolving gel, this volume was removed using blotting paper and the 3.75% stacking gel added on top.

Table 2.6: Resolving gel and Stacking gel for SDS-page analysis.

Reagent	Final concentration		
	10% resolving gel	**12% resolving gel**	**3.75% stacking gel**
Tris pH 8.5	--	--	125mM
Tris pH 6.8	380 mM	380 mM	--
30% acrylamide-bisacrylamide 29:1	10%	12%	3.75%
SDS	0.1%	0.1%	0.1%
APS	0.1%	0.1%	0.1%
TEMED	0.1%	0.1%	0.1%

Samples were mixed with sample dissociation buffer and incubated at 95 °C for 5 minutes before loading onto the gel. In all blots, a molecular weight protein marker (Cleaver Scientific, CSL-BBL) occupied at least 1 lane on the gel. Samples were electrophoresed in SDS-running buffer (102 mM Glycine, 25 mM Tris, 0.1% SDS) at 80 V through the stacking gel and 180V through the resolving gel.

2.4.6 Western blotting and immunodetection

Following electrophoresis, the proteins were transferred to PVDF membranes (Immobilon-P, Millipore). The PVDF membrane was activated in $H_2O$for 15 seconds before equilibrating in transfer buffer (192 mM glycine, 25 mM Tris, 0.02% SDS, 25% methanol). The polyacrylamide gel was also equilibrated in transfer buffer while the membrane was activating. The gel and activated membrane were sandwiched between 3MM Whatman filter paper and gel sponges, avoiding bubbles. The transfer was effected in the Mini Trans-BlotTM module (BioRad®) at 100 V, 1 hour, 4 °C. The membrane was blocked in 5% milk/TBST (Tris-buffered saline (50 mM Tris, 150 mM NaCl, pH 7.6), 0.1% Tween 20) for 1hr with agitation. Membranes were incubated overnight at 4 °C with primary antibody (diluted in 5% milk/TBST) with agitation before washing 3 times in TBST, 15 minutes per wash. The membranes were then incubated with the appropriate secondary antibody (diluted in 5% milk/TBST) for 1 hour at room temperature with agitation before washing 3 times in TBST, 15 minutes per wash.

ECL Prime reagents (GE Healthcare) was prepared according to the manufacturer's instructions and the signals were visualised on the Chemi-Doc™ MP Imaging System (Bio-Rad®) using the Image Lab™ Software.

Chapter 3:

Visualisation of mitochondrial RNA using RNA Fluorescent In Situ Hybridisation (RNA FISH)

3.1 Introduction

At the time of initiating this research, single molecule labelling of RNA by DNA probes was a known method that could be used for visualization and quantification of both mt-rRNA and mt-mRNA. RNA FISH generates specific fluorescence signals with low noise or false positive fluorescence, and it can be used in tandem with immunolabelling (Femino et al., 1998; Kochan et al., 2015; Raj et al., 2008). In addition, this method had previously been used to visualise the mt-rRNA, *RNR1* and *RNR2*, in mouse embryos (Zheng et al., 2016). This technique, however, had not been used to visualise mt-RNA in adherent human-derived cells or in combination with super resolution microscopy. I designed this study to investigate the positioning of mitoribosomes and their association with specific mt-mRNAs or proteins. The distribution of fluorescently labelled *RNR1* and *RNR2* within the mitochondrial network can indicate the sub-mitochondrial location of the mitoribosomal small subunit and large subunit, respectively. Overlap, or colocalization, between signals could so reveal the proportion of assembled mitoribosomes. This labelling could then be used in tandem with either further RNA FISH labelling of mt-mRNA or immunolabeling of mitochondrial proteins to provide a better understanding of the spatial organisation of the subunits and the process of mitoribosomal loading.

Mitochondrial networks can be visualised by fluorescence microscopy using a conventional light microscope. These microscopes are limited to a fixed resolution of ~180 nm x >500 nm in the focal plane and optic axis due to the fundamental constraints of light waves. Mitochondrial networks are predominantly this size or larger so can be effectively imaged. For this research, a much higher resolution is required as it is crucial to visualise sub-mitochondrial localisation of these RNA molecules. To visualise beyond the optical diffraction limits, super resolution microscopy such as STimulated Emission Depletion (STED) microscopy is required. The maximal resolution limitation of STED microscopy is ~30-50 nm which is comparable to the size of the mitochondrial monosome. STED microscopy had been successfully applied to visualise sub-mitochondrial regions prior to the start of this study (Jakobs and Wurm, 2014). To fit in my scale and address reproducibility, I chose to use a commercial provider for the custom DNA oligonucleotide probes, Stellaris® RNA FISH. These probes allowed simultaneous detection, localization, and quantification of individual RNA molecules in fixed cell samples. Nanoscale RNA FISH is achieved as each target RNA

species is probed with >25 individually labelled oligonucleotide probes, making each molecule identifiable as a discrete fluorescent signal (Raj et al., 2008). Following consultation with the Newcastle University Bioimaging Unit, three fluorophores readily available from Stellaris® were identified as STED compatible: Quasar 570, CAL Fluor 610, and Quasar 670. At the time of this research, none of these fluorophores has been used in combination with STED microscopy in published literature.

This study was designed to compare the fluorescent distributions and colocalizations of labelled mt-rRNA, mt-mRNA, and mitochondrial proteins. Colocalization analysis in microscopy is a function of two main parameters: concurrence – the spatial overlap of two signals, and correlation – two signals not only overlap but also co-distribute statistically (Adler and Parmryd, 2010). Multiple colocalization coefficients exist that can be used to understand colocalization for specific biological questions in fluorescence microscopy. In this study I will user two such coefficients: Pearson correlation coefficient (PCC) and Manders coefficients (M_1 and M_2).

Equation 3.1: Equations for Pearson correlation coefficient (PCC) and Manders coefficients (M_1 and M_2)

$$\mathbf{PCC} = \frac{\sum\left(\left(R_i - R_{avg}\right)\left(G_i - G_{avg}\right)\right)}{\sqrt{\sum\left(R_i - R_{avg}\right)^2 \sum\left(G_i - G_{avg}\right)^2}} \qquad \boldsymbol{M}_1 = \frac{\sum R_{coloc,i}}{\sum R_i} \qquad \boldsymbol{M}_2 = \frac{\sum G_{coloc,i}}{\sum G_i}$$

PCC is a linear correlation measurement that was applied to fluorescence by Manders in 1993 (Manders et al., 1993). Components R_i and G_i represent the intensity of the red and green channels for each voxel; R_{avg} and G_{avg} are the average intensity of the red and green channels across the entire image. Images with perfectly linear fluorescent intensities would have a PCC of +1, and images with perfectly, but inversely related, fluorescent intensities would have a PCC of -1. A score of zero indicates the fluorescence intensities on the images are uncorrelated. The main limitation of using PCC to analyse fluorescence data is that it does not provide clear information about colocalization when the scores are not found at the extremities (-1 or +1). As both intensity and distribution across the image are used in the calculation, mild/moderate PCC values could infer either different red/green distributions or different red/green intensities (Landmann, 2002). PCC values +/-0.1-0.48 are generally considered to be "moderate" and values +/-0.49-0.84 are "strong" (Zinchuk et al., 2013). To investigate the overlap of the two

signals rather than the intensity relationship between these pixels, Manders coefficients (M_1 and M_2) are more appropriate (Zeiss). These coefficients are defined by whether a pixel has detected fluorescence above a threshold using scatterplot data for each channel (Figure 3.1). Above the threshold, all pixels are all given an arbitrary value of '1', therefore intensity is not included in the calculation. M_1 is calculated by dividing the sum of pixels in the colocalized quadrant 3 by the sum of total pixels in channel 1 (quadrants 1 + 3), and M_2 is calculated by dividing the sum of pixels in the colocalized quadrant 3 by the sum of total pixels in channel 1 (quadrants 2 + 3). The pixels in quadrant 4 are low intensity values of each channel and are considered background. Manders coefficients are most often applied when channel intensities are not equal due to imaging constraints and where the biological question is answered by presence of the signal or not. The degree of colocalization for Manders values is considered weak (0.55-0.77), moderate (0.78-0.94), strong (0.96-0.98) or very strong (0.99+) (Zinchuk et al., 2013). To understand relationships between different RNA species in this research, both PCC and Manders coefficients were calculated.

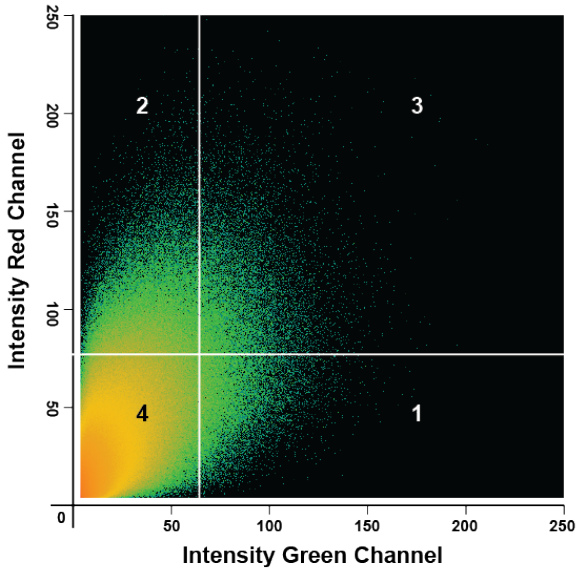

Figure 3.1: Example scatterplot generated using the Huygens Colocalization Software. Arbitrary intensity values are determined by the Huygens software and a threshold determined, above which is considered a high intensity of signal. **1:** pixels with high green intensities and low red intensities. **2:** pixels with high red intensities and low green intensities. **3:** pixels with both high red and green intensities; these pixels are considered colocalized. **4:** pixels with low high red and green intensities; these pixels are considered background.

3.2 Materials and Methods

3.2.1 RNA FISH Probe Design

All the RNA FISH probes used were designed and ordered using the Biosearch Tools Stellaris Probes designer (https://www.biosearchtech.com/). DNA sequences of interest were extracted from the *Homo sapiens* complete genome sequence and input into the probe designer tool (Andrews et al., 1999, RefSeq NC_012920.1). Probe sets comprised of 25-38 DNA oligonucleotides, each conjugated to a fluorophore, that selectively bind transcripts of interest (Table 3.1).

Table 3.1: Probe set RefSeq sequences and design information

Target	RefSeq (nucleotide position)	Number of probes	Masking Level	Fluorophore
MT-RNR1	NC_012920.1 (648-1601)	36	5	Quasar 570
MT-RNR2	NC_012920.1 (1671-3229)	38	5	CAL fluor 610, Quasar 670
MT-ND1	NC_012920.1 (3307-4262)	35	4	Quasar 570
MT-CO2	NC_012920.1 (7586-8269)	25	4	CAL Fluor 610

The design tool includes species-specific masking to avoid off-target hybridization to RNAs commonly expressed at high levels. When fewer than 25 probes, the suggested minimum, were generated at the most stringent level, the masking level was reduced to 4. For each probe set a minimum of 10 randomly selected probes were BLAST (The Basic Local Alignment Search Tool) searched to investigate any off-target binding sites. Following consultation with the Bioimaging Unit at Newcastle University, Quasar 570, CAL Fluor 610, and Quasar 670 were determined as the most STED-compatible fluorophores available from Stellaris. A full list of probes and their positions on the relevant transcripts can be found in Appendix III.

3.2.2 RNA FISH

All buffers and solutions involved were prepared in diethyl pyrocarbonate treated (DEPC-treated) water to be RNase free. All other standard consumables were of analytical grade. For fluorescent imaging (2.3.4) U2OS cells were cultured (2.3.2) on baked coverslips inside a 6 well plate. Cells were seeded such that they occupied the centre of the coverslip at between 20-30% on the day of the experiment (2.3.4). High performance coverslips (Zeiss, 0.17 mm) were used during all slide preparations to ensure the thickness of the coverslip remained consistent across the coverslip.

Cell culture media was removed from each well and the coverslip washed twice with warm 1xPBS to prevent cell shock. The PBS was removed, and the cells were fixed with 1ml fixative (4% paraformaldehyde, 0.2% glutaraldehyde) for 10 minutes at room temperature. The fixative was removed, the coverslips washed twice with 1ml 1xPBS and the cells were permeablized using 70% ethanol for 1 hour at room temperature or overnight at 4°C. Ethanol was removed and coverslips were washed twice with 1xPBS before cells were equilibrated in of 1ml wash buffer (10% formamide, 2× SSC) for 5 minutes. Stellaris Probes were resuspended in TE buffer (10mM Tris-HCl, 1mM EDTA pH 7.5) to produce a 100µM stock solution and stored at -20°C prior to use. The stock solution was diluted in TE buffer to a working concentration of 12.5µM and was added 1:100 to hybridization buffer (10% formamide, 10% dextran sulphate, 2× SSC). A humidified chamber was prepared using a sealable plastic container with the base lined with a damp paper towel, then covered with a layer of parafilm. Forceps were used to gently lower the coverslips, cell side down, onto the droplet ensuring no bubbles were formed. The humidified chamber was sealed and incubated overnight at 37°C.

Coverslips were transferred, cell side up, into a 6 well plate containing 1ml wash buffer. The wash buffer was removed, and coverslips were washed twice in 1ml wash buffer for 30 min. Where DAPI was used, 300 nm (final concentration) was added during the final 30 min 1xPBS wash. The wash buffer was removed, and coverslips were stored in 1ml 1xPBS until mounted. Using forceps, a coverslip was gently lowered onto a droplet of ProLong® Diamond Antifade Mountant on a microscope slide avoiding the formation of air bubbles. The mountant was allowed to set overnight at 4°C for confocal imaging, or a minimum of 3 days for STED imaging. In most cases the coverslips were sealed with clear nail polish to secure the coverslip in place during cleaning before and after oil immersion imaging.

3.2.3 RNA FISH and immunofluorescence

To couple RNA FISH and immunofluorescence additional steps must be taken prior to FISH probe incubation. Cells were cultured and fixed as described in 3.2.2. Cells were then incubated in 1ml of blocking/permeabilization buffer (1% acetylated BSA, 0.3% Triton X-100, 2mM vanadyl ribonucleoside complexes in DEPC-treated 1xPBS) for 1 hour at room temperature on a platform rocker while a humidified chamber (3.2.2) was prepared and TOM20 (rabbit polyclonal, sc-11415, Santa Cruz Biotechnology) was diluted in blocking/permeabilization buffer (final concentration 2µg/ml). The diluted antibodies were vortexed and centrifuged briefly, before 100µl droplets were added to the parafilm. Forceps were used to gently lower

the coverslip, cell side down, onto the droplets ensuring no bubbles were formed. The humidified chamber was sealed and incubated overnight at 4°C.

Coverslips were transferred, cell side up, into a fresh 6 well plate containing 1ml 1xPBS and washed three times in 1xPBS for 5 minutes each on a rocking platform. Secondary antibody Atto647N (Anti-Rabbit, 40839, Merck) was diluted in blocking/permeabilization buffer (final concentration 10µg/ml) and 100µl droplets placed onto parafilm in a humidified chamber. The coverslip lowered onto the droplet and the chamber was sealed and incubated for 1 hour at room temperature in the dark. All subsequent steps were carried out in the dark where possible.

Coverslips were transferred and washed in 1xPBS as before on a rocking platform. Coverslips were incubated with 1ml fixative for 10 minutes before a 3x5 minute 1xPBS washes on a lab rocker. Coverslips were equilibrated in 1ml RNA FISH wash buffer for 5 minutes prior to incubation with RNA FISH probes as described in 3.2.2.

3.2.4 VapC20 cell culture and induction

The inducible HEK293-VapC20-His Flp-In™ cell line was prepared by Dr Francesco Bruni within my host lab. Cells were revived from liquid nitrogen and maintained (2.3.2), feeding with Blasticidin^{S} every third feed. Cells were induced with tetracycline (1**µ**g/ml) for 3-6 days. The day before imaging cells were passaged and an aliquot seeded onto coverslips for fluorescent imaging (2.3.4) via RNA FISH. The remainder of the cells were returned to the flask and all cells continued to be induced overnight. RNA FISH was used to probe the cells on the coverslips (3.2.2) and the cells in the flask were harvested for western blot analysis (2.4.1) to confirm induction.

3.2.5 Confocal and STED Imaging

All images were generated using the Zeiss Axio Imager 2 Research Microscope or the Leica SP8 gated STED microscope fitted with a Leica HyD hybrid detector. The Zeiss Axio Imager was used for initial visualisation to confirm labelling during the optimisation of the RNA FISH protocol. A CY3 filter used for Q570 and Texas Red for C610 however crosstalk was observed using this microscope and these filters. The Leica SP8 was used for all confocal and STED imaging throughout this chapter. The wavelengths of white light (WL) lasers used to excite each fluorophore, and the STED depletion lasers are listed in Table 3.2.

Table 3.2: Fluorophore properties and their associated depletion laser wavelength

Fluorophore	White light excitation wavelength	STED depletion laser wavelength
Quasar 570	520 nm and 548 nm	660 nm
CAL Fluor 610	590 nm	660 nm
Quasar 670	647 nm	775 nm
Atto 647N	647 nm	775 nm

For each sample preparation the imaging parameters were optimised. These included WL laser power, STED laser power, STED gating and acquisition window size. The acquisition window was reduced where bleed-through was detected. To allow better deconvolution of the images, stacks were acquired at 4-10µm intervals, depending on the levels of photobleaching observed. Where images were deconvolved, they were processed by Huygens Professional Deconvolution software (version 14.10; Scientific Volume Imaging) using the inbuilt routines designed specifically for STED images.

3.2.6 Quantification of fluorescence and colocalization analysis

Maximum intensity projection for each channel (RNR1-Q570 and RNR2-C610) were generated and analysed using FIJI. To segment fluorescence signal from background, thresholding was used to define a selection area. In all cases, selections were determined by thresholding the RNR1-Q570 image and using the automatic parameters. The mean intensity of signal was measured for each maximum projection within the defined selection area. The measurements were analysed using GraphPad Prism 8 software. Following normality distribution testing using Shapiro-Wilk, significances between experimental data were calculated using Welch's t-test. Colocalization was analysed using Huygens Professional Deconvolution software using the Colocalization Analyzer.

3.3 Results

3.3.1 Visualisation of RNR1 and RNR2 using super resolution microscopy

Independent RNA FISH slides were prepared with RNR1-Q570 and RNR2-C610, with nuclei stained with DAPI (3.2.2). The slides were imaged on the Zeiss Axio Imager 2 Research microscope to confirm fluorescent signal before proceeding to confocal or STED microscopy (Figure 3.2).

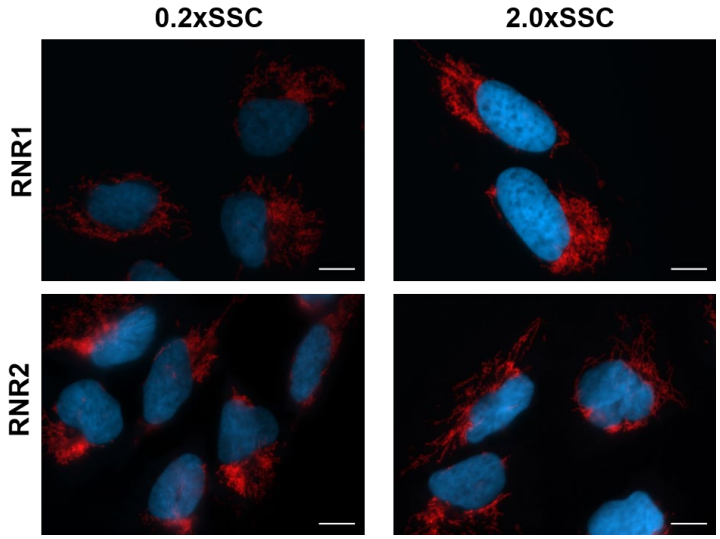

Figure 3.2: RNA FISH labelling of mt-rRNA. Conventional light microscopy of U2OS cells independently labelled with RNR1-Q570 (top panel) or RNR2-C610 (bottom panel) and nuclei stained with DAPI. Wash buffer SSC salt concentration was varied between 0.2xSSC (left panel) and 2.0xSSC (right panel). Scale bar 10µm. Cells were fixed with fresh 4% PFA+0.2% GA for 10min at RT, permeabilized in 70% EtOH for 1 hour prior to probe incubation O/N at 37ºC. Fluorescence was visualised using the Zeiss Axio Imager 2 Research Microscope using CY3 (Q570) and TexasRed (C610) filter sets. PFA, paraformaldehyde, GA, glutaraldehyde.

The signals had a characteristically mitochondrial distribution, forming a network within the cell. To see if a higher salt concentration would result in a reduction of background signal without breaking up the mitochondrial network, two salt concentrations in the RNA FISH wash buffer (0.2xSSC and 2xSSC) were investigated. The images suggested the higher salt concentration in the wash buffer slightly reduced background fluorescence without any effect on the mitochondrial network, this was not quantified. The slides prepared with 2.0xSSC were imaged in confocal and STED mode using the Leica SP8 gated STED microscope (Figure 3.3). Quasar 570 and CAL Fluor 610 were successfully depleted using the 660 nm STED laser, resulting in a higher resolution image.

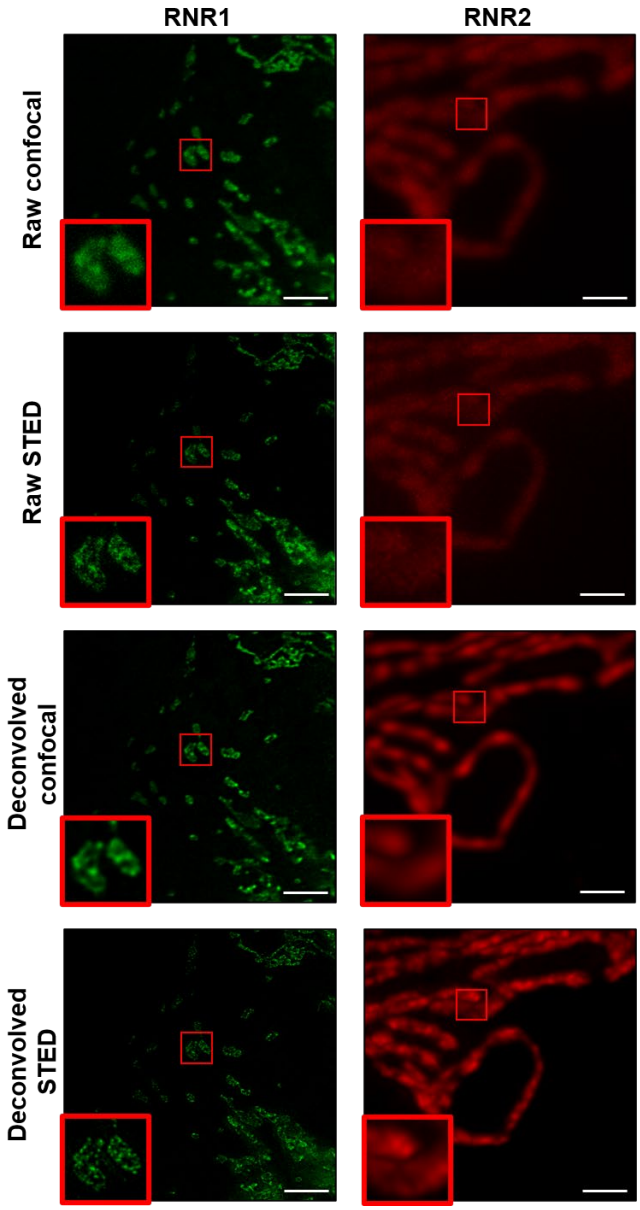

Figure 3.3: Super resolution imaging of mt-rRNA using RNA FISH labelling. Independent preparations of fixed U2OS cells labelled with RNR1-Q570 (left panel) or RNR2-C610 (right panel) were visualised using confocal and STED microscopy. Scale bar 5µm. Cells were prepared as in Figure 3.2. Images are the maximum projection of a Z-stack. All images were gathered on the Leica SP8 gated STED microscope.

Using the depletion laser to deactivate fluorophores within the STED doughnut often accelerated the photobleaching of samples. For both Quasar 570 and CAL Fluor 610, it was possible to image short Z stacks before the fluorescent signal was bleached. Obtaining stacks was required to improve the accuracy of Huygens deconvolution software. The parameters for deconvolution were optimised for each image individually. There was an increase in resolution when switching to STED imaging from confocal imaging with both fluorophores, as internal

structures within the mitochondria become clearer. There was also an increase in the visibility of these structures following deconvolution of both the confocal and STED images.

With an aim to investigate the comparative distribution of *RNR1* and *RNR2* in the mitochondria, I simultaneously labelled these two mitoribosomal RNAs using RNA FISH. Proof of concept for this dual labelling is shown in Figure 3.4.

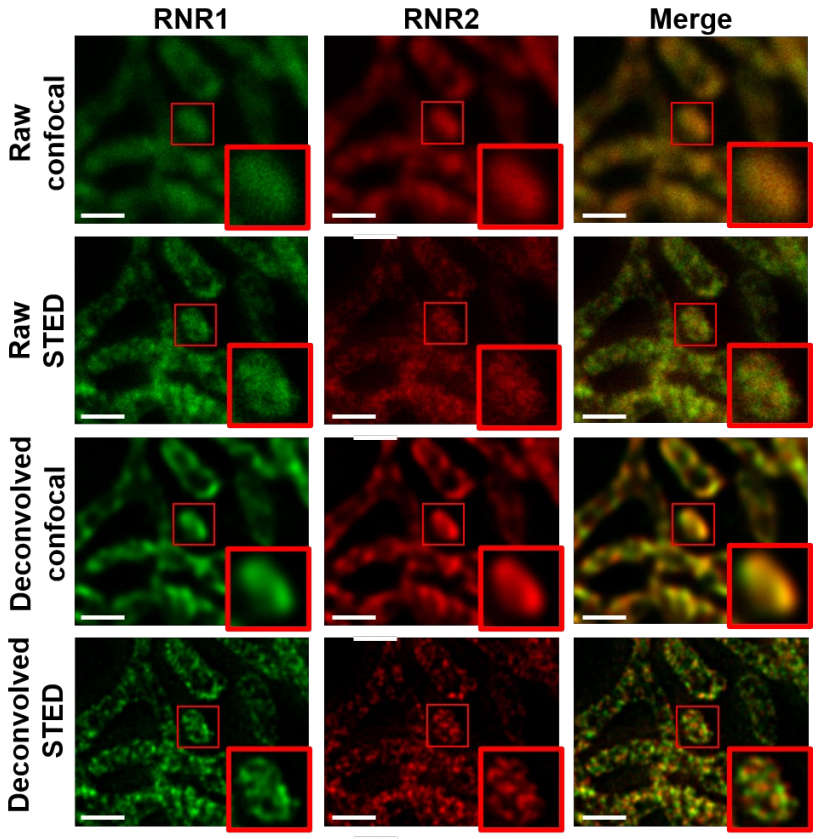

Figure 3.4: Super resolution imaging of mt-rRNA in tandem. Confocal and STED images of fixed U2OS preparations labelled simultaneously with RNR1-Q570 and RNR2-C610. Scale bar 1µm. Cells were fixed with fresh 4% PFA+0.2% GA for 10min at RT, permeabilized in 70% EtOH for 1 hour prior to dual probe incubation O/N at 37ºC. Images gathered on the Leica SP8 gated STED microscope are all maximum projection of Z-stacks. Deconvolved panels were processed using Huygens Professional Deconvolution software. PFA, Paraformaldehyde, GA, glutaraldehyde.

These samples could not be imaged using Zeiss Axio Imager 2 Research Microscope as it does not have a filter set that could excite Q570 without also exciting C610, resulting in bleed through. The close nature of C610 excitation wavelength (590 nm) and the emission wavelength of Q570 (570 nm) also created obstacles for confocal and STED imaging. To avoid this, the acquisition window for Q570 was reduced when both fluorophores were imaged together. To combat any reduction in Q570 emission, I used two lasers to increase excitement

of Q570 fluorophores, at 520 nm and 548 nm. Following this optimisation, the resolution seen for RNR1-Q570 and RNR2-C610 is very similar (Figure 3.33). There is, however, a small visible difference in resolution when comparing the raw STED images of RNR1-Q570 when imaged alone (Figure 3.3), as opposed to imaging in combination with CAL Fluor 610 (Figure 3.4). There is a clear improvement in the resolution for RNR2-C610 between the initial attempts at this protocol (Figure 3.3) and the later slides (Figure 3.4). Much of this is because of improved sample preparation and a better understanding of how to operate Leica SP8 microscope and Huygens deconvolution software. In both the raw and the deconvolved STED images, there are regions of the mitochondria where *RNR1* or *RNR2* appear separately. The ability to distinguish these RNA signals, which may be reflective of the location of mitoribosomal subunits, is a valuable tool. This can be used to investigate how often *RNR1* and *RNR2* are found together in different cellular environments, potentially including drug treatments.

To measure if using two spectrally close fluorophores was limiting the possible resolution available, I conjugated the RNR2 probes to the far-red fluorophore Quasar 670. These new fluorophore conjugated probes were purchased, and RNA FISH hybridisations prepared using RNR1-Q570 and RNR2-Q670 (Figure 3.5).

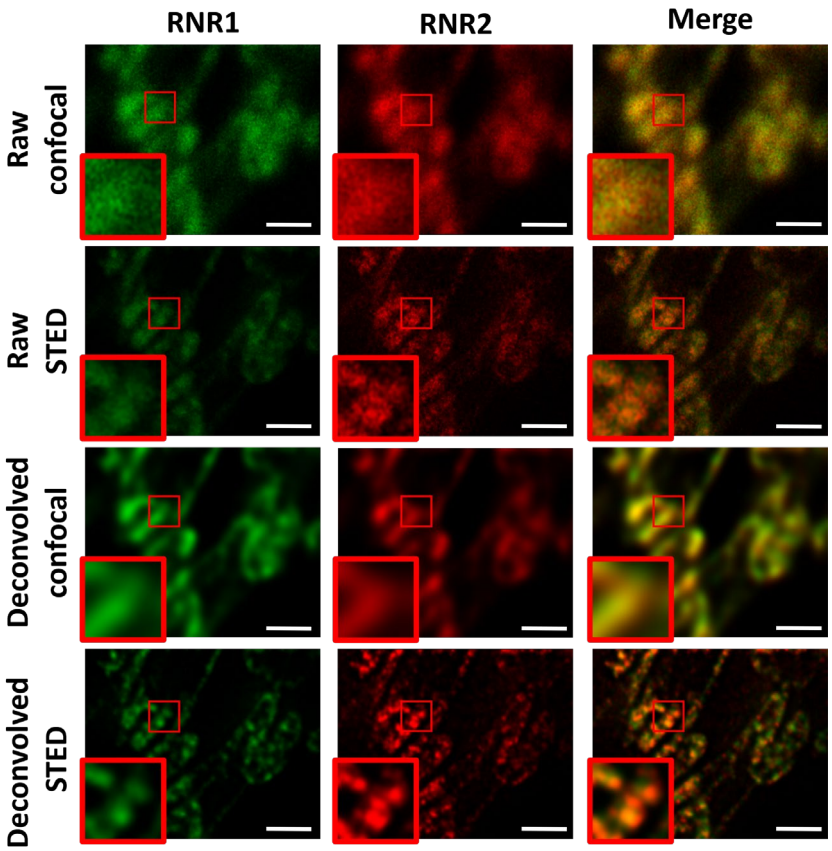

Figure 3.5 Super resolution imaging of mt-rRNA using Quasar 570 and Quasar 670. Confocal and STED images of fixed U2OS preparations labelled simultaneously with RNR1-Q570 and RNR2-Q670. Scale bar 1µm. Cells were fixed with fresh 4% PFA+0.2% GA for 10min at RT, permeabilized in 70% EtOH for 1 hour prior to dual probe incubation O/N at 37ºC. Images gathered on the Leica SP8 gated STED microscope are all maximum projection of Z-stacks. Deconvolved panels were processed using Huygens Professional Deconvolution software. PFA, Paraformaldehyde, GA, glutaraldehyde.

The acquisition window for Q570 was larger when imaging with RNR2-Q670 as the excitation wavelength was 647 nm. There was no clear visible increase in the raw STED image resolution when compared to the images for Q570 imaged with RNR2-C610 (Figure 3.3). This suggested that the imaging parameters for visualising RNR1-Q570 and RNR2-C610 together were optimal. As in Figure 3.4, both the raw and the deconvolved STED images have areas where *RNR1* and *RNR2* appear independently. For example, within the enlarged area displayed in Figure 3.4 there are clearly red and green areas present in the merged image. Across Figures 3.4 and 3.5 there is a similar distribution of *RNR1* and *RNR2* in the STED images, however the

distribution is not identical. This observation could suggest that this assay is labelling mt-rRNA that is within the separate subunits in addition to mt-rRNA that is found after assembly of the monosome. To understand more about the comparative distributions of *RNR1* and *RNR2* in human cells, this experiment was repeated and colocalization of the signals analysed.

3.3.2 Colocalization analysis of RNR1 and RNR2 using super resolution RNA FISH

Following optimisation of the super resolution RNA FISH protocol, I applied this technique to visualise *RNR1* and *RNR2* signals in HEK293, HeLa and U2OS human cell lines. The HEK293 cells used were HEK293 Flp-In™ T-Rex™, untransfected with a genetic construct. Cells were labelled with RNR1-Q570 and RNR2-C610, imaged using the Leica STED microscope, and analysed using Huygens deconvolution software (Figure 3.6).

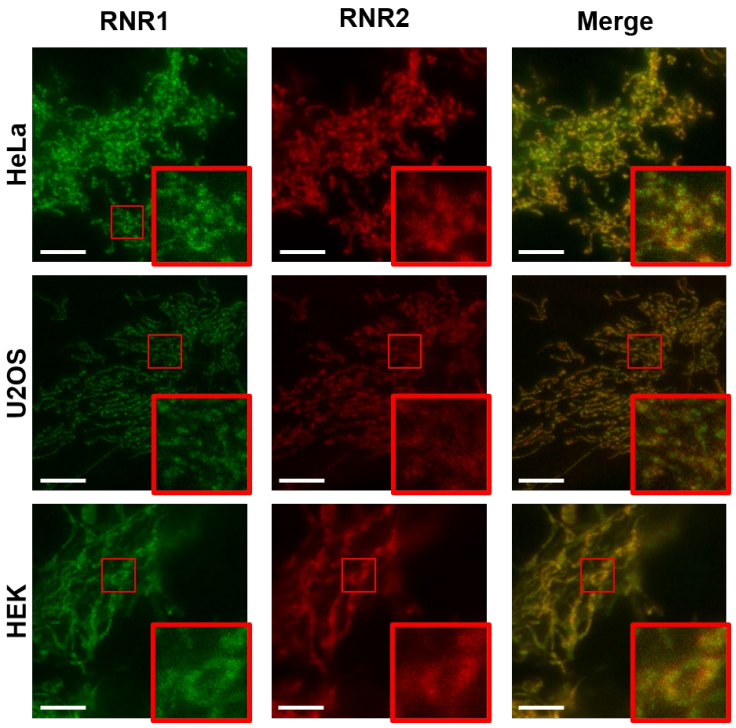

Figure 3.6: STED imaging of mt-rRNA in fixed human cells. Representative deconvolved STED images of HeLa (top panel), U2OS (middle panel), and HEK293 (bottom panel) cells labelled with RNR1-Q570 and RNR2-C610 probes. n=11, scale bar 4µm. Cells were fixed with fresh 4% PFA+0.2% GA for 10min at RT, permeabilized in 70% EtOH for 1 hour prior to dual probe incubation O/N at 37ºC. Images gathered on the Leica SP8 gated STED microscope are all maximum projection of Z-stacks. All panels were processed using Huygens Professional Deconvolution software.

Previously, all imaging and optimisation took place using U2OS as their flatter morphology was optimal for visualising the mitochondrial network. Internal mitochondrial structures, such as cristae, were less defined when *RNR1* and *RNR2* were visual in HEK293 cells and HeLa cells. There was a clear reduction in resolution when HEK293 cells were imaged. The spherical shape of HEK293 cells causes a reduction in the quality of STED imaging as there is more mitochondria, therefore more fluorophores, above and below the focal point which cause increased background signal. HEK293 Flp-In™ T-Rex™, were included in this experiment as I aimed to apply this technique to these cells, engineered to express an RNase that caused RNR2 to be degraded (see 3.3.4).

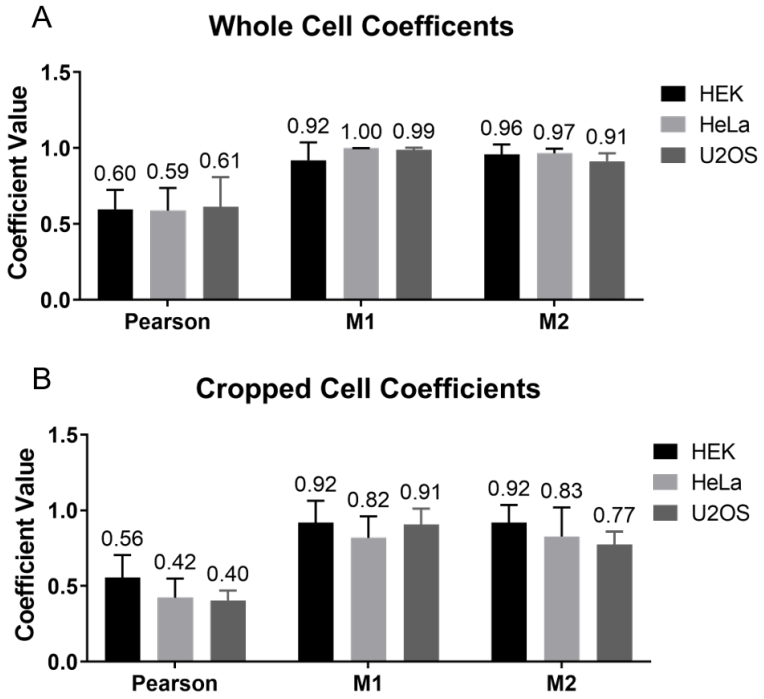

Figure 3.7: Colocalization analysis for STED RNA FISH preparations. *RNR1* and *RNR2* levels were measured by RNA FISH in fixed U2OS, HeLa, and HEK293 cells. Correlation coefficients were calculated from **A:** whole images and **B:** cropped images. Images were deconvolved and Pearson correlation coefficient and Manders coefficient values calculated in Huygens software and values imported into Prism. M_1= the fraction of *RNR2* where there is also *RNR1*. M_2= the fraction of *RNR1* where there is also *RNR2*.

STED images (n=11 for each cell type, across 3 biological repeats) were deconvolved and colocalization values calculated in Huygens software (Figure 3.7 A). The level of background can vary across an image as light is diffracted from planes above and below the region of interest. Each raw image was cropped into regions where the background was more homogenous and the deconvolution and colocalization analysis repeated (Figure 3.7 B). Three

correlation coefficients were measured for each 'whole' image and the following cropped regions: Pearson correlation coefficient (PCC) and Manders coefficients (M_1 and M_2). In theory, cropping an image of a cell can provide a more accurate Pearson correlation coefficient value as the average intensity across the image is used within the calculation. Deconvolution parameters were optimised for each image.

As expected, there were moderate to high levels of colocalization between *RNR1* and *RNR2* across all correlation coefficients. When the intensity of signal was included in the calculation, in PCC, the colocalization was lower. Although imaging using Quasar 570 and CAL Fluor610 was optimised, the lower intensity of Quasar 570 signal may have resulted in some reduction in colocalization by these two measures. Additionally, the PCC value was lower when a cropped region of an image was analysed. This was likely due to extracellular areas where there was very low signal being removed when the image was cropped, therefore when the increased average intensity was subtracted within the PCC equation the resulting values were lower. I believe the lower values better represent the actual levels of correlation, as it is more representative to signal found within the cell. As previously discussed, PCC values at the extremities (1, 0 and -1) are easily interpreted. However, when there is a value between these figures, it can be difficult to extract a clear relationship between samples; this was the case in Figure 3.7. There was strong correlation between *RNR1* and *RNR2* when whole cell images were analysed and moderate-strong correlation when the areas were cropped.

Quantification of colocalization using the Manders coefficient suggested a more moderate relationship between the signals. Across the three cell types, there was variation between whether M1, representing the colocalization of *RNR2* in pixels where *RNR1* was found, or M2, which indicates the colocalization of *RNR1* in pixels where *RNR2* was found, was higher. As previously discussed, the resolution generated from imaging U2OS was higher than for HeLa and HEK293 cells, allowing for a more accurate colocalization analysis. In U2OS, M1 was higher than M2 suggesting that there is more *RNR2* found without *RNR1*, concurring with RNASeq data in the literature (Mercer et al., 2011). In all but HEK293 M1, the Manders coefficients decreased after images were cropped. Manders does not include intensity in the calculation of the coefficient, it specifically measures the fractional overlap between two fluorophores. The reduction after removal of background by cropping, suggests that the Manders coefficients are inflated by inclusion of the background. It is likely there are low levels of both Q570 and C610 autofluorescence or noise in these regions that contribute to a positive overlap between signals.

Overall, the resolution of the images obtained from this dual RNA FISH staining is not high enough to convincingly determine co-localisation of *RNR1* and *RNR2* at the mitoribosomal level. Expert preparations have allowed for nanoscopic super resolution images using STED microscopy, including live scale imaging (Ishigaki et al., 2016; Stephan et al., 2019) but these experiments have not used RNA FISH probes and have instead relied on other methods of fluorescent labelling such as immunofluorescence.

3.3.3 Super resolution RNA FISH and Immunofluorescence

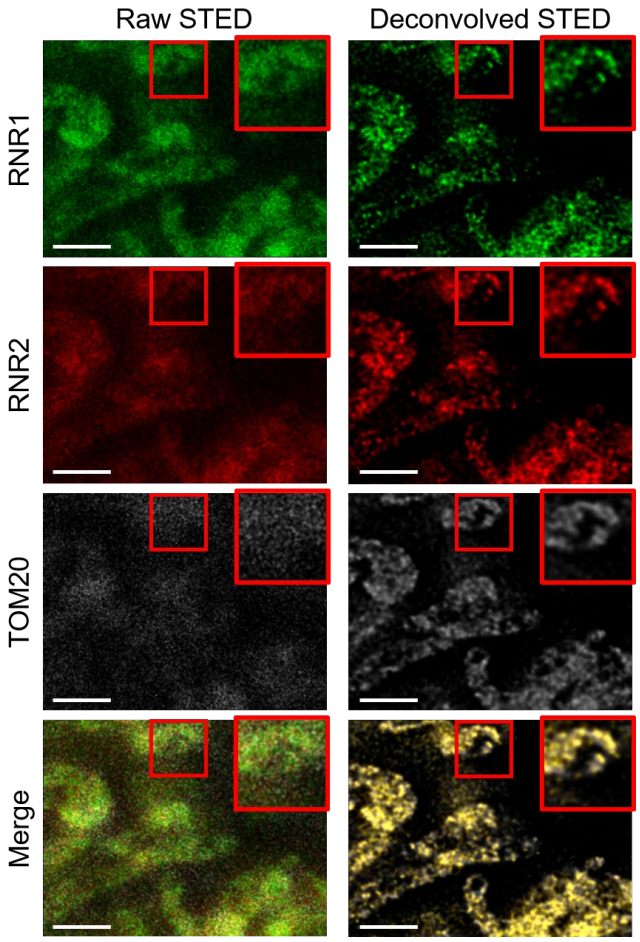

Figure 3.8: STED imaging of mt-rRNA and TOM20 immunofluorescence in fixed human cells. Raw (left panel) and deconvolved (right panel) STED images of fixed U2OS cells. n=5, scale bar 4µm. Cells were fixed, permeabilized, and blocked prior to incubation O/N at 4ºC with polyclonal TOM20 antibodies. Cells were then probed by Atto647N followed by RNA FISH labelling. Images gathered on the Leica SP8 gated STED microscope are all maximum projection of Z-stacks. All panels were processed using Huygens Professional Deconvolution software.

To allow proteins of interest to be visualised alongside mitochondrial RNA, it was important to optimise imaging RNR1-Q570 and RNR2-C610 to allow a far-red fluorophore (Atto647N) to be used for simultaneous capture of immunofluorescence signals. To be compatible with

RNA FISH, the immunofluorescence protocol involved additional steps before incubation of the samples with the RNA FISH probes. The optimised protocol was published recently (Zorkau et al., 2021).

The outer-mitochondrial membrane protein TOM20 was selected for staining as it is a classical marker of the mitochondrial network, routinely used in immunofluorescence (Figure 3.8). These preparations confirmed that the signal I have been measuring thus far was indeed mitochondrial, as all fluorophores overlapped strongly and showed a characteristic mitochondrial morphology. The images obtained have the same visual limitation with resolution as those discussed earlier.

3.3.4 Selective RNR2 degradation as a tool to investigate mitoribosomal loading of mt-mRNA

The life cycle of mt-mRNA, specifically the distribution of mitochondrial RNA and loading of the transcript onto the mitoribosome was unclear at the time of these investigations although more recent work has shed some light on this process (Khawaja et al., 2020). Equipped with an assay that could visualise the mitoribosomal RNAs, I sought biological conditions wherein one of the mt-rRNAs was selectively removed or reduced. Dr. Francesco Bruni developed a human HEK293 cell line that could inducibly express a mutant form of VapC20 endonuclease from *Mycobacterium tuberculosis*, which specifically cleaves at a conserved site present in human mitochondrial *RNR2* (Bruni et al., 2020). This cleavage results in the loss of the LSU, as shown by sucrose gradient analysis. The endonuclease was engineered to be targeted to mitochondria using the pre-sequence of F_0-ATPase subunit 9 from *Neurospora crassa* (Su9) and with a C-terminal 6xHIS tag for easy immuno-visualisation.

Cells induced to express VapC20 (3 days, 1 µg/ml tetracycline) were analysed by RNA FISH and western blotting (Figure 3.9). RNR1-Q570 and RNR2-C610 signals were imaged using the confocal settings on the Leica SP8 microscope as STED Imaging did not result in a higher resolution (Figure 3.9 A). Imaging parameters were optimised for the brightness of each fluorophore across the untreated samples. These parameters were then used to image all samples, across three biological repeats. Fluorescence intensity (in arbitrary units) were measured using FIJI software and the raw intensities scores analysed using GraphPad prism (Figure 3.9 B). The induction of VapC20 was confirmed by western blotting of cell lysates and immune detection using an antibody to the 6xHis tag and β-actin was used as a loading control (Figure 3.9 C). There was a clear reduction in the brightness of RNR2-C610 following VapC20 induction for three days compared to the untreated control ($p<0.0001$), confirming the selective

labelling of *RNR2* with these probes. The fluorescence intensity of RNR2-C610 was reduced slightly in the untreated cells compared to the intensity of RNR1-Q570.

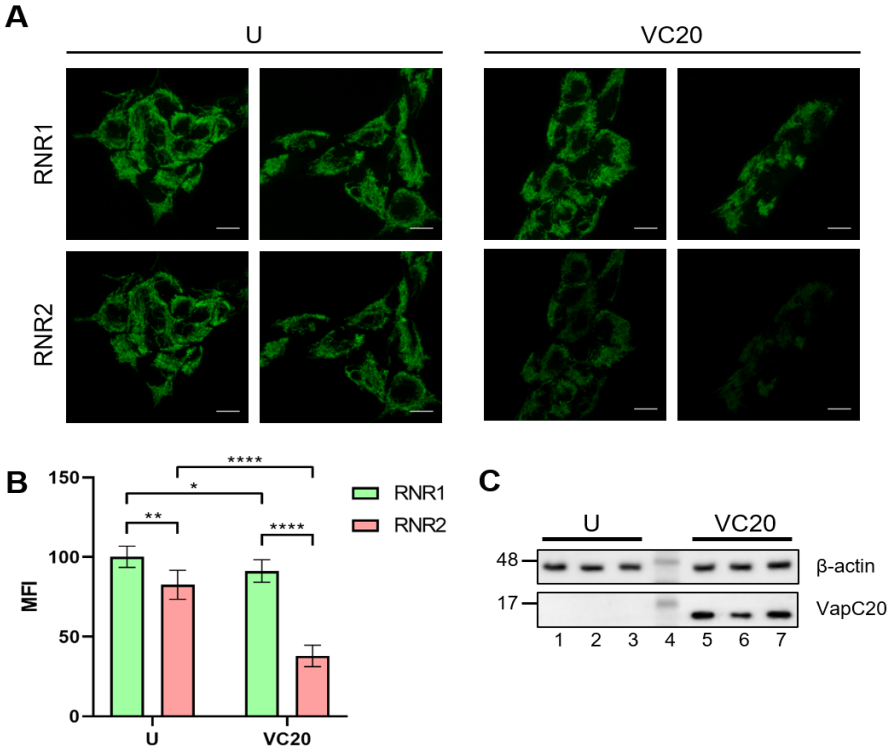

Figure 3.9: Induction of mutant VapC20 reduces the levels of RNR2 after 3 days. HEK293 cells were treated to induce expression of VapC20 endonuclease (VC20) by 1 µg/ml tetracycline or remain untreated (U) for 3 days. **A:** Levels of *RNR1* (top panel) and *RNR2* (bottom panel) were measured by RNA FISH. Representative images are shown, scale bar 10 µm. **B:** Quantitative analysis of fluorescence intensities was performed using FIJI and Graphpad Prism8 as detailed in 3.2.4. Results are presented as the mean ± SD. Statistical analysis was performed using the Welch's T test (*P < 0.05; **P< 0.01; ****P < 0.0001). MFI = Mean Fluorescence Intensity (n=9). **C:** VapC20 expression was validated by western blot analysis of cell culture used for cell imaging. Lanes 1-3: lysates from untreated cells. Lanes 5-7: cell lysates (25 µg) from cell treated with 1 µg/ml tetracycline. Lane 4: molecular weight protein marker (Cleaver Scientific, CSL-BBL)

This may have been due to leaky expression of VapC20 by the Flp-In™ system. This leaky expression has been previously observed in my host lab using this system. I also observed a modest but significant decrease in the fluorescence intensity of RNR1-Q570 in the cells expressing VapC20, compared to the untreated control (Figure 3.9 B, p<0.0). Sucrose gradient and northern blot analyses within this paper, performed by Dr Francesco Brui, showed that SSU assembly is independent of LSU, and that *RNR1* was associated as normal with the SSU even when *RNR2* and the LSU were depleted (Bruni et al., 2020). This northern blotting also showed that inducing the endonuclease for an extended period of time caused a greater

reduction in the levels of *RNR2* in human cells (Bruni et al., 2020). RNA FISH analysis of *RNR1* and *RNR2* was repeated following induction for 3 and 6 days (Figure 3.10).

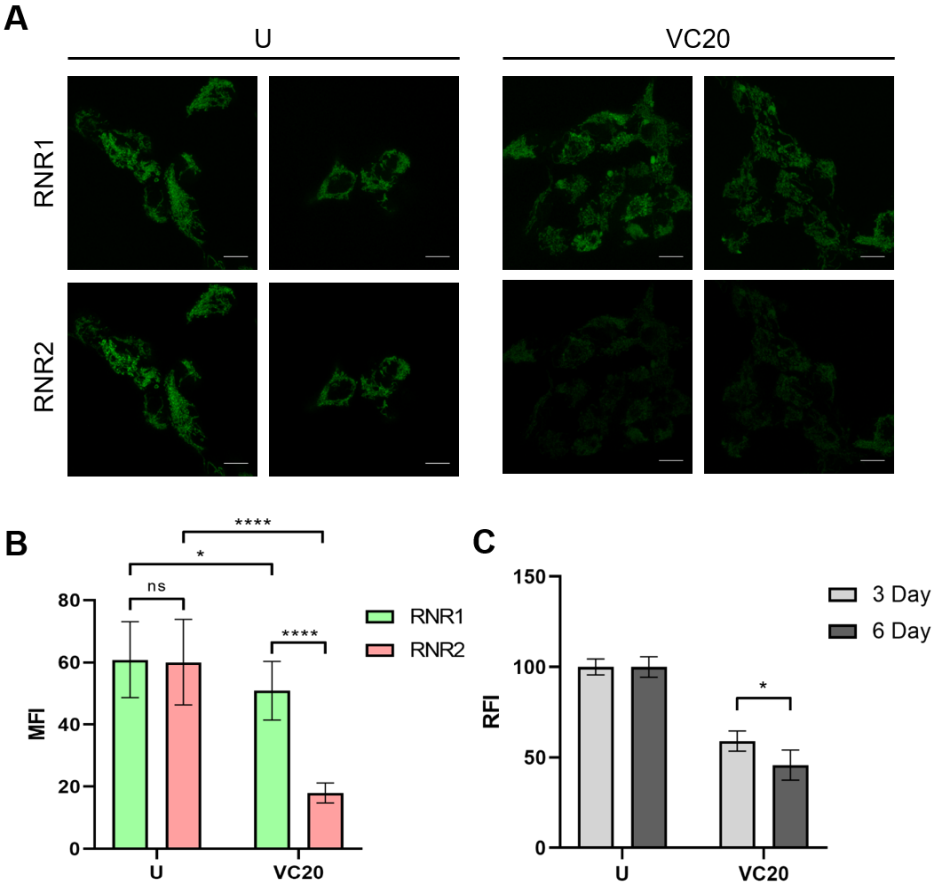

Figure 3.10. Induction of mutant VapC20 causes a greater reduction of RNR2 after 6 days. HEK293 cells were treated to induce expression of VapC20 endonuclease (VC20) by 1 µg/ml tetracycline or remain untreated (U) for 3 and 6 days. **A:** Levels of *RNR1* (top panel) and *RNR2* (bottom panel) were measured by RNA FISH after 6 days induction. Representative images are shown, scale bar 10 µm, n=6. **B:** Quantitative analysis of fluorescence intensities (following 6-day induction) was performed using FIJI and GraphPad Prism8 as detailed in 3.2.4. Results are presented as the mean ± SD. Statistical analysis was performed using the Welch's T test (*P < 0.05; ****P < 0.0001). MFI = Mean Fluorescence Intensity **C:** Quantitative analysis of the relative fluorescence intensities (RFI) of *RNR2* following 3 days and 6 days VapC20 induction. Intensities are relative to the mean *RNR1* intensity, normalised to 100 for each condition.

There was a marked decrease in the mean fluorescence intensity of *RNR2* after 6 days of VapC20 induction compared to the untreated control (Figure 3.10 A-B). The modest but significant (* P<0.05) reduction of *RNR1* in the induced cells relative to the untreated controls persisted. There was, however, no significant difference between the levels of *RNR1* and *RNR2* in the untreated samples across these 6 repeats. The difference seen after 3 days of expression may still have resulted from leaky expression or may have been due to human errors in sample preparation or imaging. To analyse the relative fluorescence intensity of *RNR1* and *RNR2* after

3 and 6 days of induction, the levels of RNR1 in both conditions were normalised (Figure 3.10 C). The relative reduction in *RNR2* compared to *RNR1* was significantly reduced (p-value<0.05) after an additional 3 days of induction. This is consistent with northern blot data presented by Bruni et al., 2020.

To investigate whether leaky expression was the cause of the reduction of *RNR2* in the untreated samples, HEK293 cells without the VapC20 inducible cassette (untransfected HEK293 cells) were analysed by RNA FISH. Repeats of *RNR1* and *RNR2* FISH analysis after 3- and 6-day induction were carried out concurrently. Data is presented as the percentage change in relative fluorescence intensity between *RNR1* and *RNR2* across all conditions, and all relative fluorescence signals are normalised to the levels measured in the untransfected HEK293 cells without tetracycline induction (Figure 3.11).

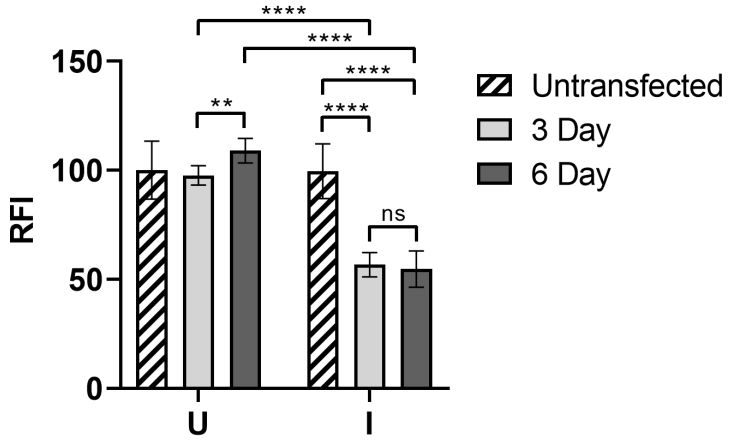

Figure 3.11: Relative RNR2 fluorescence in VapC20 expressing and untransfected cells. Untransfected HEK293 cells and HEK293 cells containing the inducible VapC20 cassette were treated by 1 µg/ml tetracycline (I = induced) or remain untreated (U) for 3 and 6 days. n=6 for 3-day and 6-day treatment, n=9 for untransfected cells. B: Quantitative analysis of the relative fluorescence intensities (RFI) of the difference between *RNR1* and *RNR2* in each condition was performed using FIJI and GraphPad Prism8 as detailed in 3.2.4. Results are presented as the mean ± SD. Statistical analysis was performed using the Welch's T test (*P < 0.05; ****P < 0.0001).

There were significant differences between *RNR1* and *RNR2* following VapC20 endonuclease expression after 3 and 6 days. As expected, there was no significant difference in fluorescence when untransfected cells were treated with tetracycline. With this normalisation, there was no significant difference after an additional 3-day induction. However, when the data for fluorescence levels were normalised to the untreated values in each condition, as in Figure 3.9, there was a significant difference after the additional three days induction (p-value<0.05, data not shown). This is likely to be influenced by the observed increased fluorescence of *RNR2*

over *RNR1* in the 6-day untreated sample. This increase was not observed in any other experiments and remains an outlier, although it was consistent across all 6 biological repeats.

3.4 Discussion

This chapter presents data that show that mt-rRNA can effectively be visualised by RNA FISH, at both the confocal and the super resolution level. The fluorophores Quasar-570, CAL Fluor-610 and Quasar-670 were all compatible with STED depletion allowing Z-stacks to be obtained prior to photobleaching. The RNA FISH protocols did not cause any aberration to mitochondrial networks across U2OS, HeLa or HEK293 cells.

Colocalization analysis of *RNR1* and *RNR2* following RNA FISH experiments across these different cell types did not yield consistent measure of colocalization between RNR1 and RNR2. The experiments in HEK293 and HeLa cells were marred by low resolution due to cell morphology. The U2OS cell data suggested there was a very strong colocalization of *RNR1* and *RNR2*, and that *RNR2* was present at higher levels than *RNR1*, consistent with published RNASeq data (Mercer et al., 2011). Overall, the resolution of the images obtained from this STED RNA FISH is similar to those gathered in the literature (Dumbović et al., 2020). However, they do not achieve the resolution needed to clearly distinguish *RNR1* and *RNR2* signal, namely when these are also paired with immunofluorescence. I had hoped for resolution at the 30-40 nm range in raw STED images, to visualise individual monosomes. After deconvolution this was achieved (Figures 3.3 and 3.4.), however not within the raw STED images. This is the accepted limits of STED microscopy and is consistently achieved by those at the forefront of the mitochondrial STED imaging in the literature (Jakobs and Wurm, 2014; Stephan et al., 2019).

The limitations faced in this experimentation included variation in slide preparation and imaging itself, and that the fluorophores used do not have the photo stability for the highest clarity of STED imaging. Quasar 570-labelled FISH probes have appeared in the literature with similar resolution levels to those observed in this chapter (Dumbović et al., 2020), but these are not equivalent to the STED resolutions at the peak of this research sphere. The images obtained have, however, contributed to two published scientific papers: Bruni et al., 2020; Zorkau et al., 2021. A further limitation of using multiplex RNA FISH probes is that we do not know whether the probes are labelling newly transcribed mt-rRNA molecules, or the RNR1 and 2 that are embedded within the mitochondrial ribosome. Should I have had an increased amount of time, I would have attempted to use markers of newly transcribed RNA in

combination with mt-RNA FISH, such as GRSF1 which has been found to accumulate in foci composed on nascent mt-RNA (Antonicka et al., 2015). If it were possible to devise a method to distinguish so that only mt-rRNA within the mitoribosome was labelled in these experiments, the resolution may be increased as there would be less background created by the mt-rRNA in the matrix or RNA granules. To increase the resolution of these images, I attempted to use expansion microscopy on the labelled samples. This was not successful, and the data is, therefore, not included in this thesis.

The optimised mt-rRNA FISH labelling was further validated in a background where *RNR2* was selectively degraded by VapC20 induction. These sets of data displayed this selective degradation at different time points following induction. Across these experiments there were elements of variability, such as possible leaky expression of the VapC20 protein, and differences between *RNR1* and *RNR2* control levels with each cell preparation, which may be affected by cell cycle. Leaky expression from the Flp-In™ system has be seen within my host lab and other groups. Overall, my data displayed a consistent message that the VapC20 induction assay is reliable at specifically reducing levels of RNR2 within a 3- to 6-day period. As part of Bruni et al 2020, the RNA FISH data have contributed to a model wherein mt-mRNA stability and translation are driven by formation of the monosome. It has been shown that translation initiation complex is preferentially assembled on the AUG codon within the 55S the monosome. The complex can also form on the mt-SSU at a lower efficiency (Christian and Spremulli, 2010). Recent findings have bolstered these initiation models using single-particle cryo-EM, displaying distinct initiation complexes which assembly of the monosome (in combination with mtIF3 and mtIF2) accommodates mt-mRNA (Khawaja et al., 2020). In the experimental conditions used by Bruni et al, in which the mt-LSU was missing, the initiation complex could still form on the stabilised transcript but was not translated due to lack of monosome formation. In VapC20-expressing cells mt-mRNA levels were reduced, while LRPPRC levels were unchanged. If reduction in mt-mRNA levels were reduced because of diminished synthesis, the literature suggests LRPPRC would also be reduced, as in POLRMT knock out cells (Kühl et al., 2016). Hence, selective loss of mt-mRNA is caused by degradation, likely because the transcripts, matured and stabilised by LRPPRC/SLIRP, cannot associate with the monosome. In this model, there are still biological questions that remain, including when in the initiation process LRPPRC/SLIRP are displaced, and whether there are proteins which aid this process and/or contribute to the preference for assembly onto monosome. To

investigate this and identify if any additional proteins are present at the mt-mRNA entry site, I utilized a proximity-labelling assay. The remainder of this thesis describes this investigation.

Chapter 4:

Generation of proximity labelling tools for investigating mt-RNA loading

4.1 Introduction

Proximity-dependent biotin identification (BioID) is a relatively recently established and reliable tool for investigating protein-protein interactions (Kim et al., 2016; Roux et al., 2012; Trinkle-Mulcahy, 2019). The BioID system involves the generation of a fusion protein comprising a protein of interest (bait) and a promiscuous biotin ligase molecule. Expression of the fusion protein within cultured cells, in the presence of biotin added to the media, results in the biotinylation of proteins within a 10 nm radius of the ligase (Roux et al., 2012). The biotinylated proteins are then captured by streptavidin bead affinity purification with high stringency and analysed by western blotting or mass spectrometry. A significant benefit of this interactome mapping tool includes the ability to highlight indirect interactors and vicinal proteins that may be lost in conventional affinity purification protocols. The strength of the biotin-streptavidin bond allows efficient extraction of the proteins from the reaction mixture. Furthermore, direct digestion of peptides off the beads for mass spectrometry analysis resolves elution complications found in other methods, where more biotinylated proteins elute less efficiently due to the strong bond with streptavidin.

The first generation of the BioID technique was derived from a mutated *E. coli* ligase, BirA, which contained a mutation in the catalytic site thus removing the selectivity of the ligase (R118G) (Kwon and Beckett, 2000; Roux et al., 2012). The resulting ligase (BirA*) was able to be fused upstream or downstream of coding sequences in order to biotinylate proximal proteins. However, this system was limited due to properties of the BirA*, including its relatively large size (35 kDa) that led to frequent mislocalisation or degradation, and the ligase requiring local concentrations of ~50 μM biotin for optimum activity. Replacing this moiety with a smaller biotin ligase from *Aquifex aeolicus* (27 kDa) reduced these limitations. The ligase was mutated in the catalytic site (R40G) to remove ligase specificity and designated 'BioID2'. In addition, BioID2 requires significantly less biotin (~2 μM) for efficient biotinylation and the smaller size reduced mislocalisation of tagged bait proteins (Kim et al., 2016).

The first step in the synthesis of mitochondrially-encoded proteins requires the mt-mRNA to be stabilised and transported to the mitoribosome. A stable complex of LRPPRC and SLIRP is known to be involved in the first of these roles, as knockdown of either LRPPRC (Gohil et al., 2010) or SLIRP (Baughman et al., 2009) results in a decrease of the steady state levels of mt-

mRNA without affecting mt-tRNA or mt-rRNA levels. This effect is due to the LRPPRC/SLIRP complex suppressing the PNPase and SUV3- mediated degradation of mt-mRNA and modulation of polyadenylation by MTPAP (Chujo et al., 2012; Wilson et al., 2014). Mutations in *LRPPRC* in humans cause a severe and progressive mitochondrial disorder, Leigh Syndrome French Canadian (LSFC) characterised by defects in assembly in OXPHOS complexes 1, 3-5 (Sasarman et al., 2015). Furthermore, in tissues from people with LSFC, the extremely low steady state levels of LRPPRC were accompanied by decreased levels of SLIRP (Oláhová et al., 2015). A reciprocal state was seen where a reduction of SLIRP mimicked the post-transcriptional defect observed in LSFC patient fibroblasts, highlighting their functional dependence (Sasarman et al., 2015). In these cases, the poly(A) tail of mt-mRNA was unaffected, and the transcript was still translated, albeit at a reduced level. This data suggests that the process of mt-RNA stability and delivery to the mitoribosome may involve proteins other than LRPPRC and SLIRP.

To investigate if there are any supplementary proteins associated with mt-mRNA stability and transport, we require an understanding of which proteins are proximal to LRPPRC/SLIRP and the mt-mRNA entry site of the mitoribosome.

Following the publication of the structure of the human mitochondrial ribosome (Amunts et al., 2015, PDB: 3J9M), Pymol® was used to identify a range of target proteins so as to generate BioID2-HA fusion proteins. All the mitoribosomal proteins (MRPs) fused to BioID2 in this study are encoded by nuclear genes, synthesised in the cytosol, and then imported into mitochondria. As with the MRPs, other nuclear-encoded mitochondrial matrix proteins are targeted using N-terminal pre-sequences, which bind to Tim23 and Tim50 facilitating import into the mitochondria (Mokranjac et al., 2005; Tamura et al., 2009). After import, the N-terminal targeting sequences are cleaved by mitochondrial processing peptidases (MPP). Hence, in the interest of preserving the correct localisation and processing, full-length rather than mature coding sequences were cloned upstream of the BioID2-HA.

Amongst the mitoribosomal proteins that surround the mRNA entry site are MRPS5, MRPS24, MRPS33, MRPS35, and MRPS39. The historical nomenclature for mitoribosomal proteins will be use throughout this thesis as these were used for notation throughout this study. To generate these fusions, custom plasmids were designed to incorporate these sequences with restriction recognition sites flanking the open reading frames (ORF). In order to discriminate specific from non-specific binding of proteins that are enriched at the mt-mRNA entry site, I included an

additional protein as a control. This was MRPS27, an MRP of the small subunit (mt-SSU) located on the distal side of the mt-SSU from the mt-mRNA entry channel, as a BioID2 bait protein. As a positive control for the various stages of the biotin ligation process, SLIRP was also fused upstream of and in-frame with BioID2. The coding sequences for MRPS27 and SLIRP were amplified by PCR from plasmids maintained in my host lab. The primers used for this amplification provided the restriction sites necessary to insert the MRPS27 and SLIRP coding sequences upstream of the BioID2-HA coding sequence. As a further control, the mitochondrial targeting sequence (MTS) of the Complex IV protein COX8 was fused upstream of the BioID2-HA coding sequence. This would target the BioID2 to the mitochondrial matrix, allowing identification of BioID2 biotinylation that is matrix located but not specifically vicinal to the mitoribosome. The approach was to use the Flp-In™ T-Rex™ 293 system to allow inducible expression of the BioID2 fusion protein in human HEK293T cell lines. To this end, a construct containing the BioID2-HA sequence downstream of the pcDNA™5/FRT/TO was utilized. The design and production of this battery of BioID2 tools will be described in this chapter.

4.2 Methods

4.2.1 Generation of BioID2-HA vector with a linker insertion

One of the tools needed for this approach was a BioID2-HA tag with a 13xGGGGS linker inserted upstream. It was generated in my host lab with assistance from a Masters student under my supervision, Reece Farren. The pcDNA™5/FRT/TO/BioID2-HA host vector into which the linker was to be inserted was a kind gift from the lab of Professor Claes Gustafsson (University of Gothenburg). Chemically competent bacterial cells were transformed with this vector DNA (2.1.2) and cultured to amplify the DNA. The vector was verified by DNA isolation (2.2.1), overnight digestion with BamHI and XhoI (2.2.2) and the DNA fragment sizes confirmed by agarose gel electrophoresis (2.2.8). In order to insert the linker with compatible ends, the pcDNA™5/FRT/TO/BioID2-HA was digested with XhoI and ApaI, dephosphorylated (2.2.5), and purified by phenol/chloroform extraction and ethanol precipitation (2.2.6).

PCR was used to amplify the linker-BioID2-HA sequence from MCS-13X Linker-BioID2-HA (Addgene #80899) with flanking XhoI and ApaI digestion sites (957 bp) using the primer sequences listed in Table 4.1.

Table 4.1: Primer sequences for Linker-BioID2-HA amplification.

Primer	Primer Sequence (5'- 3')
LINKER_FOR	ATATATC*TCGAGGGTGGAGGCGGGTCTGGAG (31)
LINKER_REV	GCATATG*GGCCCCTATGCGTAATCCGGTACATCGTAAGG (39)

Sequence complementary to linker DNA, XhoI restriction recognition sequence, ApaI restriction recognition sequence, asterisk indicate precise cut sites, sequence complementary to HA tag DNA, stop codon.

The PCR product was digested overnight with XhoI and ApaI (2.2.2) and analysed by gel electrophoresis (2.2.8). The species migrating at the correct molecular weight to be the linker-BioID2-HA fragment, was then extracted from the agarose gel (2.2.4). DNA concentrations of both the recipient vector and linker fragment were estimated by gel electrophoresis (2.2.8). The ligation (3:1 insert:vector molar ratio) was carried out overnight, at 22˚C (2.2.7). Chemically competent cells (Bioline α-select bronze efficiency) were transformed with the ligation mix and plasmid extracted from successful transformants (2.2.1). Diagnostic digests identified successful linker insertion.

In preparation for insertion of the mitoribosomal protein open reading frames, both the original pcDNA™5/FRT/TO/BioID2-HA and the linker containing derivative were digested (overnight; BamHI and XhoI, 2.2.2) dephosphorylated (to prevent re-circularisation, 2.2.5), phenol/chloroform extracted and ethanol precipitated (2.2.6).

4.2.2 Construction of plasmids containing MRP coding sequences

The coding sequences for the mitoribosomal proteins MRPS5, MRPS24, MRPS33, MRPS35 and MRPS39 were custom synthesized by the GeneArt® Gene Synthesis service and inserted into host plasmids. These inserts were designed for in-frame integration into the pcDNA™5/FRT/TO/BioID2-HA using BamHI and XhoI restriction sites.

Using information from the GenBank® genetic sequence database, the coding sequence for each target protein was analysed in SnapGene® 4.2.9. The sequences ordered from GeneArt® were designed to be preceded with a BamHI target sequence (GGATCC), a Kozak consensus sequence, and succeeded by a XhoI target site (CTCGAG). The plasmids containing the designated target MRPs, the accession number for the GenBank sequence, and their appropriate antibiotic needed for retention are listed in Table 4.2.

Table 4.2: Plasmids containing MRP coding sequences

Plasmid	MRP target	Accession no.	Antibiotic resistance	Antibiotic concentration in LB
18AAFOP_MRPS5 pMA-T	MRPS5	NC_000002.12	Ampicillin	100 µg/ml
18AAZFNP2_MRPS24_pMA-RQ	MRPS24	NC_000007.14	Ampicillin	100 µg/ml
18AAZFMP_MRPS33 pMA-RQ	MRPS33	NC_000007.14	Ampicillin	100 µg/ml
18AAZFKP_MRPS35_pMA-T	MRPS35	NC_000012.12	Ampicillin	100 µg/ml
18AAZFLP_MRPS39_pMK-RQ	MRPS39	NC_000002.12	Kanamycin	50 µg/ml

The purchased plasmids were supplied as lyophilized DNA which was reconstituted in distilled water as per manufacturer instructions. Competent bacterial cells were transformed with the custom plasmids (2.1.2) and streaked onto Luria-Bertani (LB) agar plates containing the appropriate antibiotic for selection (Table 4.2). Plasmid DNA was isolated (2.2.1) and digested overnight with BamHI and XhoI (2.2.2). The DNA fragments were separated by agarose gel electrophoresis (2.2.8) and the insert released by XhoI/BamHI (2.2.4), phenol/chloroform extracted and ethanol precipitated (2.2.6).

My host lab already possessed plasmids containing the MRPS27 and SLIRP coding sequences (pCMV-Sport_6_MRPS27 and pDNR-LIB_SLIRP). These were propagated and the DNA isolated (2.2.1). PCR was used to amplify these ORFs with flanking BamHI and XhoI digestion sites (2.2.3) using primers listed in Table 4.3.

Table 4.3: Primer sequences for amplification of MRPS27 and SLIRP coding sequences.

Primer	Primer Sequence (5'- 3')	Size (bp)
MRPS27_FOR	GCATACG*GATCCCTCCAAG**ATG**GCTGCCTCCATA (34)	1273
MRPS27_REV	GCATATC*TCGAGGGCAGATGCCTTTGCTGCT (31)	
SLIRP_FOR	ATCGATG*GATCCAGTCTGAAG**ATG**GCGG (28)	360
SLIRP_REV	GCGCGCC*TCGAGAAAATCTTTCTTTTCATCATCAGATGT (39)	

Flanking regions, BamHI restriction recognition sequence, XhoI restriction recognition sequence, asterisk indicate precise cut sites, sequences complementary to protein cDNA. ATG start codons are bold.

Initial annealing temperatures were selected using the SnapGene® Tm prediction tool. Where this resulted in unsuccessful amplification, gradient PCR was used to find optimal temperature

conditions (2.2.3). The final conditions for the PCR amplification of MRPS27 and SLIRP are shown in Table 4.4.

Table 4.4: PCR conditions for MRPS27 and SLIRP open reading frame amplification

Target	Target Size (kb)	PCR Conditions				
		Initial Denaturation	Denaturation	Annealing	Extension	Final Extension
MRPS27	1.273	95°C - 3 min	95°C - 15 sec	64°C - 45 sec	72°C - 90 sec	72°C - 7 min
SLIRP	0.360			61.5°C - 45 sec	72°C - 45 sec	

The PCR amplicons were digested overnight using BamHI and XhoI (2.2.2) and purified by phenol/chloroform extraction and then ethanol precipitated (2.2.6). All ligations were carried out overnight for each coding sequence, with a 3:1 (insert:vector) molar ratio (2.2.7).

Bioline α-select chemically competent cells were transformed with the ligation mix (2.1.2). DNA was isolated from bacterial colonies (2.2.1) and diagnostic digests were prepared (2.2.2) and analysed by gel electrophoresis to verify if the ligation was successful (2.2.8).

4.2.3 Confirmation of plasmid sequence by Sanger sequencing

To confirm that sequence of plasmids contained fragments of the predicted molecular weight, reactions were initiated with sequencing primers designed to amplify a 300-600bp region from the middle of the inserted ORF across the junction of the fusion, and into the BioID2 sequence (Table 4.5). The BIOID2_SEQ_REV primer was designed to be compatible with all the different construct amplifications.

Table 4.5: Primer sequences used to amplify the region of fusion for each generated plasmid

Primer	Primer Sequence (5'- 3') (length in nt)
MRPS5_SEQ_FOR	GCTCAGCCTCACCCAGGGCCTCTT (24)
MRPS24_SEQ_FOR	GGATGGAGAGGACCATGCCGCAGAGC (26)
MRPS27_SEQ_FOR	TGTGAAGCAGAGGACATCGCCACCTATGAG
MRPS33_SEQ_FOR	CCGAGCTCGGATCCACCATGTCCTCCC (27)
MRPS35_SEQ_FOR	CCCTTTAAGGAGGCAGAATTACGATTATGCAGTG (34)
MRPS39_SEQ_FOR	GGATTGGCCAGCCACCTCTCTCAACTG (27)
SLIRP_SEQ_FOR	CTTTGCACAGTTCGGCCATGTCAGAAG (27)
CMV_FORWARD	CGCAAATGGGCGGTAGGCGTG (21)
BIOID2_SEQ_REV	GTTCAGCAGGAAGCTGAAGTACAGGCCG (28)

Accordingly, the forward primers were designed to have a similar annealing temperature as the reverse and each other, allowing the same PCR protocol to be used for all fragments (Table 4.6). An established sequencing primer, CMV_Forward, was used to analyse the pcDNA™5/FRT/TO/Linker_BioID2-HA. Amplification was confirmed by gel electrophoresis and the DNA was sequenced as described in 2.2.9.

Table 4.6: The PCR protocol to amplify fragments for DNA sequencing

Amplicon size (bp)	Sequencing PCR Conditions				
	Initial Denaturation	Denaturation	Annealing	Extension	Final Extension
300-600	95°C - 3 min	95°C – 15 sec	66°C - 30 sec	72°C - 30 sec	72°C - 7 min

4.3 Results

4.3.1 Selection of target mitoribosomal proteins surrounding the mt-mRNA entry site

To identify target proteins for that are implicated in delivering mt-mRNA to the mitoribosome, relevant literature and available structures were explored. Pymol (Open Source, Version 2.3.3) was used to analyse the structure of the human mitochondrial ribosome resolved by cryo-electron microscopy (PDB 3J9M) (Amunts et al., 2015). This analysis allowed me to identify the best positioned MRPs to investigate the mRNA entry site of the mitoribosomal small subunit, in addition to biologically relevant proteins that have a role in mRNA loading. Mitoribosomal proteins are encoded by the nucleus, and accordingly contain mitochondrial targeting sequences at the N-terminus of the coding sequence. To avoid disruption of this localisation signal, the cloning procedure was designed to fuse BioID2-HA to the C-terminal region of each target. The position of the C-terminus was examined in Pymol in consideration of mRNA delivery and mitoribosomal assembly. Bait proteins were selected to encompass a range of accessibility, including those which may disrupt mRNA delivery and mitoribosomal assembly, as these could produce interesting phenotypes if successfully expressed within cells. The small subunit proteins chosen for this investigation were MRPS5, MRPS24, MRPS33, MRPS35, and MRPS39 (Figure 4.1 and Video 4.1 https://figshare.com/s/687841c3db8a16d68fee). SLIRP was also investigated because of the defined role LRPPRC/SLIRP has in mRNA stability and a potential role in chaperoning mt-mRNA to the monosome (Bruni et al., 2020). As a control for proteins proximal to the mitoribosome, but distal to the mt-mRNA entry site, MRPS27 was fused to BioID2 (Figure 4.1

and Video 4.1 Frame 8 https://figshare.com/s/687841c3db8a16d68fee). Finally, a BioID2-HA molecule fused to Complex IV protein COX8 mitochondrial targeting sequence (COX8MTS-BioID2) was used as a control for background interaction levels within the mitochondrial matrix. Pymol was then used to model the fusion of these targets to the structure of the biotin protein ligase from *Aquifex aeolicus* (BioID2) as solved by x-ray diffraction (PDB 2EAY). These structures were derived from BioID2 ligase expressed in *E. coli* without the HA tag and as a homodimer. However, all structures within this thesis will only display one ligase monomer, as would be translated in the BioID2-HA fusion.

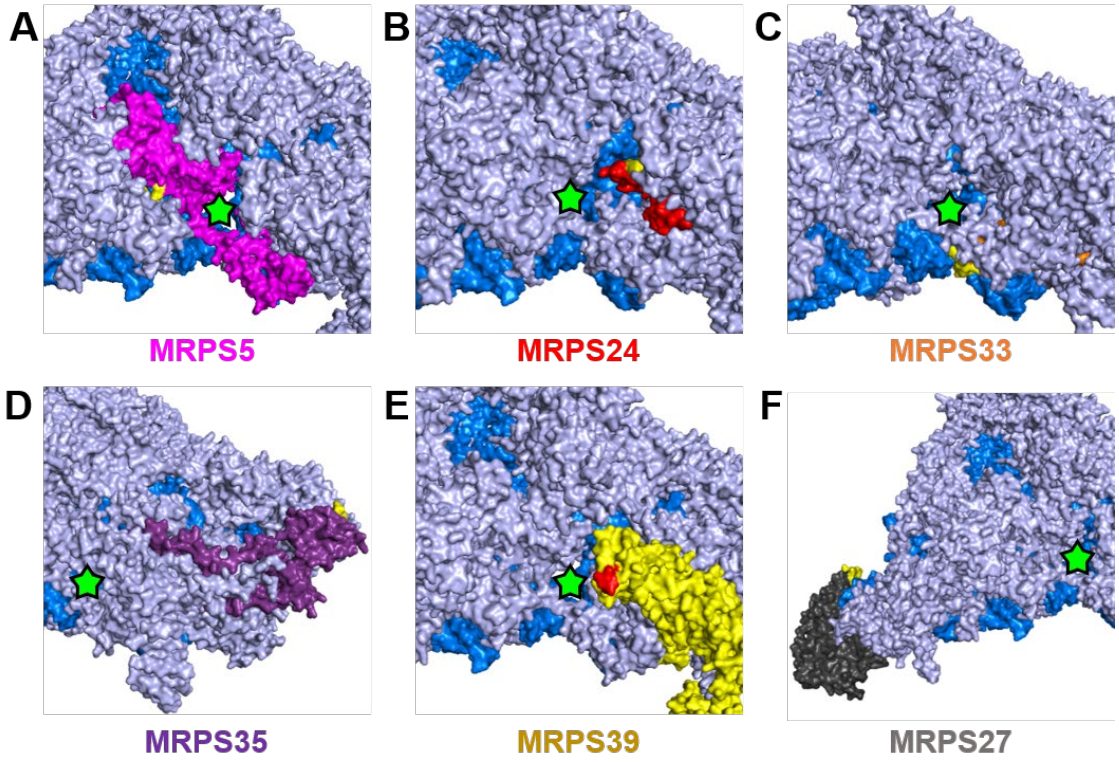

Figure 4.1: Structural analysis of MRPS5, MRPS24, MRPS33, MRPS35, MRPS39 and MRPS27 as BioID2 targets. The structure of the human mitoribosome (PDB 39JM) was analysed with Pymol (Open Source, Version 2.3.3). Visible is the 12S ribosomal RNA (dark blue) and small subunit proteins (light blue). The location of the mRNA entry tunnel (MET) is marked by a green star. **A:** MRPS5 surrounds the MET and with the C-terminus (yellow) positioned on the interior of the ribosome. **B:** MRPS24 is located close to the MET and the C-terminus (yellow) is in the interior of the SSU. **C:** MRPS33 is found close to the entry tunnel and the C-terminus (yellow) is on the exterior of the mitoribosome. **D:** MRPS35 has contacts with the MET (not visible) and the C-terminus (yellow) is on the exterior of the ribosome distal to the MET. **E:** MRPS39 (yellow) is present next to the MET and the C-terminus (red) of MRPS39 is directly above the MET. **F:** MRPS27 (grey) located on the distal face of the mt-SSU away from the MET and the C-terminus (yellow) is on the exterior of the ribosome.

4.3.2 Suitability of MRPS5 as a bait for trapping mt-mRNA delivery factors

MRPS5 is a prominent protein that sits at the mRNA entry site and is strongly represented in the literature describing mitochondrial translation (Figure 4.1 A). In humans, MRPS5 contains an extension compared to the orthologue uS5 in the yeast mitoribosome and *E. coli* ribosome (Figure 4.2). As there is no equivalent of yeast uS4 or the C-terminal region of yeast uS3 in humans, this MRPS5 extension is thought to partially compensate for this absence. Thus, the helicase activity conferred by basic residues in yeast uS3 and uS4 is not present in human MRPS5.

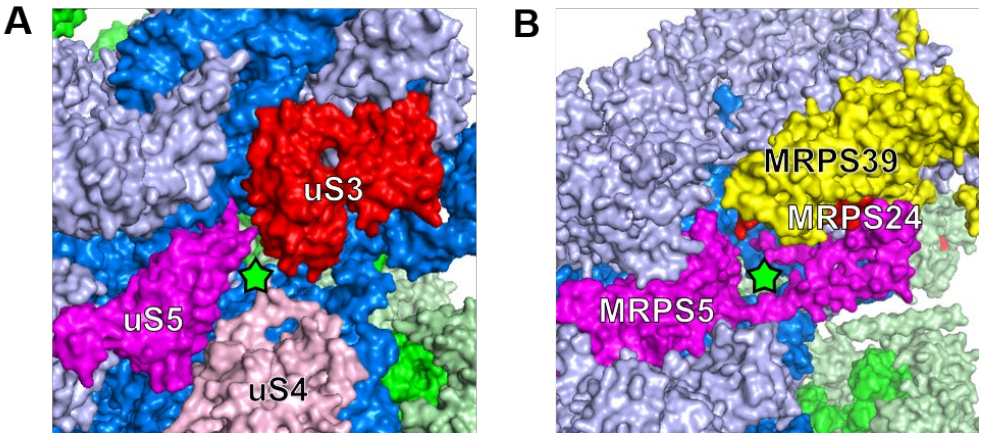

Figure 4.2: The structure of the mRNA entry tunnel in the *E. coli* ribosome and human mitochondrial ribosome. In each structure, colouring is as follows: large subunit (LSU) proteins (pale green), LSU RNA (bright green), mt-SSU proteins (light blue), mt-SSU RNA (dark blue), and the mRNA entry site (green star). **A:** The structure of the *E. coli* ribosome (PDB 4YBB) at the mRNA entry site. Surrounding this site are uS5 (magenta), uS3 (red) and uS4 (light pink). **B:** The structure of human mitoribosome (PDB 39JM) at the mt-mRNA entry site. Surrounding this site are MRPS24 (red), MRPS5 (magenta), and MRPS39 (yellow).

Mutated versions of MRPS5 or its depletion have been implicated in mitoribosomal dysfunction within different genetic models. *E. coli* uS5 has been identified as an important ribosomal protein for translational accuracy, which is consistent with the depletion of *Mrps5* in *Caenorhabditis elegans* resulting in disruption of mitochondrial translation and the balance between nuclear- and mitochondrial-encoded proteins (Houtkooper et al., 2013). It was found that the S200Y point mutation in bacterial uS5 generates a ribosomal ambiguity mutation that results in ribosome misreading (Synetos et al., 1996). This was modelled in cell culture in the human mitoribosome by the mutation V336Y and also within a homozygous knock-in mouse model where it also conferred mitoribosomal misreading and mitochondrial dysfunction (Akbergenov et al., 2018). The site of V336 in human MRPS5 is close in space to the C-terminus of the protein (V336 residue visible in cyan in Video 4.2, Frame 3

https://figshare.com/s/32732695bde6d92621a7). Should the BioID2-HA extension to MRPS5 assemble into the mitoribosome, it is possible that there could be a misreading phenotype, as seen in the V336Y mutation.

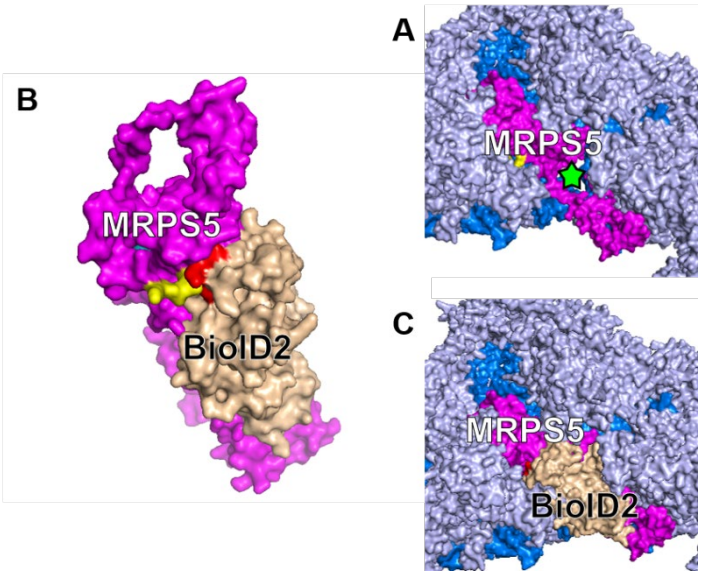

Figure 4.3: Modelling of MRPS5-BioID2 fusion protein. The structures of the human mitoribosome (PDB 39JM) and biotin ligase (BioID2) from *Aquifex aeolicus* (PDB 2EAY) manipulated with Pymol. In ribosomal structures mt-SSU proteins (light blue) and 12S rRNA (dark blue) are visible. **A:** MRPS5 (pink) surrounds the mRNA entry sitel (green star) **B:** MRPS5 with the C-terminus (yellow) aligned next to the N-terminus (red) of BioID2 (wheat). **C:** Modelled structure of MRPS5-BioID2 fusion in the presence of other mt-SSU proteins and rRNA.

In early assembly of the human mt-SSU there are two main groups that bind to the 12S rRNA, distal to the interface with the large subunit. MRPS5 is also involved at an early stage wherein it strongly interacts with members of both groups of early binding proteins and is thought to form a bridge between them (Bogenhagen et al., 2018). The impact of the addition of the biotin ligase moiety to MRPS5 on this role is unknown.

Pymol was used to model the addition of BioID2 (without the HA tag) onto the C-terminus of MRPS5 (Figure 4.3 A and Video 4.2, Frame 3 https://figshare.com/s/32732695bde6d92621a7). The N-terminus (red) of the BioID2 molecule (wheat) was oriented such that it aligned with the C-terminus (yellow) of MRPS5 (pink) and did not appear to greatly disturb the interfaces it has with other mitoribosomal proteins (Figure 4.3 C). During the structural analysis I sought to select proteins that not only surrounded the mRNA entry tunnel but also had C-termini that faced into the mitoribosome structure such as MRPS5 (Video 4.2, Frame 2 https://figshare.com/s/32732695bde6d92621a7). It is possible that the addition of BioID2-HA to this internal region would cause steric hindrance and prevent mitoribosome assembly, or that

the BioID2 molecule would block access to the mRNA entry tunnel. This could result in the disruption of ribosome assembly, or possible sequestering of mitoribosome protein binding partners by MRPS5-BioID2, generating models that could be used to further study mitoribosome assembly.

4.3.3 Suitability of MRPS24 as a candidate for BioID2 fusion

MRPS24 was selected as a candidate for BioID2 tagging as it is found lining the mt-mRNA entry site. MRPS24 is present in *E. coli* and *S. cerevisiae* designated as uS3, with all three derivatives occupying a similar space within the small subunit (Figure 4.2). However, there are marked differences between these proteins. The human mitochondrial MRPS24 is smaller than the bacterial uS3 equivalent (167 vs 233 amino acids), with some of the space occupied by uS3 replaced by the extension to MRPS5 as discussed earlier.

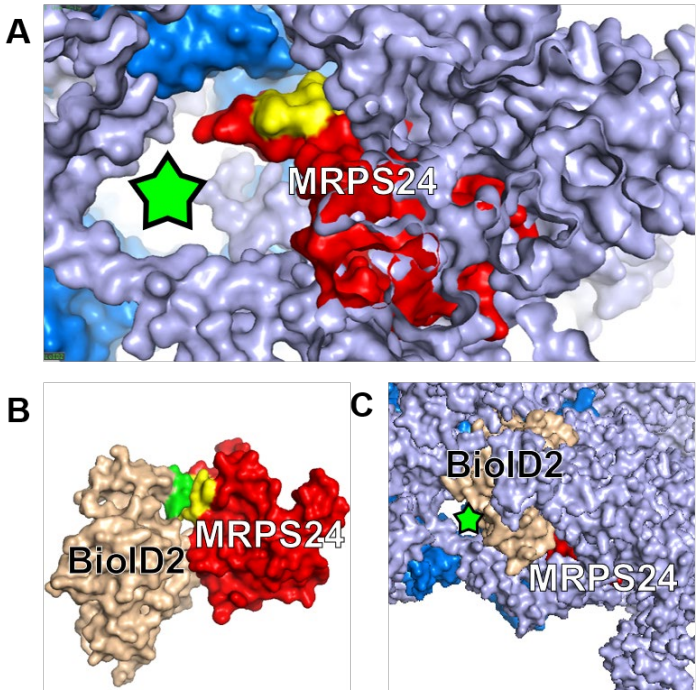

Figure 4.4: Modelling of MRS24-BioID2 fusion protein. The structures of the human mitoribosome (PDB 39JM) and biotin ligase (BioID2) from *Aquifex aeolicus* (PDB 2EAY) manipulated with Pymol. In ribosomal structures mt-SSU proteins (light blue) and 12S rRNA (dark blue) are visible. **A:** MRPS24 (red) is proximal to the mRNA entry tunnel (green star) **B:** MRPS24 with the C-terminus (yellow) aligned next to the N-terminus (green) of BioID2 (wheat). **C:** Modelled structure of MRPS24-BioID2 fusion in the presence of other mt-SSU proteins and rRNA.

In contrast to human MRPS24, the *S. cerevisiae* uS3 is the only MRP encoded by the mitochondrial genome and the only soluble protein (Terpstra et al., 1979). The role of this hydrophilic subunit is unknown; however, mutations in MRPS24 have been implicated in reduced mitochondrial translation activity and reduced respiratory function in a temperature-

sensitive manner (Murphy et al., 1980). In addition, its hydrophilic nature is not conserved across all yeast species. There has not been a putative role in human mitochondrial disorders ascribed to MRPS24, although disease-causing mutations have been implied by Crispr-Cas9 knockout modelling (Arroyo et al., 2016). This predicted MRPS24 to be an essential gene for OXPHOS, however this was not validated within the experimental screening. MRPS24 has also been found to be upregulated in lymphoma cells alongside many other mt-SSU proteins (Gopisetty and Thangarajan, 2016) but the specific role of MRPS24 within the mitoribosome in human cells remains unclear.

The C-terminus of MRPS24 is inside the mRNA entry tunnel, facing towards the opening (Figure 4.4 A). I modelled the addition of BioID2 in Pymol (Video 4.3, Frame 2 https://figshare.com/s/f68dfa53f0651a78f534), aligning the N-terminus of the BioID2 molecule (wheat) with the C-terminus of MRPS24 (Figure 4.4 B). Similarly, to MRPS5, the addition of the BioID2-HA protein to this terminus could provide a model that sterically hinders assembly or translation.

4.3.4 Suitability of MRPS33 as a candidate for BioID2 tagging

Structural analysis of the human mitoribosome using Pymol identified MRPS33 as another candidate for BioID2 labelling because of its proximity to the mt-mRNA entry site, where it sits below MRPS5. MRPS33 is not strongly represented in the literature, although a mutation of MRPS33 has been associated with autosomal recessive deafness in a predictive model (Masmoudi et al., 2004). It is not present in *E. coli* ribosomes but is highly conserved across mammals, *Drosophila* and *C. elegans* (Lai et al., 2000). The role of MRPS33 in the human mitoribosome is unknown, but we do know that it is a late binding protein in a cluster with MRPS24 (Bogenhagen et al., 2018).

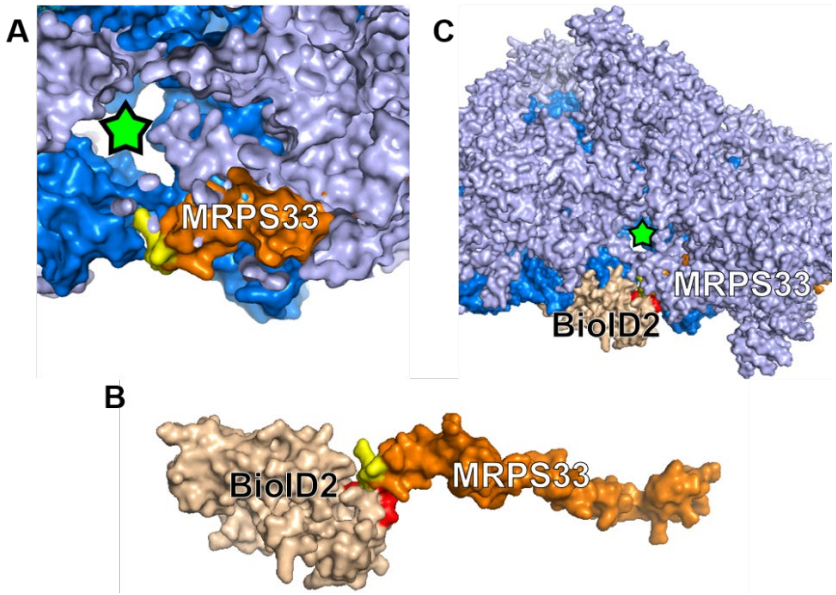

Figure 4.5: Modelling of MRS33-BioID2 fusion protein. The structures of the human mitoribosome (PDB 39JM) and biotin ligase (BioID2) from *Aquifex aeolicus* (PDB 2EAY) manipulated with Pymol. In ribosomal structures small subunit (SSU) proteins (light blue) and 12S rRNA (dark blue) are visible. **A:** MRPS33 (orange) is at the base of the mt-mRNA entry site (green star) **B:** MRPS33 with the C-terminus (yellow) aligned next to the N-terminus (red) of BioID2 (wheat). **C:** Modelled structure of MRPS33-BioID2 fusion in the presence of other SSU proteins and rRNA.

The C-terminus of MRPS33 sits at the base of the mRNA tunnel and the very final residues are not buried within the monosome (Figure 4.5 A), which may make integration of the BioID2-HA tagged S33 more likely. The addition of the BioID2 was modelled as described previously and in this orientation the ligase sits below the entry site but does not block it (Figure 4.5 B and Video 4.4 https://figshare.com/s/e565d10fca4f2184e56e).

4.3.5 Suitability of MRPS35 as a candidate for BioID2 tagging

MRPS35 was identified as a target for BioID2 fusion because of the proximity to the mt-mRNA entry site. Structurally MRPS35 is very different to previous targets; it has an interface with the mRNA entry site, but the C-terminus is located away from the tunnel entrance (Figure 4.6 A and Video 4.5 https://figshare.com/s/f4295dc01ba267dc14ba).

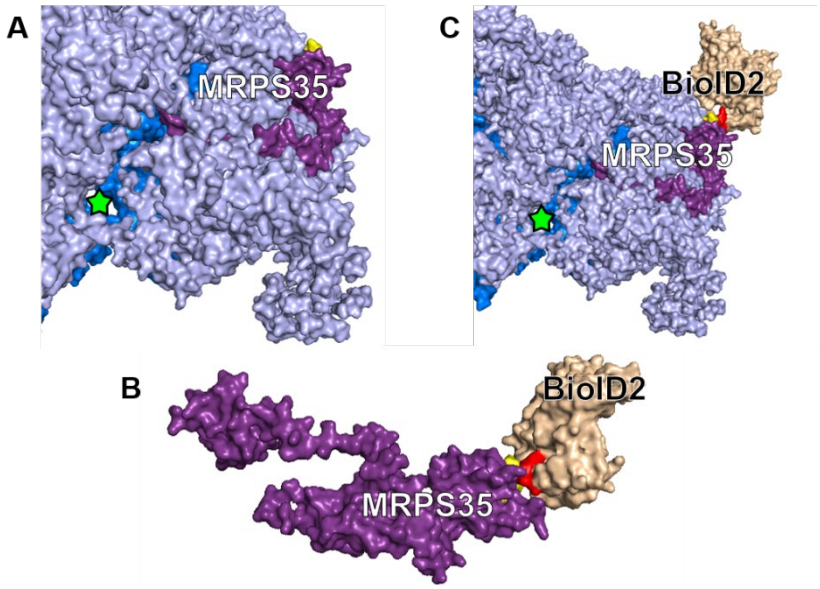

Figure 4.6: Modelling of MRS35-BioID2 fusion protein. The structures of the human mitoribosome (PDB 39JM) and biotin ligase (BioID2) from *Aquifex aeolicus* (PDB 2EAY) manipulated with Pymol. In ribosomal structures small subunit (SSU) proteins (light blue) and 12S rRNA (dark blue) are visible. **A:** MRPS35 (purple) has an interface with the mRNA entry site (green star) **B:** MRPS35 with the C-terminus (yellow) aligned next to the N-terminus (red) of BioID2 (wheat). **C:** Modelled structure of MRPS35-BioID2 fusion in the presence of other SSU proteins and rRNA.

MRPS35 is an early binding protein in mitoribosome assembly (Bogenhagen et al., 2018). MRPS35 has not been found to interact with the mt-rRNA, therefore it is likely that MRPS35 depends on close interactions with other proteins to be recruited to the mitoribosome, which may be disturbed by the addition of BioID2-HA. The possible interacting partners identified through biotin ligation from this assay may present with a different profile than those directly interacting at the tunnel. This was planned to serve as an additional 'bait' protein to allow me to identify proteins specifically enriched at the entry site.

MRPS35 does not have a bacterial ribosome homologue and there is no clear function ascribed in yeast or other organisms (Kaushal et al., 2014). There is very little known about its role within the ribosome. The precise function of MRPS35 in the human mt-SSU remains undefined, although MRPS35 mutations have been found in patients with of congenital heart

disease and in those with Alzheimer's disease. There is no discussion however of the mechanism of action using these predicted models (He et al., 2017; Wang et al., 2017).

4.3.6 Suitability of MRPS39 as a candidate for BioID2 tagging

Structural analysis reveals that, MRPS39 is a prominent protein within the mt-SSU head at the mRNA entry site, with the C-terminal region overhanging in front of the tunnel (Figure 4.7 A and Video 4.6 https://figshare.com/s/8f44cfbdcd8593ad796d). This, in theory, is an ideal location to attach the BioID2-HA molecule, as it should not disrupt integration into the mitoribosome and is placed directly in front of the mRNA gate (Figure 4.7 C).

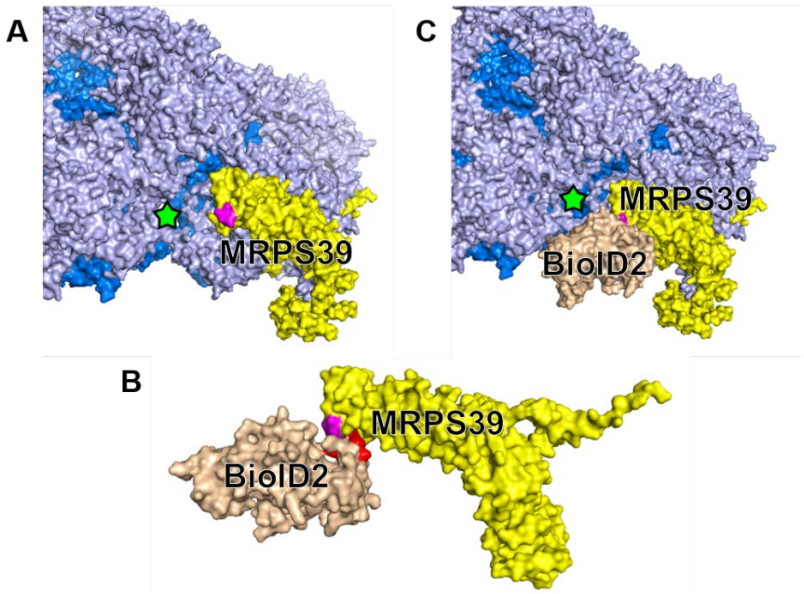

Figure 4.7: Modelling of MRS39-BioID2 fusion protein. The structures of the human mitoribosome (PDB 39JM) and biotin ligase (BioID2) from *Aquifex aeolicus* (PDB 2EAY) manipulated with Pymol. In ribosomal structures small subunit (SSU) proteins (light blue) and 12S rRNA (dark blue) are visible. **A:** MRPS39 (yellow) is proximal to the mRNA entry tunnel (green star) **B:** MRPS39 with the C-terminus (yellow) aligned next to the N-terminus (red) of BioID2 (wheat). **C:** Modelled structure of MRPS39-BioID2 fusion in the presence of other SSU proteins and rRNA.

Another reason for selecting MRPS39 (also termed PTCD3) as a BioID 'bait', is its conserved ability to bind RNA in a sequence specific manner. This is imparted by pentatricopeptide repeats (PPR) that characterise this group of proteins. PPR proteins contain this repeated canonical motif that form a structural array of α-helices. They have been widely researched due the diverse roles PPR proteins play in RNA metabolism across a wide range of different organisms (Lightowlers and Chrzanowska-Lightowlers, 2013). MRPS39 is one of seven human mitochondrial PPR proteins, however its knockdown did not affect the levels of mitochondrial transcripts but did decrease the levels of mitochondrially-encoded polypeptides.

Additionally, increasing the abundance of MRPS39 did not stimulate an increased level of mitochondrial translation (Davies et al., 2009). The combination of the placement of MRPS39 at the mRNA gate, its potential to bind RNA through the PPR motifs, and its effect on mitochondrial translation, could suggest that it is involved in recruiting mRNA to the mitochondrial ribosomes making it an ideal 'bait for my research project.

4.3.7 Suitability of SLIRP, MRPS27 and COX8MTS as controls for MRP-BioID2 tagging

The mitochondrial matrix, where the mitoribosome is located, is a compartment of high protein density (Kühlbrandt, 2015). Fusion of the promiscuous biotin ligase to proteins within this compartment is likely to result in high background levels of biotinylation. Hence the need to design controls that allow me to separate proteins biotinylated non-specifically from those biotinylated because of their proximity to the mt-mRNA entry site. To do this, two BioID2 fusion proteins were used to identify levels of biotinylation distal to the entry site (MRPS27) and within non-specific regions of the mitochondrial matrix (COX8MTS). An additional positive control (SLIRP) was utilized to validate the various subsequent experimental steps, including mitochondrial isolation, streptavidin pulldown, and mass spectrometry. I produced a mitoribosomal control designed to biotinylate proteins close to the foot of the ribosome, located on the opposite face of the mt-SSU to the entry site. MRPS27 was selected as it was located away from the entry site (green star in Figure 4.8 and Video 4.7 https://figshare.com/s/ae3a466f8e0faa7f8713) and has previously been C-terminally tagged with a FLAG octopeptide (by a member of the Lightowlers lab) and successfully integrated into the mitoribosome. The ability to compare the streptavidin pulldown output from BioID2-tagged MRPS27, with the targets of bait proteins located close to the mt-mRNA entry site is designed to discover which proteins are specifically enriched at this site.

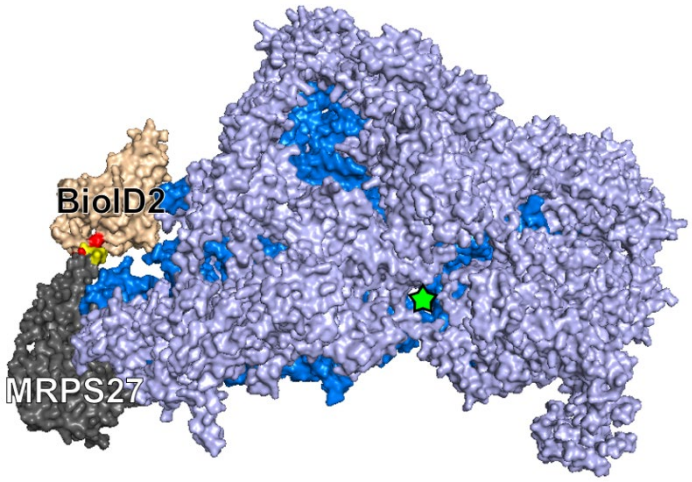

Figure 4.8: Modelling of MRS27-BioID2 fusion protein. The structures of the human mitoribosome (PDB 39JM) and biotin ligase (BioID2) from *Aquifex aeolicus* (PDB 2EAY) manipulated with Pymol. In ribosomal structures small subunit (SSU) proteins (light blue) and 12S rRNA (dark blue) are visible. MRPS27 (grey) is distal to the mRNA entry tunnel (green star). The C-terminus (yellow) of MRPS27 aligned next to the N-terminus (red) of BioID2 (wheat).

The other control for background biotinylation levels was the BioID2-HA targeted to the mitochondrial matrix by fusion downstream of the mitochondrial targeting sequence of a Complex IV protein, COX8 (COX8MTS). This fusion was designed and validated by colleagues at The University of Gothenburg and provided generously for these experiments. The COX8MTS will allow the biotin ligase to be shuttled into the mitochondrial matrix with no specific internal localisation, providing a measure of background levels of biotinylation across matrix proteins. The BioID2 fusion to SLIRP was utilized an additional positive control for the project. The extensive literature indicates that we should expect a very strong interaction with LRPPRC (Chujo et al., 2012; Sasarman et al., 2015; Spåhr et al., 2016). Confirmation of this result will be used to determine if the mitochondrial preparation and mass spectrometry protocols are working effectively. SLIRP has a clear role in the stability of mt-mRNA prior to translation by the mitochondrial ribosome as discussed earlier in this chapter; therefore, this fusion could also be used to investigate any remaining interactors involved prior to ribosome loading. The structure of SLIRP is not available in the protein data bank so I was unable to model the addition of BioID2-HA (27kDa) to SLIRP (12.7kDa). SLIRP has, however, previously been C-terminally tagged within the Lightowlers lab without disruption to localisation.

4.3.8 Preparation and cloning of host vectors

To generate pcDNA™5/FRT/TO/Linker_BioID2-HA, primers were designed to amplify the linker-BioID2-HA sequence from MCS-13X Linker-BioID2-HA (Addgene #80899) with flanking XhoI and ApaI restriction recognition sites (Figure 4.9). The vector, pcDNA™5/FRT/TO/BioID2-HA and PCR product were digested with XhoI and ApaI and the latter purified by gel extraction. Successful ligation of these fragments generated the pcDNA™5/FRT/TO/Linker_BioID2-HA plasmid, this was identified by diagnostic digest (Figure 4.2 B) and confirmed by sequencing. An overview of these cloning steps is provided in Figure 4.10.

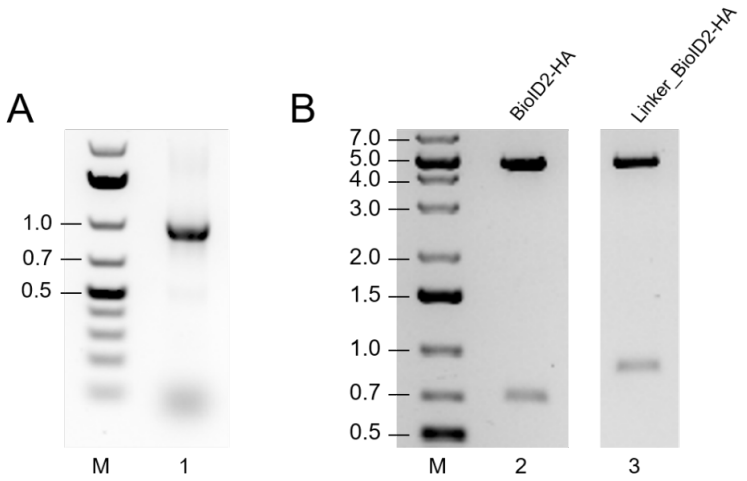

Figure 4.9: Generation of linker containing fragments to construct host BioID2-HA vectors variants. M designates molecular weight marker lane. **A:** Lane 1: PCR amplification product of the linker-BioID2-HA sequence from MCS-13X Linker-BioID2-HA (0.9kb). **B:** Vectors were digested with XhoI and ApaI. Lane 2: Restriction digest of pcDNA™5/FRT/TO/BioID2-HA resulted in a BioID2-HA coding sequence band (0.79kb) and the vector backbone (5.1kb). Lane 3: Restriction digest of pcDNA™5 /FRT/TO/Linker_BioID2-HA double digest resulted in a Linker-BioID2-HA coding sequence band (0.99kb) and the vector backbone band (5.1kb). M, Generuler™ 1kb plus. DNA fragments were separated in a 1% TAE agarose gel.

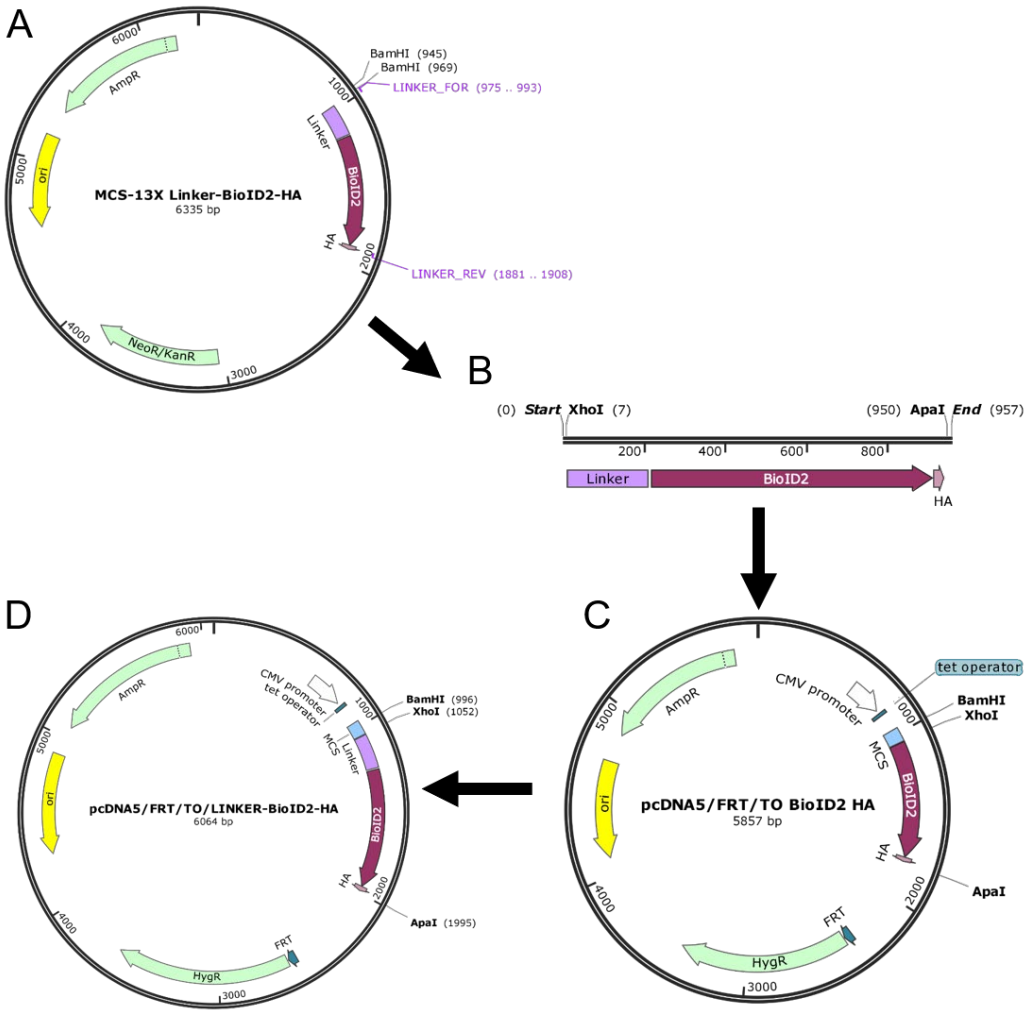

Figure 4.10: Cloning strategy to generate pcDNA™5/FRT/TO/Linker_BioID2-HA. Plasmid maps were produced using Snapgene. **A:** The plasmid map of MCS-13X Linker-BioID2-HA (Addgene #80899) showing the primer binding sites used to amplify the 13x Linker-BioID2-HA coding sequence. **B:** The following PCR amplification from A, including XhoI and ApaI restriction sites. **C:** The pcDNA™5/FRT/TO/BioID2-HA plasmid map showing the XhoI and ApaI insertion sites. **D:** The final plasmid map of pcDNA™5/FRT/TO/Linker_BioID2-HA generated by digestion of B and C with XhoI and ApaI digestion and ligation of the fragments**.**

These vectors were designed such that all the target sequences could be cloned upstream of the BioID2 coding sequence using BamHI and XhoI. Aliquots of the verified clones were pre-digested and dephosphorylated in preparation for insertion of the 'bait' open reading frames. These were precipitated and stored at -20°C until required.

4.3.9 Identifying MRP coding sequences for custom synthesis

The coding sequences for MRPS5, MRPS24, MRPS33, MRPS35 and MRPS39 were analysed in SnapGene® 4.2.9 using information from the GenBank® genetic sequence database. Sequences were designed with a BamHI restriction site upstream of the start codon and a Kozak consensus sequence, which was incorporated to increase recognition of the translation initiation start codon by the cytosolic ribosome and promote gene expression. The stop codon was removed from the sequence to allow generation of a fusion protein and a downstream XhoI restriction recognition site incorporated. Several of the target ORFs contained internal BamHI and XhoI target sequences. To overcome potential for digestion at these sites, silent mutations were introduced whilst production of identical protein products was retained. The plasmids were then ordered from GeneArt® Gene Synthesis.

4.3.10 Preparation of coding sequences from synthetic plasmids

The lyophilized synthetic genes were reconstituted and used to transfect bacterial cells followed by selection with the appropriate antibiotic. For each coding sequence, two bacterial colonies were amplified and the plasmid DNA isolated and each was subjected to two diagnostic digests; BamHI and XhoI was used to confirm the size of the open reading frame insert, and linearization with XhoI estimated the entire plasmid molecular size.

Table 4.7: The predicted molecular weights of custom synthesized plasmids after restriction digest by XhoI and BamHI

Plasmid	Coding sequence	Linear size (kb)	Backbone (kb)	Coding sequence(kb)
18AAFOP MRPS5 pMA-T	MRPS5	3.7	2.4	1.3
18AAZFNP2_MRPS24_pMA-RQ	MRPS24	2.8	2.3	0.5
18AAZFMP MRPS33 pMA-RQ	MRPS33	2.6	2.3	0.3
18AAZFKP_MRPS35_pMA-T	MRPS35	3.3	2.3	1.0
18AAZFLP_MRPS39_pMK-RQ	MRPS39	4.3	2.2	2.1

The linearized (L) and double digested (DD) samples were analysed by gel electrophoresis (2.2.8) (Figure 4.11). Predicted fragment sizes are listed in Table 4.7. For the MRPS39 double digest from 18AAZFLP_MRPS39_pMK-RQ, the resulting fragments are very similar in size and are therefore not distinguishable in Figure 4.11 Lane 10. The double digestion was electrophoresed in a longer 1% TAE agarose gel to separate the two species (Figure 4.11 Lane 11).

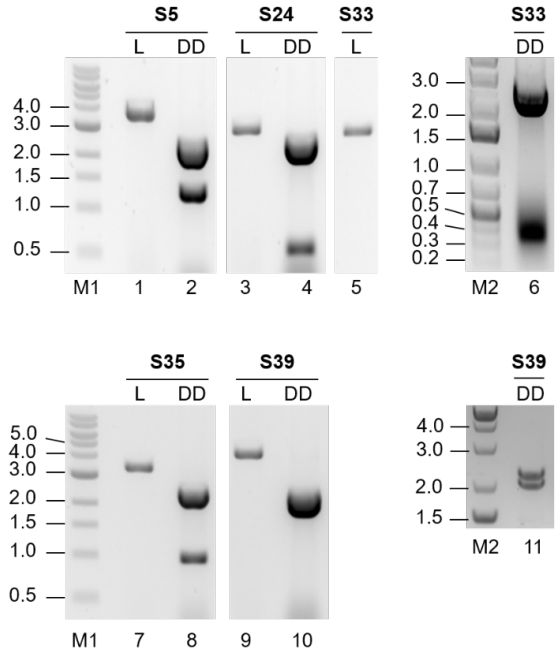

Figure 4.11: Digestion of custom synthesized plasmids. All linearizations (L) were digested with XhoI and all double digests (DD) were digested with XhoI and BamHI. All DNA fragments were separated in a 1% TAE agarose gel. The ORF contained within the plasmid and the digestion is indicated above each lane. M designates molecular weight marker lane. Lane 11: the digestion product from Lane 10 following extended electrophoresis to distinguish the two molecular weight bands. M1, NEB 1kb DNA ladder; M2 GeneRuler 1kb Plus DNA ladder.

The double digestion released the insert and confirmed the size of each insert. The DNA corresponding to each MRP coding sequences was extracted from the gel and 1µl was analysed via gel electrophoresis to confirm fragment recovery and predict molar concentrations (Figure 4.12).

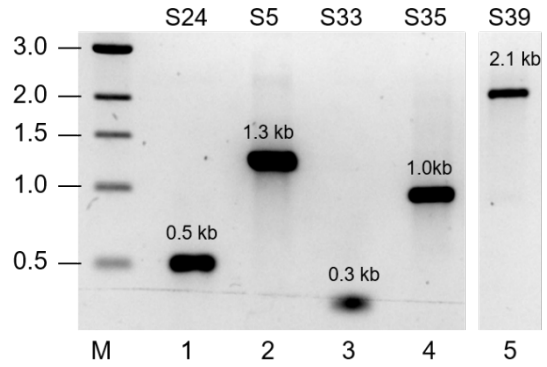

Figure 4.12: Isolation of MRP coding sequences. Following digestion with XhoI and BamHI, the DNA species containing the MRP coding sequences were excised and recovered from the agarose and re-analysed by gel electrophoresis (1% TAE agarose). The expected molecular weight is depicted above the species of interest for each ORF (as indicated above each lane). M designates molecular weight marker lane. M, NEB 1kb DNA ladder.

4.3.11 Preparation of MRPS27 and SLIRP open reading frames for cloning

Plasmids containing the coding sequences for MRPS27 (pCMV-Sport_6_MRPS27) and SLIRP (pDNR-LIB_SLIRP) were extracted from glycerol stocks, cultured, and the DNA isolated. To confirm the identity of the plasmids, each was linearized, and the coding sequences excised by restriction digest (Figure 4.13).

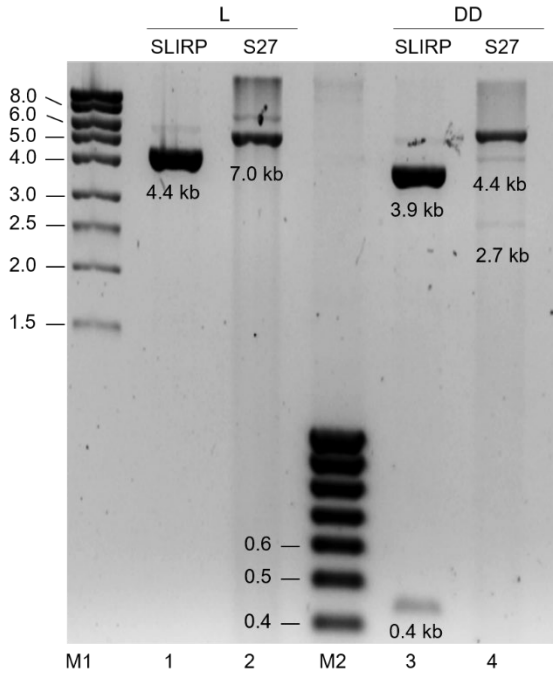

Figure 4.13: Diagnostic digests to verify MRPS27 and SLIRP coding sequence molecular weight. The type of digestion and the ORF contained in the plasmid are depicted above each lane. M designates molecular weight marker lane. Linearization (L) was by XhoI digestion. Excision of the coding sequences (E) was by SfiI for SLIRP and NotI and SalI for MRPS27. M1: MassRuler™ High Range DNA Ladder M2: HyperLadder™ 1kb. DNA fragments were separated in a 1% TAE agarose gel.

Primers were designed to amplify the coding sequences from the pCMV-Sport_6_MRPS27 and pDNR-LIB_SLIRP plasmids where the coding sequence was flanked by BamHI and XhoI restriction sites. Upon restriction digestion, these PCR amplicons had compatible ends to facilitate integration into the pcDNA™5/FRT/TO/BioID2-HA vector. To improve digestion efficiency, six bases were added upstream of the restriction recognition sequence of each primer. The reverse primers were designed to anneal to the open reading frame before the stop codon to allow the generation of fusion proteins with BioID2-HA in the recipient vector. PCR successfully amplified the MRPS27 and SLIRP products generating expected amplicon sizes (Figure 4.14 A). Optimisation was required for the amplification of the MRPS27 coding sequence.

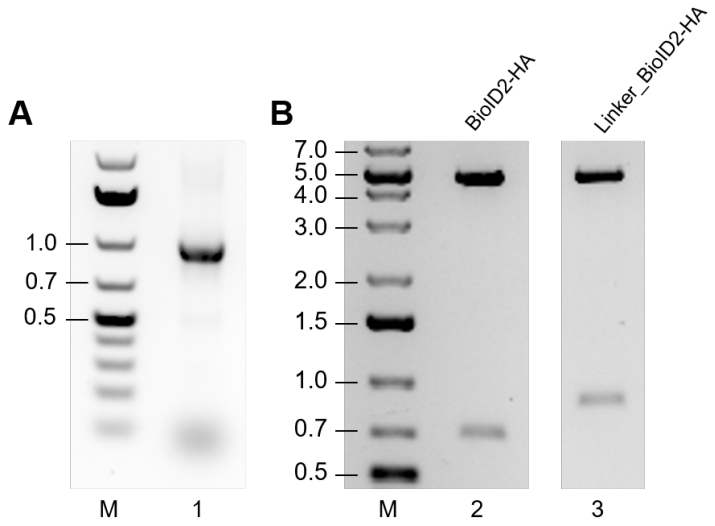

Figure 4.14: PCR products of the coding sequences of MRPS27 and SLIRP. M designates molecular weight marker lane. **A:** PCR amplification of the coding sequences for MRPS27and SLIRP following optimisation. The expected molecular weight is depicted below the species of interest for each ORF (as indicated above each lane). **B:** Temperature gradient PCR to determine the optimal temperature for MRPS27 coding sequence amplification. Annealing temperature varied from 54-68°C. M1, HyperLadder™ 1kb (Bioline). M2, NEB 1kb DNA ladder. DNA fragments were separated in a 1% TAE agarose gel.

A temperature gradient PCR reaction with annealing temperatures ranging from 54°C to 68°C was used to determine the optimal annealing temperature of 64°C (Figure 4.14 B). The PCR products were digested with BamHI and XhoI overnight and purified using phenol chloroform extraction to remove the digestion reagents and primers prior to the ligation steps.

5.3.12 Cloning coding sequences into vectors and screening

The pre-digested dephosphorylated host vectors and gel-extracted coding sequences were ligated overnight, and each ligation reaction (4µl) was used to independently transform chemically competent α-select bacterial cells. Single colonies were amplified, plasmids digested (BamHI/ApaI) to determine which had been successfully cloned into pcDNA™5/FRT/TO. The different digestion products were separated by agarose gel electrophoresis (Figure 4.15).

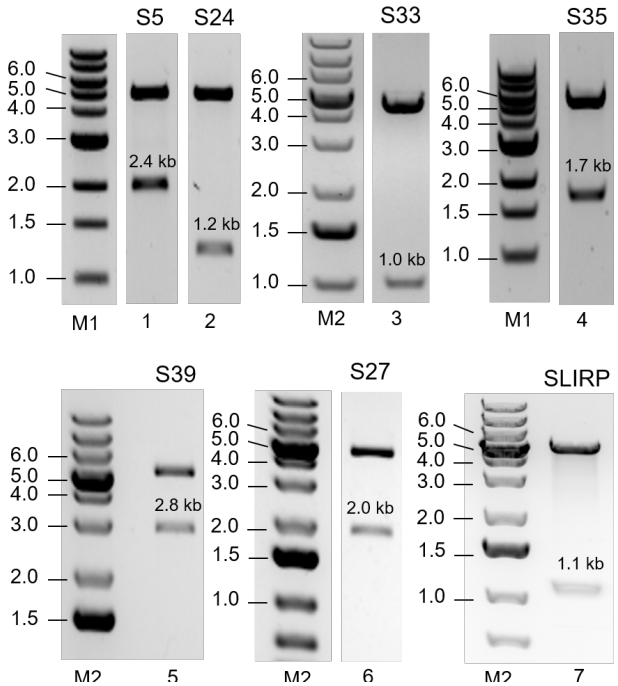

4.15: Verification of insertion of coding sequences into pcDNA™5/FRT/TO/BioID2-HA plasmids. All samples were digested with BamHI/ApaI. M designates molecular weight marker lane. The expected molecular weight is depicted below the species of interest for each ORF (as indicated above each lane). M1, NEB 1kb DNA ladder, M2, GeneRuler 1kb Plus DNA ladder. DNA fragments were separated in a 1% TAE agarose gel.

Each ORF was also intended to be cloned into pcDNA™5/FRT/TO/Linker_BioID2-HA, however due to time constraints this could not be accomplished. Constructs observed to have the predicted molecular weight species following restriction digest were subjected to Sanger sequencing analysis. This was to confirm sequence at the insertion junctions as well as the inserts themselves to ensure faithful subsequent expression of the desired proteins. Sequencing primers were designed to amplify the insertion junctions for each construct, with a product length of 300 to 600bp as this was the optimal fragment size for Sanger sequence analysis. The same reverse primer was used for all sequencing PCR amplifications, complementary to DNA positioned 174 base pairs into the BioID2 sequence. The forward primer for each construct was designed for optimal fragment size and to have a similar melting temperature to the reverse primer, to ensure compatibility of the PCR cycle for all sequencing PCR reactions. An example alignment of the MRP coding sequence (Panel A) and the sequencing product (Panel B) following cloning are displayed in Figure 4.16. Clones with the incorrect DNA sequence were discarded.

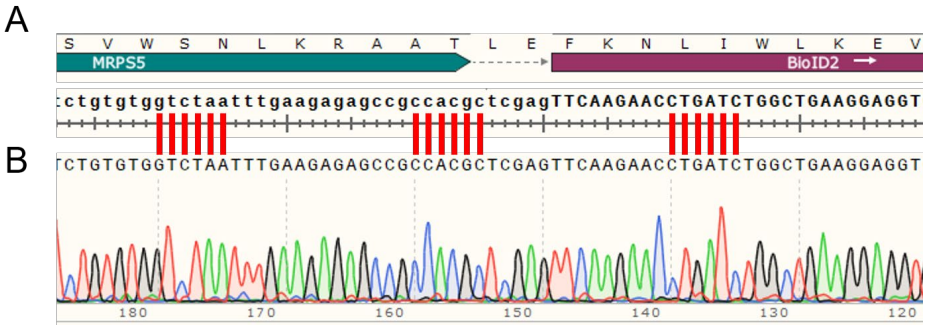

Figure 4.16: Confirmation of MRPS5-BioID2-HA construct generation by Sanger sequencing. Red lines are used to aid visualising sequence alignment. A: The known sequence of MRPS5 succeeded by the BioID2 sequence visualised SnapGene®. B: The electropherogram of pcDNA™5/FRT/TO/MRPS5-BioID2-HA Clone 1 from the derived sequencing primers. A full list of sequences for bait-BioID2-Ha constructs can be found in Appendix IV.

4.4 Discussion

This chapter describes the generation of seven proximity labelling tools using the established process of fusion to BioID2, a small biotin ligase. A subset of the mitoribosomal proteins that surround the small subunit mRNA entry site were selected as 'bait' (MRPS5, MRPS24, MRPS33, MRPS35 and MRPS39). The RNA-binding protein SLIRP has a role in mt-mRNA stability and potentially delivery to the mitoribosome and so BioID2-HA fusion was used as a control for the experimental process. Additional controls for mitoribosome association and matrix targeted proteins were also employed. MRPS27 was selected as a suitable non-specific mitoribosomal bait and the COX8MTS-BioID2 controlled for non-specific interactions with mitochondrial matrix proteins. The results arising from these control constructs will be used as a measure of the background biotinylation of proteins unrelated to mt-mRNA delivery to the mt-SSU, thus giving confidence to those proteins that appear to be enriched at the mt-mRNA entry tunnel.

For the MRP fusion proteins (excluding MRPS27), inserts were custom synthesized with incorporated silent changes that would result in a synonymous protein, without including restriction sites that would disrupt the planned cloning steps. Furthermore, each ORF containing fragment was designed to contain a Kozak sequence to promote expression once integrated into the host cell genome. In the case of MRPS27 and SLIRP, the coding sequences were amplified from vectors already established in my host laboratory.

This chapter summarises the construct design, generation, digest validation and final confirmation by Sanger sequencing of all the vectors designed for implementing this project.

In all cases the coding sequences were successfully integrated into the pcDNA™5/FRT/TO/BioID2-HA vector. In the next chapter I will detail the assessment of the functionality of human Flp-In™-293 cells transfected with these constructs. The ability of each cell line to inducibly express each protein had to be confirmed. Additionally, mitochondrial localisation of the SLIRP and COX8MTS controls also needed to be confirmed. Once this was established the induction conditions needed to be identified to determine conditions for expression of near endogenous levels of each MRP and finally to confirm whether the BioID2-fused MRPs have retained the ability to integrate into the mitoribosome. These steps are the subject of the next chapter.

Chapter 5:

Validation of BioID2 Fusion Protein Expression and Mitoribosomal Integration

5.1 Introduction

In order for the biotin ligase to biotinylate proteins only when they were proximal to the mt-mRNA entry site, the inducibly expressed MRP 'bait' proteins needed to be incorporated into the mitoribosomal small subunit (mt-SSU), and not free or in mitoribosomal subcomplexes. For this reason, the amount of the fusion proteins not integrated into the mt-SSU needed to be minimised to reduce confounding signals that could otherwise be generated by the active and unincorporated biotin ligase. In addition, it was necessary to confirm that the biotin ligase moiety was not cleaved off the MRP after import, generating background signal. Hence it was crucial to confirm fusion protein integration into the mitoribosome. This was assessed by pulse-chase experiments. Upon induction with tetracycline-class compounds, the Flp-In™ expression cell lines overexpressed the proteins of interest that had been integrated into the expression cassette. The pulse-chase experimental design was chosen to allow for this overexpression of the BioID2-tagged proteins during the pulse phase, and both integration of the fusion protein into the mitoribosome, and degradation of the unintegrated overexpressed protein. The fusion protein was induced with doxycycline, after which the cells were washed and transferred to inducer-free media wherein they were 'chased' for 24- or 48-hours. Analysis was performed by isokinetic sucrose gradients of cell lysates from different pulse-chase conditions. The position of the fusion protein in the gradient was determined by western blotting and was compared to markers of the mitoribosome small subunit (mt-SSU) and large subunit (mt-LSU). The antibodies used to visualise the small and large subunits varied as they needed to be of different molecular weights to the fusion protein investigated. Throughout this chapter antibodies to MRPS26, MRPS27, MRPS39, MRPL11 and MRPL45 have been used in different combinations. The optimal pulse-chase conditions for subsequent experimentation were determined as those which resulted in fusion protein integration into the mitoribosome which mirrored both the distribution and signal strength of small subunit proteins across the gradient. In this instance, the bait protein was integrated at approximately the same levels as endogenous mt-SSU proteins.

This chapter presents confirmation of the expression of all the BioID2 fusion proteins and assessed their ability to integrate into the mitoribosome. The outcomes of these analyses determined the optimal conditions for induction and biotinylation to generate a biologically relevant output from subsequent streptavidin pulldown and mass spectrometry analysis. In

addition, I will also present evidence that the controls, SLIRP- and COX8MTS-BioID2-HA, are localised to the mitochondrial matrix.

5.2 Materials and Methods

5.2.1 Generation of stable cell lines able to overexpress BioID2 fusion proteins

The BioID2 fusion constructs were independently stably transfected into HEK Flp-In™ T-REx™-293 (2.3.5) and selected for integration using 100 µg/ml Hygromycin^{B} and 10 µg/ml Blasticidin^{S}. Over a period of 2-3 weeks, the growth of clonal colonies was monitored using AxiovertVert 25M microscope. Individual clones that survived selection were expanded into separate wells in a 6 well plate, without Hygromycin^{B} supplement. Clonal lines were maintained (2.3.2) with the addition of 10 µg/ml Blasticidin^{S} every third feed. When a clone reached ~80% confluency it was harvested (2.3.2) and split into 3 wells in a new plate. One well was untreated and allowed to grow confluent as a stock of this clone. Two wells were used to confirm successful integration and inducibility; one well was treated with 1 µg/ml of tetracycline for 48 hours and one was left untreated. Cell lysates were prepared (2.4.1) and the protein concentration was estimated by Bradford Assay (2.4.2). Each sample (25 µg) was incubated with an equal volume of with sample dissociation buffer (2.4.6) and heated at 95 °C for 5 minutes before analysis by SDS-PAGE. Subsequent western blot immunodetection (2.4.7) used anti-HA antibodies to detect the fusion protein. A full list of primary and secondary antibodies used is included in Appendix II.

5.2.2 Pulse-chase experiments

Inducible clonal lines were cultured in T175 flasks, grown under different conditions for each induction and chase, allowing all cell samples to be harvested concurrently. All cells were pulsed by induction with 50 ng/ml doxycycline for 16 hours. For chase experiments, the cells were pelleted and resuspended in fresh media and transferred to a new flask to ensure no doxycycline was present in the culture environment. After the desired pulse or pulse/chase time, cells were harvested, lysed in sucrose gradient lysis buffer (2.4.5), and the concentration determined by Bradford assay (2.4.2).

5.2.3 Sucrose gradient analysis

The sucrose gradient was prepared (2.4.5) and stored at 4 ºC prior to harvesting and preparation of cell lysate. Cell lysate (700 µg), made up to a total volume of 100 µl with sucrose gradient lysis buffer (2.4.5), was loaded carefully on top the gradient by pipetting slowly with the tip

pressed to the side of the ultracentrifuge tube as to not disturb the gradient. In cases where 700 µg of protein would occupy a larger volume than 100 µl, only 100 µl was loaded on top of the gradient (and the mass noted). The samples were centrifuged at 100 *kg* for 2.25 hours at 4°C before eleven 100 µl fractions were carefully collected from the top of the gradient and stored on dry ice (2.4.5). To analyse the distribution of proteins across the gradient, 10 µl of each fraction was mixed with sample dissociation buffer (final concentration: 6.25 mM Tris/HCl pH 6.8, 2% SDS, 10% glycerol, ~0.01% bromophenol blue and 100 mM DTT) and analysed by SDS-PAGE and western blot immunodetection (2.4.5, 2.4.6). A sample of the initial lysate (50µg) was analysed on the same blot to visualise the input onto the gradient.

The volume analysis tool of ImageLab (Version 4.1.0.2177) was used to quantify the immunoblotting results. Boxes of equal volume were drawn around the signal for each fraction and the intensity volume was calculated. Using Microsoft Excel 2016, the intensity across fractions 1-10 was totalled and analysed to show the distribution of signal across the gradient.

5.2.4 Mitochondrial subfractionation

Stably transfected cells were propagated in T300 flasks, induced with tetracycline (1 µl/ml) for 3 days. Mitochondria were isolated using a glass:teflon dounce homogeniser (process described in 2.4.3). All subsequent steps were carried out at 4°C. To separate mitochondria into subfractions, mitochondrial preparations (360µg, or as many µg as available in the preparation) were diluted in homogenisation buffer (0.6 M mannitol, 1 mM EGTA, 10 mM Tris pH 7.4) to a total volume of 90 µl. A 15 µl aliquot (60 µg) was taken, mixed with sample dissociation buffer (5.2.3), and snap frozen on dry ice as a sample of whole mitochondria (Sample A).

Proteinase K (1.5 µg) was added to the remaining sample and incubated on ice for 30 minutes. To inhibit further digestion PMSF (final concentration: 5 mM) was added to the sample and centrifuged at 11000 g, 10 minutes, 4°C. The supernatant was discarded, and the pellet resuspended in 75 µl of homogenisation buffer (as above). A 15 µl aliquot (60 µg) of this was mixed with sample dissociation buffer and snap frozen on dry ice, as a sample of mitochondria with outer membrane-bound proteins removed (Sample B).

The remaining 60 µl of the sample was centrifuged at 11000 g, 10 minutes, 4 °C, and the supernatant discarded. The pellet was resuspended in 900 µl of hypotonic buffer (10 mM Tris-HCl pH 7.4) and 450 µl was transferred to a clean microcentrifuge tube. Proteinase K (0.6 µg) was added to this new tube, and both tubes incubated on ice for 30 minutes. PMSF was added to both tubes to a final concentration of 5 mM before addition of an equal total volume of buffer

(1.2 M mannitol, 2 mM EGTA, 10 mM Tris pH 7.4, final concentration). These samples were centrifuged at 12000 g, 10 minutes, 4 °C, and the supernatant discarded. Both pellets were resuspended in 30 µl of homogenisation buffer and 15 µl (60 µg) of each was removed, mixed with sample dissociation buffer, and snap frozen on dry ice, to represent mitoplasts (mitochondria without the outer membrane, Sample C) and mitoplasts with membrane-bound proteins removed (the sample treated with proteinase K, Sample D). The final 15 µl of each sample was discarded.

Samples (A: whole mitochondria, B: mitochondria with outer membrane bound proteins removed, C: mitoplasts, and D: mitoplasts with membrane-bound proteins removed) were then analysed by western blotting and immunodetection (2.4.5) to confirm whether each mitochondrial fraction had been cleanly isolated using antibodies to marker proteins to each compartment.

5.3 Results

5.3.1 Characterising expression of stably transfected cell lines

Stable transfectant clones were generated in HEK Flp-In™ T-Rex™-293 cells with each of the MRP or SLIRP pcDNA5/FRT/TO plasmids (2.3.5). Control untransfected cells were grown concurrently in the presence of these antibiotics, as the point when these cells had died indicated that the surviving clonal cells were antibiotic resistant and should have been stably transfected. Single clones were then expanded and maintained before confirming protein overexpression by immunodetection with an HA antibody.

To confirm inducibility of the transfected cell lines, and whether the induced protein was of the correct molecular weight, cell lines were induced with tetracycline (1 µg/ml) for 3 days. Cell lysates were prepared and proteins from uninduced and induced conditions, subjected to SDS-PAGE and immunodetected using antibodies to HA to visualise the fusion protein. To control for comparable loading of each sample, levels of SDHA and β-Actin were determined. For each BioID2 fusion, there was at least one successful clone that displayed an induced protein of the correct molecular weight. The molecular weights of the fusion proteins, including after mitochondrial targeting site (MTS) cleavage, were determined using SnapGene® 4.2.9 (Table 5.1).

Table 5.1: Molecular weights of BioID2 fusion proteins for MRPs and controls.

Protein	Protein length (aa)	Molecular weight (kDa)	Molecular weight after MTS cleavage (kDa)	MRP UniProt identifier
MRPS5-BioID2-HA	673	75.7	72.8	P82675
MRPS24-BioID2-HA	410	46.8	43.0	Q96EL2
MRPS33-BioID2-HA	349	40.4	N/A	Q9Y291
MRPS35-BioID2-HA	566	64.6	61.4	P82673
MRPS39-BioID2-HA	932	106.3	103.0	Q96EY7
MRPS27-BioID2-HA	657	75.3	72.1	Q92552
SLIRP-BioID2-HA	355	40.4	37.0	Q9GZT3
COX8MTS-BioID2-HA	274	31.1	27.5	P10176

Only one of each construct was carried forward for subsequent investigation (Figure 5.1). In all successful transfections there was a clear expression of the correctly sized fusion protein after induction. In the uninduced MRPS27-, SLIRP- and MRPS24-BioID2 cell lines, there was evidence of a weak signal for the fusion protein. This was interpreted as resulting from leaky expression of the Flp-In integrated coding sequences. This leaky expression has been seen several times in my host lab and other groups (Pham et al., 2018).

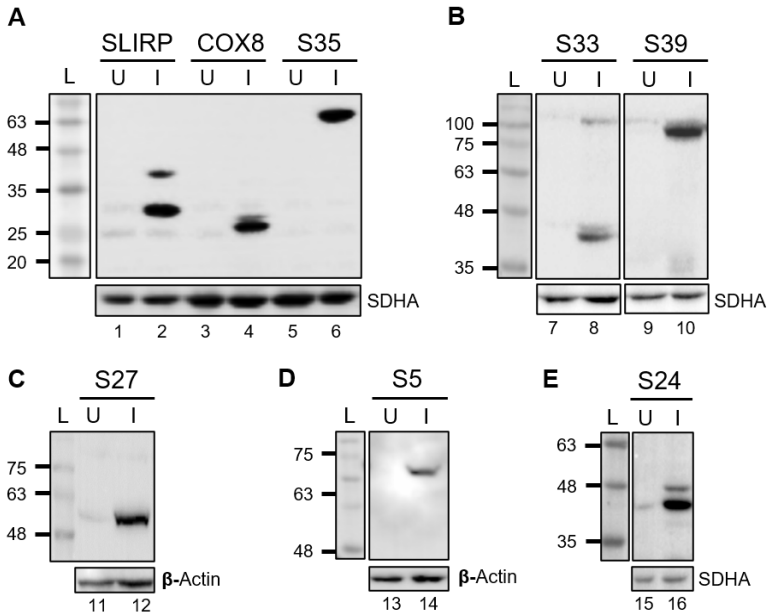

Figure 5.1: Confirmation of expression of MRP-fusion proteins in HEK293 cells. Cell lysates (25 µg) from uninduced (U) and induced (I, 3 days 1 µg/ml tetracycline) HEK cells stably transfected to overexpress BioID2 fusion proteins. Proteins were separated by 12% SDS-PAGE western blot were detected with antibodies to HA, SDHA, and β-Actin. Multiple gels were required to analyse the BioID2-HA fusion proteins as follows **A:** SLIRP, COX8MTS, and MRPS35. **B:** MRPS33 and MRPS39. **C:** MRP27. **D:** MRPS5 **E:** MRPS24. L, protein size marker (kDa).

Overexpression of SLIRP-, COX8MTS-, MRPS33- and MRPS24-BioID2-HA (Figure 5.1 A, B, E) resulted in two species, with the upper species at the predicted molecular weight (Table 5.1). This observation was consistent across multiple clones, and in biological repeats that were testing expression. The doublet for the COX8 fusion was also observed by colleagues at the University of Gothenburg who provided the plasmid DNA for a control transfection. This was consistent with cleavage of a mitochondrial targeting sequence after entry and only a small amount of the 27.5 kDa BioID2-HA protein remaining (Figure 5.1 A, lanes 3 and 4). For the other fusion proteins where a doublet is observed, the lower species is not present at 27.5 kDa (BioID2-HA), which suggests that there is no cleavage event at the fusion site. I used in silico targeting sequence prediction tools iPSORT (http://ipsort.hgc.jp/predict.cgi) and MITOPROT (https://ihg.gsf.de/ihg/mitoprot.html) to predict any cleavage sites and the molecular weight of the mature protein after cleavage. Both tools estimated a cleavage site in the MRPS24 amino acid sequence, producing a protein of ~43 kDa. The observed signals from MRPS24-BioID2-HA overexpression correlated with this prediction (Figure 5.1 E). MITOPROT predicted a cleavage site in the amino acid sequence for MRPS33-BioID2-HA, producing a cleaved protein ~37 kDa in size. This also correlated with the species observed by western following overexpression of the fusion protein. The cleavage of MRPS24 and MRPS33 is predicted within the endogenous protein and may reflect the MTS site. MITOPROT predicted a cleavage site in the amino acid sequence for SLIRP-BioID2-HA, however cleavage at this site did not correlate with the observed lower species when the fusion protein was overexpressed. The cleaved protein from SLIRP is predicted to be ~37 kDa, however the lower species observed was much smaller (~30 kDa). It was not clear if this lower band represented aberrant migration or a degradation product. It was important to assess which protein signal, if either, localised to the mitochondria and for the MRPs whether they integrated into the mitoribosome.

5.3.2 Investigating whether BioID2-tagged MRPs integrated into the mitoribosome

To gather biologically relevant information from the BioID2 pull down experiments, the tagged MRPs must be integrated into the mitoribosome when they biotinylate nearby proteins. To be able to determine whether the tagged MRPs colocalised with the mitoribosome, the migration of the small and large subunits was established on 10-30% sucrose isokinetic gradients (2.4.5). Lysates from untransfected HEK293 Flp-In™ T-Rex™ cells were subjected to high-speed centrifugation on sucrose gradients to separate proteins and complexes according to their density. Fractions (F1-F10) from the sucrose gradient were obtained and analysed via western

blot alongside a 50 µg aliquot of total lysate (Figure 5.2 Lys). Unless otherwise stated, western blotting for MRPs was carried out concurrently and visualised with the same HRP-conjugated secondary antibody. The signal strength from the immunoblot was measured using ImageLab and analysed in Microsoft Excel (5.2.4).

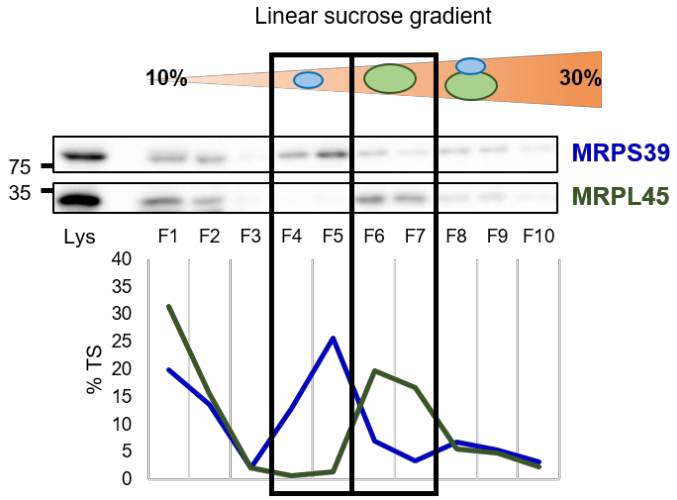

Figure 5.2: Isokinetic sucrose gradient analysis to assess mitoribosome subunit distribution from untransfected HEK293 Flp-In™ T-Rex™ cells. Cell lysate (Lys, 700 µg) from wild type HEK293 cells was separated across a 10-30% sucrose gradient by centrifugation. Ten 100 µl fractions (F1-F10) were obtained and analysed via western blot. The mt-SSU and mt-LSU were visualised by antibodies against MRPS39 (78.6 kDa) and MRPL45 (35.3 kDa) respectively. A scheme depicting the anticipated separation in a sucrose gradient of the mt-SSU (blue), mt-LSU (green), and mt-monosome is aligned about above the western. Signals were quantified using ImageLab and the distribution of each of the subunits was calculated as a percentage of total signal (TS) for that subunit.

This data indicated that the signals in the lowest sucrose density fractions (fractions 1-3) represent free proteins or small protein complexes with a low molecular weight. The small subunit, visualised by anti-MRPS39, began to appear in fraction 4 and was strongest in fraction 5. The large subunit, visualised by anti-MRPL45, appeared first in fraction 6 and was strongest in fraction 7. The later fractions (fractions 8-10) represented large complexes of proteins wherein the monosome is found. Signal for MRPS39 and MRPL45 was visible across these fractions. The distribution of MRPS39 and MRPL45 was consistent across sucrose gradient biological repeats, with minor variation due to human error when removing fractions.

Sucrose gradients were then used to assess whether the doxycycline-induced MRP-BioID2-HA proteins had integrated into the mitoribosome. For all MRPs investigated, sucrose gradients were conducted at two time points; after 16 hours of induction, and after 16 hours induction followed by a 24-hour chase period where the doxycycline inducer had been removed. Where

the gradient data was a strong indication that the MRP-BioID2 construct integrated into the ribosome, gradients at these timepoints were repeated in parallel with gradients from an uninduced sample and a sample induced for 16 hours and chased for 48 hours. The 24- and 48-hour chase timepoints were performed to investigate whether the overexpressed fusion protein that did not integrate into the mitoribosome was degraded over time. These unintegrated BioID2-tagged proteins would still be able to biotinylate proximal proteins, contaminating the subsequent pull-down results. Western blotting using an anti-HA antibody was used to visualise the induced BioID2-HA fusion proteins of MRPS5, MRPS24, MRPS33 and MRPS35. For the cell lines expressing MRPS27-BioID2-HA and MRPS39-BioID2-HA, the antibodies to the endogenous proteins were able to visualise both the endogenous and the higher molecular weight fusion protein. In these cases, it was preferable to use the antibody to the endogenous protein.

5.3.3 Integration of MRPS27-BioID2-HA into the mitoribosome

MRPS27-BioID2-HA, the control found distal to the mt-mRNA entry site, was induced and analysed by isokinetic sucrose gradients in four conditions, uninduced (Figure 5.3, panel A), 16 hours induction (panel B), 16 hours induction and 24 hours chase (panel C) and 16 hours induction and 48 hours chase (panel D). There was some expression from the uninduced cells for MRPS27-BioID2-HA visible in the lysate, suggesting there was a small amount of leaky expression. The line graph below each series of blots shows that the signals for the two small subunit proteins reflected one another, as do the signals for the two large subunit proteins (Figure 5.3 A). The fusion protein was induced using 50 ng/ml doxycycline for 16 hours, as in all other experiments. Following the induction period, there was a clear signal for the fusion protein, which was distributed mainly in the early fractions 1-3 (Figure 5.3 B, red line in graph below). The signal continues throughout the gradient, suggesting a level of integration into the mitoribosome but that the majority was free. Following a 24-hour chase, the distribution of the tagged protein mirrored the free vs integrated proportions seen in the endogenously expressed MRPS27 (Figure 5.3 C). The ratio of free vs integrated protein is also displayed in the line graph where the red (induced) and pale blue (endogenous) traces for MRPS27 are almost superimposed. Additionally, the intensities of the fusion protein in each fraction is very similar to the intensities of the endogenous MRPS27.

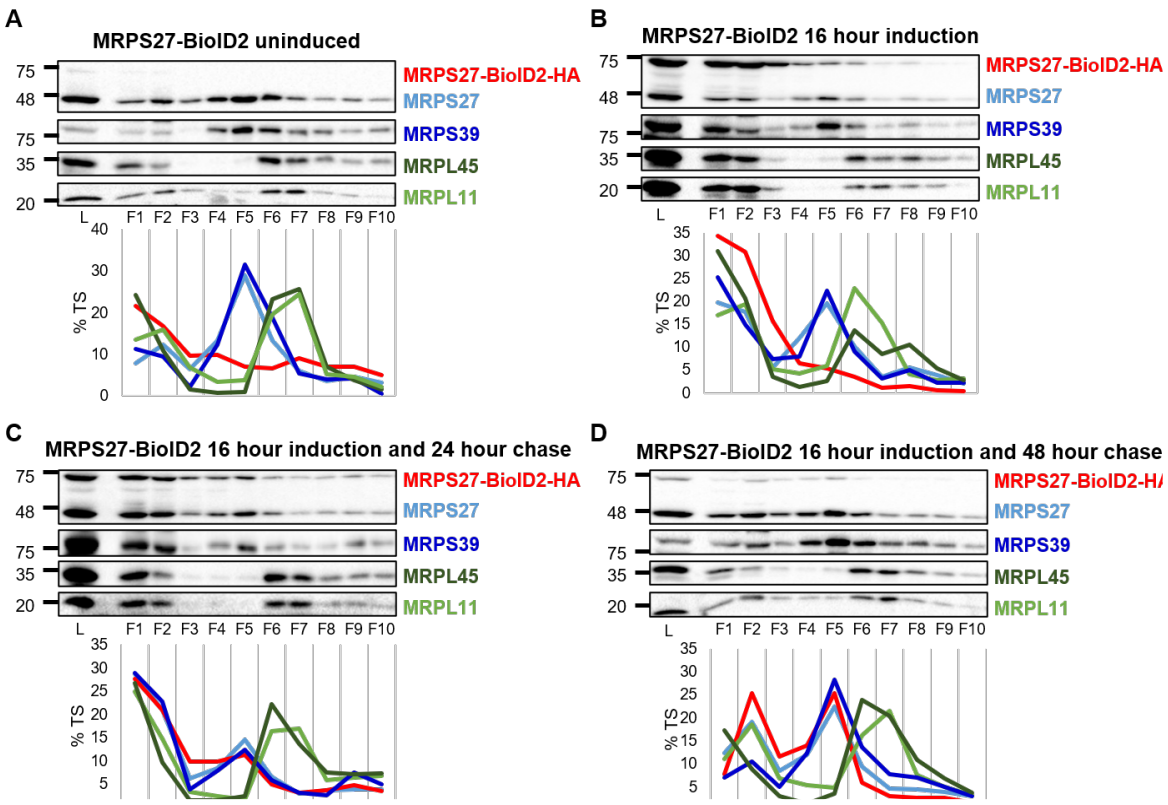

Figure 5.3: Integration of the MRPS27-BioID2-HA fusion protein into the mitoribosome. Cell lysates (L, 700 µg) from HEK293T stably transfected with MRPS27-BioID2-HA from 4 conditions were separated on 10-30% sucrose gradient by ultracentrifugation. Cells were **A:** uninduced, **B:** induced for 16 hrs (50 ng/ml doxycycline) with no chase, **C:** or chased for 24 hrs, **D:** or 48 hrs. Fractions (100µl, F1-F10) were analysed in parallel SDS-PAGE, immunodetected with antibodies to MRPS27 (fusion 75.3 kDa, endogenous 47.6 kDa), MRPS39 (78.6 kDa), MRPL45 (35.3 kDa) and MRPL11 (20.6 kDa).

Since the blotting for both the fusion protein and the endogenous protein were derived from incubation with a single antibody, it suggests similar levels of expression in each fraction and that approximately half of the assembled mt-SSU particles contained BioID tagged MRPS27. After a 48-hour chase, the distribution of the tagged protein still strongly resembled that of the endogenous MRPS27, but the overall signal intensities of the fusion protein decreased when compared to the endogenous protein (Figure 5.3 D). This reduction in intensity, compared to the endogenous MRPS27, suggested higher incorporation of the untagged protein. Overall, the distribution of the MRPS27-BioID2-HA signal across the gradient after a 16-hour induction and 24-hour chase most closely resembled that of the endogenously expressed MRPS27 while also providing the highest incorporation into the mt-SSU. The slight shift in the mt-SSU being in F5/6 compared to F4/5 in the untransfected control was observed in various experimental repeats and reflects experiment or variation when removing each 100 µl fraction. This emphasising the importance of using markers against the mt-SSU and mt-LSU to ensure correct interpretation of the signal derived from tagged MRPs. The best induction/chase conditions

established here, a 16-hour induction followed by a 24-hour chase period, were selected for the BioID2 streptavidin pull down experiment and subsequent analysis by mass spectrometry.

5.3.4 Integration of MRPS39-BioID2-HA into the mitoribosome

As with MRPS27, four induction/chase conditions were used in combination with sucrose gradients to investigate whether expressed MRPS39-BioID2-HA could stably integrate into the mt-SSU and mitoribosome (Figure 5.4). In the gradient from uninduced cells (Figure 5.4 A), there was a small amount of the fusion protein visible in the cell lysate lane and fraction 5. This suggested that the expression cassette, without any induction, allowed for some production of the fusion protein. The signal corresponded to where the small subunit was most strongly localised, as determined by signals of endogenous MRPS39 and MRPS27.

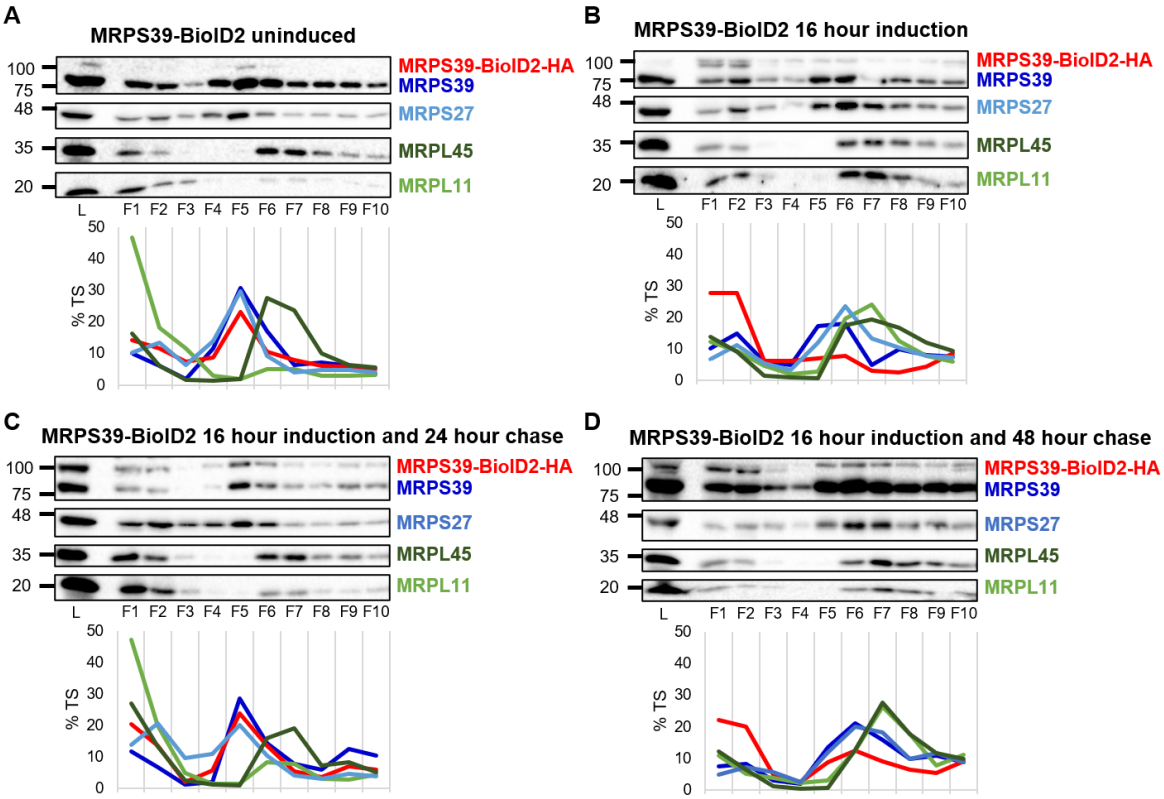

Figure 5.4: Integration of the MRPS39-BioID2-HA fusion protein into the mitoribosome. Cell lysates (L, 700 µg) from HEK293T stably transfected with MRPS39-BioID2-HA from 4 conditions were separated on 10-30% sucrose gradients by ultracentrifugation. Cells were **A:** uninduced, **B:** induced for 16 hrs (50 ng/ml doxycycline) with no chase, **C:** or chased for 24 hrs, **D:** or 48 hrs. Fractions (100µl, F1-F10) were analysed in parallel SDS-PAGE, immunodetected with antibodies to MRPS39 (fusion 106.3 kDa, endogenous 78.6 kDa), MRPS27 (47.6 kDa MRPL45 (35.3k Da) and MRPL11 (20.6 kDa).

This indicated that when MRPS39-BioID2-HA was present at a low level it integrated into the mitoribosome. When the fusion protein was induced for 16 hours with 50 ng/ml doxycycline (Figure 5.4 B), the signal of the protein was weakly visible across all fractions. The strongest two fractions were 1 and 2, indicating that most of the protein was not within a protein complex at this time point. When the 16-hour induction was chased for 24 hours (Figure 5.4 C), the distribution of MRPS39-BioID2-HA protein appeared to strongly mirror that of endogenous MRPS39, however, the intensity of signals differed. The endogenous protein had a stronger signal than the fusion protein across fractions 5-10, suggesting there was more monosome that contained the endogenous MRPS39 than the tagged variant. When the induction was chased for 48 hours (Figure 5.4 D), a longer exposure was required to visualise the signal of the fusion protein. The distribution of MRPS39-BioID2-HA continued to resemble the distribution of the endogenous protein as it did in the 24-hour chase. The higher intensity of signal for endogenous MRPS39 relative to the tagged version, however, could represent a preferential degradation of the fusion protein containing mt-SSU during this additional time. Comparing the levels of integrated fusion protein, and considering the distribution and the intensity of signal, the conditions that most closely replicate the behaviour of the endogenous protein were the 16-hour induction followed by a 24-hour chase period. These were the conditions taken forward for the biotinylation and subsequent mass spectrometry experiment.

5.3.5 Integration of MRPS24-BioID2-HA into the mitoribosome

MRPS24 is buried within the mitoribosome. Modelling of the fusion protein found that, if the fusion protein were to integrate, the BioID2-HA moiety would occupy much of the entry site. Sucrose gradient analysis was used to determine whether MRPS24-BioID2-HA would integrate into mitochondrial ribosomes (Figure 5.5). Following a 16-hour induction (Figure 5.5 A), there was a clear expression of the tagged MRPS24 protein that was strongest in fractions 1-3, and represented the uncomplexed protein. This was consistent with the expression pattern seen in the tagged variants of MRPS27 and MRPS39 after the same period of induction. There was also a faint signal visible in fractions 5 and 6 which suggested a low level of integration. When induction was chased for 24 hours (Figure 5.5 B), the tagged MRPS24 was predominantly found in the free fractions 1 and 2 but some migrated through to fractions 4 and 5. The overall distribution was very similar to the gradient in panel A, however, the tagged fusion protein presented a weaker signal fractions 4 and 5, where the small subunit normally migrates. This suggests very low levels of integration of the MRPS24-BioID2-HA protein into the mitoribosome. There was limited time to optimise conditions to improve this integration, therefore MRPS24 was not carried forward for further experimentation.

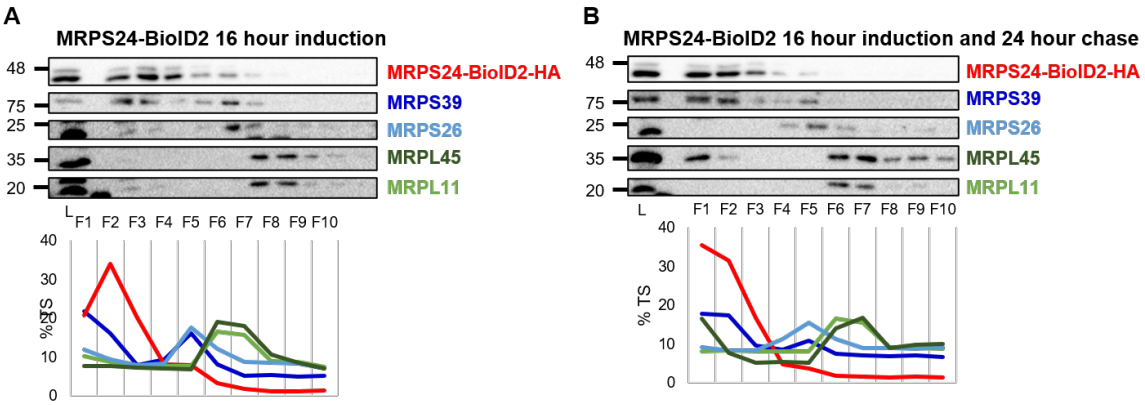

Figure 5.5: Integration of the MRPS24-BioID2-HA fusion protein into the mitoribosome. Cell lysates (L, 700 µg) from HEK293T stably transfected with MRPS24-BioID2-HA from conditions were separated on 10-30% sucrose gradients by ultracentrifugation. Cells were **A:** induced for 16 hrs (50 ng/ml doxycycline) with no chase or **B:** chased for 24 hrs. Fractions (100 µl, F1-F10) were analysed in parallel SDS-PAGE, immunodetected with antibodies to HA (46.8 kDa), MRPS39 (78.6 kDa), MRPS26 (19.2 kDa), MRPL45 (35.3 kDa) and MRPL11 (20.6 kDa)

5.3.6 Integration of MRPS5-BioID2-HA into the mitoribosome

MRPS5 was a clear candidate for this experiment as it encircles the mRNA entry site. When the mitoribosome structure was analysed in Pymol, the C-terminus of MRPS5, where BioID2-HA would be fused, was found positioned within the mRNA entry tunnel. Integration of the fusion protein may well be reduced if the BioID-HA extension caused a blockage of the entry site or created steric hindrance to the formation of the mt-SSU or monosome. Sucrose gradient analysis was used to evaluate the level of incorporation of MRPS5-BioID2-HA into the mt-SSU. Cells which contained MRPS5-BioID2-HA under the control of an inducible cassette were induced for 16 hours, with or without a 24-hour chase. The derived lysates were analysed by sucrose gradients with fractions immunoblotted with antibodies to detect the migration of the tagged protein and its relative position compared to mt-SSU and mt-LSU components (Figure 5.6). The gradients were run in parallel; with the mt-SSU represented in fractions 5 and 6 and the mt-LSU in fractions 7 and 8. Following 16 hours induction (Figure 5.6 A), a strong signal is detected across fractions 2-10, with the peak appearing in fraction 4. This distribution was not seen by any other BioID2-tagged protein subjected to sucrose gradient analysis. When this induction period was followed by a 24-hour chase (Figure 5.6 B), the signal remained distributed across the entire gradient but there was a clear peak in fractions 3 and 4. The distribution of MRPS5 did not closely resemble the small subunit markers in either of these two conditions.

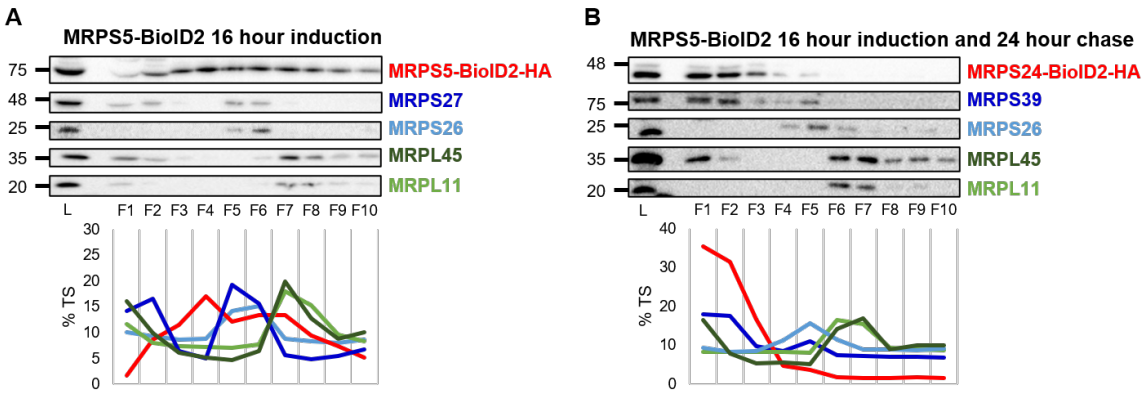

Figure 5.6: Integration of the MRPS5-BioID2-HA fusion protein into the mitoribosome. Cell lysates (L, 700 µg) from HEK293T stably transfected with MRPS5-BioID2-HA from conditions were separated on 10-30% sucrose gradients by ultracentrifugation. Cells were **A:** induced for 16 hrs (50 ng/ml doxycycline) with no chase or **B:** chased for 24 hrs. Fractions (100 µl, F1-F10) were analysed in parallel SDS-PAGE, immunodetected with antibodies to HA (75.7 kDa), MRPS27 (47.6 kDa), MRPS26 (19.2 kDa), MRPL45 (35.3 kDa) and MRPL11 (20.6 kDa).

Due to the widely distributed migration of this tagged MRP, there was an overlap of signal with mt-SSU in fractions 5 and 6 after the induction and after a subsequent 24-hour chase. This might suggest a low-level integration; however, the most intense signal is clearly in earlier fractions. As was the case with MRPS24, I did not have the time to fully optimise conditions for MRPS5 integration to the mitoribosome. Moreover, this was a protein that was positioned in a way that might preclude delivery of the mt-mRNA and therefore was not the highest priority BioID 'bait'. Therefore, this protein is not investigated further within this thesis.

5.3.7 Integration of MRPS33-BioID2-HA into the mitoribosome

In the mitoribosome, the C-terminus of MRPS33 is found at the base of the mRNA entry site with the rest of the protein surrounded by other mt-SSU proteins. When MRPS33-BioID2-HA was modelled in Pymol, I was able to orient the ligase such that it did not disrupt the structure of the mt-SSU. To assess whether this was the case physiologically, and experimentally determine the the ability of this fusion protein to integrate into the mt-SSU, I used sucrose gradient analysis (Figure 5.7). Following a 16-hour induction (Figure 5.7 A) there was a small amount of the MRPS33 protein visible in fraction 4, which aligned with the mt-SSU indicator MRPS27. When this induction was chased for 24 hours (Figure 5.7 B), MRPS33-BioID2-HA was only present in fractions 1 and 2, which represented protein that was not within multiprotein complexes. From this data there was no suggestion that MRPS33 integrated into the mitoribosome and hence MRPS33 was not investigated any further within this thesis.

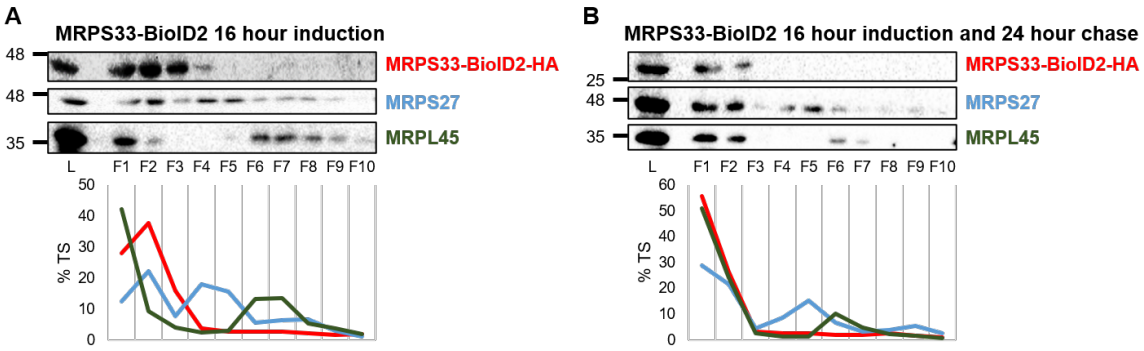

Figure 5.7: Integration of the MRPS33-BioID2-HA fusion protein into the mitoribosome. Cell lysates (L, 700 µg) from HEK293T stably transfected with MRPS33-BioID2-HA from 4 conditions were separated on 10-30% sucrose gradient by ultracentrifugation. Cells were **A:** induced for 16 hrs (50 ng/ml doxycycline) with no chase or **B:** chased for 24 hrs. Fractions (100µl, F1-F10) were analysed in parallel SDS-PAGE, immunodetected with antibodies to HA (46.8kDa), MRPS27 (47.6kDa), and MRPL45 (35.3kDa).

5.3.8 Integration of MRPS35-BioID2-HA into the mitoribosome

MRPS35 has a region that lines the mRNA tunnel, and its C-terminus is located distal to the entry site. Using Pymol, I found that the C-terminus is located on the exterior of the mitoribosome, which in theory could allow the addition of the BioID2-HA tag without disturbing the mt-SSU formation. The induction, cell preparation, and sucrose gradients for MRPS35 were carried out by Niamh Southern, an undergraduate student under my supervision (Figure 5.8). Following a 16-hour induction (Figure 5.7 A), a small amount of MRPS35 was found to be present in fractions 4 and 5, however, the distribution of the protein does not resemble the mt-SSU marker MRPS27. When induction was followed by a 24-hour chase (Figure 5.7 B), the distribution of protein did not change. Although a small fraction of the signal was found in fractions F5/6, in neither of the conditions tested did the fusion protein signal resemble the distribution of the mt-SSU protein marker, MRPS27. MRPS35-BioID2-HA, therefore, was not taken forward for further investigation.

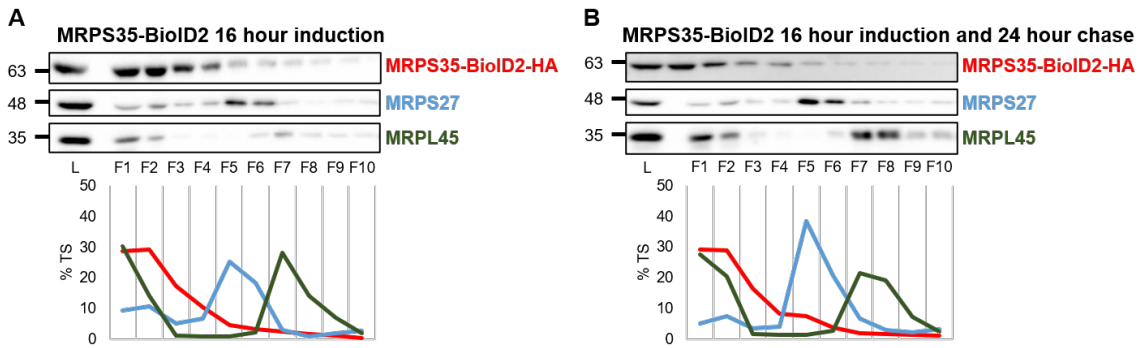

Figure 5.8: Integration of the MRPS35-BioID2-HA fusion protein into the mitoribosome. Cell lysates (L, 700 µg) from HEK293T stably transfected with MRPS35-BioID2-HA from 4 conditions were separated on 10-30% sucrose gradient by ultracentrifugation. Cells were **A:** induced for 16 hrs (50 ng/ml doxycycline) with no chase or **B:** chased for 24 hrs. Fractions (100µl, F1-F10) were analysed in parallel SDS-PAGE, immunodetected with antibodies to HA (64.6kDa), MRPS27 (47.6kDa), and MRPL45 (35.3kDa).

5.3.9 Submitochondrial localisation of COX8MTS-BioID2-HA and SLIRP-BioID2-HA

The doxycycline-induced BioID2-HA variants of COX8-MTS and SLIRP are not predicted to integrate into the mitochondrial ribosome. The COX8 targeting sequence positioned in-frame at the N-terminus of the BioID2-HA protein should cause the expressed protein to be shuttled into the mitochondrial matrix, followed by cleavage of the targeting pre-sequence. In accordance with the biological role of SLIRP, namely the binding of processed mt-RNA, I predicted SLIRP-BioID2-HA would also be in the mitochondrial matrix, proximal to the mitochondrial ribosome and the RNA granules. As these two proteins do not integrate into the mitoribosome, sucrose gradient analysis would not provide information to confirm their presence in the mitochondrial matrix. Therefore, in addition to sucrose gradient analysis, mitochondria from cells induced with tetracycline (1µl/ml) for 3 days were isolated and fractionated (5.2.4) to determine sub-mitochondrial localisation (Figure 5.9 A). The samples generated were then analysed by western blotting and immunodetection. (Figure 5.9 B). The following protein markers for mitochondrial compartments were used: TOM20, an outer membrane protein; Apoptosis-Inducing Factor (AIF), an inner membrane-bound protein; MRPS26, a MRP and matrix-localised protein. This was used to confirm that the faster migrating lower species of SLIRP-BioID2-HA was localised to the matrix as the lower species appeared in all 4 samples (Figure 5.9 C).

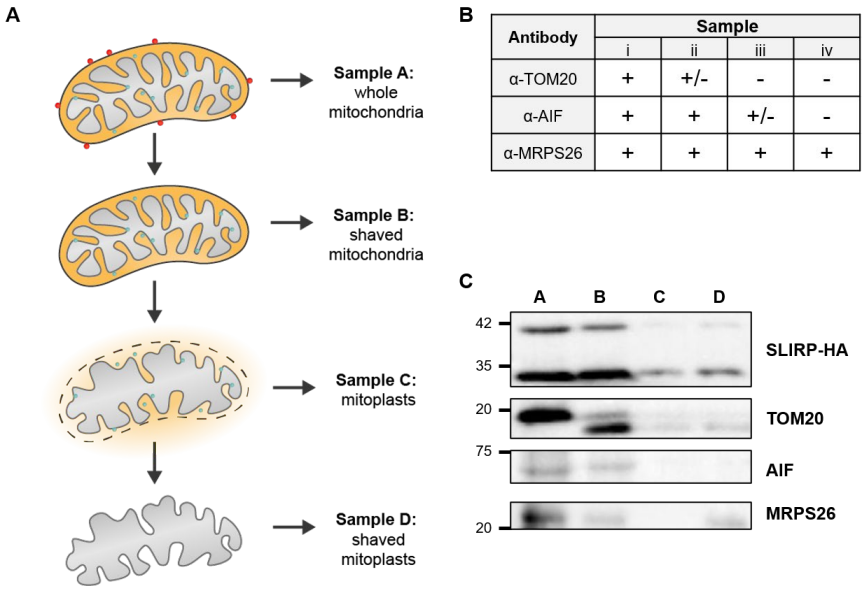

Figure 5.9: SLIRP is localised to the mitochondrial matrix. Mitochondria were isolated from HEK293T SLIRP-BioID2-HA cells induced for 3 days (tetracycline 1µg/ml) and fractionated to isolate submitochondrial compartments. **A:** A schematic representing the fractionation process and samples generated. **B:** Marker antibodies for characteristic proteins of each compartment and whether they are expected in each sample. **C:** SLIRP is localised to the mitochondrial matrix as it appears across all four samples.

The matrix localisation of COX8MTS-BioID2 was confirmed by this method by Ana-Madalina Ion within the Lightowlers lab (data not shown).

The migration of SLIRP-BioID2-HA across a 10-30% sucrose gradient was investigated after a 16-hour induction, period, with and without a 24-hour chase (Figure 5.10). The lower species of the fusion protein was present beneath the signal for MRPL45. When the fusion protein is induced for 16 hours (Figure 5.10 A), there was a clear HA signal visible in fractions 1-3, representing proteins that are not incorporated within multiprotein complexes. This distribution did not significantly change when the when the induction was chased for 24 hours (Figure 5.10 B), although there was a weak signal present in fraction 4. In both conditions, the lower band of the expressed fusion protein did not migrate differently to the larger protein. The distribution was confined to the early fractions which suggested that SLIRP-BioID2-HA did not integrate into the mitoribosome.

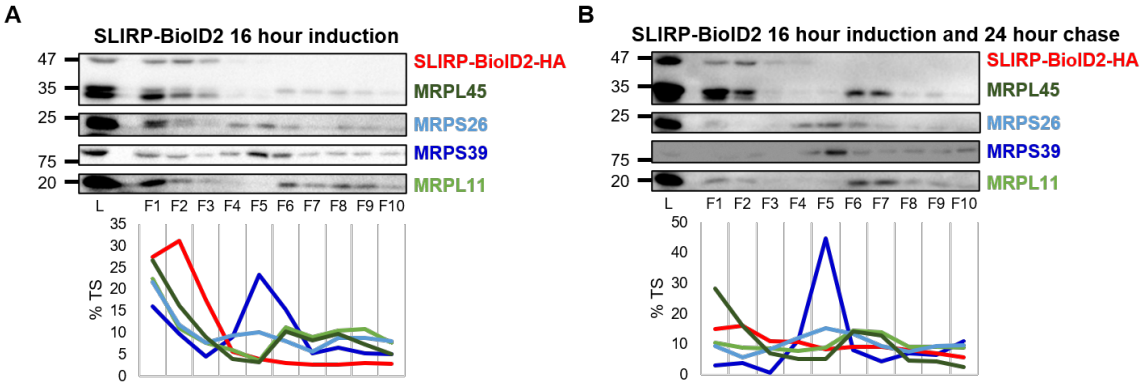

Figure 5.10: Integration of the MRPS24-BioID2-HA fusion protein into the mitoribosome. Cell lysates (L, 700 µg) from HEK293T stably transfected with SLIRP-BioID2-HA from 4 conditions were separated on 10-30% sucrose gradient by ultracentrifugation. Cells were **A:** induced for 16 hrs (50 ng/ml doxycycline) with no chase or **B:** chased for 24 hrs. Fractions (100µl, F1-F10) were analysed in parallel SDS-PAGE, immunodetected with antibodies to HA (predicted 40.4kDa), MRPS39 (78.6kDa), MRPS26 (19.2kDa), MRPL45 (35.3kDa) and MRPL11 (20.6 kDa).

It was necessary to confirm the location of COX8MTS-BioID2-HA to ensure it would act as a suitable control for the experiments designed to identify proteins putatively delivering mt-mRNA to the mitoribosome. In addition to location, it was also important to determine that COX8MTS-BioID2-HA did not behave as a mt-SSU protein. This was done by analysis of sucrose gradients after a 16hour induction period with or without a 24-hour chase (Figure 5.11). The observed distribution was similar to the SLIRP fusion protein; in both gradients the greatest percentage of the signal was present in fraction 1 and 2. A weak HA signal was visible in fractions 3 and 4 following the 24-hour chase, however the distribution did not resemble that of a protein that is part of the mitoribosome. The fusion protein is not expected to become part of any protein complexes in the mitochondria. The sucrose gradient data presented here shows that the induced protein was found primarily in the first two fraction, therefore suggesting it was not integrated into any complexes. COX8MTS-BioID2-HA is therefore a suitable negative control for the intended experiments.

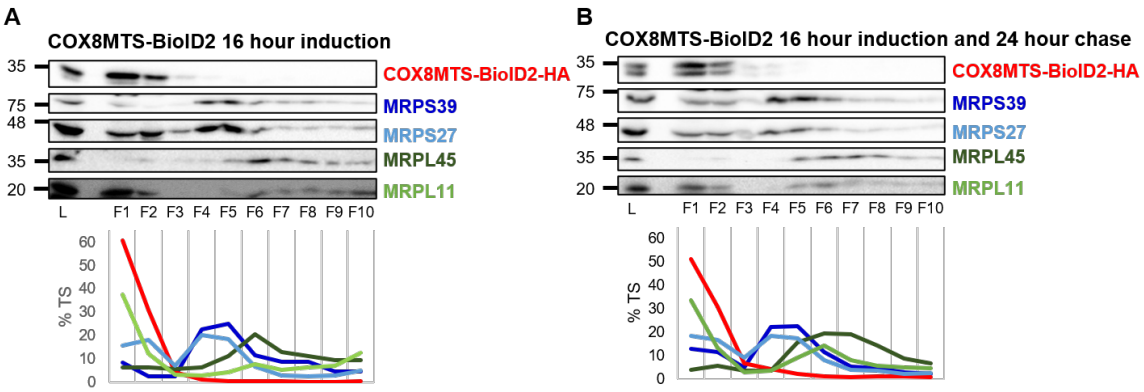

Figure 5.11: Sucrose gradient analysis of overexpressed COX8MTS-BioID2-HA. Cell lysates (L, 700 µg) from HEK293T stably transfected with MRPS35-BioID2-HA from 4 conditions were separated on 10-30% sucrose gradient by ultracentrifugation. Cells were **A:** induced for 16 hrs (50 ng/ml doxycycline) with no chase or **B:** chased for 24 hrs. Fractions (100µl, F1-F10) were analysed in parallel SDS-PAGE, immunodetected with antibodies to HA (31.1kDa), MRPS39 (78.6 kDa), MRPS26 (19.2 kDa), MRPL45 (35.3 kDa) and MRPL11 (20.6 kDa).

5.4 Discussion

My aim with this investigation was to determine the culture and induction conditions for subsequent biotinylation and streptavidin pull down experiments. Specifically, I wanted to find the optimal pulse and chase timings where induced fusion proteins became integrated into mitoribosomes at similar levels to the respective endogenous proteins, or endogenous mt-SSU proteins. As I am investigating which proteins are enriched at the mRNA entry site, it was therefore essential that I created an environment where the BioID protein was integrated into the monosome, close to the entry site. The BioID2-HA protein will promiscuously biotinylate proximal proteins, regardless of whether the fusion protein is or is not within the stable complex of the monosome. Signal from any fusion proteins that are not integrated into the monosome will not provide relevant biotinylated prey proteins and will be difficult to discern from specific signals. The pulse-chase experiment was designed to allow both integration of the fusion protein into the mitoribosome, and degradation of the unintegrated overexpressed protein. This experimental design allowed for biotin to be supplemented during the latter phase of the chase such that as much of the biotinylation by BioID2 as possible was occurring proximal to the entry site. In this chapter I have used the Flp-In TRex system to stably transfect HEK293T cells with sequences encoding each of the eight BioID2-HA fusion proteins (MRPS5, MRPS24, MRPS33, MRPS35, MRPS39, MRPS27, SLIRP and COX8MTS). Successful induction was confirmed by western blot and immunodetection of lysates from cells treated with tetracycline/ doxycycline. These eight bait proteins were selected for their proximity to the mitochondrial entry site, or for their abilities to act as controls for non-specific biotinylation by BioID2 in the mitochondria.

I have presented data that shows that two of these fusion proteins, MRPS27 and MRPS39, are integrated into the mitoribosomal small subunit following overexpression with doxycycline (50 µg/ml). In both these cases the optimal conditions for mitoribosome integration were determined to be after an induction period of 16 hours and a 24-hour chase period. I confirmed the localisation of SLIRP-BioID2-HA to be in the mitochondrial matrix, albeit the migrating band was smaller than the predicted construct. In addition, I showed that neither this fusion protein, nor COX8MTS-BioID2-HA, integrates into the mitoribosome. The MRPS27- and COX8MTS-BioID2-HA controls will be used to measure the background levels of biotinylation by BioID2 in the mitochondrial matrix. The validated fusion proteins were

available to be subjected to biotin supplementation during the chase period, promoting biotinylation of proximal proteins that my hypothesis predicts will be involved in mt-mRNA delivery. Streptavidin pulldown will be used to isolate these newly biotinylated proteins and their identity will be determined by mass spectrometry analysis (LC-MS-MS). Proteins which appear enriched at the mRNA entry site will be then investigated for possible roles within mitochondrial translation, initially using knockdown studies. These experiments will be presented in the next chapter.

Chapter 6:

Investigating mt-mRNA loading using BioID2-tagged mitoribosomal proteins

6.1 Introduction

In the preceding chapter, pulse-chase induction was used to determine optimal conditions for the integration of BioID2-tagged bait proteins into the mitochondrial ribosome. The sucrose gradient experiments confirmed the integration of MRPS39 and MRPS27 into the mitochondrial ribosome at levels similar to their respective endogenous proteins. The next step in this investigation of proteins proximal to the mRNA-entry site was the expression of these proteins, promotion of biotinylation, isolation of prey proteins, and mass spectrometry analysis of the isolated interactors.

The protocols for these procedures were heavily influenced by the formative paper on BioID2, (Kim et al., 2016). Cell culturing was completed in the conditions determined by the previous chapter, with an increase in the volume of cells cultured to provide adequate material for mass spectrometry (MS). To improve recovery of relevant data an additional mitochondrial isolation step was required for these sample preparations, as isolation of biotinylated proteins from the entire cell lysate would produce substantial background signal. This enrichment step was completed prior to isolation of prey protein by streptavidin-biotin pull down, and an intense washing process. I worked closely with the Newcastle University Laboratory for Biological Mass Spectrometry who provided guidance about sample preparations specific to the equipment and protocols they developed within their department. To increase the clarity of mass measurement, all proteins were cleaved into smaller peptides using a tryptic digest. These peptides were then ionised prior to mass spectrometry. Liquid Chromatography- Mass Spectrometry/Mass Spectrometry (LC-MS/MS) was used in all cases. Tandem ion trap mass spectrometry was utilised to separate proteins by their mass-to-charge ratio (m/z) to a selected set of ions, which are then fragmented and analysed again by MS to generate mass spectra.

During the course of this research, literature emerged which analysed the interactors of mitochondrial proteins using the BioID2 system (Antonicka et al., 2020; Liyanage et al., 2017; Silva et al., 2018). In only Silvia et al, did the author complete a crude mitochondrial preparation prior to mass spectrometry analysis. As my bait targets are translated in the cytosol, background was a key concern. I therefore opted to complete a mitochondrial isolation step prior to analysis.

6.2 Methods

6.2.1 Cell Culture for BioID2 experiments

Inducible clonal cell lines were cultured in three T300 flasks, or two T500 triple layer flasks, until they reached ~60% confluency. BioID2-protein expression was induced with 50 ng/ml doxycycline for 16 hours. Cells were pelleted and the flasks washed with PBS twice to remove doxycycline from the culture vessels. Cells were resuspended in culture medium and returned to their flask. 16 hours prior to harvest, half of the clonal lines were supplemented with 50 µM Biotin (B4501, Sigma Aldrich). Cells were harvested into a 50 ml tube, washed in cold 1xPBS centrifuged at 280g to pellet the cells.

6.2.2 Crude Mitochondrial Preparation

All buffers were stored at 4 ºC without DTT, BSA or protease inhibitors; these were added to solutions on the day. Cell pellets were weighed (1 g = 0.8 ml volume) before resuspending in 9 volumes of cold hypotonic buffer (20 mM HEPES pH 8.0, 5mM K Cl, 1.5 mM $MgCl_2$, 2 mM DTT, 1 mg/ml BSA, 1x Protease inhibitor cocktail) and stored on ice for 10 minutes. The resuspended cells were transferred to the appropriate size Dounce homogenizer and homogenised to release the mitochondria (10 strokes). The solution was transferred to a clean 15 ml tube and, for every 3 ml of volume, 2 ml of strong MSH buffer (5.25 mM mannitol, 1.75 mM sucrose, 20 mM HEPES pH 8.0, 10 mM EDTA, 2 mM DTT, 1x Protease inhibitor cocktail). Cell debris and nuclei were pelleted by centrifugation at 1600 g for 10 minutes, 4ºC. The supernatant was transferred to a fresh tube and centrifuged again with the same conditions. The supernatant was collected and centrifuged at 10000 g for 10 minutes, 4ºC to pellet the mitochondria. The supernatant was discarded carefully, and the pellet washed by resuspension in cold MSH buffer (210 mM mannitol, 70 mM sucrose, 20 mM HEPES pH 8.0, 2mM EDT, 2mM DTT, 1x Protease inhibitor cocktail). Centrifugation at 10000g for 10 minutes, 4ºC and washing in 1xMSH was repeated twice before the supernatant was discarded, and the pellet stored at -80 ºC.

6.2.3 Streptavidin-Biotin Pulldown

The mitochondrial pellet was resuspended in 1 ml of cold lysis buffer (50 mM Tris, 500 mM NaCl, 0.2% SDS, 1 mM DTT, 1x Protease inhibitor cocktail), transferred to a 2 ml tube, and placed in a tube rotator for 10 minutes at room temperature. 100 µl of 20% Triton-X 100 and 900 µl of cold 50 mM Tris-Cl pH 7.4 were added to the resuspended pellet and mixed by inversion. The tube was centrifuged at 16500 g for 10 minutes, 4º C. At this stage, an aliquot

of the supernatant (sample) was removed for future western blotting and immunodetection and stored at 20 ºC.

During centrifugation, streptavidin beads (50 µl per sample, Dynabeads™ MyOne™ Streptavidin C1, Invitrogen 65001) were resuspended by vortexing, then mixed 50:175 ml in the binding buffer (1:1 room temperature Lysis buffer and room temperature 50 mM Tris-Cl pH 7.4) and allowed to equilibrate at room temperature for 5 minutes. Pipette tips were cut and autoclaved in preparation for all steps wherein beads were handled. After equilibration, the tubes were placed in a magnetic separator for 5 minutes and the binding buffer removed. The supernatant was added to the beads and placed in a tube rotator at 4º C overnight.

After incubation overnight, the tubes containing beads and sample were placed into a magnetic separator for 5 minutes. The supernatant was removed and stored as the "unbound proteins". Beads were resuspended in 1.5 ml of wash buffer 1 (2% SDS in nH_2O) and placed in a tube rotator for 8 minutes at room temperature. Tubes were placed in a magnetic separator for 5 minutes and the supernatant saved as "Wash 1". The wash rotation and separation were repeated once more with wash buffer 1, and twice with resuspension with wash buffer 2 (0.1% Deoxycholic acid, 1mM EDTA, 1% Triton-X 100, 50 mM HEPES). The was rotation and magnetic separation were repeated 7 times using 50 mM Tris-Cl pH 7.4.

6.2.4 Mass Spectrometry: sample preparation, running, and analysis

A final wash was completed using 50 mM ammonium bicarbonate followed by magnetic separation for 5 minutes. The supernatant was removed, and the beads resuspended in 50 µl 50 mM ammonium bicarbonate. Proteins attached to the beads were reduced by the addition of 1 mM TCEP (final concentration) and incubation at room temperature for 30 minutes. Chloroacetamide (5 mM final concentration) was added to the solution and it was incubated for 30 minutes at room temperature in the dark. Trypsin (5 ng/µl, final concentration) was added to the sample and it was incubated at 37 ºC overnight. Tubes were pulsed briefly in the microcentrifuge to pellet the beads prior to the addition of 2 µl formic acid to ionise peptides for mass spectrometry. At this stage, all samples were analysed by the Newcastle University Laboratory for Biological Mass Spectrometry. Specific thanks to Dr Anetta Svitorka Hartlova, Dr Frederic Lamoliatte and Dr Akshada Gajbhiye, who completed the mass spectrometry and provided guidance.

Peptides were analysed by nanoflow-LC-MS/MS using a Fusion Lumos Tribrid Orbitrap mass spectrometer (Thermo Scientific) coupled to a Dionex Ultimate 3000. Samples were injected

on a 300 µm ID × 5 mm trap (Acclaim PepMap 100 C18 LC, #160454) and separated on a 75 µm × 50 cm nano LC column (EASY-Spray LC Columns #ES803). All solvents used were HPLC or LC-MS Grade (Millipore). Peptides were loaded for 5 minutes at 10 µL/min using 0.1% TFA, 2% Acetonitrile in Water. The column was conditioned using 97% Buffer A (0.1% FA, 3% DMSO in Water) and the separation was performed on a linear gradient from 3 to 35% Buffer B (0.1% FA, 3% DMSO, 20% Water in Acetonitrile), over 99 minutes at 300 nL/min. The column was then washed with 90% Buffer B for 5 minutes and equilibrated 10 minutes with 97% Buffer A in preparation for the next analysis. Full MS scans were acquired from m/z 400 to m/z 1600 at resolution 120000 at m/z 200, with a target AGC of 4E5 and a maximum injection time of 50 ms. MS/MS scans were acquired in HCD mode with a normalized collision energy of 30 and analysed in the ion trap in Rapid mode using a Top 3s method, with a target AGC of 1E4 and a maximum injection time of 45 ms. The MS/MS triggering threshold was set at 5E3 and the dynamic exclusion of previously acquired precursor was enabled for 35 s with a tolerance of +/-10 ppm. Peptides were searched against Uniprot Swisprot Database containing isoforms (released 16th of October 2018) to annotate the peptides.

Data analysis was completed using Perseus v1.6.15.0 (MaxQuant) and graphs were generated on GraphPad Prism 8. The data was subjected to filtering against forward and reverse combinations of this database to identify the false positive identification rate. The remaining proteins were filtered further against databases of common contaminants (BSA, FBS, Keratin etc) and protein modifications that are commonly produced during MS sample preparation. Proteins only identified by a single peptide were also filtered out as the false identification error for 1 peptide is 1%. Therefore, a peptide identified by 1 peptide has 1% error, and one identified by two peptides has a 0.01% error. LFQ (label-free quantitation) intensity data was then transformed (Log_2) to provide a normal distribution across protein intensities. Where imputation to replace missing values was used, this was done column-wise; the width of the Gaussian distribution was 0.3 relative to the standard deviation and the downshift was 1.8 of the standard deviation. All further thresholding and data manipulation are described in the results chapter as they are variable based on MS output.

6.2.5 Silver Staining

Protein concentration was estimated by Bradford Assay (2.4.2) and 1µg was electrophoresed through 12% polyacrylamide gels (2.4.6). The gel was washed for 1 hour in 50% methanol. During this time, the staining solution was prepared by adding of 0.2 g/mL silver nitrate solution (Sigma, S6506) dropwise to a flask with a magnetic stirrer that contained distilled

water, 0.075% NaOH and 1.4% NH_4OH, until the solution lost its transparency. The gel was then incubated with the staining solution for 15 minutes at room temperature and then washed with distilled water 3 times for 5 minutes. The developer solution (0.005% Citric acid (Sigma C2404) 0.05% Formaldehyde) was added to the gel until the desired intensity was achieved. The solution was discarded and replaced with the stop solution (45% methanol, 10% acetic acid). The gel was rinsed in distilled water and imaged on the Chemi-Doc™ MP Imaging System (Bio-Rad®) using the Image Lab™ Software.

6.2.6 siRNA Transfection

U2OS cells were transfected with siRNA in 6 well plates or T25 cm^2 flasks for 3 days (reverse transfection), 5 days (reverse transfection, then forward transfection on day 3), or 6 days (reverse transfection, then forward transfection on day 3). The volumes of Opti-MEM®+GlutaMax™ (Gibco 51985), Lipofectamine RNAiMAX (Invitrogen 13778030), and siRNA (Ambion, Table 6.1) were the same for transfection of both 6 well plates and T25cm^2 flasks. Where used, confluence monitoring and imaging was completed using the IncuCyte® ZOOM System. This system monitors each well of a 6-well plate by taking 12 mages per well, every three hours. Using algorithms set up for different cell morphologies, these images are used to generate confluence estimations at each of these time points.

Table 6.1: DNA sequences of small interfering RNA (siRNA)

Target	Referred to as	Company	siRNA ID	Sequence 5'-3' Sense
PHB	PHB siRNA 1	Ambion	s10424	CGU GGG UAC AGA AAC CAA Utt
	PHB siRNA 2	Ambion	s10425	GCA UCG GAG AGG ACU AUG Att
	PHB siRNA 3	Ambion	s10426	UCA CAA CUG AGA UCC UCA Att
PHB2	PHB2 siRNA 1	Ambion	s22343	ACC UUG UGC UGA ACC UAC Att

Reverse transfection: Cells were harvested, counted, and diluted such that cells were seed at the following numbers: 200,000 in a 6 well plate for a 3-day incubation, 100,000 in a 6 well plate for a 5- or 6-day incubation, 400,000 in a T25 cm^2 flask for a 3-day incubation, and 250,000 in a T25 cm^2 flask for a 5-day incubation. Pre-warmed 250µl Opti-MEM®+GlutaMax™ was added to a 1.5 ml tube before 2 µl Lipofectamine RNAiMAX and 1.5 µl siRNA were added, mixed, and incubated at room temperature for 20 minutes. This solution was added dropwise to the 6-well plates/T25 cm^2 flask containing cells and media (1.5 ml 6-well plate, 3 ml T25 cm^2). All vessels were incubated for 3 days at 37°C with humidified 5% CO_2.

Forward transfection: This method was used on cells adhered to cell culture vessels to extend the siRNA incubation time. Pre-warmed 250µl Opti-MEM®+GlutaMax™ was added to a 1.5 ml tube before 2 µl Lipofectamine RNAiMAX and 1.5 µl siRNA were added, mixed, and incubated at room temperature for 20 minutes. The culture medium on the cells was aspirated and replaced with the same volume of pre-warmed DMEM. The siRNA solution was added dropwise to the cell culture vessels. All vessels were incubated at 37°C with humidified 5% CO_2 until harvesting.

6.2.7 Northern blotting

Northern blotting was performed by Dr. Richard Temperley within my host laboratory. Northern blots were conducted as described in (Chrzanowska-Lightowlers et al., 1994; Temperley et al., 2003). In brief, aliquots of RNA (5 µg) were electrophoresed through agarose gels (1.2%) under denaturing conditions and transferred to Genescreen Plus membrane (NEN duPont) following the recommendations of the manufacturer. The membrane was blocked prior to probing with random hexamer labelled DNA fragments corresponding to *MTATP6* (nt 8563–8989), *MTCO3* (nt 9440–9841) and *MTND1* (nt 3384–4250).

6.3 Results

6.3.1 Run 1: MRPS39 and MRPS27

The initial mass spectrometry experiment analysed 3 biological repeats of BioID2-HA-MRPS39 +/- biotin and 3 repeats of BioID2-HA-MRPS27 +/- biotin. For each condition, cells were cultured in three T300 cm^2 flasks. Expression of the BioID2 construct was induced with 50 ng/ml doxycycline for 16 hours, followed by a 24-hour chase. For the last 16 hours of this chase, 50 µM Biotin was present in the cell culture media. This concentration was consistently used in BioID publications (Antonicka et al., 2020; Kim et al., 2016). Cells were harvested prior to crude isolation of the mitochondria, and streptavidin-biotin pull down procedure. I was limited technologically by the equipment within my host laboratory and could only complete sample preparation for 6 samples at one time. The protocols for cell harvesting, mitochondrial isolation, streptavidin pull down and tryptic digestion for the first six samples (S27+B 1, S27+B 2, S27-B 1, S27-B 2, S39+B 1, and S39-B 1) were carried out the day before the protocols for the remaining samples (S27+B 3, S27-B 3, S39+B 2, S39+B 3, S39-B 2, and S39-B 3). This preparation difference generated a large error that is visible when histograms of the counts of protein intensities in each sample are visualised (Figure 6.1).

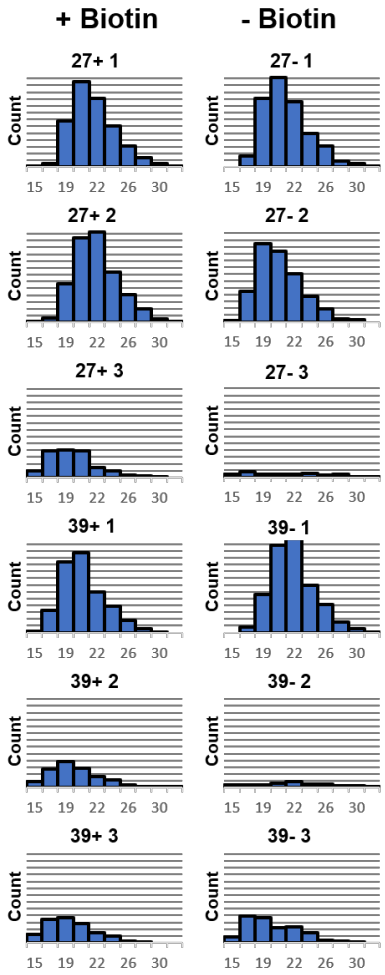

Figure 6.1: Variable protein counts of streptavidin-biotin pulldown eluates. MRPS27-BioID2-HA or MRPS39-BioID2-HA cells induced (50 ng/ml doxycycline, 16 hours) and chased (24-hours), supplemented with biotin (50 µM) for final 16 hours. Triplicate streptavidin-biotin pulldown eluates were digested by trypsin and analysed by nanoflow-LC-MS/MS. Histograms visualise protein counts for increasing LFQ intensities (x-axis).

These histograms were generated after filtering of the samples for contaminants, peptides identified in a reverse protein library, and proteins identified by only 1 peptide. The intensity data was then transformed by $\log_2(x)$ to create a normal distribution. There were far fewer proteins identified in the samples processed on the second day compared to the first, and where there are protein intensities, they were much lower. There are many steps in the streptavidin-biotin pulldown protocol in which error and loss of proteins could occur; these include inconsistences during mitochondrial isolation and in the pull down and wash procedures, or the inherent variability of tryptic digests carried out on different days. This inconsistency of intensity levels may have led to the loss of proteins which would otherwise be enriched in the MRPS39+Biotin preparations.

To investigate if any differences in proteins counts could be identified prior to mass spectrometry analysis, I used a silver stain to analyse the pulldown eluate (Figure 6.2). Protein concentrations were estimated by Bradford assay and 1 µg of each eluate was run across two 12% SDS-PAGE gels. There was no clear correlation between the protein counts visible in Figure 6.2 and the intensities of signals in the lanes in Figure 6.1.

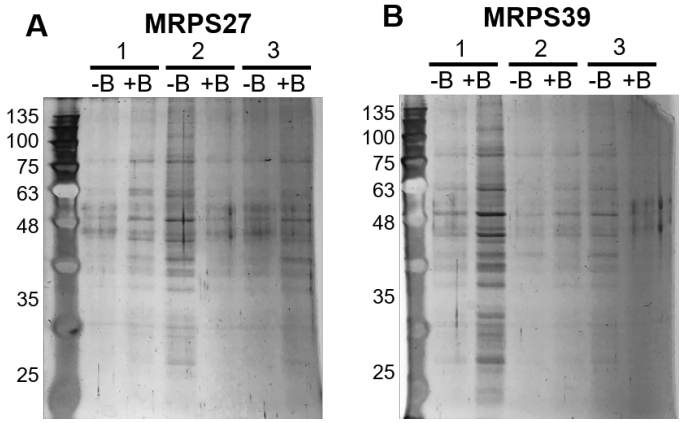

Figure 6.2: Streptavdin-biotin pull down eluate from MRPS27 and MRPS39. Silver staining of 12% SDS-PAGE gels of **A:** MRPS27-BioID2-HA and **B:** MRPS39-BioID2-HA samples (1 µg) from streptavidin-biotin pull down isolation. Cells were induced (50 ng/ml doxycycline) for 16 hours followed by a 24-hour chase, the final 16 hours of which the media was supplemented with biotin (50 µM).

The strongest signals are in lanes MRPS27+B 2 and MRPS39+B 1 in each gel. These are both runs with high protein counts. There was not enough eluate material left to attempt this assay again. The reasoning for this assay was to determine if I could visualise different protein counts prior to mass spectrometry, saving valuable resources and time. In addition, I could allow a crude analysis of any clear enriched proteins visible in the eluate of tagged MRPS compared to controls. It may be that the efficacy of this assay was hindered by inaccurate estimations of protein concentrations, or the freeze-thawing of the samples.

To identify any proteins enriched in the MRPS39+ Biotin preparations, I first filtered the results by the presence of two valid intensity values within the MRPS27+/- biotin replicates, and one valid value within the MRPS39 +/- biotin replicates. This reduced the number of identified proteins from 1078 to 619 proteins. As there was only 1 preparation in each MRPS39 experiment with high proteins counts at each intensity, filtering by two valid valued would have resulted in less than 300 identified proteins. Missing values across datasets in mass spectrometry are not unusual due to variation in sample preparations (Tyanova et al., 2016). Downstream analysis requires a complete set of data; therefore, Perseus supports imputation of these missing values by drawing random numbers from a normal distribution which

simulates expression below the detection limit. This process uses the standard deviation of the available data in the matrix to calculate a downshifted value for missing values. Imputation of missing values is standard procedure in the literature; however it is generally used for larger datasets than the matrix generated from this experiment (Tyanova et al., 2016). The average intensity across the replicates was calculated and visualised as scatter plots pre- and post-filtering by protein presence in Human Mitocarta 2.0 (Broad Institute) (Figure 6.3 A-B).

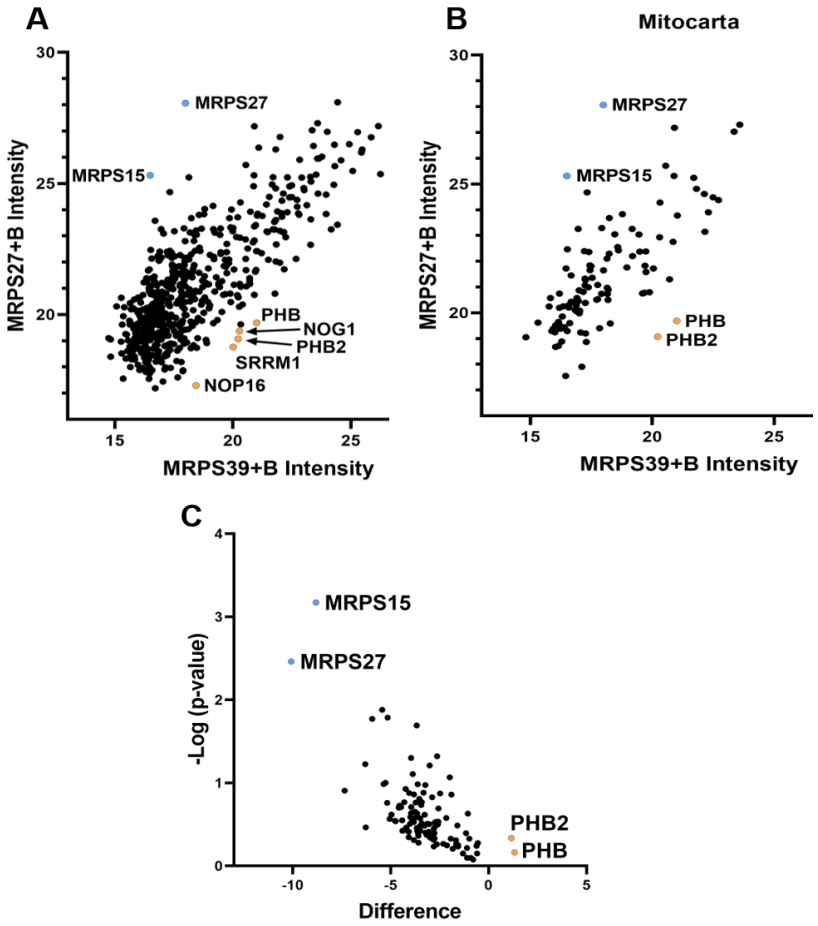

Figure 6.3: Pairwise comparison of identified preys by BioID2 analysis of MRPS27 and MRPS39. Average LFQ intensities (n=3) from **A:** all preys and **B:** filtered by proteins present in Mitocarta 3.0. **C:** Two-sample student's T-test was applied (Perseus) and the -Log T-test p-value was plotted against the difference to generate a volcano plot. Proteins found at the extremities have been labelled; blue for MRPS27 prey, and orange for MRPS39 prey.

The intensity data for all MRPS27+biotin and MRPS39+biotin replicates were Grouped in Perseus and analysed by a two-sample student's T-test using the p-value (0.05) to determine significance and plotted as a volcano plot (Figure 6.3 C). This analysis highlighted prohibitin (PHB), prohibitin 2 (PHB2), CHD4, NOG1, SSRM1 and NOP16 as proteins that were enriched in the MRPS39+biotin preparations.

When this list was filtered to those present in Mitocarta2.0, only PHB and PHB2 remained as proteins of interest. Considering the lower overall intensities for all proteins in the MRPS39 preparations, as seen by the histograms in Figure 6.1, it is strong evidence that PHB and PHB2 are enriched around MRPS39 across these repeats. These intensity scores were evaluated using a two-sample student's T-test (Figure 6.3 C). PHB and PHB2 were the only proteins identified as having a significantly higher intensity in the MRPS39+biotin preparations than in the control.

This analysis pipeline, however, removed some proteins I expected to find proximal to MRPS39, such as MRPS5, MRPS24, and self-biotinylated MRPS39. As MRPS27-Biotin did not also pull down these proteins, they were removed during the filtering process. Witnessing this, I completed an alternative analysis method wherein I only filtered for valid values in MRPS39 preparations. The missing intensities for those proteins not identified in MRPS27 preparations were imputed using Perseus. I completed this analysis with the same stringency as before, filtering out proteins without 1 valid value across the MRPS39+Biotin preparations and 1 valid value across the MRPS39-Biotin preparations (Figure 6.4).

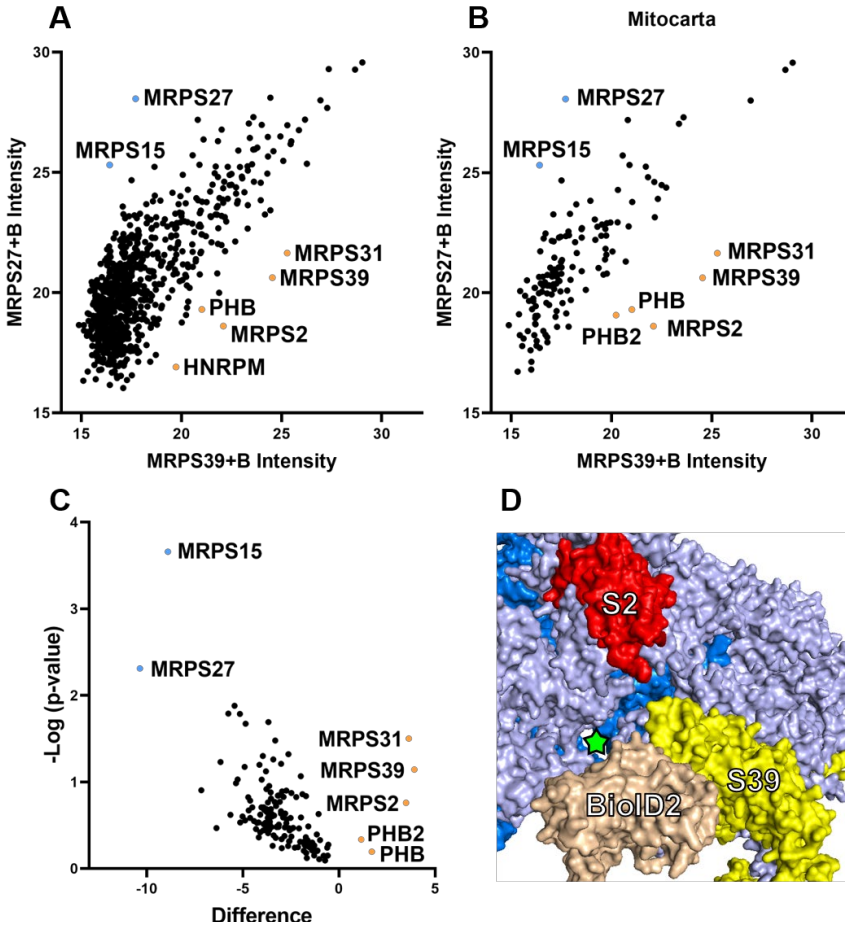

Figure 6.4: Pairwise comparison of identified preys by BioID2 analysis of MRPS27 and MRPS39 using alternative filtering. Average LFQ intensities (n=3) from **A:** all preys and **B:** filtered by proteins present in Mitocarta 3.0. **C:** Two-sample student's T-test was applied (Perseus) and the -Log T-test p-value was plotted against the difference to generate a volcano plot. Proteins found at the extremities have been labelled; blue for MRPS27 prey, and orange for MRPS39 prey. **D:** The structures of the human mitoribosome (PDB 39JM) and biotin ligase (BioID2) from Aquifex aeolicus (PDB 2EAY) manipulated with Pymol. In ribosomal structures small subunit (SSU) proteins (light blue) and 12S rRNA (dark blue) are visible. MRPS39 (yellow) and MRPS2 (red) are visible to illustrate possible orientation of BioID2.

This reduced the number of identified proteins from 1078 to 769 due to the low intensity counts in four MRPS39 preparations. Missing values across all columns were imputed by the software and I plotted the average values from all replicates in scatter plots (Figure 6.4 A), including after filtering for presence in Mitocarta 2.0 (Figure 6.4 B). I repeated the two-sample student's T-test (Figure 6.4 C). As before, this plot is overwhelmingly stronger for proteins in the MRPS27+biotin category as the intensity strengths were much stronger in these preparations. In addition to observing significant enrichment of PHB and PHB2, this analysis also identified MRPS31, MRPS2 and likely self-biotinylated MRPS39. These interactions can be explained by the kinetics of mitoribosome assembly, and the structure of the assembled mitoribosome. In

early assembly of the SSU, MRPS39 and MRPS31 are associated in a pre-complex (Bogenhagen et al., 2018). In addition, in the assembled structure, MRPS2 is found directly adjacent to the ligase modelled position of MRPS39-BioID2-HA (Figure 6.4 D). Similarly, MRPS15 is modelled adjacent to the MRPS27-BioID2-HA fusion protein. The positive identification of these proximal proteins further validates the integration of the fusion proteins into the mitoribosome.

6.3.2 Run 2: MRPS39 and MRPS27 Replicate

The main limitation with the first mass spectrometry run was inconsistency in the protein counts across preparations. To increase the validity of the data previously acquired, I repeated this experiment. For these experiments, I adapted my use of equipment to allow all preparations to be on the same day, reducing a potential source of variability. Cells were cultured in two T500 cm^2 flasks for each experiment prior to pulse induction, chasing, and supplementation with biotin as previously described. Cells were harvested and prepared for mass spectrometry as described in 6.2.1-6.2.4). Histograms of the proteins counts across different intensities were generated as in Figure 6.1, after basic filtering and log transformation of the raw intensity data (Figure 6.5).

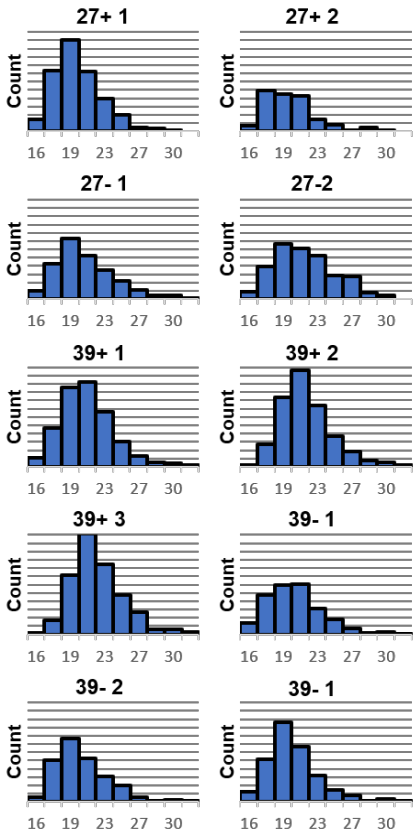

Figure 6.5: Protein counts of streptavidin-biotin pulldown eluates. MRPS27-BioID2-HA or MRPS39-BioID2-HA cells induced (50 ng/ml doxycycline, 16 hours) and chased for 24-hours, supplemented with biotin (50 µM) for final 16 hours. Streptavidin-biotin pulldown eluates were digested by trypsin and analysed by nanoflow-LC-MS/MS. Histograms visualise protein counts (y-axis) for increasing LFQ intensities (x-axis).

There is less variation across all samples, however the MRPS27+Biotin 2 preparation clearly had much lower intensities and fewer protein counts. As discussed earlier, this could be due to errors throughout the multi-step protocols prior to mass spectrometry analysis. There were no visible cues to suggest lower protein levels during the process, for example the mitochondrial pellet after crude isolation was similar in size to the other preparations. In this run, only two MRPS27+/-Biotin preparations were completed due to time constraints of running additional samples. The data was processed in Perseus by filtering for at least 1 valid value in MRPS39+Biotin and MRPS39-Biotin groups. This resulted in reducing the matrix from 425 to 275 identified proteins. Missing values across all columns were imputed and average intensity values were plotted in a scatter plot Figure 6.6 A.

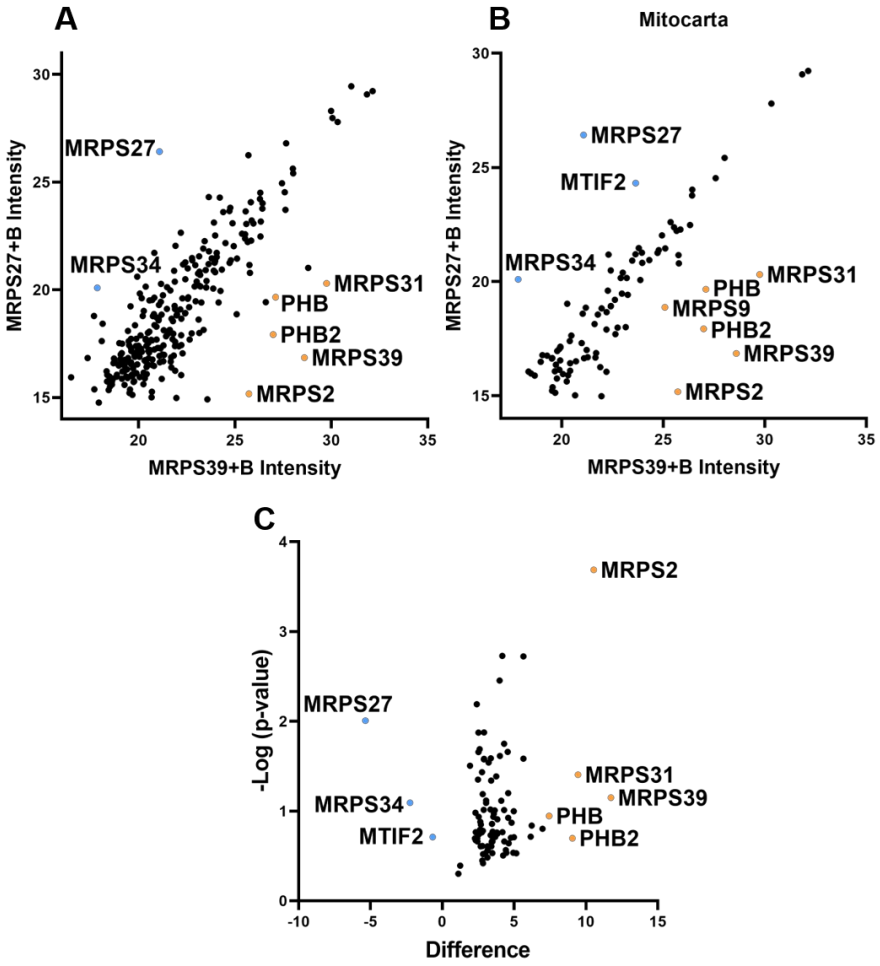

Figure 6.6: Pairwise comparison of identified preys by BioID2 analysis of MRPS27 and MRPS39. Average LFQ intensities (n=3) from **A:** all preys and **B:** filtered by proteins present in Mitocarta 3.0. **C:** Two-sample student's T-test was applied (Perseus) and the -Log T-test p-value was plotted against the difference to generate a volcano plot. Proteins found at the extremities have been labelled; blue for MRPS27 prey, and orange for MRPS39 prey.

The dataset was them filtered by presence in Mitocarta 2.0 to further visualise proteins enriched in either the MRPS27 or MRPS39 +Biotin preparations (Figure 6.6 B). The preys remained consistent between the initial run and this biological repeat; MRPS2, MRPS31, PHB, PHB2 and self-biotinylated MRPS39 identified as possible interactors with MRPS39-BioID2-HA. A Welch's t-test was employed to interrogate the data as there were unequal sample sizes across the MRPS27 and MRP39 input samples. The difference and -log(p-value) were plotted against each other to generate a volcano plot, visualising hits. It is not surprising that most proteins fall on the MRPS39-enrichment side of the plot in this run. Owing to the filtering process, there were more missing values in the MRPS27 columns, therefore more values were imputed, and

these imputed values will inherently be lower than those generated during mass spectrometry analysis.

In this replicate run, MRPS34 and MTIF2 are distinctly enriched in the MRPS27 pulldown samples (Figure 6.6 C). MRPS34 has been shown to form an early pre-complex with MRPS27 as part of the assembly of the mt-SSU (Bogenhagen et al., 2018). Recent cryo-EM research has revealed the presence of MTIF2 in mitochondrial-pre-initiation complexes within the mitoribosome (Khawaja et al., 2020). This structure reveals MTIF2 in close proximity to the body of the mt-SSU within the pre-initiation complex, distal to the mt-mRNA entry tunnel. In accord with the previous MS run, MRPS31 and MRPS2 were identified as biotinylated interactors with MRPS39-BioID-HA. MRPS9 was also identified in this experiment, supporting relevant literature on the subject of pre-complex assembly scheme for the SSU (Bogenhagen et al., 2018). MRPS31, MRPS39 and MRPS9 were all found to be associated prior to SSU super-complex formation. The most noteworthy interactors are PHB and PHB2, which are known to have mitochondrial localisation.

PHB and PHB2 are two homologous proteins which assemble into membrane scaffolding ring complexes (~1 MDa), formed of PHB/PHB2 heterodimers (Nijtmans et al., 2000). PHB1 and PHB2 have molecular weights of 32 and 34 kDa, respectively. They are ubiquitously expressed proteins that are present in across the mitochondria, cytosol, and the nucleus of cells, and their function is dependent on their cellular localisation (Merkwirth and Langer, 2009; Mitsopoulos et al., 2017; Thuaud et al., 2013). In the mitochondria, PHBs have been implicated in multiple mitochondrial processes including biogenesis, network morphology, and OXPHOS homeostasis (Bavelloni et al., 2015; Nijtmans et al., 2000; Signorile et al., 2019). The PHB heterodimer has been found to physically interact with components of OXPHOS machinery within the IMM, resulting in the stabilisation of mitochondrially-encoded respiratory chain subunits, specifically COXII (Nijtmans et al., 2000). Sucrose gradient analysis of PHB2 has shown that it does not migrate in the same pattern as the mitoribosome, however, PHB2 was present in the same fractions as the mt-SSU (Mitsopoulos et al., 2017). Finally, loss of either protein, whether by knockdown or by knockout, demonstrated impaired mitochondrial protein synthesis (He et al., 2012a).

The evidence gathered from this proteomic analysis suggested a clear enrichment of PHB and PHB2 in MRPS39-BioID-HA pulldown eluates compared to the control. Consequently, I chose to investigate the possible effects of the loss of PHB on mitochondrial translation.

6.3.6: The effects of PHB and PHB2 depletion on mitochondrial proteins and mt-RNA

To investigate if PHB and PHB2 had a role in mitochondrial translation, each protein was depleted from human U2OS cells and the consequences on mitochondrial proteins and RNA were explored. Transient siRNA transfections using siRNA targeting PHB or PHB2 was used alongside non-targeting (NT) siRNA. When one of either PHB or PHB2 is lost, the partner protein is rapidly turned over (Merkwirth and Langer, 2009). Therefore, presence of both proteins was monitored by an antibody to PHB only (RB-292-PO Neomarkers). Cells (U2OS) in a 6-well plate were transfected for 6-days using forward and reverse siRNA transfection. After 6 days, there was a clear growth defect visible in the cells treated with PHB or PHB2 siRNA oligonucleotides. The cells were imaged down the 10x objective of a Axiovert25 microscope using my smartphone (Figure 6.7).

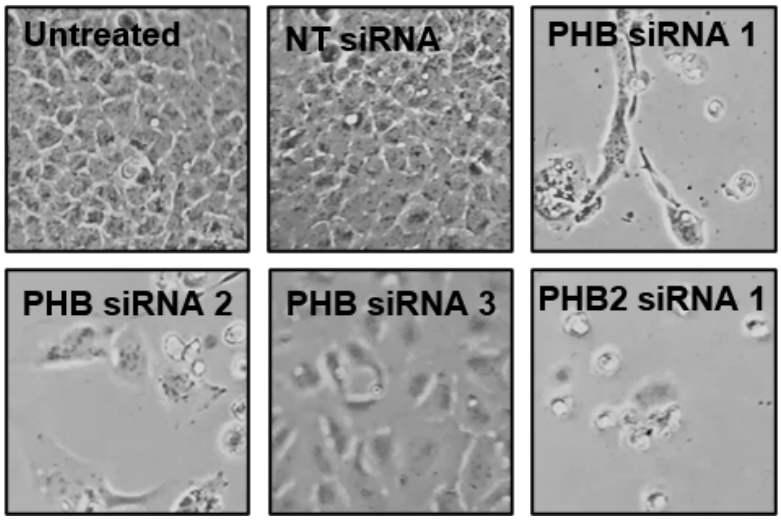

Figure 6.7: PHB and PHB siRNA affects the growth of U2OS cells. Images of cells were taken after treatment with PHB, PHB2, non-targeting (NT) siRNA, or cultured untreated for 6 days. Cells were transfected with siRNA on day 0 and day 3 of incubation. Images were acquired by photography down the 10x objective of a Zeiss Axiovert25 microscope.

To confirm PHB depletion and any effect on mitochondrial proteins, these cells were harvested, and the lysates (25 µg) were analysed by western blotting (Figure 6.8). Partial depletion of PHB was successful with all the siRNA oligonucleotides tested (Figure 6.8 lanes 3-6). There was a minor reduction in the steady state levels of MRPS39 in the cells treated with PHB siRNA 1, PHB siRNA 2, and PHB2 siRNA 1 compared to the untreated cells and NT siRNA treated cells (Figure 6.8 Lanes 3, 4, and 6). As it was MRPS39-BioID2-HA that interacted with PHB/PHB2 in the previous proximity labelling experiments, this serves as an interesting observation which I sought to repeat. In addition, there is a suggested depletion of NDUFB8 in the same three siRNAs which saw a reduction on MRPS39 (Figure 6.8 Lanes 3, 4, and 6). There was no clear reduction of mitochondrially-encoded COXII with any of the PHB siRNAs tested, however there seemed to be a fainter signal in the PHB2 siRNA1 blot. β-actin was used to validate equal loading across the blot.

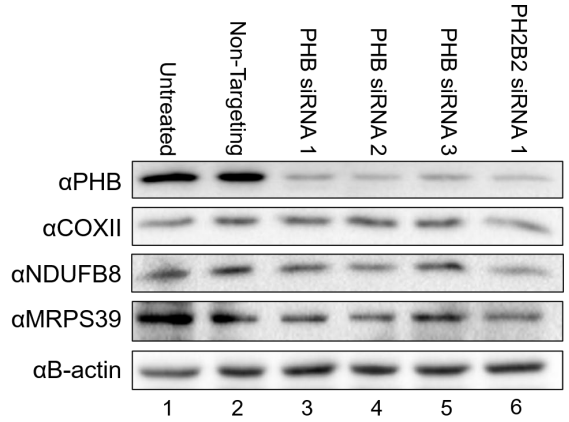

Figure 6.8: Depletion of PHB and PHB2 on U2OS cells using 4 different siRNA. U2OS cells were transfected with PHB, PHB2, non-targeting siRNA, or cultured untreated for 6 days. Cells were transfected with siRNA on day 0 and day 3 of incubation. Cell lysate (20 µg) was analysed by western blotting. Antibodies against PHB, COXII, NDUFB8 and MRPS39 were detected on the membrane. β-actin was detected as a loading control.

To confirm the results in Figure 6.8, I wanted to repeat the depletion experiments, with an additional earlier time point (3 days) to monitor any effects across the incubation. In addition, in an effort to combat loss of cellular material because of the growth defects visible in Figure 6.7, I opted to harvest cells after 5 days, rather than 6 days. U2OS cells were cultured with siRNAs for three distinct experiments: growth analysis in the *IncuCyte*, Northern blotting, and protein analysis by western blotting. Cells were grown in T25 cm^2 flasks for protein analysis and northern blotting to provide more cells. All cells were reverse transfected on day 0 and forward transfected on day 3 (6.2.6). The effects of PHB and PHB2 depletion were assessed

over 5 days in the *IncuCyte*, images from days 3 and 5 are present in Figure 6.9 (Panels A and B).

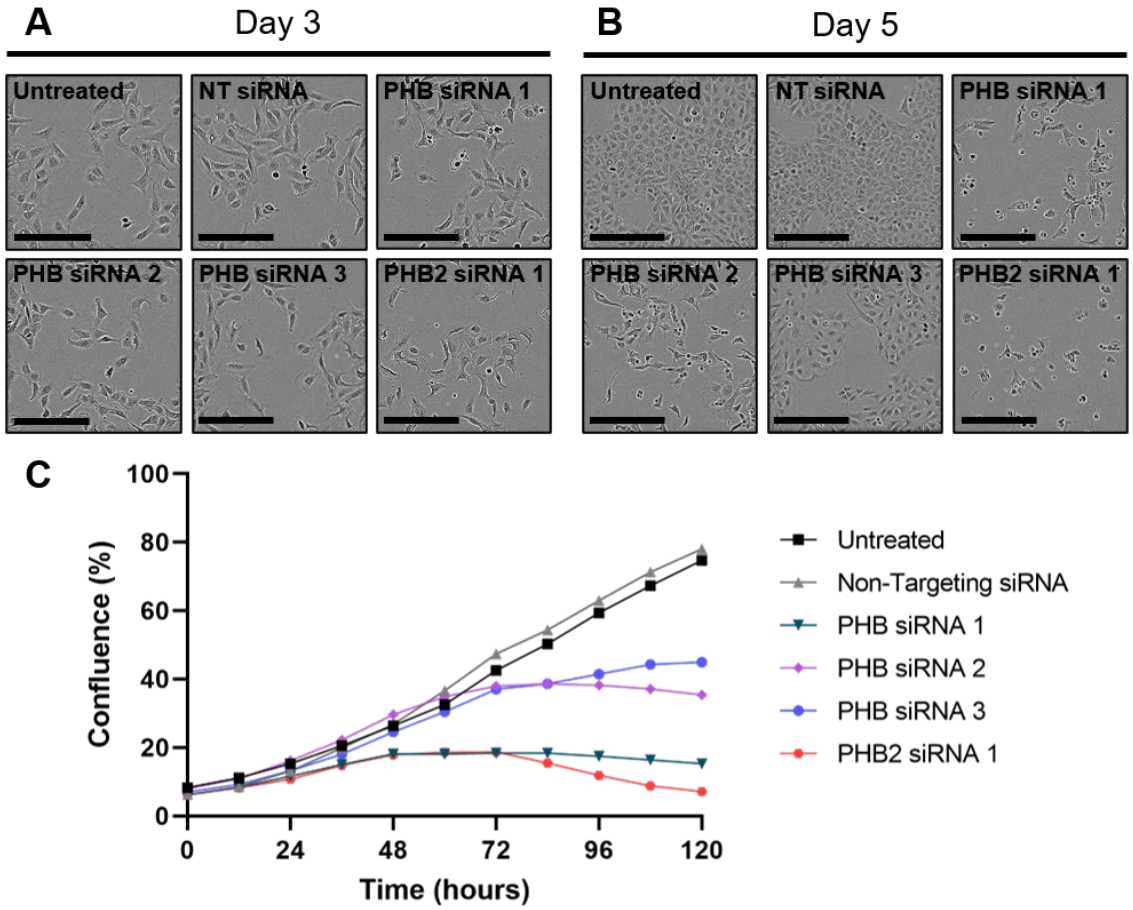

Figure 6.9: U2OS cell growth was monitored during depletion of PHB or PHB2 by siRNA treatment. U2OS cells were transfected with PHB, PHB2, non-targeting siRNA, or cultured untreated for 5 days. Cells were transfected with siRNA on day 0 and day 3 (72 hours) of incubation. Images were captured by the *IncuCyte* every three hours; representative images at **A:** 72 hours (Day 3) and **B:** 120 hours (Day 5) are displayed. Scale bar 300µm. **C:** Cell confluence was monitored throughout the experiment .

The *IncuCyte* uses 12 images per well, taken every three hours, to calculate the confluence of each well (Figure 6.9 C). Across the 5-day incubations, there was only a small difference between confluency between untreated cells and cell treated by NT siRNA, as expected. After 3 days (72 hours), and a second transfection of the siRNAs, there was a reduction in the growth rate in all wells treated with PHB/PHB2 siRNA. PHB siRNA 3 was minimally affected; cells were far less confluent than the control wells but maintained classic U2OS morphology throughout the incubation. PHB2 siRNA 1 showed the greatest phenotype from treatment, with cells forming a rounded morphology with many cells having detached from the cell surface, reducing confluency. The reduction in cell number and morphological changes seen in Figure 6.9 A-B mirror the confluency counts of the wells in Figure 6.9 C. The wells with the greatest

growth defects were PHB siRNA 1 and PHB2 siRNA, which diverge from the growth rates of all other cells after 2 days (48 hours). After the second siRNA transfects (day 3, 72 hours) the remaining PHB siRNA treated cells display a reduced growth rate. The untreated cells and cells treated with NT siRNA continue to increase in confluency until the end of the incubation period.

PHB and PHB2 are ubiquitously expressed proteins, with a multitude of roles within cells. Therefore, this growth defect may be caused by something other than mitochondrial dysfunction. To investigate if the depletion of PHB and PHB2 was affecting mitochondrial function, U2OS cells cultured and treated in tandem with those in the *IncuCyte* were harvested on Day 5 and the lysates analysed by western blotting.

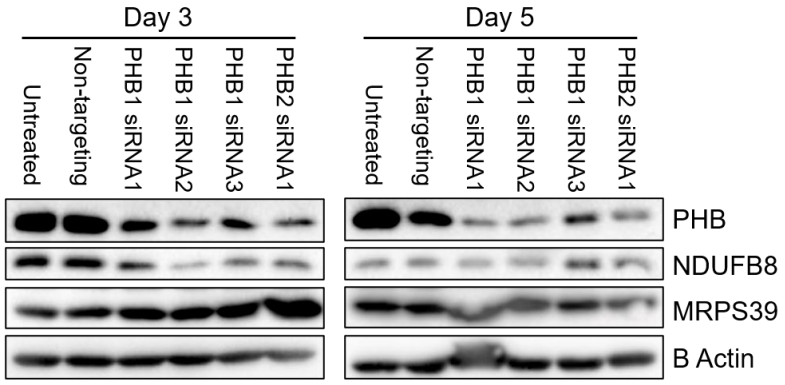

Figure 6.10: Analysis of the steady state level of mitochondrial proteins following PHB depletion. U2OS cells were transfected with PHB, PHB2, non-targeting siRNA, or cultured untreated for 3 or 5 days. Cells were transfected with siRNA on day 0 and day 3 of incubation. Cell lysate (25 µg) was analysed by western blotting. Antibodies against PHB, NDUFB8 and MRPS39 were used to determine steady state levels. Anti-β-actin was used as a loading control.

Antibody against PHB was used to confirm the depletion of the PHB heterodimer. There was a reduction in PHB in the presence of PHB or PHB2 siRNA oligonucleotides, compared to the untreated and NT siRNA controls. This decrease was also greater after 5 days than observed after 3 days. There was a greater PHB signal detected in the cells treated with PHB siRNA 3, although this was still reduced compared to the untreated and NT siRNA controls. Cells with this siRNA treatment had the greatest confluency within the data in Figure 6.9. After 3 days, there was a visible reduction of a nuclear-encoded subunit of complex I, NDUFB8, protein observed in cells treated with siRNA to PHB and PHB2. After extended treatment with siRNA, the levels of NDUFB8 in PHB/PHB2 siRNA treated wells appear to resemble those of the control. In my initial knockdown experiment (Figure 6.8), there was a weak reduction of NDUFB8 after 6 days, and PHB siRNA 3 displayed the highest levels of NDUFB8. The pattern

of PHB siRNA3 displaying the highest levels of NDUFB8 is conserved in Figure 6.10; this could be reflective of the higher levels of PHB within these cells. After 3 days of incubation, there are seemingly higher levels of MRPS39 in the cells treated with siRNA to the prohibitins. This is observation may be an artefact of western blotting, such as unequal distribution of ECL. After a 5-day incubation the pattern of protein intensities reflected the reductions in PHB after this time. Namely, there were reduced levels of MRPS39 compared to untreated or NT controls for all targeted siRNA except PHB1 siRNA 3. β-Actin antibodies were used to verify the equality of the loading. Antibody to COXII was attempted on this blot, however no signal appeared. These comparisons between 3- and 5-day siRNA treatment was only attempted once due to restricted timelines in the final year of my research. It would have been much more powerful to repeat these experiments, ever more so due to the MRPS39 blotting after 3-day treatment.

In addition to growth and protein analysis, I wanted to examine the effects of PHB and PHB2 siRNA depletion on mitochondrially-encoded RNAs. U2OS cells were grown simultaneously with those used for protein analysis, with the same treatment across 5 days. Cells from these parallel cultures were then analysed by northern blotting (Figure 6.11). This experiment was kindly conducted by Dr Richard Temperley within the Lightowlers Laboratory.

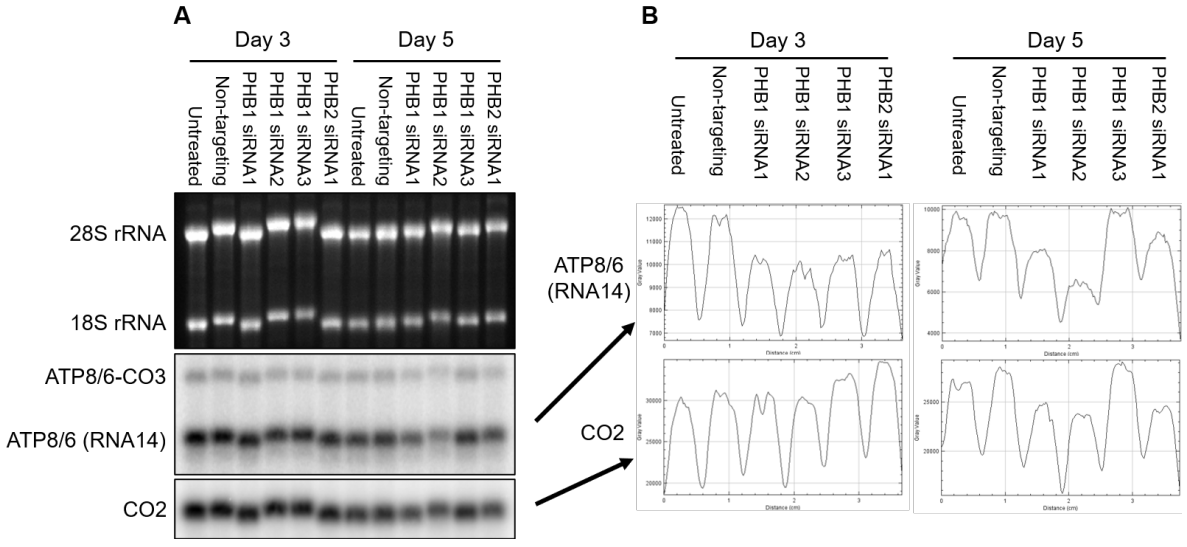

Figure 6.11: Northern blot analysis of RNA following PHB depletion. U2OS cells were transfected with PHB, PHB2, or non-targeting siRNA, or cultured untreated for 3 or 5 days. RNA was extracted and separated on a 1.2% agarose gel before transfer to a GeneScreen Plus membrane and probing with random hexamer labelled DNA fragments for the unprocessed *MTATP6*/*MTCO3,* and *MTCO2*. **A:** Cytosolic 18S rRNA was used to verify equal loading. **B:** FIJI software was used to generate a trace through all lanes across the migration lines of *MTATP6/8* (*RNA14*) and *MTCO2*.

Northern analysis of mt-RNA revealed reductions in the steady state levels of transcripts encoding ATP6/8 in cells treated for 3 days with each of the PHB siRNAs. This is most clearly visible in the line plots for Day 3 (Figure 6.11 B). This reduction is maintained after 5 days with the exception again of PHB1 siRNA3. There is less evidence for a decrease in the transcript encoding COXII after 3 days. This is consistent with the western data presented in Fig 6.8, but a modest decrease in *MTCO2* levels in 3 of the 4 PHB siRNA treated lines is apparent, consistent with the literature (He et al., 2012a; Tsutsumi et al., 2009). This pattern of reduction is reflected in the growth curves, cell growth images, and steady state levels of proteins.

6.4 Discussion

In this chapter, proximity-labelling interaction analysis was completed for MRPS39 and MRPS27 using the BioID2 system. The principal hits from this analysis, PHB and PHB2, were then investigated by siRNA depletion to elucidate if reduction in these proteins resulted in mitochondrial translation defects. My aim for this project was to identify any proteins that are vicinal to the mitoribosomal mRNA entry site and investigate their effects on mitochondrial translation. Following the validation that MRPS39-BioID-HA was integrated into the mitoribosome following induction, I was confident that BioID2-driven biotinylation would result in the identification of proteins that surround the entry site.

I have presented data from two mass spectrometry experiments. In the initial mass spectrometry run the samples were processed across two days. There was a great reduction in both the number of proteins identified, and their associated intensities, from the samples processed on the second day. This variation was most likely introduced during sample preparation, as there was no clear difference in the confluency of the cell cultures for the samples prepared the day later. The mitochondrial preparation step and the streptavidin-biotin pull down are the most likely cause of the variation, although all efforts were made during the processing of samples to adhere closely to these protocols to make the final samples consistent. I completed a silver stain of the pulldown eluates from these samples to ascertain if the inconsistent protein levels could be detected and predicted, prior to mass spectrometry analysis. Unfortunately, the silver staining intensities did not correlate with the known protein intensities, as a consequence this process was not performed prior to the second run. I included the crude mitochondrial preparation to reduce any potential background from proteins biotinylated in the cytosol. Reviewing the available literature this step does not appear to be consistently performed, with

the most prominent mitochondrial BioID2 study (Antonicka et al., 2020), forgoing the step. The authors identified the bait proteins localised to cellular compartments other than mitochondria, through the use of immunofluorescence. As I wanted to identify proteins that specifically interact when my bait proteins were in the mitochondria, the mitochondrial isolation step was necessary. Following mass spectrometry analysis, I attempted a variety of filtering and analysis steps. LFQ intensities were used upon guidance from the Newcastle University Laboratory for Biological Mass Spectrometry. LFQ intensities are similar to overall protein intensity but are normalised to exclude outliers. The identification of PHB and PHB2 were consistent across different analyses. The lower intensities of MRPS39 BioID2 samples, due to variation discussed above, increases the strength of the identification in this study. Furthermore, this experiment identified known interactors of MRPS39, namely MRPS2 and MRPS31. These acted to validate that MRPS39-BioID2-HA had successfully integrated into the mitoribosome and was able to biotinylate vicinal proteins; specifically, MRPS2 which is proximal to MRPS39 in the mt-SSU but, unlike MRPS31, it is not known to form a pre-complex with MRPS39 (Amunts et al., 2015; Bogenhagen et al., 2018). Although this experiment included three biological replicates, it was necessary that I repeated the research to confirm the finding and negate any effects of low protein counts from those samples processed on the second day.

The second mass spectrometry preparations were completed on a single day rather than split over 2 days. In general, this did not produce a wide variation of protein intensities or counts. One preparation, S27+B 2, had lower intensities compared to the other preparations, the cause of this is unknown. The proteins identified as proximal to MRPS39 in this mass spectrometry experiment were consistent with those gathered in the first. In addition to the strong identification of PHB and PHB2, MRPS31 and MRPS2 were again clearly enriched in the MRPS39 samples. In addition to these proteins, MRPS9, which is found in a pre-assembly complex with MRPS31 and MRPS39 (Bogenhagen et al., 2018), was identified in the MRPS39 preparation. Increasing the strength of the observations seen in this experiment, MRPS34 and MTIF2 were identified in the MRPS27 preparations. MRPS34 is part of an mt-SSU pre-assembly complex with MRPS27, and MTIF2 is associated with the body of the mt-SSU, where MRPS27 is located (Bogenhagen et al., 2018; Khawaja et al., 2020). As there were fewer MRPS27 preparations in this experiment, four compared to six MRPS39 preparations, I altered the statistical tests to account for this and performed a Welch's t-test.

Taken together, the consistent identification across both mass spectrometry experiments, of PHB and PHB2, among the identification of known interactors and proteins close to bait proteins in the mt-SSU, evokes a strong suggestion that they are found proximal to MRPS39. I then used the remaining laboratory time I had during my PhD, to investigate how PHB or PHB2 depletion affected mitochondria. Of the four-siRNA tested, PHB siRNA 3 had the most modest effect on cell growth, and the levels of proteins and RNA tested. The other siRNAs displayed a different and stronger phenotype. I have presented data that shows PHB depletion using PHB siRNA 1, PHB siRNA 2 or PHB2 siRNA 1, all resulted in a reduction in growth rate as determined by U2OS cell confluency and decreases in the steady state levels of MRPS39 protein as well as *MTATP6/8*, and *MTCO2* transcripts. These observations are supported by current publications reporting the roles of the prohibitins in mitochondria (He et al., 2012b; Tsutsumi et al., 2009). Prohibitins are localised to the inner mitochondrial membrane (IMM) and have been shown to interact with OXPHOS complex 1 (Bourges et al., 2004), which could explain the reduction in NDUFB8 in cells with depleted levels of PHB and PHB2 after 3 days. While stability of OXPHOS subunits within the membrane could be a clear defect resulting from the loss of prohibitins, the reduction of the mitochondrially encoded *MTATP6/8* and *MTCO2* RNA species is not explained by this phenomenon. One possible mechanism for this phenotype could be through PHB/PHB2 interactions with Stomatin-like protein-2 (SLP-2). SLP-2 is a predominantly mitochondrially expressed protein which interacts with the prohibitin heterodimer at the IMM (Christie et al., 2011; Da Cruz et al., 2008). In experiments performed in mice, SLP-2 was required for mitochondrial translation in T-cells upon activation (Mitsopoulos et al., 2017). This paper showed a reduction in the expression of COXII upon loss of SLP-2. Mitochondrial translation is closely associated with the inner mitochondrial membrane (Pfeffer et al., 2015), thus the interaction of SLP-2 with prohibitin, and cardiolipin, at the inner membrane is thought to help regulate translation by controlling membrane composition (Christie et al., 2011; Mitsopoulos et al., 2017).

The observations in this chapter support the conclusion that the methodology and refined protocol that I used was effective in identifying proteins in the proximity of the mt-SSU proteins. Furthermore, use of this protocol identified PHB and PHB2, and the investigation into their roles in the mitochondria substantiates the current literature available.

Chapter 7:

Final Discussion

7.1 Introduction

The aim of this research was to investigate the process of mitochondrial translation, specifically the sub-mitochondrial localisation of mitoribosomes and adjacent proteins as well as the delivery of mt-mRNA to mitoribosomes. I intended to do this by developing and optimising expansion microscopy and super resolution RNA fluorescence in-situ hybridisation of the mt-rRNA, pairing this with protein immunofluorescence. When it became clear that there were limitations of this methodology, I adapted my approach to utilise proximity-based proteomics. The data presented in this thesis displays the successful application of these techniques in such a manner that has reinforced the current literature available. A discussion of my intentions at the outset of this research, the progress made, and the limitations the study are described below.

7.2 Super resolution microscopy of mt-rRNA

I successfully optimised RNA FISH methodology such that mitochondrial ribosomal RNA could be effectively visualised using super resolution STED microscopy (Zorkau et al., 2021). The images gathered were consistently resolved beyond the light diffraction limit without aberration to mitochondrial networks. One of my research aims, set out in the introduction to this thesis, was to characterise the sub-mitochondrial localisations of *RNR1* and *RNR2*. Following validation of the technique on mt-rRNA labelled with Quasar 570 (Q570), CalFluor 610 (C610), and Quasar 670 (Q670), RNA FISH was then applied to HEK293, HeLa and U2OS cells. Colocalization analysis of the 2 mt-rRNAs species within these images using the Pearson correlation coefficient showed a strong correlation between *RNR1* and *RNR2*. When Manders coefficients were used, my results suggested that there was a higher level of *RNR2* compared to *RNR1*. This is consistent with the gene expression levels determined by RNASeq in human 143B mitochondrial preparations (Mercer et al., 2011). The main limitation of this investigation was the resolution of images obtained, especially when HEK293 cells were imaged. The spherical morphology of HEK293 cells generates background fluorescence as there is more mitochondria above and below the focal plane. These mitochondria have also been labelled by RNA FISH, generating fluorescence that will be detected. The flatter morphology of HeLa and U2OS cells means there is a greater proportion of the mitochondria that exist in a single Z plane, limiting the background and therefore visualising a more resolved signal. An additional objective for this method was to apply RNA FISH to quantify and characterise the distribution of 12S mt-RNA (*RNR1*) and 16S mt-rRNA (*RNR2*) in combination with immunofluorescence. The protocol developed could easily be paired with standard immunofluorescence methods,

and this was validated by imaging mt-rRNA in combination with TOM20 as a mitochondrial network marker.

As I progressed with STED imaging, it became clear that the images I was achieving did not reach the resolution required to meet this aim. Figures 3.3 and 3.4 are representative of the highest resolution I was able to achieve across this study. The morphology of cristae is clearly visible in these structures, and the smallest punctate signal is ~30-40nm after deconvolution. As discussed earlier, research at the forefront of mitochondrial STED microscopy can achieve this resolution in the raw imaging (Jakobs and Wurm, 2014; Stephan et al., 2019), but this is something that I did not manage to achieve at this juncture. The resolution of my images was limited in part by variations in slide preparations, as even with the same fluorophore pairings and methods, my results varied. In addition, the fluorophores that I chose to use have never been shown to achieve a higher resolution than what I displayed in my images. The close spectral nature of Q570 and C610 reduced the amount of light I was able to acquire from the Q570-labelled samples. The excitation wavelength of the C610 fluorophore was 590 nm, therefore I could only acquire Q570-excited emitted light up to ~580 nm to avoid detecting signal from any C610 fluorophores. While I was able to optimise the imaging of these two fluorophores concurrently by increasing the excitation of Q570 using two lasers, there may still have been signal undetected due to the small acquisition window. This may have led to the higher Manders M1 levels when colocalization analysis was completed.

Throughout generating the data presented in this thesis, I was attempting to improve the resolution I achieved using expansion microscopy (Chen et al., 2015). Quasar 570 has been successfully paired with expansion microscopy, however this study only used diffraction-limited microscopes to analyse expanded samples (Chen et al., 2016). At the time I was attempting to use expansion microscopy, there were only a few published papers providing in-depth instructions. I was not successful in increasing the resolution of my FISH-labelled samples in the timeframe I had allotted. Recently, there have been an increased number of published guidelines for expansion microscopy which have made the procedure clearer (Klimas et al., 2019; Zhang et al., 2020). Recent publications have also included expansion targeted at mitochondrial research (Kunz et al., 2020). The resolution of mitochondria and cristae in Kunz *et al* is similar to best resolution I achieved after deconvolution. The resolution obtainable with expanded microscopy, when combined with super resolution microscopy, can reach 10nm (Gao et al., 2018). Had the time frame of this research been greater, I would have liked to spend more time optimizing this protocol to *expand* RNA FISH samples to increase the resolution.

7.3 The distribution of mt-rRNA upon specific depletion of RNR2

Working in collaboration with Dr Francesco Bruni within my host laboratory, RNA FISH was applied to examine the visual distribution of mt-RNA upon loss of the 16S mt-rRNA, *RNR2*. This investigation served as an additional validation that this approach was specifically labelling mt-rRNA. I contributed to the validation of phenotypes wherein *RNR2* was selectively degraded by a mitochondrially-targeted VapC20 (mt-VapC20) endoribonuclease (Bruni et al., 2020). Specifically, I showed that the physiological levels detected by in-situ visualisation of *RNR2* were significantly reduced upon induction of mt-VapC20 for 3 or 6 days, and there was a greater reduction after a longer induction period. The findings of Bruni *et al* suggest a clear role for the formation of the monosome in mt-RNA transcript stability. Upon mt-VapC20 induction and subsequent depletion of both *RNR2* and the mt-LSU, mt-mRNA transcript levels decreased whereas the protein levels of LRPPRC/SLIRP remained the same as untreated cells. This suggested that reductions in mt-mRNA under mt-LSU depletion was driven by degradation of the transcript, rather than alterations in mtDNA transcription. This supports the presence of distinct pre-initiation complexes that assemble prior to mt-LSU binding; comprising of mt-LSU, mitochondrial initiation factors (mtIF2/mtIF3), and mt-mRNA that has displaced LRPPRC/SLIRP (Christian and Spremulli, 2010; Khawaja et al., 2020). When the mt-LSU is unable to bind these complexes, they are disassembled, and the mt-mRNA is degraded.

Imaging of mt-VapC20 cells was limited by the morphology of the HEK cells, which are not suitable for super resolution imaging as considered earlier in this discussion. I had planned to transfect the mt-VapC20 construct into U2OS cells using the Flp-In™ system to allow for STED imaging and a greater understanding of the sub-mitochondrial localisation of *RNR1* and remaining *RNR2* after depletion. This was not attempted during my PhD research due to time limitations, as I had begun focussing on the proximity labelling investigation that is described in the latter part of this thesis. Specifically, it would be interesting to have paired effective expression of mt-VapC20 in U2OS cells with a successful increase in resolution by expansion microscopy. This could have allowed examination of what constitutes typical distribution of mt-rRNA and any change in pattern due to selective degradation of *RNR2*, hopefully at a resolution smaller than 30 nm. The ability to pair this investigation with immunofluorescence opens up the option to visualise these RNA molecules alongside proteins including LRPPRC, SLIRP, mtIF2 or mtIF3 to gain new insight into mRNA loading onto the mitoribosome and translation initiation.

7.4 Generation and validation of proximity labelling tools

The remainder of my PhD research focussed on the application of the Proximity-dependent biotin identification (BioID) system to identify proteins present at the mt-mRNA entry site on the mitoribosome. This method was chosen as it only required the addition of a small moiety (BioID2, 27 kDa) and could identify transient interactions between proteins. The specific process of mt-mRNA stability and loading onto the mitoribosome has not been fully realised in humans. It is known that the LRPPRC/SLIRP complex specifically stabilises mt-mRNA levels (Baughman et al., 2009; Gohil et al., 2010). In patients with Leigh Syndrome French Canadian (LSFC) disorder, where the steady state LRPPRC levels are greatly reduced, mt-mRNA are still translated at a low level. I aimed to use proximity labelling to investigate if there are any supplementary proteins associated with mt-mRNA stability and transport.

Using the published structure of the human mitoribosome (Amunts et al., 2015, PDB: 3J9M), I identified five mitoribosomal proteins that occupy space around the mt-mRNA entry site: MRPS5, MRPS24, MRPS33, MRPS35, and MRPS39. These bait proteins were chosen to encompass a range of accessibility, including those which may disrupt mRNA delivery and assembly of the mitoribosome. SLIRP was also investigated because of the known role it has in mt-mRNA stability and delivery. MRPS27 and COX8-MTS were selected to provide a background level for non-specific biotinylation.

In addition to confirmation of overexpression, I aimed to validate that all constructs demonstrated the correct localisation. In many BioID investigations, this still is not required or completed prior to biotinylation (Antonicka et al., 2020; Koshiba and Kosako, 2020). The specificity of my investigation required that, where possible, all biotinylation from the MRP-fusion constructs occurred following integration into the mt-SSU. The expression of MRP-BioID2 fusions was characterised to minimise the levels of free or mitoribosomal subcomplex-bound when biotinylation was promoted. To do this, I determined optimal conditions for pulse-induction of all BioID-tagged MRP proteins, followed by a chase period that would allow integration into the mitoribosome and degradation of unintegrated overexpressed protein. The level of integration was determined by monitoring the position of the mt-SSU in isokinetic sucrose gradients of cell lysates following different chase periods. The western blotting to mt-SSU components identified that both MRPS39-BioID2-HA and the control MRPS27-BioID2-HA fusion proteins had successfully integrated into the mt-SSU and the monosome. Importantly, the overexpressed fusion proteins most closely resembled the endogenous protein

after 16-hour induction followed by a 24-hour chase period. These conditions were taken forward for further analysis.

Mitoribosomal integration assessments were completed for all MRP-fusion proteins, however a number of these proteins were not taken forward for proteomic analysis. Sucrose gradient analysis of the MRPS5 BioiD2 fusion after induction showed a signal across all fractions, which was not consistent with the mt-SSU subunits analysed. This distribution after induction was not seen in any other MRP-BioID2 fusions. After chasing induction there was little MRPS5-BioID2-HA signal found in the fractions when mt-SSU subunits migrated. As the C-terminus (CT) of MRPS5, where the ligase moiety was fused, is facing the interior of the mt-SSU, it may be that the fusion protein is unable to integrate into the ribosome. While the phenotype after induction was interesting, there was not time to investigate further. As MRPS5-BioID2-HA did not segregate as expected of a mt-SSU protein, it was not analysed further. There was very little evidence for any integration of MRPS33-BioID2-HA into the mt-SSU by sucrose gradient analysis. After 16 hours of induction, in the absence and presence of a chase, the fusion protein did not follow the distribution of a small subunit protein. Unlike MRPS5, modelling of MRPS33-BioID2-HA did not predict interference with mitoribosome assembly as the CT is on the exterior of the mt-SSU. The CT is, however, very close in space to the 12S ribosomal RNA therefore it may be that the fusion protein is obstructing the rRNA. As I did not have clear evidence of integration into the ribosome, MRPS33 was not investigated any further. MRPS35 was selected as a bait protein as it has an interface with the mRNA entry site, but the CT was located away from the entry site, on the exterior of the mt-SSU. Induction of MRPS35-BioID2-HA and sucrose gradient analysis did not suggest that the fusion protein was integrating into the mt-SSU. Although there was some fusion protein signal in the fractions where small subunit proteins migrated, the distribution of MRPS35-BioID2-HA did not resemble a mt-SSU protein. MRPS35 was not taken forward for further investigation. The final protein that was assessed for integration into the mitoribosome was MRPS24-BioID2-HA. The distributions upon induction, with and without a chase period, were very similar to those observed in MRPS35-BioID2-HA induction. When MRPS24-BioID2-HA was modelled, the ligase occupied the mRNA entry tunnel which could sterically hinder assembly or translation. It was not surprising that there was not stable integration of this fusion protein into the mt-SSU. This fusion was also not further investigated in this thesis.

Matrix localisation of COX8MTS- and SLIRP-BioID2-HA were confirmed by submitochondrial fractionation. This experiment showed the lower species of SLIRP-BioID2-

HA doublet (~33 kDa) was localised to the matrix. The higher detected band (~40 kDa) corresponds to the predicted molecular weight of SLIRP-BioID2-HA after cleavage of the known MTS. Since the focus was on the analysis of MRP-BioID2 constructs with successful integration patterns, this observation of 2 imported and matured SLIRP fusion proteins was not further characterised. A number of nuclear encoded mitochondrially destined proteins are known to be cleaved at 2 positions in sequential maturation steps (Calvo et al., 2017). It may be that upon entry to the mitochondria, there is a similar cleavage strategy of the BioID2-SLIRP variant. The COX8MTS and SLIRP BioID2 constructs were also analysed by sucrose gradients to confirm they did not integrate into the mt-SSU, as predicted.

The validated MRPS27- and MRPS39-BioID2-HA constructs were the primary candidates for the first proteomic assay, presented in the next section of this discussion. Unfortunately, time did not permit the analysis of the proximity interactors for SLIRP, alongside the COX8MTS control.

7.5 Investigating proteins proximal to the mitoribosomal mRNA entry site

My intention was to identify any proteins that are specifically enriched at the mitoribosomal mRNA entry site and to investigate their contributions to mitochondrial translation. Following confirmation that MRPS27 and MRPS39 BioID2 integrated in the mitoribosome, large-scale cultures were set up in tandem and subjected to identical growth and subsequent sample preparation conditions for Liquid Chromatography- Mass Spectrometry/Mass Spectrometry (LC-MS/MS). The initial mass spectrometry investigation resulted in a large variation in protein counts, most likely due to sample preparation over two days. A variety of filtering and analysis steps were completed, each identifying PHB and PHB2 at high levels in the MRPS39 samples when compared to control. The identification of proteins known to physically interact or be proximal to the bait proteins acted to validate the assay. These included MRPS2 which is close to MRPS39 within the mt-SSU structure, and MRPS31 which is part of a pre-complex with MRPS39 (Amunts et al., 2015; Bogenhagen et al., 2018). Subsequent preparations performed on the same day, removed a large amount of the variation in protein counts. Consistent with the first run, this experiment also identified PHB, PHB2, MRPS2 and MRPS31 as enriched in the MRPS39 samples. In addition, MRPS34 and MTIF2 were identified as specifically proximal to MRPS27-BioID2-HA. Similarly, to the interaction of MRPS31 and MRPS39, MRPS34 and MRPS27 are known to be part of a pre-complex prior to mt-SSU assembly (Bogenhagen et al., 2018). The identification of MTIF2 as proximal to MRPS27 is

in agreement with recent modelling of pre-initiation complex of the mt-SSU (Khawaja et al., 2020). The presence of PHB and PHB2 in independent mass spectrometry experiments suggested these proteins are found proximal to MRPS39. A recent publication performed BioID proximity labelling using variants of PHB2 as bait and identified MRPS39, supporting the data I have presented (Yoshinaka et al., 2019).

In the remaining research time, I investigated the roles of PHB and PHB2 within the mitochondria. I used siRNA depletion (3 against PHB, 1 against PHB2) of the prohibitins to examine the consequent effects on cell growth and the steady state levels of protein and RNA. As PHB and PHB2 exist as a heterodimer in the inner mitochondrial membrane (IMM), loss of either protein causes the loss of the other (Merkwirth and Langer, 2009). Depletion using any of the four siRNAs caused an apparent decrease in growth rate as determined by a reduction in U2OS cell confluency after a 6-day treatment. The strongest phenotypes were seen using PHB siRNA1, PHB siRNA2 and PHB2 siRNA1, which also caused decreases in the steady state levels of NDUFB8 after three days, and MRPS39 after 6 days. This is consistent with the known function of PHBs acting as chaperones for the integration of newly synthesized components of Complex 1 (Bourges et al., 2004; Nijtmans et al., 2000). Northern blotting revealed reductions in *MTATP6/8*, and *MTCO2* transcript levels after 6-day treatments. Similar reductions in mitochondrial protein and RNA levels upon depletion of prohibitins has previously been presented in the literature (He et al., 2012; Tsutsumi et al., 2009), and the mechanisms of action speculated.

It is thought that the prohibitins, in combination with other IMM proteins such as Stomatin-like protein-2 (SLP-2), may regulate mitochondrial translation through alterations to membrane composition, where translation occurs (Christie et al., 2011; Mitsopoulos et al., 2017). Mitsopoulos et al showed a reduction in the steady state of COXII upon loss of SLP-2, but this effect was post-transcriptional. An addition theory is that interaction of prohibitins with ATAD3 is linked to modulation of translation. Both proteins were isolated from nucleoids by affinity capture, and depletion of either protein reduced steady state levels of mitochondrial-encoded proteins (He et al., 2012). The reduction in steady state levels of RNA upon prohibitin depletion may be caused by disruptions to the role of PHB/PHB2 in the stability of mitochondrial nucleoids (Kasashima et al., 2008). Kasashima et al showed that depletion of PHB by siRNA led to alteration of mitochondrial nucleoid organisation and reduction the levels of mtDNA. They propose that these phenotypes occurred through PHB interaction with ATAD3 and modulation of TFAM levels. They witnessed a reduction of TFAM in PHB

depleted cells only after 3 days of treatment. This is an interesting similarity to the increased reduction in RNA levels I found after 5 days of PHB depletion compared to 3 days. While the roles of the prohibitins are yet to be fully characterised, these studies have shown the tight association of these proteins with mitochondrial translation.

Should the timeline of this research have been longer, I would have liked to investigate PHB and PHB2 in more detail. Specifically, I am interested in the mechanism of RNA reduction after prohibitin depletion, and if this is linked to the prohibitin association with the mitoribosome. The optimisation of RNA FISH would have been an excellent candidate for this research. In addition, the PHB complex has been linked to a plethora of roles within the cell and mitochondria, with the majority of these roles involved the modulation of the inner mitochondrial membrane. As more evidence is published supporting the association of mitochondrial translation and the IMM, I think it would also be interesting to study IMM composition alongside the RNA imaging to gather further evidence of how PHB/PHB2 may be involved in the translation process. This work could also be complemented by examining the effects of PHB depletion using the high-resolution protein synthesis imaging assay recently developed within my host laboratory (Zorkau et al., 2021).

Furthermore, I would like to have completed the BioID2 experimentation using the SLIRP- and COX8MTS-BioID2-HA cell lines described in this thesis. The main aim of this investigation was to examine if any other proteins are involved in mt-mRNA stabilisation and mt-mRNA loading. It could therefore also be revealing to repeat the MRPS39/MRPS27-BioID-ha experimentation in cells treated with siRNA to LRPPRC or SLIRP.

7.6 Final conclusions

The development and application of mt-rRNA FISH contributed to two publications, Bruni et al., 2020 and Zorkau et al., 2021. I believe this technique could be a valuable tool within mitochondrial research that can provide in situ data relevant to many biological research questions. Furthermore, the identification of PHB and PHB2 as proximal to the mt-SSU is consistent with the available literature and compounds the need for more research into these proteins.

Appendices

Appendix I: DNA Oligonucleotides

The following DNA-oligonucleotides were used for PCR reactions. They were personally designed and then synthesised by Eurogentec.

I.I Primer sequences for PCR amplification to generate inserts for cloning

Primer	Sequence (5'-3')
MRPS27 Forward	GCATACGGATCCCTCCAAGATGGCTGCCTCCATA
MRPS27 Reverse	GCATATCTCGAGGGCAGATGCCTTTGCTGCT
SLIRP Forward	ATCGATGGATCCAGTCTGAAGATGGCGG
SLIRP Reverse	GCGCGCCTCGAGAAAATCTTTCTTTTCATCATCAGATGT

I.II Primer sequences for PCR amplification for sequencing

Primer	Sequence (5'-3')
pcDNA5 BIOID Reverse	GTTCAGCAGGAAGCTGAAGTACAGGCCG
MRPS27 Forward	TGTGAAGCAGAGGACATCGCCACCTATGAG
SLIRP Forward	CTTTGCACAGTTCGGCCATGTCAGAAG
MRPS5 Forward	GCTCAGCCTCACCCAGGGCCTCTT
MRPS24 Forward	GGATGGAGAGGACCATGCCGCAGAGC
MRPS33 Forward	CCGAGCTCGGATCCACCATGTCCTCCC
MRPS35 Forward	CCCTTTAAGGAGGCAGAATTACGATTATGCAGTG
MRPS39 Forward	GGATTGGCCAGCCACCTCTCTCAACTG

Appendix II: Antibodies

II.I Primary antibodies

Antibody	Type	Dilution	Company	Product Code
MRPS26	Rabbit	1:1000	Proteintech group	15989-1-AP
MRPS27	Rabbit	1:1000	Proteintech group	17280-1-AP
MRPL11	Rabbit	1:1000	Proteintech group	15543-1-AP
MRPL45	Rabbit	1:1000	Proteintech group	15682-1-AP
TOM20	Rabbit	1:1000	Santa Cruz	sc-11415
AIF	Rabbit	1:1000	Santa Cruz	sc-4642S
β-actin	Mouse	1:10000	Sigma	A1978
COXII	Mouse	1:1000	Thermo Fisher	A6404
HA	Rabbit	1:1000	Abcam	ab9110

II.II Secondary Antibodies

Antibody	Type	Dilution	Company	Product Code
Rabbit	Swine	1:3000	Dako	P0399
Mouse	Rabbit	1:2000	Dako	P0449
Att0647N	Anti-Rabbit	1:2000	Merck	40839

Appendix III: RNA FISH Probes

The following lists the DNA oligonucleotides ordered for RNA FISH and their position the target RNA

III.I Probes for RNR1 – Masking level 5

Probe #	Probe (5'-> 3')	Probe position *	Percent gc
1	AAGGCTAGGACCAAACCTAT	2	45.0%
2	GCTTGCATGTGTAATCTTAC	36	40.0%
3	GTGAACTCACTGGAACGGGG	58	60.0%
4	TTTGATCGTGGTGATTTAGA	80	35.0%
5	TGCGTGCTTGATGCTTGTTC	102	50.0%
6	TAAGCGTTTTGAGCTGCATT	124	40.0%
7	AGGTTAATCACTGCTGTTTC	164	40.0%
8	GGGGTTAGTATAGCTTAGTT	204	40.0%
9	TGGCACGAAATTGACCAACC	226	50.0%
10	TTGGGTTAATCGTGTGACCG	253	50.0%
11	CTTTACGCCGGCTTCTATTG	275	50.0%
12	GGGAGGGGGTGATCTAAAAC	298	55.0%
13	CTCAGGTGAGTTTTAGCTTT	322	40.0%
14	GTGTCAACTGGAGTTTTTTA	345	35.0%
15	AGCCACTTTCGTAGTCTATT	367	40.0%
16	ATTGTGTGTTCAGATATGTT	389	30.0%
17	AATCCCAGTTTGGGTCTTAG	411	45.0%
18	GGCTAAGCATAGTGGGGTAT	433	50.0%
19	GTTGATTTAACTGTTGAGGT	457	35.0%
20	TAGTGTTCTGGCGAGCAGTT	479	50.0%
21	TAGAGGGATATGAAGCACCG	530	50.0%
22	TCGATTACAGAACAGGCTCC	552	50.0%
23	CAAGAGGTGGTGAGGTTGAT	581	50.0%
24	AAGATGGCGGTATATAGGCT	604	45.0%
25	TTACTTTGTAGCCTTCATCA	634	35.0%

26	AACGTCTTTACGTGGGTACT	659	45.0%
27	CTCATGGGCTACACCTTGAC	681	55.0%
28	AAATGTAGCCCATTTCTTGC	704	40.0%
29	TATCGTAGTTTTCTGGGGTA	726	40.0%
30	GACCCTTAAGTTTCATAAGG	748	40.0%
31	AGTTTACTGCTAAATCCACC	771	40.0%
32	CCTGTTCAACTAAGCACTCT	797	45.0%
33	GTATACTTGAGGAGGGTGAC	842	50.0%
34	AATGCGTAGGGGTTTTAGTT	876	40.0%
35	TACGACTTGTCTCCTCTATA	898	40.0%
36	AAGTGCACTTTCCAGTACAC	927	45.0%

III.II Probes for RNR2 – Masking level 5

Probe #	Probe (5'-> 3')	Probe position *	Percent gc
1	TGTCTGGTAGTAAGGTGGAG	23	50.0%
2	CCAGGTTTCAATTTCTATCG	79	40.0%
3	TTGCGGTACTATATCTATTG	101	35.0%
4	ATGCAGAAGGTATAGGGGTT	165	45.0%
5	GCTCTCCTTGCAAAGTTATT	200	40.0%
6	TTAGGTAGCTCGTCTGGTTT	237	45.0%
7	CCCACTATTTTGCTACATAG	281	40.0%
8	TGTCGCCTCTACCTATAAAT	304	40.0%
9	AAGGGGATTTAGAGGGTTCT	392	45.0%
10	TGTTCCTCTTTGGACTAACA	423	40.0%
11	GTTTTTTCCTAGTGTCCAAA	447	35.0%
12	CTTAATTGGTGGCTGCTTTT	508	40.0%
13	TAGTGGGTGTTGAGCTTGAA	534	45.0%
14	GTTCAGTTATATGTTTGGGA	563	35.0%
15	TAGATTGGTCCAATTGGGTG	589	45.0%
16	CATTAGTTCTTCTATAGGGT	611	35.0%
17	TGTTTTAATCTGACGCAGGC	669	45.0%
18	TGGGCTGTTAATTGTCAGTT	692	40.0%

19	ATGACTTGTTGGTTGATTGT	718	35.0%
20	TGTGTTGGGTTGACAGTGAG	745	50.0%
21	TGCCTCTAATACTGGTGATG	850	45.0%
22	AAACATGTGTCACTGGGCAG	874	50.0%
23	CAGGTTTGGTAGTTTAGGAC	1107	45.0%
24	GCCCCAACCGAAATTTTTAA	1129	40.0%
25	AAGTCTTAGCATGTACTGCT	1175	40.0%
26	TAGTAGTTCGCTTTGACTGG	1197	45.0%
27	CGTTGGTCAAGTTATTGGAT	1227	40.0%
28	TTATCCCTAGGGTAACTTGT	1249	40.0%
29	ACTCTAGAATAGGATTGCGC	1271	45.0%
30	GTCGTAAACCCTATTGTTGA	1296	40.0%
31	GATGTCCTGATCCAACATCG	1318	50.0%
32	CGAACCTTTAATAGCGGCTG	1347	50.0%
33	CGTAGGACTTTAATCGTTGA	1372	40.0%
34	TACTCCGGTCTGAACTCAGA	1395	50.0%
35	GTAGATAGAAACCGACCTGG	1417	50.0%
36	TGTGAAGTAGGCCTTATTTC	1469	40.0%
37	TATCATTTACGGGGGAAGGC	1493	50.0%
38	GTGGGTGTGGGTATAATACT	1525	45.0%

Appendix IV: DNA sequences of bait-BioID2 fusion proteins

The constructs were sequenced to verify successful integration of the BioID2-HA. Only the region of fusion was sequenced. Bait proteins (MRPS5, MRPS24, MRPS33, MRPS35, MRPS39, MRPS27, and SLIRP) and BioID2 coding sequences are distinguished and the XhoI cloning site is underlined.

IV.I MRPS5-BioID2-HA Sequence

TCAACAGCTGGCTGATAAGAAGGGCCTCCATGTTGTGGAAATCCGGGAGGAATG
TGGCCCTCTGCCCATTGTGGTTGCGTCCCCCCGGGGACCCTTGAGGAAGGACCCA
GAGCCAGAAGATGAGGTTCCAGACGTCAAACTGGACTGGGAAGATGTGAAGACT
GCACAGGGAATGAAGCGCTCTGTGTGGTCTAATTTGAAGAGAGCCGCCACGCTC
GAGTTCAAGAACCTGATCTGGCTGAAGGAGGTGGACAGC

IV.II MRPS24-BioID2-HA Sequence

CGCAAGTTCATGTGGGGCACCTTCCCAGGCTGCCTGGCTGACCAGCTGGTTTTAA
AGCGCCGGGGTAACCAGTTGGAGATCTGTGCCGTGGTCCTGAGGCAGTTGTCTCC
ACACAAGTACTACTTCCTCGTGGGCTACAGTGAAACTTTGCTGTCCTACTTTTAC
AAATGTCCTGTGCGACTCCACCTCCAAACTGTGCCCTCAAAGGTTGTGTATAAGT
ACCTCCTCGAGTTCAAGAACCTGATCTGGCTGAAGGAGGTGGACAGCACCCAGG
AGAGACTGAAGGAGTGGAACGTGAGCTACGGCACCGCCCTGGTGGCCGACAGAC
AGACCAAGGG

IV.III MRPS33-BioID2-HA Sequence

TTCCAAGTCTATGAAAGTGGTGAAACTGTTTAGTGAACTGCCCTTGGCCAAGAAG
AAGGAGACTTATGATTGGTATCCAAATCACCACACTTACGCTGAACTCATGCAGA
CGCTCCGATTTCTTGGACTCTACAGAGATGAGCATCAGGATTTTATGGATGAGCA
AAAACGACTAAAGAAGCTTCGTGGAAAGGAGAAACCAAAGAAAGGAGAAGGGA
AAAGAGCAGCAAAAAGGAAACTCGAGTTCAAGAACCTGATCTGGCTGAAGGAG
GTGGACAGCACCCAGGAGAGACTGAAGGAGTGGAACGTGAGCTACGGCACCGC
CCTGGTGGCCGACAGACAGACCAAGGGCAG

IV.IV MRPS35-BioID2-HA Sequence

TGTTATACCATGAGTCTTGGAATACTGAAGAATGGGAAAAAAGTAAGACTGAAG
CAGACATGGAAGAGTATATATGGGAAAATAGCTCATCAGAAAGAAATATCCTGG
AAACGCTTCTCCAGATGAAAGCTGCTGAGAAAAATATGGAAATAAATAAAGAAG

AGCTCCTTGGTACTAAAGAAATTGAAGAGTACAAAAAGTCTGTTGTTAGTCTTAA
AAATGAGGAGGAAAATGAAAATTCCATTTCTCAGTACAAAGAATCCGTGAAGAG
ACTATTAAATGTGACACTCGAGTTCAAGAACCTGATCTGGCTGAAGGAGGTGGA
CAGCACCCAGGAGAGACTGAAGGAGTGGAACGTGAGCTACGGC

IV.V MRPS39-BioID2-HA Sequence

AGATTCCTAGAAGTGAGTTGCTGAATGAGCTTATGGACAGTGCAAAAGTGTCTA
ACAGCCCTTCCCAGGCCATTGAAGTAGTAGAGCTGGCAAGTGCCTTCAGCTTACC
TATTTGTGAGGGCCTCACCCAGAGAGTAATGAGTGATTTTGCAATCAACCAGGA
ACAAAAGGAAGCCCTAAGTAATCTAACTGCATTGACCAGTGACAGTGATACTGA
CAGCAGCAGTGACAGCGACAGTGACACCAGTGAAGGCAAACTCGAGTTCAAGA
ACCTGATCTGGCTGAAGGAGGTGGACAGCACCCAGGAGAGACTGAAGGAGTGG
AACGTGAGCTACGGCACCGCCCTGGTGGCCGACAGACAGACCAAG

IV.VI MRPS27-BioID2-HA Sequence

GCATCTAGACCTTGTACAGTTGATCCAGAGAGAACAGCAACAGAGGGAGCAAGC
GAAGCAGGAGTACCAGGCTCAGAAAGCAGCAAAGGCATCTGCCCTCGAGTTCAA
GAACCTGATCTGGCTGAAGGAGGTGGACAGCACCCAGGAGAGACTGAAGGAGT
GGAACGTGAGCTACGGCACCGCCCTGGT

IV.VII SLIRP-BioID2-HA Sequence

TTGGGTTGGGTTCAGTTTTCTTCAGAAGAAGGACTTCGGAATGCACTACAACAGG
AAAATCATATTATAGATGGAGTAAAGGTCCAGGTTCACACTAGAAGGCCAAAAC
TTCCGCAAACATCTGATGATGAAAAGAAAGATTTTCTCGAGTTCAAGAACCTGAT
CTGGCTGAAGGAGGTGGACAGCACCCAGGAGAGACTGAAGGAGTGGAACGTGA
GCTACGGCACCGCCCTGGTGGCCGACAGACAGACCAAGGGC

References

Adler, J., and Parmryd, I. (2010). Quantifying colocalization by correlation: The pearson correlation coefficient is superior to the Mander's overlap coefficient. Cytom. Part A *77*, 733–742.

Aibara, S., Singh, V., Modelska, A., and Amunts, A. (2020). Structural basis of mitochondrial translation. Elife 9, 1–17

Akbergenov, R., Duscha, S., Fritz, A., Juskeviciene, R., Oishi, N., Schmitt, K., Shcherbakov, D., Teo, Y., Boukari, H., Freihofer, P., et al. (2018). Mutant MRPS 5 affects mitoribosomal accuracy and confers stress-related behavioral alterations . EMBO Rep. *19*.

Amunts, A., Brown, A., Toots, J., Scheres, S.H.W., and Ramakrishnan, V. (2015). The structure of the human mitochondrial ribosome. Science *348*, 95–98.

Anderson, S., Bankier, A.T., Barrell, B.G., de Bruijn, M.H.L., Coulson, A.R., Drouin, J., Eperon, I.C., Nierlich, D.P., Roe, B.A., Sanger, F., et al. (1981). Sequence and organization of the human mitochondrial genome. Nature *290*, 457–465.

Andersson, S.G., and Kurland, C.G. (1998). Reductive evolution of resident genomes. Trends Microbiol. *6*, 263–268.

Andrews, R.M., Kubacka, I., Chinnery, P.F., Lightowlers, R.N., Turnbull, D.M., and Howell, N. (1999). Reanalysis and revision of the cambridge reference sequence for human mitochondrial DNA [5]. Nat. Genet. *23*, 147.

Antonicka, H., Sasarman, F., Nishimura, T., Paupe, V., and Shoubridge, E.A. (2013). The mitochondrial RNA-binding protein GRSF1 localizes to RNA granules and is required for posttranscriptional mitochondrial gene expression. Cell Metab. *17*, 386–398.

Antonicka, H., Shoubridge, E.A., Anderson, P., Kedersha, N., Antonicka, H., Ogilvie, I., Taivassalo, T., Anitori, R.P., Haller, R.G., Vissing, J., et al. (2015). Mitochondrial RNA Granules Are Centers for Posttranscriptional RNA Processing and Ribosome Biogenesis. Cell Rep. *10*, 920–932.

Antonicka, H., Lin, Z.Y., Janer, A., Aaltonen, M.J., Weraarpachai, W., Gingras, A.C., and Shoubridge, E.A. (2020). A High-Density Human Mitochondrial Proximity Interaction Network. Cell Metab. *32*, 479-497.e9.

Arroyo, J.D., Jourdain, A.A., Calvo, S.E., Ballarano, C.A., Doench, J.G., Root, D.E., and Mootha, V.K. (2016). A Genome-wide CRISPR Death Screen Identifies Genes Essential for Oxidative Phosphorylation. Cell Metab.

Artal-Sanz, M., and Tavernarakis, N. (2009a). Prohibitin and mitochondrial biology. Trends Endocrinol. Metab. 20, 394–401.

Artal-Sanz, M., and Tavernarakis, N. (2009b). Prohibitin couples diapause signalling to mitochondrial metabolism during ageing in C. elegans. Nature 461, 793–797.

Artal-Sanz, M., and Tavernarakis, N. (2010). Opposing function of mitochondrial prohibitin in aging. Aging (Albany. NY). 2, 1004–1011.

Ban, N., Beckmann, R., Cate, J.H.D., Dinman, J.D., Dragon, F., Ellis, S.R., Lafontaine, D.L.J., Lindahl, L., Liljas, A., Lipton, J.M., et al. (2014). A new system for naming ribosomal proteins. Curr. Opin. Struct. Biol. *24*, 165–169.

Barchiesi, A., and Vascotto, C. (2019). Transcription, Processing, and Decay of Mitochondrial RNA in Health and Disease. Int. J. Mol. Sci. *20*, 2221.

Baughman, J.M., Nilsson, R., Gohil, V.M., Arlow, D.H., Gauhar, Z., and Mootha, V.K. (2009). A computational screen for regulators of oxidative phosphorylation implicates SLIRP in mitochondrial RNA homeostasis. PLoS Genet.

Bavelloni, A., Piazzi, M., Raffini, M., Faenza, I., and Blalock, W.L. (2015). Prohibitin 2: At a communications crossroads. IUBMB Life *67*, 239–254.

Benz, R. (1994). Permeation of hydrophilic solutes through mitochondrial outer membranes: review on mitochondrial porins. Biochim. Biophys. Acta *1197*, 167–196.

Berk, A.J., and Clayton, D.A. (1974). Mechanism of mitochondrial DNA replication in mouse L-cells: Asynchronous replication of strands, segregation of circular daughter molecules, aspects of topology and turnover of an initiation sequence. J. Mol. Biol. *86*, 801–824.

van der Bliek, A.M., Shen, Q., and Kawajiri, S. (2013). Mechanisms of mitochondrial fission and fusion. Cold Spring Harb. Perspect. Biol. *5*, a011072.

Bogenhagen, D.F., Rousseau, D., and Burke, S. (2008). The Layered Structure of Human Mitochondrial DNA Nucleoids. J. Biol. Chem. *283*, 3665–3675.

Bogenhagen, D.F., Martin, D.W., and Koller, A. (2014). Initial steps in RNA processing and ribosome assembly occur at mitochondrial DNA nucleoids. Cell Metab. *19*, 618–629.

Bogenhagen, D.F., Ostermeyer-Fay, A.G., Haley, J.D., and Garcia-Diaz, M. (2018). Kinetics and Mechanism of Mammalian Mitochondrial Ribosome Assembly. Cell Rep. *22*, 1935–1944.

Borna, N.N., Kishita, Y., Kohda, M., Lim, S.C., Shimura, M., Wu, Y., Mogushi, K., Yatsuka, Y., Harashima, H., Hisatomi, Y., et al. (2019). Mitochondrial ribosomal protein PTCD3 mutations cause oxidative phosphorylation defects with Leigh syndrome. Neurogenetics.

Borowski, L.S., Dziembowski, A., Hejnowicz, M.S., Stepien, P.P., and Szczesny, R.J. (2013). Human mitochondrial RNA decay mediated by PNPase-hSuv3 complex takes place in distinct foci. Nucleic Acids Res. *41*, 1223–1240.

Bourges, I., Ramus, C., Mousson De Camaret, B., Beugnot, R., Remacle, C., Cardol, P., Hofhaus, G., and Issartel, J.P. (2004). Structural organization of mitochondrial human complex I: Role of the ND4 and ND5 mitochondria-encoded subunits and interaction with prohibitin. Biochem. J. *383*, 491–499.

Brown, A., Amunts, A., Bai, X.C., Sugimoto, Y., Edwards, P.C., Murshudov, G., Scheres, S.H.W., and Ramakrishnan, V. (2014). Structure of the large ribosomal subunit from human mitochondria. Science (80-.). *346*, 718–722.

Bruni, F., ProctorKent, Y., Lightowlers, R.N., and ChrzanowskaLightowlers, Z.M. (2020). Messenger RNA delivery to mitoribosomes: hints from a bacterial toxin. FEBS J.

Brzezniak, L.K., Bijata, M., Szczesny, R.J., and Stepien, P.P. (2011). Involvement of human ELAC2 gene product in 3' end processing of mitochondrial tRNAs. RNA Biol. *8*, 616–626.

Buchan, J.R. (2014). MRNP granules Assembly, function, and connections with disease. RNA

Biol. *11*, 1019–1030.

Burger, G., Lang, B.F., Reith, M., and Gray, M.W. (1996). Genes encoding the same three subunits of respiratory complex II are present in the mitochondrial DNA of two phylogenetically distant eukaryotes. Proc. Natl. Acad. Sci. U. S. A. *93*, 2328–2332.

Calvo, S.E., Julien, O., Clauser, K.R., Shen, H., Kamer, K.J., Wells, J.A., and Mootha, V.K. (2017). Comparative analysis of mitochondrial N-termini from mouse, human, and yeast. Mol. Cell. Proteomics *16*, 512–523.

Carroll, J., Fearnley, I.M., Skehel, J.M., Shannon, R.J., Hirst, J., and Walker, J.E. (2006). Bovine complex I is a complex of 45 different subunits. J. Biol. Chem. *281*, 32724–32727.

Chang, D.D., and Clayton, D.A. (1984). Precise identification of individual promoters for transcription of each strand of human mitochondrial DNA. Cell *36*, 635–643.

Chapman, J., Ng, Y.S., and Nicholls, T.J. (2020). The maintenance of mitochondrial DNA integrity and dynamics by mitochondrial membranes. Life *10*, 1–42.

Chen, F., Tillberg, P.W., and Boyden, E.S. (2015). Expansion microscopy. Science (80-.). *347*, 543–548.

Chen, F., Wassie, A.T., Cote, A.J., Sinha, A., Alon, S., Asano, S., Daugharthy, E.R., Chang, J.-B., Marblestone, A., Church, G.M., et al. (2016). Nanoscale imaging of RNA with expansion microscopy. Nat. Methods *13*, 679–684.

Chen, H., Detmer, S.A., Ewald, A.J., Griffin, E.E., Fraser, S.E., and Chan, D.C. (2003). Mitofusins Mfn1 and Mfn2 coordinately regulate mitochondrial fusion and are essential for embryonic development. J. Cell Biol. *160*, 189–200.

Chinnery, P.F. (2015). Mitochondrial disease in adults: what's old and what's new? EMBO Mol Med *7*, 1503–1512.

Chomyn, A. (2001). Mitochondrial genetic control of assembly and function of complex I in mammalian cells. J. Bioenerg. Biomembr. *33*, 251–257.

Christian, B.E., and Spremulli, L.L. (2010). Preferential Selection of the 5'-Terminal Start Codon on Leaderless mRNAs by Mammalian Mitochondrial Ribosomes. J. Biol. Chem. *285*, 28379–28386.

Christian, B.E., and Spremulli, L.L. (2012). Mechanism of protein biosynthesis in mammalian mitochondria. Biochim. Biophys. Acta - Gene Regul. Mech. *1819*, 1035–1054.

Christie, D.A., Lemke, C.D., Elias, I.M., Chau, L.A., Kirchhof, M.G., Li, B., Ball, E.H., Dunn, S.D., Hatch, G.M., and Madrenas, J. (2011). Stomatin-Like Protein 2 Binds Cardiolipin and Regulates Mitochondrial Biogenesis and Function. Mol. Cell. Biol. *31*, 3845–3856.

Chrzanowska-Lightowlers, Z.M.A., Preiss, T., and Lightowlers, R.N. (1994). Inhibition of mitochondrial protein synthesis promotes increased stability of nuclear-encoded respiratory gene transcripts.

Chrzanowska-Lightowlers, Z.M.A., Pajak, A., and Lightowlers, R.N. (2011). Termination of protein synthesis in mammalian mitochondria. J. Biol. Chem. *286*, 34479–34485.

Chujo, T., Ohira, T., Sakaguchi, Y., Goshima, N., Nomura, N., Nagao, A., and Suzuki, T. (2012). LRPPRC/SLIRP suppresses PNPase-mediated mRNA decay and promotes polyadenylation in human mitochondria. Nucleic Acids Res. *40*, 8033–8047.

Crosby, A.H., Patel, H., Chioza, B.A., Proukakis, C., Gurtz, K., Patton, M.A., Sharifi, R., Harlalka, G., Simpson, M.A., Dick, K., et al. (2010). Defective mitochondrial mrna maturation is associated with spastic ataxia. Am. J. Hum. Genet. *87*, 655–660.

Da Cruz, S., Parone, P.A., Gonzalo, P., Bienvenut, W. V., Tondera, D., Jourdain, A., Quadroni, M., and Martinou, J.C. (2008). SLP-2 interacts with prohibitins in the mitochondrial inner membrane and contributes to their stability. Biochim. Biophys. Acta - Mol. Cell Res. *1783*, 904–911.

Davies, S.M.K., Rackham, O., Shearwood, A.-M.J., Hamilton, K.L., Narsai, R., Whelan, J., and Filipovska, A. (2009). Pentatricopeptide repeat domain protein 3 associates with the mitochondrial small ribosomal subunit and regulates translation. FEBS Lett. *583*, 1853–1858.

Desai, N., Brown, A., Amunts, A., and Ramakrishnan, V. (2017). The structure of the yeast mitochondrial ribosome. Science (80-.).

Desai, N., Yang, H., Chandrasekaran, V., Kazi, R., Minczuk, M., and Ramakrishnan, V. (2020). Elongational stalling activates mitoribosome-associated quality control. Science (80-.). *370*, 1105–1110.

Diodato, D., Ghezzi, D., Tiranti, V., Diodato, D., Ghezzi, D., and Tiranti, V. (2014). The Mitochondrial Aminoacyl tRNA Synthetases: Genes and Syndromes. Int. J. Cell Biol. *2014*, 787956.

Dubin, D.T., and Taylor, R.H. (1978). Modification of mitochondrial ribosomal RNA from hamster cells: The presence of GmG and late-methylated UmGmU in the large subunit (17 S) RNA. J. Mol. Biol. *121*, 523–540.

Dumbović, G., Sanjuan, X., Perucho, M., and Forcales, S. V. (2020). Stimulated emission depletion (STED) super resolution imaging of RNA- and protein-containing domains in fixed cells. Methods.

Edwards, R., Eaglesfield, R., and Tokatlidis, K. (2021). The mitochondrial intermembrane space: the most constricted mitochondrial sub-compartment with the largest variety of protein import pathways. Open Biol. *11*, 210002.

Embley, T.M., and Martin, W. (2006). Eukaryotic evolution, changes and challenges. Nature *440*, 623–630.

Embley, T.M., van der Giezen, M., Horner, D., Dyal, P., Bell, S., and Foster, P. (2003). Hydrogenosomes, Mitochondria and Early Eukaryotic Evolution. IUBMB Life (International Union Biochem. Mol. Biol. Life) *55*, 387–395.

Endo, T., Yamano, K., and Kawano, S. (2011). Structural insight into the mitochondrial protein import system. Biochim. Biophys. Acta - Biomembr. *1808*, 955–970.

Englmeier, R., Pfeffer, S., and Förster, F. (2017). Structure of the Human Mitochondrial Ribosome Studied In Situ by Cryoelectron Tomography. Structure *25*, 1574-1581.e2.

Falkenberg, M., Gaspari, M., Rantanen, A., Trifunovic, A., Larsson, N.G., and Gustafsson, C.M. (2002). Mitochondrial transcription factors B1 and B2 activate transcription of human mtDNA. Nat. Genet. *31*, 289–294.

Femino, A.M., Fay, F.S., Fogarty, K., and Singer, R.H. (1998). Visualization of single RNA transcripts in situ. Science *280*, 585–590.

Fontanesi, F., Soto, I.C., Horn, D., and Barrientos, A. (2006). Assembly of mitochondrial cytochrome c-oxidase, a complicated and highly regulated cellular process. Am. J. Physiol. - Cell Physiol. *291*, 1129–1147.

Galbraith, C.G., and Galbraith, J.A. (2011). Super-resolution microscopy at a glance. J Cell Sci *124*, 1607–1611.

Gao, M., Maraspini, R., Beutel, O., Zehtabian, A., Eickholt, B., Honigmann, A., and Ewers, H. (2018). Expansion Stimulated Emission Depletion Microscopy (ExSTED). ACS Nano acsnano.8b00776.

Gaur, R., Grasso, D., Datta, P.P., Krishna, P.D.V., Das, G., Spencer, A., Agrawal, R.K., Spremulli, L., and Varshney, U. (2008). A Single Mammalian Mitochondrial Translation Initiation Factor Functionally Replaces Two Bacterial Factors. Mol. Cell *29*, 180–190.

Gohil, V.M., and Greenberg, M.L. (2009). Mitochondrial membrane biogenesis: phospholipids and proteins go hand in hand. J. Cell Biol. *184*, 469–472.

Gohil, V.M., Nilsson, R., Belcher-Timme, C.A., Luo, B., Root, D.E., and Mootha, V.K. (2010). Mitochondrial and nuclear genomic responses to loss of LRPPRC expression. J. Biol. Chem. *285*, 13742–13747.

Gopisetty, G., and Thangarajan, R. (2016). Mammalian mitochondrial ribosomal small subunit (MRPS) genes: A putative role in human disease. Gene *589*, 27–35.

Gray, M.W. (2012). Mitochondrial evolution. Cold Spring Harb. Perspect. Biol. *4*, a011403.

Greber, B.J., Boehringer, D., Leibundgut, M., Bieri, P., Leitner, A., Schmitz, N., Aebersold, R., and Ban, N. (2014). The complete structure of the large subunit of the mammalian mitochondrial ribosome. Nature *515*, 283–286.

Greber, B.J., Bieri, P., Leibundgut, M., Leitner, A., Aebersold, R., Boehringer, D., and Ban, N. (2015). The complete structure of the 55S mammalian mitochondrial ribosome. Science (80-.). *348*, 303–308.

Gustafsson, C.M., Falkenberg, M., and Larsson, N.G. (2016). Maintenance and Expression of Mammalian Mitochondrial DNA. Annu. Rev. Biochem. *85*, 133–160.

He, J., Cooper, H.M., Reyes, A., Di Re, M., Sembongi, H., Gao, J., Neuman, K.C., Fearnley, I.M., Spinazzola, A., Walker, J.E., et al. (2012a). Mitochondrial nucleoid interacting proteins support mitochondrial protein synthesis. Nucleic Acids Res. *40*, 6109–6121.

He, J., Cooper, H.M., Reyes, A., Di Re, M., Sembongi, H., Gao, J., Neuman, K.C., Fearnley, I.M., Spinazzola, A., Walker, J.E., et al. (2012b). Mitochondrial nucleoid interacting proteins support mitochondrial protein synthesis. Nucleic Acids Res. *40*, 6109–6121.

He, Y.E., Qiu, H.X., Jiang, J.B., Wu, R.Z., Xiang, R.L., and Zhang, Y.H. (2017). Microarray analysis reveals key genes and pathways in Tetralogy of Fallot. Mol. Med. Rep. *16*, 2707–2713.

Hell, S.W., and Wichmann, J. (1994). Breaking the diffraction resolution limit by stimulated emission: stimulated-emission-depletion fluorescence microscopy. Opt. Lett. *19*, 780.

Holt, I.J., and Reyes, A. (2012). Human mitochondrial DNA replication. Cold Spring Harb. Perspect. Biol. *4*, a012971.

Holt, I.J., Lorimer, H.E., and Jacobs, H.T. (2000). Coupled leading- and lagging-strand

synthesis of mammalian mitochondrial DNA. Cell *100*, 515–524.

Holzmann, J., Frank, P., Löffler, E., Bennett, K.L., Gerner, C., and Rossmanith, W. (2008). RNase P without RNA: Identification and Functional Reconstitution of the Human Mitochondrial tRNA Processing Enzyme. Cell *135*, 462–474.

Houtkooper, R.H., Mouchiroud, L., Ryu, D., Moullan, N., Katsyuba, E., Knott, G., Williams, R.W., and Auwerx, J. (2013). Mitonuclear protein imbalance as a conserved longevity mechanism. Nature *497*, 451–457.

Hunte, C., Zickermann, V., and Brandt, U. (2010). Functional modules and structural basis of conformational coupling basis of conformational coupling in mitochondrial complex I. Science (80-.). *329*, 448–451.

Ikon, N., and Ryan, R.O. (2017). Cardiolipin and mitochondrial cristae organization. Biochim. Biophys. Acta - Biomembr. *1859*, 1156–1163.

Ishigaki, M., Iketani, M., Sugaya, M., Takahashi, M., Tanaka, M., Hattori, S., and Ohsawa, I. (2016). STED super-resolution imaging of mitochondria labeled with TMRM in living cells. Mitochondrion *28*, 79–87.

Itoh, Y., Andréll, J., Choi, A., Richter, U., Maiti, P., Best, R.B., Barrientos, A., Battersby, B.J., and Amunts, A. (2021). Mechanism of membrane-tethered mitochondrial protein synthesis. Science 371, 846.

Jakobs, S., and Wurm, C.A. (2014). Super-resolution microscopy of mitochondria. Curr. Opin. Chem. Biol. *20*, 9–15.

Jonckheere, A.I., Smeitink, J.A.M., and Rodenburg, R.J.T. (2012). Mitochondrial ATP synthase: Architecture, function and pathology. J. Inherit. Metab. Dis. *35*, 211–225.

Jourdain, A.A., Koppen, M., Wydro, M., Rodley, C.D., Lightowlers, R.N., Chrzanowska-Lightowlers, Z.M., and Martinou, J.-C. (2013). GRSF1 Regulates RNA Processing in Mitochondrial RNA Granules. Cell Metab. *17*, 399–410.

Kamer, K.J., and Mootha, V.K. (2015). The molecular era of the mitochondrial calcium uniporter. Nat. Rev. Mol. Cell Biol. *16*, 545–553.

Kasamatsu, H., and Vinograd, J. (1973). Unidirectionality of Replication in Mouse Mitochondrial DNA. Nature, Publ. Online 24 January 1973; | Doi10.1038/10.1038/Newbio241103a0 *241*, 103.

Kasashima, K., Sumitani, M., Satoh, M., and Endo, H. (2008). Human prohibitin 1 maintains the organization and stability of the mitochondrial nucleoids. Exp. Cell Res. *314*, 988–996.

Kaushal, P.S., Sharma, M.R., Booth, T.M., Haque, E.M., Tung, C.-S., Sanbonmatsu, K.Y., Spremulli, L.L., and Agrawal, R.K. (2014). Cryo-EM structure of the small subunit of the mammalian mitochondrial ribosome. Proc. Natl. Acad. Sci. U. S. A. *111*, 7284–7289.

Khawaja, A., Itoh, Y., Remes, C., Spåhr, H., Yukhnovets, O., Höfig, H., Amunts, A., and Rorbach, J. (2020). Distinct pre-initiation steps in human mitochondrial translation. Nat. Commun. *11*.

Kim, D.I., Jensen, S.C., Noble, K.A., Kc, B., Roux, K.H., Motamedchaboki, K., and Roux, K.J. (2016). An improved smaller biotin ligase for BioID proximity labeling. Mol. Biol. Cell *27*, 1188–1196.

Kitazaki, K., and Kubo, T. (2010). Cost of Having the Largest Mitochondrial Genome: Evolutionary Mechanism of Plant Mitochondrial Genome. J. Bot. *2010*, 1–12.

Klimas, A., Gallagher, B., and Zhao, Y. (2019). Basics of Expansion Microscopy. Curr. Protoc. Cytom. *91*.

Koc, E.C., and Spremulli, L.L. (2002). Identification of Mammalian Mitochondrial Translational Initiation Factor 3 and Examination of Its Role in Initiation Complex Formation with Natural mRNAs. J. Biol. Chem. *277*, 35541–35549.

Koc, E.C., Burkhart, W., Blackburn, K., Moyer, M.B., Schlatzer, D.M., Moseley, A., and Spremulli, L.L. (2001a). The large subunit of the mammalian mitochondrial ribosome: Analysis of the complement of ribosomal proteins present. J. Biol. Chem. *276*, 43958–43969.

Koc, E.C., Burkhart, W., Blackburn, K., Moseley, A., and Spremulli, L.L. (2001b). The small subunit of the mammalian mitochondrial ribosome: Identification of the full complement of ribosomal proteins present. J. Biol. Chem. *276*, 19363–19374.

Kochan, J., Wawro, M., and Kasza, A. (2015). Simultaneous detection of mRNA and protein in single cells using immunofluorescence-combined single-molecule RNA FISH. Biotechniques *59*, 209–221.

Koshiba, T., and Kosako, H. (2020). Mass spectrometry-based methods for analysing the mitochondrial interactome in mammalian cells. J. Biochem. *167*, 225–231.

Kozjak-Pavlovic, V. (2017). The MICOS complex of human mitochondria. Cell Tissue Res. *367*, 83–93.

Kühl, I., Dujeancourt, L., Gaisne, M., Herbert, C.J., and Bonnefoy, N. (2011). A genome wide study in fission yeast reveals nine PPR proteins that regulate mitochondrial gene expression. Nucleic Acids Res. 39, 8029.

Kühl, I., Miranda, M., Posse, V., Milenkovic, D., Mourier, A., Siira, S.J., Bonekamp, N.A., Neumann, U., Filipovska, A., Polosa, P.L., et al. (2016). POLRMT regulates the switch between replication primer formation and gene expression of mammalian mtDNA. Sci. Adv. *2*.

Kühlbrandt, W. (2015). Structure and function of mitochondrial membrane protein complexes. BMC Biol. *13*, 89.

Kummer, E., Schubert, K.N., Schoenhut, T., Scaiola, A., and Ban, N. (2021). Structural basis of translation termination, rescue, and recycling in mammalian mitochondria. Mol. Cell.

Kunz, T.C., Götz, R., Gao, S., Sauer, M., and Kozjak-Pavlovic, V. (2020). Using Expansion Microscopy to Visualize and Characterize the Morphology of Mitochondrial Cristae. Front. Cell Dev. Biol. *8*.

Kwon, K., and Beckett, D. (2000). Function of a conserved sequence motif in biotin holoenzyme synthetases. Protein Sci. *9*, 1530–1539.

Labrousse, A.M., Zappaterra, M.D., Rube, D.A., and Van der Bliek, A.M. (1999). C. elegans dynamin-related protein DRP-1 controls severing of the mitochondrial outer membrane. Mol. Cell *4*, 815–826.

Lagouge, M., Mourier, A., Lee, H.J., Spåhr, H., Wai, T., Kukat, C., Silva Ramos, E., Motori, E., Busch, J.D., Siira, S., et al. (2015). SLIRP Regulates the Rate of Mitochondrial Protein

Synthesis and Protects LRPPRC from Degradation. PLOS Genet. 11, e1005423.

Lai, C.H., Chou, C.Y., Ch'ang, L.Y., Liu, C.S., and Lin, W.C. (2000). Identification of novel human genes evolutionarily conserved in Caenorhabditis elegans by comparative proteomics. Genome Res. *10*, 703–713.

Landmann, L. (2002). Deconvolution improves colocalization analysis of multiple fluorochromes in 3d confocal data sets more than filtering techniques. J. Microsc. *208*, 134–147.

Lang, B.F., Gray, M.W., and Burger, G. (1999). Mitochondrial Genome Evolution and the Origin of Eukaryotes. Annu. Rev. Genet. *33*, 351–397.

Lee, K.W., and Bogenhagen, D.F. (2014). Assignment of 2′-O-methyltransferases to modification sites on the mammalian mitochondrial large subunit 16 S ribosomal RNA (rRNA). J. Biol. Chem. *289*, 24936–24942.

Lightowlers, R.N., and Chrzanowska-Lightowlers, Z.M.A. (2013). Human pentatricopeptide proteins: only a few and what do they do? RNA Biol. *10*, 1433–1438.

Lightowlers, R.N., Taylor, R.W., and Turnbull, D.M. (2015). Mutations causing mitochondrial disease: What is new and what challenges remain? Science (80-.). *349*.

Lill, R. (2009). Function and biogenesis of iron–sulphur proteins. Nature *460*, 831–838.

Litonin, D., Sologub, M., Shi, Y., Savkina, M., Anikin, M., Falkenberg, M., Gustafsson, C.M., and Temiakov, D. (2010). Human mitochondrial transcription revisited: Only TFAM and TFB2M are required for transcription of the mitochondrial genes in vitro. J. Biol. Chem. *285*, 18129–18133.

Liyanage, S.U., Coyaud, E., Laurent, E.M.N., Hurren, R., Maclean, N., Wood, S.R., Kazak, L., Shamas-Din, A., Holt, I., Raught, B., et al. (2017). Characterizing the mitochondrial DNA polymerase gamma interactome by BioID identifies Ruvbl2 localizes to the mitochondria. Mitochondrion *32*, 31–35.

Lodeiro, M.F., Uchida, A., Bestwick, M., Moustafa, I.M., Arnold, J.J., Shadel, G.S., and Cameron, C.E. (2012). Transcription from the second heavy-strand promoter of human mtDNA is repressed by transcription factor A in vitro. Proc. Natl. Acad. Sci. U. S. A. *109*, 6513–6518.

Lopez Sanchez, M.I.G., Cipullo, M., Gopalakrishna, S., Khawaja, A., and Rorbach, J. (2020). Methylation of Ribosomal RNA: A Mitochondrial Perspective. Front. Genet. 0, 761.

Lourenço, A.B., Muñoz-Jiménez, C., Venegas-Calerón, M., and Artal-Sanz, M. (2015). Analysis of the effect of the mitochondrial prohibitin complex, a context-dependent modulator of longevity, on the C. elegans metabolome. Biochim. Biophys. Acta 1847, 1457–1468.

Luo, Y., Wang, Y., and Huang, Y. (2021). Schizosaccharomyces pombe Ppr10 and Mpa1 together mediate mitochondrial translational initiation. J. Biol. Chem. 297.

Mai, N., Chrzanowska-Lightowlers, Z.M.A., and Lightowlers, R.N. (2016). The process of mammalian mitochondrial protein synthesis. Cell Tissue Res. 1–16.

Manders, E.M.M., Verbeek, F.J., and Aten, J.A. (1993). Measurement of co-localization of objects in dual-colour confocal images. J. Microsc. *169*, 375–382.

Mannella, C.A. (1992). The "ins" and "outs" of mitochondrial membrane channels. Trends

Biochem. Sci. *17*, 315–320.

Martinou, J.-C., and Youle, R.J. (2011). Mitochondria in Apoptosis: Bcl-2 Family Members and Mitochondrial Dynamics. Dev. Cell *21*, 92–101.

Masmoudi, S., Charfedine, I., Rebeh, I., Rebai, A., Tlili, A., Ghorbel, A., Belguith, H., Petit, C., Drira, M., and Ayadi, H. (2004). Refined mapping of the autosomal recessive non-syndromic deafness locus DFNB13 using eight novel microsatellite markers. Clin. Genet. *66*, 358–364.

Mays, J.N., Camacho-Villasana, Y., Garcia-Villegas, R., Perez-Martinez, X., Barrientos, A., and Fontanesi, F. (2019). The mitoribosome-specific protein mS38 is preferentially required for synthesis of cytochrome c oxidase subunits. Nucleic Acids Res. *47*, 5746–5760.

McKinney, E.A., and Oliveira, M.T. (2013). Replicating animal mitochondrial DNA. Genet. Mol. Biol. *36*, 308–315.

Mclean, J.R., Cohn, G.L., Brandt, I.K., and Simpson, M. V. (1958). Incorporation of labeled amino acids into the protein of muscle and liver mitochondria. J. Biol. Chem. *233*, 657–663.

Mears, J.A., Lackner, L.L., Fang, S., Ingerman, E., Nunnari, J., and Hinshaw, J.E. (2011). Conformational changes in Dnm1 support a contractile mechanism for mitochondrial fission. Nat. Struct. Mol. Biol. *18*, 20–26.

Mercer, T.R., Neph, S., Dinger, M.E., Crawford, J., Smith, M.A., Shearwood, A.-M.J., Haugen, E., Bracken, C.P., Rackham, O., Stamatoyannopoulos, J.A., et al. (2011a). The human mitochondrial transcriptome. Cell *146*, 645–658.

Mercer, T.R., Neph, S., Dinger, M.E., Crawford, J., Smith, M.A., Shearwood, A.M.J., Haugen, E., Bracken, C.P., Rackham, O., Stamatoyannopoulos, J.A., et al. (2011b). The human mitochondrial transcriptome. Cell *146*, 645–658.

Merkwirth, C., and Langer, T. (2009). Prohibitin function within mitochondria: Essential roles for cell proliferation and cristae morphogenesis. Biochim. Biophys. Acta - Mol. Cell Res. *1793*, 27–32.

Merkwirth, C., Martinelli, P., Korwitz, A., Morbin, M., Brönneke, H.S., Jordan, S.D., Rugarli, E.I., and Langer, T. (2012). Loss of Prohibitin Membrane Scaffolds Impairs Mitochondrial Architecture and Leads to Tau Hyperphosphorylation and Neurodegeneration. PLOS Genet. 8, e1003021.

Metodiev, M.D., Lesko, N., Park, C.B., Cámara, Y., Shi, Y., Wibom, R., Hultenby, K., Gustafsson, C.M., and Larsson, N.G. (2009). Methylation of 12S rRNA Is Necessary for In Vivo Stability of the Small Subunit of the Mammalian Mitochondrial Ribosome. Cell Metab. *9*, 386–397.

Metodiev, M.D., Spåhr, H., Loguercio Polosa, P., Meharg, C., Becker, C., Altmueller, J., Habermann, B., Larsson, N.-G., and Ruzzenente, B. (2014). NSUN4 Is a Dual Function Mitochondrial Protein Required for Both Methylation of 12S rRNA and Coordination of Mitoribosomal Assembly. PLoS Genet. *10*, e1004110.

Mick, D.U., Dennerlein, S., Wiese, H., Reinhold, R., Pacheu-Grau, D., Lorenzi, I., Sasarman, F., Weraarpachai, W., Shoubridge, E.A., Warscheid, B., et al. (2012). MITRAC Links Mitochondrial Protein Translocation to Respiratory-Chain Assembly and Translational Regulation. Cell *151*, 1528–1541.

Mitchell, P. (1967). Proton current flow in mitochondrial systems [12]. Nature *214*, 1327–1328.

Mitsopoulos, P., Lapohos, O., Weraarpachai, W., Antonicka, H., Chang, Y.-H., and Madrenas, J. (2017). Stomatin-like protein 2 deficiency results in impaired mitochondrial translation. PLoS One *12*, e0179967.

Mohanraj, K., Nowicka, U., and Chacinska, A. (2020). Mitochondrial control of cellular protein homeostasis. Biochem. J. *477*, 3033–3054.

Mokranjac, D., Popov-Čeleketić, D., Hell, K., and Neupert, W. (2005). Role of Tim21 in mitochondrial translocation contact sites. J. Biol. Chem. *280*, 23437–23440.

Mulkidjanian, A.Y. (2010). Activated Q-cycle as a common mechanism for cytochrome bc1 and cytochrome b6f complexes. Biochim. Biophys. Acta - Bioenerg. *1797*, 1858–1868.

Murphy, M., Choo, K.B., Macreadie, I., Marzuki, S., Lukins, H.B., Nagley, P., and Linnane, A.W. (1980). Biogenesis of mitochondria: A temperature sensitivity mutation affecting the mitochondrially synthesized var1 protein of Saccharomyces cerevisiae. Arch. Biochem. Biophys. *203*, 260–270.

Nagaike, T., Suzuki, T., Tomari, Y., Takemoto-Hori, C., Negayama, F., Watanabe, K., and Ueda, T. (2001). Identification and Characterization of Mammalian Mitochondrial tRNA nucleotidyltransferases. J. Biol. Chem. *276*, 40041–40049.

Nagaike, T., Suzuki, T., Katoh, T., and Ueda, T. (2005). Human mitochondrial mRNAs are stabilized with polyadenylation regulated by mitochondria-specific poly(A) polymerase and polynucleotide phosphorylase. J. Biol. Chem. *280*, 19721–19727.

Neupert, W., and Herrmann, J.M. (2007). Translocation of proteins into mitochondria. Annu. Rev. Biochem. *76*, 723–749.

Nicholls, T.J., Nadalutti, C.A., Motori, E., Sommerville, E.W., Gorman, G.S., Basu, S., Hoberg, E., Turnbull, D.M., Chinnery, P.F., Larsson, N.G., et al. (2018). Topoisomerase 3α Is Required for Decatenation and Segregation of Human mtDNA. Mol. Cell *69*, 9-23.e6.

Nijtmans, L.G.J., De Jong, L., Sanz, M.A., Coates, P.J., Berden, J.A., Back, J.W., Muijsers, A.O., Van Der Spek, H., and Grivell, L.A. (2000). Prohibitins act as a membrane-bound chaperone for the stabilization of mitochondrial proteins. EMBO J. *19*, 2444–2451.

O'Brien, T.W. (1971). The general occurrence of 55 S ribosomes in mammalian liver mitochondria. J. Biol. Chem. *246*, 3409–3417.

Oláhová, M., Hardy, S.A., Hall, J., Yarham, J.W., Haack, T.B., Wilson, W.C., Alston, C.L., He, L., Aznauryan, E., Brown, R.M., et al. (2015). LRPPRC mutations cause early-onset multisystem mitochondrial disease outside of the French-Canadian population. Brain *138*, 3503–3519.

Osawa, S., Jukes, T.H., Watanabe, K., and Muto, A. (1992). Recent evidence for evolution of the genetic code. Microbiol. Rev. *56*, 229–264.

Osman, C., Merkwirth, C., and Langer, T. (2009). Prohibitins and the functional compartmentalization of mitochondrial membranes. J. Cell Sci. *122*, 3823–3830.

Ow, Y.-L.P., Green, D.R., Hao, Z., and Mak, T.W. (2008). Cytochrome c: functions beyond respiration. Nat. Rev. Mol. Cell Biol. *9*, 532–542.

Peng, Y.T., Chen, P., Ouyang, R.Y., and Song, L. (2015). Multifaceted role of prohibitin in cell survival and apoptosis. Apoptosis 20, 1135–1149.

Perrone, E., Cavole, T.R., Oliveira, M.G., Virmond, L.D.A., Silva, M. de F.B., Soares, M. de F.F., Iglesias, S.B. de O., Falconi, A., Silva, J.S., Nakano, V., et al. (2020). Leigh syndrome in a patient with a novel c12orf65 pathogenic variant: Case report and literature review. Genet. Mol. Biol. *43*.

Pfeffer, S., Woellhaf, M.W., Herrmann, J.M., and Förster, F. (2015). Organization of the mitochondrial translation machinery studied in situ by cryoelectron tomography. Nat. Commun. *6*, 6019.

Pham, D.H., Moretti, P.A.B., Goodall, G.J., and Pitson, S.M. (2018). Attenuation of leakiness in doxycycline-inducible expression via incorporation of 3′ AU-rich mRNA destabilizing elements. Https://Doi.Org/10.2144/000112896 45, 155–162.

Popow, J., Alleaume, A.M., Curk, T., Schwarzl, T., Sauer, S., and Hentze, M.W. (2015). FASTKD2 is an RNA-binding protein required for mitochondrial RNA processing and translation. RNA *21*, 1873–1884.

Priesnitz, C., and Becker, T. (2018). Pathways to balance mitochondrial translation and protein import. Genes Dev. *32*, 1285–1296.

Rackham, O., Mercer, T.R., and Filipovska, A. (2012). The human mitochondrial transcriptome and the RNA-binding proteins that regulate its expression. Wiley Interdiscip. Rev. RNA 3, 675–695.

Raj, A., van den Bogaard, P., Rifkin, S.A., van Oudenaarden, A., and Tyagi, S. (2008). Imaging individual mRNA molecules using multiple singly labeled probes. Nat. Methods *5*, 877–879.

Ray, P.D., Huang, B.-W., and Tsuji, Y. (2012). Reactive oxygen species (ROS) homeostasis and redox regulation in cellular signaling. Cell. Signal. *24*, 981–990.

Renner, L.D., and Weibel, D.B. (2011). Cardiolipin microdomains localize to negatively curved regions of Escherichia coli membranes. Proc. Natl. Acad. Sci. U. S. A. *108*, 6264–6269.

Richter-Dennerlein, R., Dennerlein, S., and Rehling, P. (2015). Integrating mitochondrial translation into the cellular context. Nat. Rev. Mol. Cell Biol. *16*, 586–592.

Richter-Dennerlein, R., Oeljeklaus, S., Lorenzi, I., Ronsor, C., Bareth, B., Schendzielorz, A.B., Wang, C., Warscheid, B., Rehling, P., and Dennerlein, S. (2016). Mitochondrial Protein Synthesis Adapts to Influx of Nuclear-Encoded Protein. Cell *167*, 471-483 e10.

Richter, R., Rorbach, J., Pajak, A., Smith, P.M., Wessels, H.J., Huynen, M.A., Smeitink, J.A., Lightowlers, R.N., and Chrzanowska-Lightowlers, Z.M. (2010). A functional peptidyl-tRNA hydrolase, ICT1, has been recruited into the human mitochondrial ribosome. EMBO J. *29*, 1116–1125.

Rizzuto, R., De Stefani, D., Raffaello, A., and Mammucari, C. (2012). Mitochondria as sensors and regulators of calcium signalling. Nat. Rev. Mol. Cell Biol. *13*, 566–578.

Robberson, D.L., Kasamatsu, H., and Vinograd, J. (1972). Replication of mitochondrial DNA. Circular replicative intermediates in mouse L cells. Proc. Natl. Acad. Sci. U. S. A. *69*, 737–741.

Roises, D., and Schatz, G. (1988). THE JOURNAL OF BIOLOGICAL CHEMISTRY

Mitochondrial Presequences".

Rorbach, J., Boesch, P., Gammage, P.A., Nicholls, T.J.J., Pearce, S.F., Patel, D., Hauser, A., Perocchi, F., and Minczuk, M. (2014). MRM2 and MRM3 are involved in biogenesis of the large subunit of the mitochondrial ribosome. Mol. Biol. Cell *25*, 2542–2555.

Rorbach, J., Gao, F., Powell, C.A., D'Souza, A., Lightowlers, R.N., Minczuk, M., and Chrzanowska-Lightowlers, Z.M. (2016). Human mitochondrial ribosomes can switch their structural RNA composition. Proc. Natl. Acad. Sci. U. S. A. *113*, 12198–12201.

Roux, K.J., Kim, D.I., Raida, M., and Burke, B. (2012). A promiscuous biotin ligase fusion protein identifies proximal and interacting proteins in mammalian cells. J. Cell Biol. *196*, 801–810.

Russell, O., and Turnbull, D. (2014). Mitochondrial DNA disease—molecular insights and potential routes to a cure. Exp. Cell Res. *325*, 38–43.

Rustin, P., Bourgeron, T., Parfait, B., Chretien, D., Munnich, A., and Rötig, A. (1997). Inborn errors of the Krebs cycle: a group of unusual mitochondrial diseases in human. Biochim. Biophys. Acta *1361*, 185–197.

Rutter, J., Winge, D.R., and Schiffman, J.D. (2010). Succinate dehydrogenase - Assembly, regulation, and role in human disease. Mitochondrion *10*, 393–401.

Ruzzenente, B., Metodiev, M.D., Wredenberg, A., Bratic, A., Park, C.B., Cámara, Y., Milenkovic, D., Zickermann, V., Wibom, R., Hultenby, K., et al. (2012). LRPPRC is necessary for polyadenylation and coordination of translation of mitochondrial mRNAs. EMBO J. 31, 443–456.

Saraste, M. (1999). Oxidative phosphorylation at the fin de siecle. Science (80-.). *283*, 1488–1493.

Sasarman, F., Nishimura, T., Antonicka, H., Weraarpachai, W., Shoubridge, E.A., Allen, B., Burelle, Y., Charron, G., Coderre, L., DesRosiers, C., et al. (2015). Tissue-specific responses to the LRPPRC founder mutation in French Canadian Leigh Syndrome. Hum. Mol. Genet.

Scarpulla, R.C. (2008). Transcriptional paradigms in mammalian mitochondrial biogenesis and function. Physiol. Rev. *88*, 611–638.

Schneider, R.E., Brown, M.T., Shiflett, A.M., Dyall, S.D., Hayes, R.D., Xie, Y., Loo, J.A., and Johnson, P.J. (2011). The Trichomonas vaginalis hydrogenosome proteome is highly reduced relative to mitochondria, yet complex compared with mitosomes. Int. J. Parasitol. *41*, 1421–1434.

Sharma, M.R., Koc, E.C., Datta, P.P., Booth, T.M., Spremulli, L.L., and Agrawal, R.K. (2003). Structure of the mammalian mitochondrial ribosome reveals an expanded functional role for its component proteins. Cell *115*, 97–108.

Signorile, A., Sgaramella, G., Bellomo, F., and De Rasmo, D. (2019). Prohibitins: A Critical Role in Mitochondrial Functions and Implication in Diseases. Cells *8*, 71.

Silva, J., Aivio, S., Knobel, P.A., Bailey, L.J., Casali, A., Vinaixa, M., Garcia-Cao, I., Coyaud, É., Jourdain, A.A., Pérez-Ferreros, P., et al. (2018). EXD2 governs germ stem cell homeostasis and lifespan by promoting mitoribosome integrity and translation. Nat. Cell Biol. *20*, 162–174.

Smith, D.R., and Keeling, P.J. (2015). Mitochondrial and plastid genome architecture:

Reoccurring themes, but significant differences at the extremes. Proc. Natl. Acad. Sci. U. S. A. *112*, 10177–10184.

Smits, P., Smeitink, J., and van den Heuvel, L. (2010). Mitochondrial translation and beyond: processes implicated in combined oxidative phosphorylation deficiencies. J. Biomed. Biotechnol. *2010*, 737385.

Spåhr, H., Rozanska, A., Li, X., Atanassov, I., Lightowlers, R.N., Chrzanowska-Lightowlers, Z.M.A., Rackham, O., and Larsson, N.-G. (2016). SLIRP stabilizes LRPPRC via an RRM–PPR protein interface. Nucleic Acids Res. *44*, 6868–6882.

St-Pierre, J., Drori, S., Uldry, M., Silvaggi, J.M., Rhee, J., Jäger, S., Handschin, C., Zheng, K., Lin, J., Yang, W., et al. (2006). Suppression of Reactive Oxygen Species and Neurodegeneration by the PGC-1 Transcriptional Coactivators. Cell *127*, 397–408.

De Stefani, D., Raffaello, A., Teardo, E., Szabò, I., and Rizzuto, R. (2011). A forty-kilodalton protein of the inner membrane is the mitochondrial calcium uniporter. Nature *476*, 336–340.

Stephan, T., Roesch, A., Riedel, D., and Jakobs, S. (2019). Live-cell STED nanoscopy of mitochondrial cristae. Sci. Rep. *9*.

Stokes, G. (1852). On the change of refrangibility of light. Philos. Trans. R. Soc. London *142*, 463–562.

Synetos, D., Frantziou, C.P., and Alksne, L.E. (1996). Mutations in yeast ribosomal proteins S28 and S4 affect the accuracy of translation and alter the sensitivity of the ribosomes to paromomycin. Biochim. Biophys. Acta *1309*, 156–166.

Tamura, Y., Harada, Y., Shiota, T., Yamano, K., Watanabe, K., Yokota, M., Yamamoto, H., Sesaki, H., and Endo, T. (2009). Tim23 - Tim50 pair coordinates functions of translocators and motor proteins in mitochondrial protein import. J. Cell Biol. *184*, 129–141.

Taylor, R.W., and Turnbull, D.M. (2005). Mitochondrial DNA mutations in human disease. Nat. Rev. Genet. *6*, 389–402.

Temperley, R., Richter, R., Dennerlein, S., Lightowlers, R.N., and Chrzanowska-Lightowlers, Z.M. (2010a). Hungry Codons Promote Frameshifting in Human Mitochondrial Ribosomes. Science (80-.). *327*, 301–301.

Temperley, R.J., Seneca, S.H., Tonska, K., Bartnik, E., Bindoff, L.A., Lightowlers, R.N., and Chrzanowska-Lightowlers, Z.M.A. (2003). Investigation of a pathogenic mtDNA microdeletion reveals a translation-dependent deadenylation decay pathway in human mitochondria. Hum. Mol. Genet. *12*, 2341–2348.

Temperley, R.J., Wydro, M., Lightowlers, R.N., and Chrzanowska-Lightowlers, Z.M. (2010b). Human mitochondrial mRNAs-like members of all families, similar but different. Biochim. Biophys. Acta - Bioenerg. *1797*, 1081–1085.

Terpstra, P., Zanders, E., and Butow, R.A. (1979). The association of var1 with the 38 S mitochondrial ribosomal subunit in yeast. J. Biol. Chem. *254*, 12653–12661.

Terzioglu, M., Ruzzenente, B., Harmel, J., Mourier, A., Jemt, E., López, M.D., Kukat, C., Stewart, J.B., Wibom, R., Meharg, C., et al. (2013). MTERF1 Binds mtDNA to prevent transcriptional interference at the light-strand promoter but is dispensable for rRNA gene transcription regulation. Cell Metab. 17, 618–626.

Thuaud, F., Ribeiro, N., Nebigil, C.G., and Désaubry, L. (2013). Prohibitin ligands in cell death and survival: Mode of action and therapeutic potential. Chem. Biol. *20*, 316–331.

Timmis, J.N., Ayliffe, M.A., Huang, C.Y., and Martin, W. (2004). Endosymbiotic gene transfer: organelle genomes forge eukaryotic chromosomes. Nat. Rev. Genet. *5*, 123–135.

Tomecki, R., Dmochowska, A., Gewartowski, K., Dziembowski, A., and Stepien, P.P. (2004). Identification of a novel human nuclear-encoded mitochondrial poly(A) polymerase. Nucleic Acids Res. *32*, 6001–6014.

Trinkle-Mulcahy, L. (2019). Recent advances in proximity-based labeling methods for interactome mapping. F1000Research *8*.

Tsuboi, M., Morita, H., Nozaki, Y., Akama, K., Ueda, T., Ito, K., Nierhaus, K.H., and Takeuchi, N. (2009). EF-G2mt Is an Exclusive Recycling Factor in Mammalian Mitochondrial Protein Synthesis. Mol. Cell *35*, 502–510.

Tsutsumi, T., Matsuda, M., Aizaki, H., Moriya, K., Miyoshi, H., Fujie, H., Shintani, Y., Yotsuyanagi, H., Miyamura, T., Suzuki, T., et al. (2009). Proteomics analysis of mitochondrial proteins reveals overexpression of a mitochondrial protein chaperon, prohibitin, in cells expressing hepatitis C virus core protein. Hepatology *50*, 378–386.

Tu, Y.T., and Barrientos, A. (2015). The Human Mitochondrial DEAD-Box Protein DDX28 Resides in RNA Granules and Functions in Mitoribosome Assembly. Cell Rep. *10*, 854–864.

Tyanova, S., Temu, T., Sinitcyn, P., Carlson, A., Hein, M.Y., Geiger, T., Mann, M., and Cox, J. (2016). The Perseus computational platform for comprehensive analysis of (prote)omics data. Nat. Methods *13*, 731–740.

Uhler, J.P., and Falkenberg, M. (2021). In Vitro Analysis of mtDNA Replication. In Methods in Molecular Biology, (Humana Press Inc.), pp. 1–20.

Wang, C., and Youle, R.J. (2009). The role of mitochondria in apoptosis. Annu. Rev. Genet. *43*, 95–118.

Wang, C., Richter-Dennerlein, R., Pacheu-Grau, D., Liu, F., Zhu, Y., Dennerlein, S., and Rehling, P. (2020). MITRAC15/COA1 promotes mitochondrial translation in a ND2 ribosome–nascent chain complex. EMBO Rep. *21*, e48833.

Wang, Z., Yan, X., and Zhao, C. (2017). Dynamical differential networks and modules inferring disrupted genes associated with the progression of Alzheimer's disease. Exp. Ther. Med. *14*, 2969–2975.

Wei, Y., Chiang, W.C., Sumpter, R., Mishra, P., and Levine, B. (2017). Prohibitin 2 Is an Inner Mitochondrial Membrane Mitophagy Receptor. Cell 168, 224.

Weraarpachai, W., Antonicka, H., Sasarman, F., Seeger, J., Schrank, B., Kolesar, J.E., Lochmüller, H., Chevrette, M., Kaufman, B.A., Horvath, R., et al. (2009). Mutation in TACO1, encoding a translational activator of COX I, results in cytochrome c oxidase deficiency and late-onset Leigh syndrome. Nat. Genet. 41, 833–837.

Wiedemann, N., and Pfanner, N. (2017). Mitochondrial Machineries for Protein Import and Assembly. Annu. Rev. Biochem. *86*, 685–714.

Wiesner, R.J., Rüegg, J.C., and Morano, I. (1992). Counting target molecules by exponential polymerase chain reaction: copy number of mitochondrial DNA in rat tissues. Biochem.

Biophys. Res. Commun. *183*, 553–559.

Wilson, W.C., Hornig-Do, H.T., Bruni, F., Chang, J.H. o., Jourdain, A.A., Martinou, J.C., Falkenberg, M., Spåhr, H., Larsson, N.G., Lewis, R.J., et al. (2014). A human mitochondrial poly(A) polymerase mutation reveals the complexities of post-transcriptional mitochondrial gene expression. Hum. Mol. Genet. *23*, 6345–6355.

Wredenberg, A., Lagouge, M., Bratic, A., Metodiev, M.D., Spåhr, H., Mourier, A., Freyer, C., Ruzzenente, B., Tain, L., Grönke, S., et al. (2013). MTERF3 Regulates Mitochondrial Ribosome Biogenesis in Invertebrates and Mammals. PLoS Genet. *9*, 1003178.

Wu, Z., Cuthbert, J.M., Taylor, D.R., and Sloan, D.B. (2015). The massive mitochondrial genome of the angiosperm Silene noctiflora is evolving by gain or loss of entire chromosomes. Proc. Natl. Acad. Sci. U. S. A. *112*, 10185–10191.

Yin, P., Li, Q., Yan, C., Liu, Y., Liu, J., Yu, F., Wang, Z., Long, J., He, J., Wang, H.W., et al. (2013). Structural basis for the modular recognition of single-stranded RNA by PPR proteins. Nature *504*, 168–171.

Yoshinaka, T., Kosako, H., Yoshizumi, T., Furukawa, R., Hirano, Y., Kuge, O., Tamada, T., and Koshiba, T. (2019). Structural Basis of Mitochondrial Scaffolds by Prohibitin Complexes: Insight into a Role of the Coiled-Coil Region. IScience *19*, 1065–1078.

Zeiss Acquiring and Analyzing Data for Colocalization Experiments in AIM or ZEN Software.

Zhang, C., Kang, J.S., Asano, S.M., Gao, R., and Boyden, E.S. (2020). Expansion Microscopy for Beginners: Visualizing Microtubules in Expanded Cultured HeLa Cells. Curr. Protoc. Neurosci. *92*.

Zheng, Z., Li, H., Zhang, Q., Yang, L., and Qi, H. (2016). Unequal distribution of 16S mtrRNA at the 2-cell stage regulates cell lineage allocations in mouse embryos. REPRODUCTION *151*, 351–367.

Zhu, J., Vinothkumar, K.R., and Hirst, J. (2016). Structure of mammalian respiratory complex I. Nature *536*, 354–358.

Zinchuk, V., Wu, Y., and Grossenbacher-Zinchuk, O. (2013). Bridging the gap between qualitative and quantitative colocalization results in fluorescence microscopy studies. Sci. Rep. *3*.

Zorkau, M., Proctor-Kent, Y., Berlinguer-Palmini, R., Hamilton, A., Chrzanowska-Lightowlers, Z.M., and Lightowlers, R.N. (2021). Visualizing Mitochondrial Ribosomal RNA and Mitochondrial Protein Synthesis in Human Cell Lines. In Methods in Molecular Biology, (Humana Press Inc.), pp. 159–181.

STED Microscopy | Scientific Volume Imaging.